APPLICATION OF ELECTRONIC STRUCTURE CALCULATIONS TO VIBRATIONAL SPECTROSCOPY AND GAS ENCAPSULATION IN ZEOLITES

A Dissertation

presented to

the Faculty of the Graduate School

at the University of Missouri

In Partial Fulfillment

of the Requirements for the Degree

Doctor of Philosophy

---

by

AMIR MEHDI MOFRAD

Dr. Karl D. Hammond, Dissertation Supervisor

DECEMBER 2020

The undersigned, appointed by the dean of the Graduate School, have examined the dissertation entitled

APPLICATION OF ELECTRONIC STRUCTURE CALCULATIONS
TO VIBRATIONAL SPECTROSCOPY AND GAS
ENCAPSULATION IN ZEOLITES

presented by Amir Mehdi Mofrad,
a candidate for the degree of Doctor of Philosophy,
and hereby certify that, in their opinion, it is worthy of acceptance.

Professor Karl D. Hammond, chair

Professor Heather K. Hunt, member

Professor Patrick J. Pinhero, member

Professor Bret D. Ulery, member

To my family, whose support and love has always been unconditional.

“We never are right, we can only be sure we are wrong.”

—Richard Feynman

ACKNOWLEDGMENTS

First and foremost, I express my sincere gratitude and appreciation to my advisor, Professor Karl Hammond, for all of his continual support, encouragement, and mentorship throughout my time at Mizzou. I have been fortunate to work in his lab for five and a half years, and none of this work would have been possible without his help, suggestions, and care to teach and convey information. I will always be grateful to him for giving me this opportunity and believing in me.

I also owe special thanks to my committee members, Professor Patrick Pinhero, Professor Heather Hunt, and Professor Bret Ulery. Their suggestions and inputs have been very helpful during both my qualifying and comprehensive exams. They have always been kind and supportive to me in my studies.

I also thank my office mates, some of whom have already graduated and some who are still here. I am really grateful for having the opportunity to work with you all. I hope I am not missing anyone: Jiasen Guo, Rafi Iasir, Andrea Saltos, Zhuocen Yang, Brandon Laufer, Luke Kruse, Cannon Hackett, Brandon Lee, Joshua MacGregor, Gabriel Ort, Kaylee (née Libbert) Parr, Chase Skawinski, Marissa Zirges, Maria de Almeida Monteiro, Anqi Zhang, Valerie Wilson, Jason Ogle, Derek Ruff, Parker Schellenberg, Ian Naeger, Kenneth Distefano, James Congdon, and Zachary Valleroy.

Great recognition should be given to my girlfriend Peyton Flewelling. I met her in the Ellis library in my second year and ever since she has always been supportive during my studies. She has always been there for me during rigorous and stressful times. Words cannot describe how much I am grateful for having her in my life.

I owe special thanks to my best friend James Hopfenblatt. I first met him at "The Shack" in the Student Center playing pool during my first semester. He has always been a

good, supportive friend. He and his family always tried to look after me and made me feel like I had a second family here. I am grateful to have met him and call him my best friend.

During my time at Mizzou, I had the privilege to meet other graduate students from different countries who became my friends. People who shared the same lifestyle, concerns, and so on, including David and Lale Porciani, Habib A Islam, Hedieh Attai, Carlos and Melissa Martinez, Morgan Halane, Veniamin Katykhov, Amanda Howland, Lisa Shephard, Hamid Sepassi, and Omid Taleghani.

I also thank the Persian Community at Mizzou. They are doing a great job in terms of welcoming new students (regardless of whether you are an undergraduate or graduate student, international or non-international) into their community. I recommend stopping by in case there is an event. There will be lots of delicious Persian food.

I thank the Research Computing Support Services (RCSS) group, who are in charge of maintaining our computer cluster on campus (named Lewis) and providing support to us whenever needed. All of the results in this dissertation were obtained using that resource. I had the privilege to meet with many of the individuals working there, including Dr. Middelkoop, Jacob Gotberg, Predrag, Ahmed, Brian, Quinn, and Derek.

Most important, I thank my parents, Farzaneh Dadkhah and Ahmad Mofrad. It has been 5 years and 8 months since I last saw them. Their support and love have always been unconditional. I love them both and I hope to see them soon. Huge appreciation should be given to my sister, Ghazal, and my brother-in-law, Zhubin Najafi. Their love, kindness, and support have been limitless, and I am really grateful to have them close to me in the U.S. so I can visit them.

I love you all; none of this would be possible without you. I hope you enjoy/learn something from this dissertation and say “That is a cool looking graph” or “Cat litter can do that too?”

TABLE OF CONTENTS

LIST OF TABLES

Table **Page**

LIST OF FIGURES

APPLICATION OF ELECTRONIC STRUCTURE CALCULATIONS TO VIBRATIONAL SPECTROSCOPY AND GAS ENCAPSULATION IN ZEOLITES

Amir Mehdi Mofrad

Dr. Karl D. Hammond, Dissertation Supervisor

ABSTRACT

Zeolites are an important class of aluminosilicate materials that have wide applications in heterogeneous catalysis, gas separations, and ion-exchange processes at industrial scales. The desire to continue doing research on zeolites and zeolitic materials continues to be strong for two reasons: (i) to discover new zeolites with unique framework structures and (ii) to modify existing zeolites to discover new functionalities for applications that utilize zeolites. These goals require extensive use of characterization techniques, which can be expensive and heavily reliant on conjecture or supposition. Thanks to the advancement of computational power as well as improved numerical algorithms, theoretical studies of zeolites have become a powerful and complementary tool in the zeolite science community over the last few decades. This dissertation uses computational techniques to aid in the characterization and analysis of zeolites. We first investigate the vibrational properties (i.e., infrared and Raman spectra) of sodalites, including sodalites that have been ion exchanged, by means of density functional theory (DFT) calculations. The resulting spectra serve as a reference for scientists (either experimentalists or theoreticians) in the zeolite community and guide future experimental efforts but might not be sensitive enough for quantitative measurements of ion-exchange levels. We then use DFT and the nudged elastic band method to investigate the rate of release of ^{85}Kr from zeolites used to encapsulate radioactive krypton. Results from our theoretical analysis reveal that although zeolites should entrap ^{85}Kr, they might not entrap the decay product, corrosive ^{85}Rb. These findings lead to interpretations and conclusions that are difficult if not impossible to acquire experimentally.

CHAPTER 1

INTRODUCTION

1.1 Boiling Stones—a.k.a. Zeolites

The history of zeolites dates back to approximately 1756, when a Swedish geologist named Baron Axel Fredrik Cronstedt observed that upon heating stilbite—a type of tectosilicate rock—water was vaporized. In addition, he observed that the rock (stilbite) could be rehydrated at lower temperatures. He published this finding in a Swedish magazine with the article name "*Rön Beskrifning Om en oberkant bärg art, som kallas Zeolites*," which is translated to "Observation and Description of an Unknown Species of Rock, Called Zeolites." The name "zeolite" has an etymological root from the Greek words ζειν (zein, meaning boil) and λιθος (lithos, meaning stone). Therefore, zeolites actually mean boiling stones.[1] These naturally-occurring zeolites can be found in geological environments where siliceous materials (volcanic rocks, clays, feldspars, silica rocks, etc.) are abundant. In fact, natural zeolites are formed when volcanic rocks and ash layers react with alkaline

Figure 1.1. Different naturally occurring zeolites. The primary composition found in these minerals are silicon, aluminum, and oxygen. These rocks are formed through thousands to millions of years. Reprinted form Mineralogy Database.[2]

(high pH) ground water, which is then crystallized in sedimentary environments over thousands to millions of years. Natural zeolites are seldom pure because they contain other types of minerals; metals, quartz, etc. The level of impurities in natural zeolites is so high that they are excluded from many important industrial applications. Figure 1.1 shows several natural zeolites. Sodalites are also used in gems and as jewelry. It is worth mentioning that there have been more than forty different types of natural zeolites discovered since the finding of the first one by Cronstedt.[3]

1.2 Zeolite Structure and Nomenclature

In the 1940s, Richard M. Barrer's early pioneering work marked the beginning of the era of synthetic zeolites.[4] As a convention in the zeolite community, silicon, oxygen, and aluminum are known to be the primary building units (PBU) of synthetic zeolites. Silicon and aluminum atoms in zeolites bond with oxygen in a tetrahedral coordination, so they are often called T-atoms. It is noteworthy that the nature of the bonds in the zeolite structure lies somewhere between ionic and covalent,[5] which directly depends on the amount of silica and alumina present. The PBUs can then connect with one another in different forms, which comprise so-called secondary building units (SBU). Some of these SBUs are shown in Figure 1.2. Common SBUs in zeolite structures include single six-membered rings (S6R), single eight-membered rings (S8R), and double four-membered rings (D4R).

The SBUs can connect with one another through oxygen atoms in numerous three-dimensional fashions to construct larger constituents in a zeolite framework, such as pores and channels. As of 2020, there are more than 250 framework topologies that have been synthesized for zeolites.[3] Therefore, based on the aforementioned descriptions, a reasonable definition of zeolites is: "Zeolites are crystalline microporous[(1)] aluminosilicate materials with three-dimensional framework structures that form pores and channels with uniform sizes of molecular dimensions."[7] Although this definition is technically correct, it

[(1)]This means the material contains pores with diameters less than 2 nm. On the other hand, mesoporous materials contain pores with diameters between 2 and 50 nm.

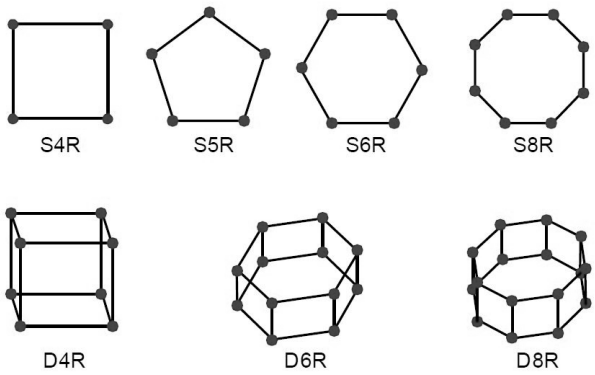

Figure 1.2. Different secondary building units (SBUs) found in zeolites. Dots denote T-atoms (silicon, aluminum, germanium, etc.). For clarity, the oxygen atoms are omitted. However, in a real structure, they are placed in between dots given some obtuse angles. Reprinted with permission from Ref. 6.

only encompasses certain materials with specific compositions. In actuality, zeolitic materials can have different compositions ranging from alumino-phosphates (ALP) to silico-alumino-phosphate (SAPO).[1] Figure 1.3 shows how a zeolite structure can be formed from PBUs and SBUs schematically.

1.2.1 Zeolite Codes

The International Union of Pure and Applied Chemistry's (IUPAC) Commission on Zeolite Nomenclature and The International Zeolite Association (IZA)[3] have developed certain rules governing the naming of zeolite structures using three-letter codes.[9] For instance, framework code **SOD** refers to the framework of sodalite, **CHA** is the framework of chabazite, **MOR** is attributed to mordenite, and so on. Other framework codes are derived from the letters of their industrial names. For instance, framework **MFI**, refers to the industrial name ZSM-5 (Zeolite Socony-**M**obil **FI**ve). In addition, the structure code **LTA** is based on the original trade-name "Linde Type A." As a convention, these three letter codes are written in bold face.[10] It should be noted that some codes are preceded by either an asterisk or a hyphen. An asterisk indicates that the framework is partially disordered. One example is ***BEA**, which consists of an intergrowth of two distinct struc-

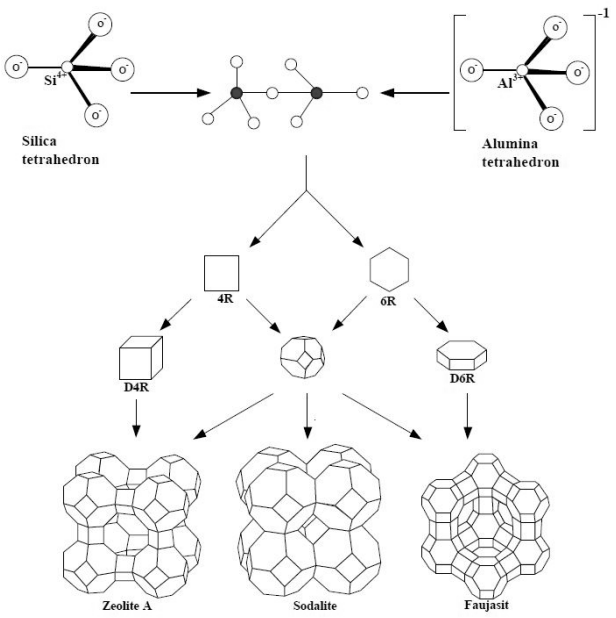

Figure 1.3. From primary building unit (PBU) to secondary building unit (SBU), and subsequently to crystal structure of a zeolite. Reprinted from Ref. 8.

tures termed polymorphs A and B. These polymorphs, which grow as two-dimensional sheets, randomly alternate between each other.[1,3] A hyphen indicates that the framework is interrupted, meaning that not all T-atoms are tetrahedrally connected. For a more comprehensive description of the nomenclature of all the zeolite codes, the interested reader is referred to the *Atlas of Zeolite Framework Types*.[11]

1.3 Important Terminology

In order to understand fully the applications of zeolites as well as the scope of this dissertation, it is necessary to discuss some of the terminology frequently used in the zeolite community.

1.3.1 Löwenstein's Rule and Si/Al Ratio

Löwenstein's Rule (sometimes written as Loewenstein's Rule) states that in a zeolite, the presence of two adjacent $[AlO_4]^-$ tetrahedra is prohibited.[(2)] However, it is possible to have as many as $[SiO_4]$ tetrahedra connected in the framework.[12] A consequence of this rule is that the ratio of silicon to aluminum in a zeolite structure cannot be lower than one. To put this another way, the Si/Al ratio[(3)] can vary from infinity (siliceous,[(4)] or pure silica) to one. Based on the Si/Al ratio (aluminum content), some zeolites are assigned different names even though they have the same framework structure. For instance, the **FAU** framework, which is the structure of naturally-occurring faujasite, also encompasses zeolite X ($1 < Si/Al < 1.5$) and/or zeolite Y ($2 < Si/Al$).

Note that Löwenstein's Rule only applies to zeolites, that is, aluminosilicate materials. In fact, there exist non-aluminosilicate materials in which this rule is violated. Aluminate sodalites (belonging to the **SOD** framework) are one group of materials that disobeys Löwenstein's Rule. The general formula of these materials is $M_8[AlO_2]_{12}X_2$ ($M = Ca^{2+}$, Sr^{2+}, Cd^{2+}; $X = {CrO_4}^{2-}$, ${MoO_4}^{2-}$, ${SO_4}^{2-}$, ${TeO_3}^{2-}$, etc.). In Chapter 5, we explore the vibrational (i.e., infrared and Raman spectra) and structural properties of these materials in depth.

1.3.2 Extra-Framework Ions

The presence of $[AlO_4]^-$ tetrahedra in zeolites and other zeolitic materials requires charge-compensating cations to neutralize the framework. This is due to the fact that aluminum has three electrons in its valence band and therefore one of the oxygen atoms has to have an additional electron. These charge-compensating cations are not covalently bound to the framework; rather, they are loosely bound to oxygen atoms located in the vicinity of

[(2)] It should be stressed that the tetrahedra formula in zeolite community are also written as $[SiO_4]^{4-}$ and $[AlO_4]^{5-}$. I personally disagree with this notation because in the case of siliceous zeolite, the system is neutral and therefore it should not be thought of as having negative four charges.

[(3)] Another convention that is used in the community is SiO_2/Al_2O_3 ratio, which is half the Si/Al ratio. The silica:alumina ratio is more convenient to use during synthesis, when pure alumina or pure silica may be added to the precursor. We use Si/Al ratio throughout this dissertation.

[(4)] In experimental arenas, the term pure silica is more often used than siliceous.

and/or inside the SBUs. They are also referred to as extra-framework cations. For instance, in the **SOD** framework, there is only one crystallographically-distinct site for these cations to occupy, which is in the center of the S6R, either in front or in back. However, in frameworks such as **LTA** and **FAU**, there are multiple crystallographically-distinct sites on which these ions can be located. Common nomenclature for zeolite A (framework **LTA**) uses the the approximate diameter of the 8-ring windows to denote the charge-compensating cation. For example, if sodium is the extra framework cation, the zeolite is denoted 4A. This means the zeolite can exchange species with effective diameters of 4 Å or smaller. On the other hand, if potassium or calcium is the extra-framework cation, the zeolite is named 3A or 5A, respectively. We will discuss these cations and their sites in more detail in Chapter 6. It should be noted that some frameworks such as **SOD** can occlude both extra-framework cations and anions. This ability of **SOD** sets this structure apart from many other materials, as the presence of anions opens up certain applications in the areas of optics and electronics.[13–15]

1.3.3 Notation

The general notation of a zeolite structure and its corresponding composition can be written[16]

$$\text{|Extra-Framework Species|[Unit Cell Composition]-}\textbf{Framework Code}, \tag{1.1}$$

where the "Extra-framework Species" include cations, water molecules, and anions. It should be noted that the cell here is what is referred to as the conventional unit cell. As an example, hydrated zeolite 4A can be written as $|Na_{12}(H_2O)_{27}|[Si_{12}Al_{12}O_{48}]$-**LTA**, natural sodalite (also known as chloro-sodalite) can written as $|Na_8Cl_2|[Si_6Al_6O_{24}]$-**SOD**, $|K_2Na_{10}|[Si_{12}Al_{12}O_{48}]$-**LTA** denotes zeolite A exchanged partially with potassium, and so forth.

1.4 Applications of Zeolites

Zeolites can be considered as one of the widely investigated and topical of inorganic materials. Their synthesis, structure, and physicochemical properties offer interesting challenges, and their numerous applications have stimulated both modification/alteration of existing zeolitic materials and searches for new materials with new functionalities.[17] The industrial applications of zeolites are discussed below.

1.4.1 Catalysis

One of the first successful uses of synthetic zeolites dates back to 1962 with the use of zeolite Y in fluid catalytic cracking (FCC) plants.[(5)] Soon after, zeolites found their way into other acid-catalyzed processes such as isomerization, alkylation of aromatic hydrocarbons, methanol to hydrocarbon conversion, reduction of NO_x, and so forth. It is worth mentioning catalytic cracking still remains the largest single application of zeolites in catalysis. Because of their importance to the petrochemical industry, zeolites make up more than 40% of the solids used in catalysis.[18]

The basis of selective catalysis in zeolites lies in their crystal structures. As mentioned in Section 1.3.2, zeolites require extra-framework cations to electronically neutralize the structure. In the case in which these extra-framework cations are protons (H^+), zeolites can behave as Brønsted acids. The acid strength depends on the Si/Al ratio; the higher the Si/Al ratio, the more likely zeolites are to lose the proton. On the other hand, certain extra-framework species such as extra-framework aluminum and heteroatoms substituted at T-sites can act as Lewis acids.

Although acidic zeolites have been the backbone of the petroleum industry since their first use, there has been a growing interest in developing/modifying zeolites to serve as bases, especially over the past three decades.[19,20] For instance, one method is to substitute the framework oxygen atoms with nitrogen in which the nitrogen centers can then act as

[(5)] FCC is a process in which long chain hydrocarbons (heavy fraction of crude oil) is converted into shorter chain hydrocarbons which are more useful. For instance, gasoline is one of the products of FCC.

Lewis bases.[21] Another method to achieve basic zeolites is to ion exchange with alkali metals.[22] Two of the biggest applications of nitrogen-substituted zeolites are Knoevenagel condensation of benzaldehyde with malononitrile, ethyl cyanoacetate, propanedinitrile, or diethyl malonate; and ethylation of ethylbenzene with ethanol.[23] Using zeolites as solid bases is still an active area of research.

1.4.2 Gas Separation

This application of zeolites directly relates to the structure of the zeolite as well as adsorption[(6)] affinity. Gas molecules, based on their shapes and sizes, can either get trapped or pass through the zeolites structures. This property has led to zeolites being given the nickname "molecular sieves" in both separations and catalytic processes. To name a few examples, zeolite 4A (NaA) can adsorb CO_2, H_2O, and NH_3 to purify natural gas;[(7)], zeolite 3A (KA) can be used for drying gas streams in which the zeolite traps (adsorbs) water and ammonia from other species such as alcohols and alkanes; and zeolite 5A (CaA) is used to remove *n*-alkanes from branched isomers.[24]

The adsorption selectivity in zeolites is highly dependent on the polarity of the adsorbate and the composition as well as the structure of the zeolite. One of the factors governing this interaction is the Si/Al ratio. Siliceous (high-silica) zeolites tend to be more hydrophobic (less polar), whereas, higher aluminum content (lower Si/Al ratio) increases hydrophilicity (polarity) in zeolites. This is due to the fact that the presence of both negative charges in the framework and the positive charges of the extra-framework cations create a strong electrostatic field inside the pores with which molecules having a permanent (or induced) dipole moment can interact and eventually be adsorbed.[6] One of the domestic applications of zeolites is in cat litter, in which it adsorbs ammonia.

[(6)]The term adsorption differs from absorption. Adsorption refers to the adhesion of a gas onto the surface of a solid. Absorption to the diffusion of species into the bulk of substrate.

[(7)]Components of natural gas are methane (94%), ethane (4.2%), propane (0.2%), carbon dioxide (0.3%), etc.

1.4.3 Ion Exchange

The ion exchange technique is one of the processes that people have been incorporating into their lives since the times of Aristotle.[25] It was Eichorn who first studied the ion exchange property of natural chabazite and natrolite scientifically.[26] The presence of extra-framework cations (and sometimes anions as well) in the zeolite structure allows efficient ion exchange to occur in both aqueous and non-aqueous solutions.[27] This is exploited in many industrial applications. For example, large amounts of zeolite NaA are used to soften water by exchanging Na^+ from the zeolite with Ca^{2+} in hard water. Zeolite A is also a major component of concentrated washing powder formulations, where it replaces sodium tripolyphosphate to reduce the environmentally problematic phosphate concentration.[28,29] Ammonium and potassium zeolites are also frequently added to soil to improve crop yields.[28] Another important use of zeolites as ion-exchangers is radioactive decontamination.[30–33] Clinoptilolite, for example, was used extensively after the Chernobyl nuclear disaster to remove radioactive ions such as ^{90}Sr and ^{137}Cs from the water supply.[28,34] Figure 1.4 summarizes the three aforementioned applications of zeolites. Because of the aforementioned numerous applications, these materials have been an active area of research for scientists to synthesize new zeolitic materials and/or optimize existing ones for greater usability. However, the very first step that has to be taken is to characterize the synthesized zeolites. Vibrational spectroscopy is one of the characterization techniques used in the zeolite realm, which we will discuss in the next section.

1.5 Vibrational Spectroscopy in Zeolites

With the first synthesis of an artificial zeolite in the 1950s,[35] the interest in characterization techniques of such materials started to grow. Spectroscopic techniques such as X-ray diffraction (XRD), infrared (IR), Raman, nuclear magnetic resonance (NMR), and electron spin resonance (ESR) are used to characterize zeolites, to name a few. For a comprehensive discussion on virtually all of the existing characterization techniques in the zeolite commu-

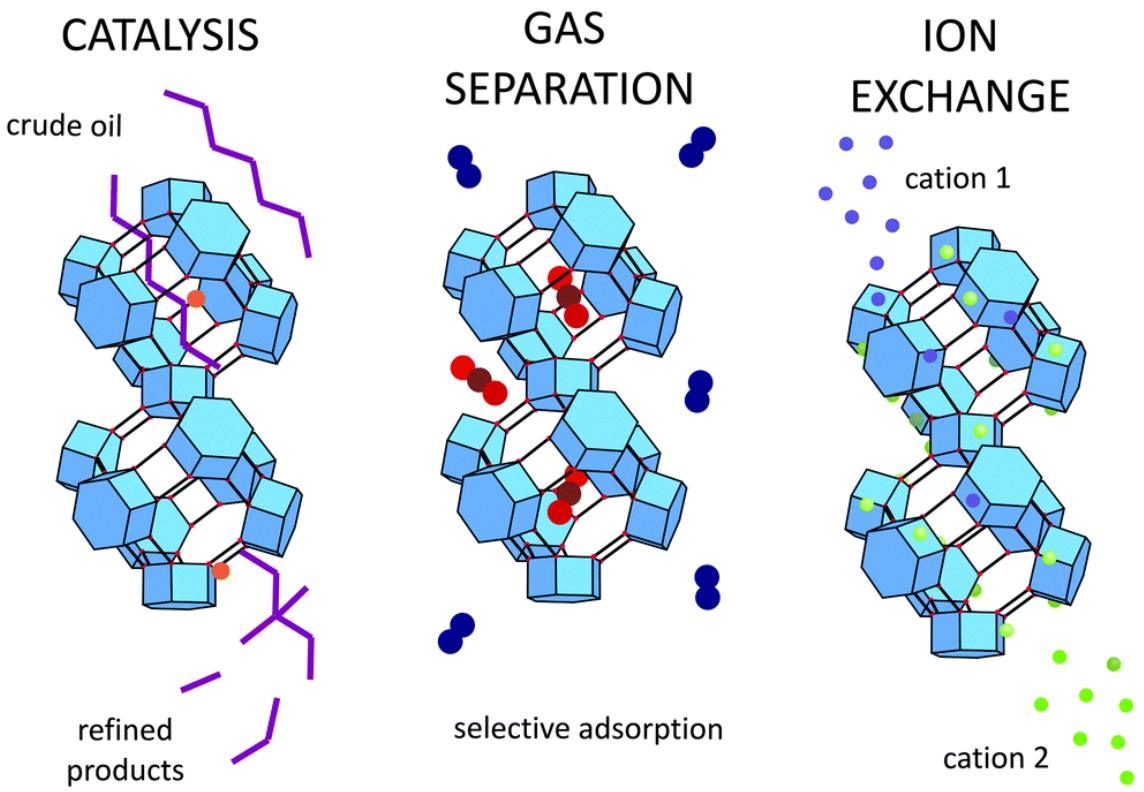

Figure 1.4. Schematic representation of three main applications of zeolite Y. Picture is reprinted with permission from Ref. 17.

nity, one can refer to Refs. 36–38. However, some common characterization techniques are briefly discussed in Appendix A.

Properties of zeolites mainly depend on their crystal structures and the molecules they accommodate in their pores and channels. Monitoring the zeolite structure after it has undergone a chemical reaction is crucial to acquire information about the structure; that is, the interaction between the zeolite and the adsorbates. Vibrational spectroscopy, namely infrared and Raman spectroscopy, is a common characterization technique in the zeolite community because it can provide information about the structure of zeolites as well as the guest species inside. In addition, vibrational spectroscopy is also a non-destructive and relatively inexpensive method that can be used for different applications in the zeolite domain, such as (i) adsorption and catalytic reactions on zeolites, (ii) finding active sites, which is usually done by a probe molecule, (iii) framework and extra-framework vibrations, and (iv) guest–host chemistry and interaction in zeolites.[39,40] It is worth mentioning that, due to the structural complexity of the frameworks in zeolites, interpretation of experimental vibrational spectra has often been troublesome and obliges scientists to rely on supposition. Computational vibrational spectroscopy has been shown to give promising results in the interpretation of infrared and Raman spectra.[41,42] Furthermore, thanks to the advancement of computational power as well improved algorithms, calculation of vibrational frequencies has become more feasible. Most important, employing periodic boundary conditions (which take into account the effect of long-range order) is now something feasible for zeolitic materials.[43]

1.6 Dissertation Overview and Objectives

The overall objective of this dissertation is to employ electronic structure methods to predict the physical properties of zeolites—mainly vibrational properties (infrared and Raman spectra) as well as interpretation of experimental results, specifically prediction of diffusion rates—based on first-principles (i.e., DFT) calculations. As mentioned earlier, in

the process of synthesizing zeolites, vibrational spectroscopy is a common characterization step. As a matter of fact, acquiring Raman spectra of zeolites is a difficult task for many reasons, such as sample preparation and a strong fluorescence background. These experimental challenges necessitate having another complementary resource on which one can rely. One of the main goals of this dissertation is to provide an additional/complementary source to the zeolite community, specifically in the realm of vibrational spectroscopy. The outline of this dissertation is as follows.

In Chapter 2, we cover some of the fundamental theory and equations which are used to acquire and interpret data throughout this dissertation. We predict the vibrational and structural properties of siliceous and aluminosilicate sodalites with varying compositions in Chapter 3. The motivation behind Chapter 3 is three-fold: (i) to investigate the effects of aluminum content (especially intermediate Si/Al ratios) of sodalite, which may not be possible to do experimentally, (ii) predict Raman spectra, which are not easily measured, and (iii) to explore the effects of local composition on vibrational spectra. Chapter 4 explores the effects of extra-framework species on the vibrational spectra of sodalite. The goal of Chapter 4 is to determine whether the theoretical vibrational spectra of sodalite are sensitive enough to provide a "signature" associated with the presence of certain heavy metals in water. Chapter 5 investigates the vibrational properties of another sodalite family called aluminate sodalites. These materials are of interest because they disobey the Löwenstein aluminum avoidance rule discussed in Section 1.3.1. Not much attention has been given to these types of materials in the literature, despite their potential applications in optics and electronics. In Chapter 6, we shift our focus towards modeling the behavior of guest species inside sodalite and zeolite A to estimate the diffusion rates of entrapped atoms using DFT and the nudged elastic band (NEB) method. The guest species of interest in Chapter 6 are krypton and rubidium, and the motivation of this work was to determine whether the zeolite getter was able to trap radioactive krypton species, or whether such species would likely escape prior to decay. Finally, the overall conclusions of this dissertation are summarized

in Chapter 7. Appendix A provides a brief explanation of some characterization techniques and Appendix B contains the specific details of the experimental methods of Chapter 4.

CHAPTER 2

METHODS AND RESEARCH APPROACH

2.1 Introduction and Rationale

The purpose of this chapter is to provide a general overview of the fundamental theories as well as the methods we have used throughout this dissertation. Explicit details, however, will not be discussed, and the interested reader will be referred to more comprehensive references for each section. Refs. 44–48 contain details on electronic structure calculations, including density functional theory (DFT) methods.

Electronic structure calculations aim to predict and analyze the properties of a configuration of atoms using the nuclear configuration as input. Macroscopic properties can then be calculated based on the electronic states of the system. Thanks to the power of modern computers, many quantum (and classical) mechanical problems are now tractable. However, despite having analytical solutions to certain single-body problems (particle in a box, harmonic oscillator, particle in a finite square well, etc.), computing the behavior of complex systems has remained a difficult task. The reason can be explained through an example: a bulk system such as a zeolite contains an extremely large number of electrons and nuclei, which makes it impossible to solve the Schrödinger equation analytically. Therefore, approximations are needed. Amongst other methods, we have used DFT for data acquisition.

2.2 Schrödinger's Equation and the Many Body Problem

Just like solving Newton's equations of motion will give information about the time evolution of classical objects, in quantum mechanics, the properties (structural, vibrational, optical, etc.) of systems can be derived from solving the Schrödringer equation. Schrödringer's equation for a single electron interacting with a one-dimensional potential energy $V(x)$ at time t is

$$i\hbar\frac{\partial\Psi}{\partial t} = \hat{H}\Psi(x,t) \tag{2.1}$$

$$\hat{H} = -\frac{\hbar^2}{2m}\frac{\partial^2}{\partial x^2} + V(x), \tag{2.2}$$

where, $\hat{H}$ is the Hamiltonian operator (sum of all kinetic and potential energy, respectively), $\Psi(\boldsymbol{x},t)$ is the total wavefunction, which depends on the positions of the electron in one-dimensional space, and time. This is also referred to as the time-dependent Schrödinger equation. Through the separation of variables technique, one can separate the spatial domain from the time domain:

$$\Psi(x,t) = \psi(x)T(t) \tag{2.3}$$

plugging the above equation back to Equation 2.1, we get

$$\left(\frac{-\hbar^2}{2m}\frac{\partial^2\psi(x)}{\partial x^2} + V(x)\psi(x)\right)T(t) = i\hbar\psi(x)\frac{\partial T(t)}{\partial t} \tag{2.4}$$

$$\left[\frac{\left(\frac{-\hbar^2}{2m}\frac{\partial^2\psi(x)}{\partial x^2} + V(x)\psi(x)\right)}{\psi(x)}\right] = \frac{i\hbar\psi(x)\frac{\partial T(t)}{\partial t}}{T(t)} = \text{const.} = E, \tag{2.5}$$

where, the constant E is the total energy of the system. By solving for t, we have

$$i\hbar\frac{\partial T(t)}{\partial t} = ET(t) \tag{2.6}$$

$$T(t) = Ce^{-iEt/\hbar} \tag{2.7}$$

The spatial domain also yields:

$$\left[\frac{-\hbar^2}{2m}\nabla^2 + V(x)\right]\psi(x) = E\psi(x) \tag{2.8}$$

Equation 2.8 is the time-independent Schrödinger equation, also written $\hat{H}\psi(x) = E\psi(x)$. Combining Equations 2.6 and 2.8, the overall wavefunction then becomes

$$\Psi(x,t) = \psi(x)e^{-iEt/\hbar} \tag{2.9}$$

It should be noted that in this dissertation, the overall wavefunction Ψ does not change with time. In other words, the system is stationary and we are dealing with the spatial part of the wavefunction. Equation 2.8 is the backbone of all electronic structure calculations.

Now consider a solid, such as a zeolite, in which there are many electrons as well as nuclei present. Equation 2.8 will then have another form:

$$\hat{H}\psi(\{r_i\},\{R_I\}) = E\psi(\{r_i\},\{R_I\}), \tag{2.10}$$

where $\{r_i\}$ and $\{R_I\}$ denote the positions of the electrons and the nuclei, respectively. Equation 2.10, which is a secular equation, is known as the time-independent Schrödinger Equation, which can be solved analytically only for few systems (hydrogen atom, helium ion, Li^{2+} ion, etc.). In fact, there exists no analytical solution even for the helium atom. Expanding the overall Hamiltonian from the above equation yields:

$$\begin{aligned}\hat{H} = &-\sum_{I=1}^{N}\frac{\hbar^2}{2M_I}\nabla_{R_I}^2 + \frac{1}{2}\sum_{I=1}^{N}\sum_{\substack{J=1\\J\neq I}}^{N} k\frac{Z_I Z_J e^2}{|R_I - R_J|} - \frac{\hbar^2}{2m}\sum_{i=1}^{n}\nabla_{r_i}^2 \\ &-\sum_{I=1}^{N}\sum_{i=1}^{n} k\frac{Z_I e^2}{|R_I - r_i|} + \frac{1}{2}\sum_{i=1}^{n}\sum_{\substack{j=1\\j\neq i}}^{n} k\frac{e^2}{|r_i - r_j|},\end{aligned} \tag{2.11}$$

where, in order, the terms are the kinetic energy of the nuclei, the potential (Coulomb repulsion) energy of the nuclei, the kinetic energy of the electrons, the Coulombic attraction between the nuclei and the electrons, and the repulsion energy between the electrons. The constant k is the proportionality constant in Coulomb's law.

It should be noted that because the nuclei are at least 1800 times more massive than electrons, one can assume that the ions are essentially stationary relative to the electrons. In addition, one can treat the ion–ion interactions classically. The outcome of these assumptions results in decoupling the Hamiltonian in Equation 2.11 to an electronic and ionic part, which reduces the complications of solving the many-body problem significantly. These approximations were first made by Max Born and Robert Oppenheimer and are known as the Born–Oppenheimer approximation.[49] Therefore, the electronic Hamiltonian, $\hat{H}_{el}$, becomes

$$\hat{H}_{el} = -\frac{\hbar^2}{2m}\sum_{i=1}^{n}\nabla_{r_i}^2 - \sum_{I=1}^{N}\sum_{i=1}^{n} k\frac{Z_I e^2}{|R_I - r_i|} + \frac{1}{2}\sum_{i=1}^{n}\sum_{\substack{j=1 \\ j\neq i}}^{n} k\frac{e^2}{|r_i - r_j|} \tag{2.12}$$

Due to the complexity of the electronic motion as well as presence of large numbers of them in the system, one cannot simply solve for the electronic energy based on Equation 2.12. Some approximations have been developed over the past hundred years to solve the many-body problem numerically.

2.3 Independent Particle Model—Hartree Approximation

This approximation is the first in the field of quantum chemistry, proposed by Douglas Hartree in the early 1920s. The assumption behind this model is that each electron sees an effective potential, which comprises the attraction from the nuclei and an average repulsion from all the other electrons in the system. The mathematical formalism of this approximation is that the overall electronic wavefunction of the system, $\psi(r_1, ..., r_n)$, is the product of

single-electron wavefunctions:

$$\psi(r_1, \ldots, r_n) = \phi_1(r_1)\phi_2(r_2)\phi_3(r_3)\cdots\phi_n(r_n) \tag{2.13}$$

Applying the electronic Hamiltonian to the above wavefunction leads to sets of equations which can be solved:

$$\left(\frac{-\hbar^2}{2m}\nabla_i^2 + V_{\text{ext}}(r_i) + \sum_{\substack{j=1 \\ j\neq i}}^{n} \int \frac{e^2|\phi_j(r)|^2}{|r_j - r|}dr\right)\phi_i(r) = \epsilon_i\phi_i(r), \tag{2.14}$$

where $V_{\text{ext}}(r)$ is the Coulombic attraction from the ions felt by the single electron and ϵ_i is the total energy of the single electron. The term with the sum is associated with the repulsive interactions of the other electrons, which is an electrostatic interaction. This term is also called the Hartree potential, V_{Ha}. The energy is calculated through self-consistent iterations. One of the drawbacks of the Hartree approximation is that it does not force the wavefunction to obey Pauli exclusion principle.[(1)]

2.4 Hartree–Fock Method

The Hartree–Fock method improves on the Hartree method by forcing the resulting wavefunction and approximate Hamiltonian to be antisymmetric upon exchange of electrons; that is, to construct an anti-symmetric wavefunction. This is done by using a Slater determinant,[50]

$$\psi(r_1, ..., r_n) = \frac{1}{\sqrt{n!}}\begin{bmatrix} \phi_1(r_1) & \phi_2(r_1) & \ldots & \phi_n(r_1) \\ \phi_1(r_2) & \phi_2(r_2) & \ldots & \phi_n(r_2) \\ \vdots & \vdots & \ddots & \vdots \\ \phi_1(r_n) & \phi_2(r_n) & \ldots & \phi_n(r_n) \end{bmatrix} \tag{2.15}$$

Hartree–Fock theory is the foundation of molecular orbital theory.

[(1)]The wavefunction of fermions, that is particles with half a spin ($\pm 1/2, \pm 3/2, \pm 5/2$, etc.) have to be anti-symmetric. One of the outcomes of this dictation is the Pauli exclusion principle.

2.5 Post Hartree–Fock Methods

Numerous methods have been developed that go beyond the Hartree–Fock approximation to resolve the issue of correlation energy. We have used DFT, which is not a post Hartree–Fock method, in this dissertation, and other post Hartree–Fock methods are beyond the scope of this work. The interested reader is referred to References 51 and 52. The message to take away here is that in computational chemistry and/or solid-state physics, you are faced with a trade-off between accuracy and computational time. Using the highest levels of theory would give you the most accurate results, but these methods also take the most computational time. DFT is a reasonable compromise between accuracy and computational expense for many systems.

2.6 Density Functional Theory

Density functional theory (DFT) has become a practical tool with which it is possible to compute many properties of complex many-body systems. This is due to the fact that instead of dealing with the wavefunction, which is a function of at least $3N$ variables, it deals with the electron density, a function of only three spatial coordinates. DFT dates back to a paper by Pierre Hohenberg and Walter Kohn,[44] which for the most part, contains the basis of electronic structure calculations in materials. It should be noted that the backbone of DFT is based on two fundamental theorems:

Theorem 1: The external potential, V_{ext}, is uniquely determined by the non-degenerate ground state electron density, $n_0(r)$. Therefore, the total energy is a functional[(2)] of the ground-state electron density. Since there is a one-to-one mapping between the ground state electron density and the total energy, all the properties of a system can be derived as a consequence of this theorem. In summation, the total ground state energy of a system is a direct functional of the electron density of that system.

Theorem 2: In continuation of Theorem 1, a universal functional for the energy $E[n(r)]$

[(2)] A functional is basically a function of another function; in this case, total energy is a function of electron density, which is a function of positions of electrons, therefore energy is a functional of electron density.

in terms of the electron density $n(r)$ exists. The exact ground state energy E_0 (which is the global minimum) can be obtained variationally using the exact ground state electron density.

2.7 Kohn–Sham Equations

Although the Hohenberg–Kohn theorem guarantees the existence of universal density functional, it does not provide any information about what it is. Kohn and Sham[45] took a big step to finding the electron in a system of **non-interacting electrons** with the same electron density as the interacting system with the following formalism:

$$E[n(r)] = T[n(r)] + E_H[n(r)] + E_{xc}[n(r)], \tag{2.16}$$

where the terms on the right-hand side are the kinetic energy, the Hartree energy, and the exchange–correlation energy, respectively. With some simplifications, the Kohn–Sham equations for the single-particle orbital $\phi_i(r)$ are

$$\left[-\frac{\hbar^2}{2m}\nabla^2 + V_H(r) + V_{ext}(r) + V_{xc}(r)\right]\phi_i(r) = \epsilon_i\phi_i(r) \tag{2.17}$$

where V_H is the Hartree potential, V_{ext} is the electron–nuclei potential, and V_{xc} is the exchange–correlation potential, which we will discuss below.

2.8 Exchange–Correlation Functional

The most prominent challenge in DFT calculations lies in the exchange–correlation functional, as it is unfortunately unknown. There are different approximations of both increasing accuracy as well as computational time. For the most part in this dissertation, we have used the local density approximation (LDA). The reason is two-fold: (i) Quantum ESPRESSO is only capable of computing both infrared and Raman spectra at this level of theory, and (ii) for inorganic oxides, it produces reasonable results within reasonable com-

putational time. However, it should be noted that LDA generally overestimates binding, which results in underestimating the cell parameters. As the name suggests, the exchange–correlation functional depends only on the local electron density (not its gradient, curvature, etc.) and is derived from a homogeneous electron gas with density $n(r)$:

$$E_{\mathrm{xc}}^{\mathrm{LDA}}[n(r)] = \int n(r)\epsilon_{xc}[n(r)]dr, \tag{2.18}$$

where ϵ_{xc} is the exchange–correlation energy density of the uniform electron gas (jellium).

The next level of approximation to the exchange–correlation functional is the generalized gradient approximation (GGA), in which the gradient of the electron density, $\nabla n(r)$, is also taken into account:

$$E_{\mathrm{xc}}^{\mathrm{GGA}}[n(r)] = \int n(r)\epsilon_{xc}[\nabla n(r), n(r)]dr. \tag{2.19}$$

In addition to GGA, there exists another approximation in which the Laplacian (second derivative) of the electron density is included, which are called meta-GGA.[53,54] There are also hybrid functionals, which we will discuss below.

2.9 Hybrid Functionals

One popular method to construct more robust functionals is to mix the exact exchange energy (from Hartree–Fock) with the exchange–correlation functionals from DFT. These types of functionals are called hybrid functionals, and the percentage of exact exchange is based on empirical data (i.e., B3LYP).[55] Only in Chapter 6 for the cluster calculations do we employ the hybrid functional B3LYP.[56]

2.10 Plane Wave Basis Sets

One of the common ways to describe Kohn–Sham orbitals is to use plane-wave basis sets, which is to expand the orbitals by determining the coefficients $c_{\mathbf{k},\mathbf{G}}$ below:

$$\psi_{\mathbf{k}}(\mathbf{r}) = \sum_{\mathbf{G}} c_{\mathbf{k},\mathbf{G}} \mathrm{e}^{-i(\mathbf{k}+\mathbf{G})\cdot\mathbf{r}}. \tag{2.20}$$

In a periodic system, using plane-wave basis sets is advantageous over localized basis sets because the plane waves are periodic. Quantum ESPRESSO employs such basis sets, in which the highest energy plane wave is defined by an energy cutoff. It is worth mentioning that due to the presence of the core electrons, the oscillations near the nuclei can be relatively high due to the number of nodes involved in the atomic orbitals. This requires including many plane waves to describe the electrons, which adds computing time for the system of investigation. To overcome this dilemma, modern solid-state computational packages employ pseudopotentials to reduce the number of plane waves required for the calculations, which we will discuss in the subsequent sections.

2.11 Molecular Orbital Basis Sets

The discussion of different types of basis sets in computational chemistry/physics is a very broad topic because there have been many basis sets developed for most of the elements in the periodic table. There is a database, called Basis Set Exchange,[57] in which different types of basis sets for different elements have been developed. Some of the well-known basis sets are Slater Type Orbitals (STOs), which are exponentially decaying functions ($\propto\ e^{-\zeta r}$) and Gaussian Type Orbitals (GTOs), which are similar to STO's but the decaying function is proportional to e^{-ar^2}. It is best understood if the concept of basis sets is explained through examples.

The **Minimal Basis Sets**, also known as single-zeta (ζ), for the nitrogen atom are 1s, 2s, and 2p orbitals (derived from nitrogen's electronic configuration). This means you need

at least those functions to be able to describe all the electrons in a nitrogen atom. This is sometimes written as 2s1p, meaning there are two types of s-type orbitals and one type of p-type orbital. The names associated with these minimal basis sets are STO-nG (a Slater type orbital represented as the sum of n Gaussian functions). Similarly, if you add another wavefunction to the minimal basis set (single zeta), you end up with double zeta (DZ) basis functions, and our nitrogen example would become 3s2p. Finally, triple zeta (TZ) is when you have three sets of valence orbitals; for nitrogen, this would be 4s3p. As another example, for carbon we have

$$\mathrm{C} = \overbrace{\underbrace{1s\,\underbrace{2s\,2p}_{\text{single zeta (SZ)}}}_{\text{double zeta (DZ)}}\;3s3p\;\;4s4p}^{\text{triple zeta (TZ)}}.$$

Split valence It is common to separate valence and core orbitals. For instance, the 3-21G basis set is a split-valence basis set in which the core electrons are described by three Gaussian basis functions (denoted by a 3 before the hyphen) and the valence electrons are each described by two orbitals (one consisting of 2 Gaussian functions and the other consisting of one). The 6-31G basis set is another well-known and more accurate basis set in which the core orbitals are expanded using six Gaussian functions and the valence orbitals are described by two orbitals, using three and one Gaussian primitives, respectively.

Polarization functions are another modification of basis sets that take into account the effect of angular momentum and describe the polarization of the electron density. The 6-31G(d) basis set adds an additional d orbital to describe the valence electrons. For instance, for the second row in the periodic table, where p is the valence orbital, the 6-31G(d) basis set adds an additional d orbital. However, for iron, since a d orbital is the valence orbital, using this basis set adds an additional f orbital. It is also called 6-31G$*$. In order to add angular momentum to hydrogen (light atoms), the 6-31G(d,p) basis set can be used. Another notation for this basis set is 6-31G$**$.

It is also common to split the valence orbitals even further. For instance, 6-311G(d,p) is another and well-known basis set in which the valence orbitals are described using three, one, and one Gaussian primitives.[3] We will use this type of basis set for cluster calculations in Chapter 6.

2.12 Pseudopotentials

The concept of a pseudopotential emerges from the idea that the properties of molecules and/or solids depend primarily on the valence electrons. The core electrons are not significantly affected by the chemical environment of an atom. Employing pseudopotentials allows us to separate the core electrons from the valence electrons. There are two fundamental assumptions to construct a pseudopotential: (i) the core-electron wavefunctions do not participate in bonding, and (ii) the valence electrons "feel" an effective potential from the core electrons. Figure 2.1 shows a schematic representation of a pseudopotential and its corresponding pseudo-wavefunction (also referred to as an effective atomic wavefunction). The core electrons are inside of r_c, and the valence electrons are on the outside. The governing equations then can be written as,

$$\psi_{\text{pseudo}}(r > r_c) = \psi_{\text{real}}(r > r_c) \tag{2.21}$$

$$\epsilon_{\text{pseudo}}(r > r_c) = \epsilon_{\text{real}}(r > r_c) \tag{2.22}$$

where, ψ_{pseudo} and ϵ_{pseudo} are pseudowavefunction and pseudopotential, respectively.

2.12.1 Norm-Conserving Pseudopotential

It should be stressed that both versions of Quantum ESPRESSO[59,60] that were employed throughout this dissertation were capable of computing both infrared and Raman spectra only with norm-conserving pseudopotentials with the local density approximation

[3] In the same context, in order to model anions more accurately, a "diffuse function" can also be added to the basis set. The notation is 6-31+G(d,p), and similarly, another + sign indicates diffuse functions on hydrogen atoms.

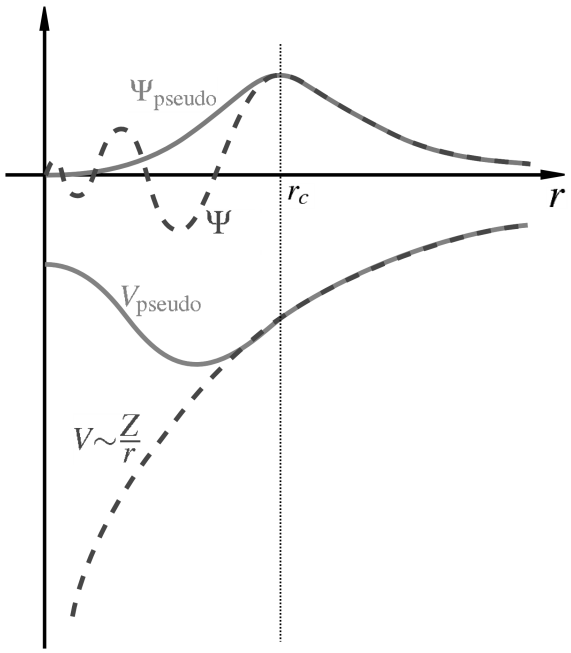

Figure 2.1. Schematic representation of pseudowavefunction and pseudopotential. Figure inspired by Ref. 58.

(LDA). Therefore, most of the studies in this dissertation have been carried out using norm-conserving pseudopotentials. Norm-conserving pseudopotentials were developed by Hamann et al.,[61] the fundamental principle behind them is the identity

$$\int_0^{r_c} |\psi_{\text{pseudo}}(r)|^2 r^2 dr = \int_0^{r_c} |\psi_{\text{real}}(r)|^2 r^2 dr, \tag{2.23}$$

which essentially means that the charge density of the pseudo-wavefunction below the cutoff should be the same as that of the real wavefunction of the system. In the norm-conserving pseudopotential scheme, the valence and core wavefunctions have to be orthogonal to one another. This restriction is crucial, as it allows good transferability of atomic pseudopotentials of an element to many chemical environments.[61,62]

2.12.2 Ultra-Soft Pseudopotentials

Ultra-soft psuedopotentials were originally developed by Vanderbilt.[63] In the ultra-soft formalism, the charge conservation constraint is removed and the value of r_c can be larger than in the norm-conserving case, resulting in a decrease in the kinetic energy. In addition, having a higher cutoff distance causes the valence electrons to experience a "softer" potential as well as requiring fewer plane waves, resulting in less computational time. The transferability of these pseudopotentials to other chemical environments is not as robust as for norm-conserving pseudopotentials. However, as demonstrated by Laasonen,[64] good transferability has been observed for small oxygen molecules. We use ultra-soft psuedopotentials for some calculations in Chapters 3 and 6.

2.12.3 Projector Augmented Wave (PAW) Method

The full explanation and the theory of the PAW method is beyond the scope of this dissertation. The interested reader is referred to Ref. 65. The PAW formalism is essentially a hybrid/generalization of both ultra-soft pseudopotentials and the linearized augmented-plane-wave (LAPW) method,[66] which uses an all-electron approach to solve for the potential energy. The accuracy of the PAW method is generally higher than ultra-soft and norm-conserving pseudopotentials. In addition, using a linear transformation, the all-electron wavefunction can be reconstructed from a smooth pseudo-wavefunction, resulting in less computational time.[62] We use PAW pseudopotentials only in Chapter 6 to test the robustness of our results.

2.13 Density Functional Perturbation Theory

In condensed matter systems such as zeolites, many observed phenomena are the consequences of lattice vibrations (phonons). The first part of this dissertation—which focuses on the infrared and Raman spectra of sodalites families—is one of the examples that is associated with the vibrations of small segments of zeolites. In addition, other properties

such as heat capacity, thermal conductivity, neutron diffraction, and thermal expansion are directly related to the motion of the atoms (vibrations) in materials. Density functional perturbation theory (DFPT) is a modern and robust computational method to calculate lattice dynamics from DFT calculations. As the name suggests, DFPT is a combination of linear perturbation theory with density functional theory, which works by applying a linear perturbation to the system. The way materials "respond" is what determines their properties, the so-called response functions. For instance, these response functions can be first, second, or higher- order derivatives of the total energy with respect to the applied perturbations.

These calculated derivatives of the total energy with respect to atomic positions result in a dynamical matrix, which is then diagonalized to yield the phonon frequencies and normal modes. In the case of vibrational frequencies, the variables involved in the derivatives are displacements of the atoms from their equilibrium positions and the response function is the second-order derivative of the total energy with respect to atomic displacements, which eventually leads to infrared spectra. For Raman spectra, on the other hand, it is the third-derivative of the total energy with respect to two electric fields applied and one atomic displacement. One of the main advantages of DFPT compared to other methods, such as the frozen-phonon method,[67] is the flexibility of calculating phonon frequencies at any wave-vector.[68]

The equations for DFPT are not provided here. The interested reader is referred to more comprehensive resources on this topic.[69–73]

2.14 Transition State Theory

This section describes the theoretical background for Chapter 6 in which we study the encapsulation of krypton and rubidium in zeolites. The core concept of that study lies in transition state theory (TST), which is designed to calculate the rate at which a system leaves its initial configuration,[(4)] overcomes a barrier, and reaches another equilibrium

[(4)] Other words which can be used interchangeably are state and basin.

state.[74] At any given temperature, the atoms in a solid have some thermal energy, causing them to vibrate and collide with each other. To better understand the importance of TST, we start with an illustrative example of a silicon computer chip. At room temperature, the silicon atoms only vibrate around their equilibrium positions. In relatively rare events, a silicon atom or a group of atoms might receive enough energy to overcome bonds in the lattice and reach another stable state. Transition state theory allows us to get a better insight of not only the aforementioned example, but also other important processes (e.g., release of radionuclei).

TST is associated with the concept of a potential energy surface (PES). A PES describes the relationship between the (potential) energy of the nuclei and their positions. Figure 2.2 shows a PES in two dimensions. Let us assume the system resides in basin A and the final state is at B. The transition from A to B requires a certain amount energy, which is called the activation energy (sometimes referred to as the "barrier"). If the thermal energy present in the system is significantly higher than the activation energy, which is the difference between 1 or 2 and A in Figure 2.2, then the system can move quickly between basins. However, for events in which the thermal energy given is small compared to the heights of the barriers, then these transitions will occur rarely.

The biggest challenge to use TST for finding the rates of rare events is to find the transition states and subsequently the barriers associated with them. One can estimate the rates of transitions using harmonic transition state theory (hTST).[74,75] Classical harmonic transition state theory gives the rate expression

$$\Gamma_{\mathrm{hTST}} = \frac{k_B T}{h} \frac{Q^{\ddagger}}{Q} \exp\left(\frac{-\Delta E_A}{k_B T}\right), \tag{2.24}$$

where Γ_{hTST} is the jump rate from harmonic transition state theory (hTST), k_B is the Boltzmann constant, T is the absolute temperature, and h is the Planck constant. The quantity ΔE_A is the difference between the electronic energies of the transition state and the initial

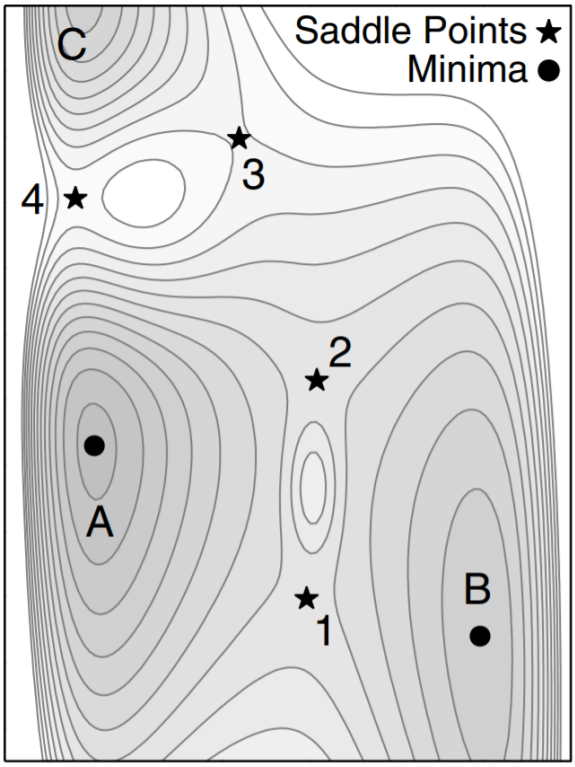

Figure 2.2. A topographic map of a potential energy surface. The local minima are A, B, and C. The saddle points (transition states) are denoted by stars. Figure reprinted with permission from Ref. 74.

state. $Q^{\ddagger}$ and Q are the total vibrational partition functions of the transition state and initial state, respectively, with the normal mode in $Q^{\ddagger}$ associated with vibration of the transition state along the minimum-energy pathway removed. Expanding the partition functions in Equation (2.24) gives

$$\begin{aligned}\Gamma_{\mathrm{hTST}} &= \frac{k_B T}{h}\left[\frac{\prod_{j=1}^{3N-4}\left(\frac{e^{-h\nu_j/2k_BT}}{1-e^{-h\nu_j/k_BT}}\right)^{\ddagger}}{\prod_{i=1}^{3N-3}\left(\frac{e^{-h\nu_i/2k_BT}}{1-e^{-h\nu_i/k_BT}}\right)}\right]\exp\left(\frac{-\Delta E_A}{k_BT}\right) \\ &= \frac{k_B T}{h}\left[\frac{\prod_{i=1}^{3N-3}\left(1-e^{-h\nu_i/k_BT}\right)}{\prod_{j=1}^{3N-4}\left(1-e^{-h\nu_j/k_BT}\right)^{\ddagger}}\right]\exp\left(\frac{-(\Delta E_A+\Delta E_{\mathrm{ZPE}})}{k_BT}\right),\end{aligned} \tag{2.25}$$

where N is the number of atoms present in the system. The three translational modes are not included in the rate expression (and, given that the crystal is at rest, the frequencies of these modes will be zero based on the accoustic sum rule[76]). The fourth mode excluded from the transition state (‡) terms corresponds to the "upside-down" well, which has an imaginary frequency and is associated with vibration of the transition state along the minimum-energy pathway to form the product state. The term ΔE_{ZPE} is the zero-point energy, the sum of all $\frac{1}{2}h\nu$ terms for each real-valued vibrational frequency in the transition state minus similar terms from the initial state.

2.15 Saddle Point Finding Method

Finding the minimum energy path (MEP) has been an important challenge in the fields of theoretical chemistry, condensed matter physics, and materials science.[77] The MEP describes the mechanisms of chemical reactions,[77] including transition states (also referred to as activated complexes), and energy barriers along the path, which together can be used to calculate the reaction rate. In order to find the MEP, one needs to find the initial state (reactant configuration) and final state (product configuration) of the reaction. Among different methods[78] to find the MEP, we have employed the nudged elastic band (NEB) method developed by Jónsson et al.[79] The idea behind the NEB is that a set of "images" (the gray dots in Figure 2.3) of the system of interest is constructed and connected with "springs" from reactants, $\mathbf{R}$, to products, $\mathbf{P}$. Initially, the path is a straight line in 3N-dimensional space from $\mathbf{R}$ to $\mathbf{P}$ as seen in Figure 2.3, which is then optimized based on the NEB algorithm.

2.15.1 Nudged Elastic Band

In a generic NEB scheme, M images are specified $\{\mathbf{R}_0, \mathbf{R}_1, \mathbf{R}_2, \ldots, \mathbf{R}_M\}$, where $\mathbf{R}_0$ and $\mathbf{R}_M$ are the initial and final states, respectively. The initial and final states should be local minima. The total force acting on each image has the following form:

$$\mathbf{F}_i^{\mathrm{NEB}} = \mathbf{F}_i^{S\parallel} + \mathbf{F}_i^{\perp}, \tag{2.26}$$

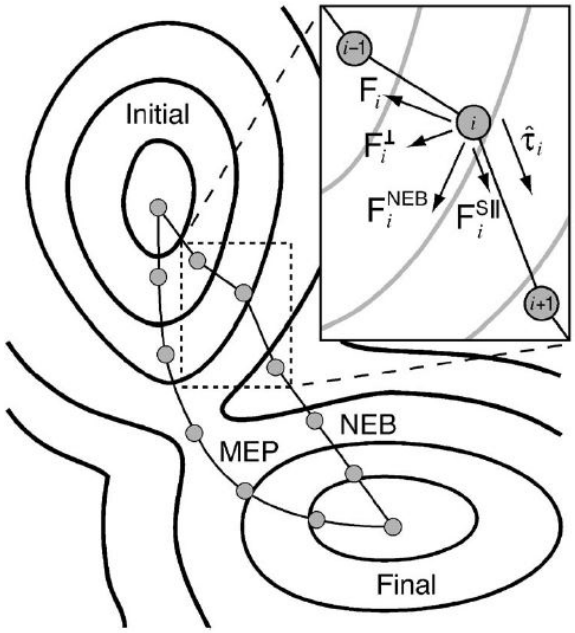

Figure 2.3. Schematic representation of NEB method. The NEB force $\mathbf{F}_i^{\mathrm{NEB}}$, consists of spring force $\mathbf{F}_i^{S\parallel}$, along the tangent, and the perpendicular force because of the potential $\mathbf{F}_i^{\perp}$. Reprinted with permission from Ref. 77.

where, $\mathbf{F}_i^{S\parallel}$ is the sum of the spring forces (with k being the force constant) along the local tangent ($\hat{\boldsymbol{\tau}}_i$):

$$\mathbf{F}_i^{S\parallel} = k(|\mathbf{R}_{i+1} - \mathbf{R}_i| - |\mathbf{R}_i - \mathbf{R}_{i-1}|)\hat{\boldsymbol{\tau}}_i, \tag{2.27}$$

and $\mathbf{F}_i^{\perp}$ is the true force (due to the potential) perpendicular to the local tangent:

$$\mathbf{F}_i^{\perp} = -\nabla(\mathbf{R}_i) + \nabla(\mathbf{R}_i).\hat{\boldsymbol{\tau}}_i.\hat{\boldsymbol{\tau}}_i, \tag{2.28}$$

It should be noted that the spring forces are ignored for $\mathbf{R}$ and $\mathbf{P}$. The nudging algorithm in NEB ensures that the images are evenly spaced along the path in the $3N$ dimensional space if the stiffness of all the springs is chosen to be the same. In addition, the nudging algorithm eliminates corner cutting and leads to convergence to practically the same barrier height.[79]

2.15.2 Climbing Image NEB

An improvement to the regular NEB method is the climbing image NEB (CI-NEB) method, in which a more accurate convergence to finding the saddle point (transition state) is achieved. After a few iterations in regular NEB, the image with the highest energy, i_{max}, is identified. Unlike Equation 2.26, the forces on this particular image is calculated by:

$$\begin{aligned} \mathbf{F}_{i_{max}} &= -\nabla E(\mathbf{R}_{i_{max}}) + 2\nabla E(\mathbf{R}_{i_{max}})\Big|_{\parallel} \\ &= -\nabla E(\mathbf{R}_{i_{max}}) + 2\nabla E(\mathbf{R}_{i_{max}}).\hat{\boldsymbol{\tau}}_{i_{max}}\hat{\boldsymbol{\tau}}_{i_{max}} \end{aligned} \tag{2.29}$$

We use CI-NEB in Chapter 6 to find the transition states as well as the activation energies of the diffusion of krypton and rubidium through sodalite and zeolite A.

CHAPTER 3

VIBRATIONAL SPECTROSCOPY OF SODALITE: THEORY AND EXPERIMENTS

This chapter was previously published as Ref. 41, an article in The Journal of Physical Chemistry C. *The authors of that article are Amir M. Mofrad, Caio Peixoto, Jack Blumeyer, Jinrui Liu, Heather K. Hunt, and Karl D. Hammond from the University of Missouri.*

3.1 Summary

This chapter discusses the effects of compositional variation (Si/Al ratios of infinity, 11, 5, 3, 2, 1.4, and 1) on the vibrational spectra of sodalite (framework code **SOD**), one of the simplest zeolite frameworks, through density functional theory (DFT) calculations. Additionally, we report the results of testing our DFT calculations on experimentally-obtained infrared spectra of sodalites using different synthesis conditions to obtain spectra for sodalites with Si/Al = 1 and Si/Al $\rightarrow \infty$ (siliceous sodalite). The experimental spectra are in good agreement with our DFT calculations in terms of predicting the characteristic vibrational modes of sodalites. However, we observe substantial peak broadening in the asymmetric stretching region and additional peaks in the experimental spectra that are not present in the calculated spectra. The second part of the study tests whether these additional peaks could arise from the existence of defects (i.e., hydroxyl groups and/or adsorbed water) in synthetic sodalite powders. The vibrational spectra in the high-frequency OH stretching region from DFT calculations are also compared to experimental spectra. With the help of DFT calculations and prior studies, we conclude that the defects in siliceous

sodalites are likely to be silanol (SiOH) groups. Although hydroxyl groups and adsorbed water are not the only defects that can occur in zeolitic materials, our DFT calculations suggest that their inclusion is able to account for many of the discrepancies between the experimental and simulated spectra.

3.2 Introduction

Microporous materials have long attracted interest because of their high surface-area-to-volume ratios and their ability to admit molecules in their pores in a size- and shape-selective manner; these properties have led to their extensive industrial use in catalytic, adsorption, and separation processes.[7,35] Microporous materials are defined as materials whose pores have radii smaller than 2 nm;[80] this class of materials includes metal–organic frameworks (MOFs),[81,82] microporous carbon,[83] and zeolites,[7,84] among others.[85] Zeolites are crystalline microporous materials with inherently ordered microporous atomic frameworks, catalytic capabilities, and compositional tunability.[86] They are composed of groups of interconnected SiO_4 and AlO_4 tetrahedra called secondary building units (SBU) that form long-range microporous networks containing cavities and channels of molecular dimensions. These complex frameworks are metastable arrangements of the framework tetrahedra.[87] Moreover, their open framework allows zeolites to act as hosts to adsorbed species, such as inert gases,[21,88] hydrocarbons and oxygenated hydrocarbons,[89,90] water,[91,92] and dyes;[93] serve as ion exchange substrates and water softening agents;[94] and to remove radionuclides[95] or toxic elements such as lead, cadmium, or arsenic.[96] For these and other applications, obtaining detailed structural information of the specific zeolite under study is crucial for understanding their resulting properties and behavior.

Sodalite (framework code **SOD**), having the general formula $Na_8Si_6Al_6O_{24}Cl_2$, with 46 atoms per unit cell, is one of the highest-symmetry zeolite frameworks. It consists of six-membered rings (S6R) and four-membered rings (S4R) shaped in structures called sodalite cages (Figure 3.1).

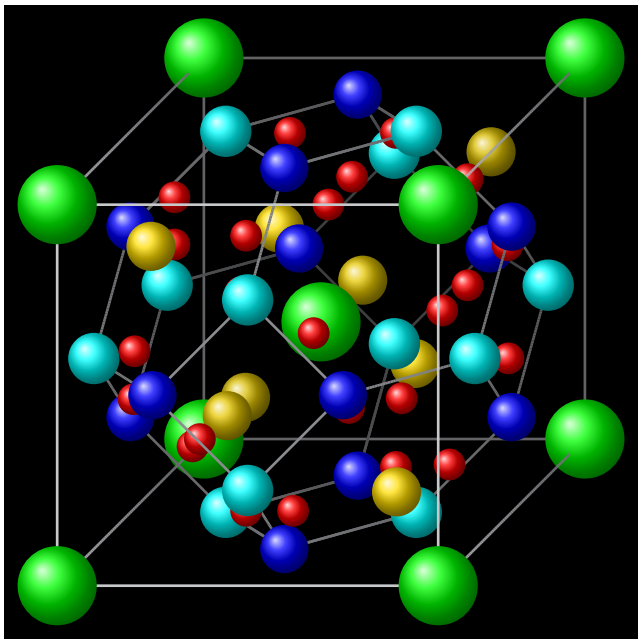

Figure 3.1. Structure of sodalite (**SOD** framework; $a = 8.756$ Å). Colors indicate different elements: blue, silicon; cyan, aluminum; yellow, sodium; red, oxygen; and green, bromine. Spheres are drawn with a radius half the value of either the ionic radius (Br^-, Na^+) or the covalent radius (Al, Si, O). **SOD** has a simpler structure, higher degree of symmetry, and a smaller number of atoms per unit cell compared with most other zeolite frameworks.

Sodalite cages—also called β-cages, particularly in the **LTA** framework—are common secondary building units in zeolite frameworks, occurring in **EMT**, **FAR**, **FAU**, **FRA**, **GIU**, **IFY**, **LTA**, **LTN**, **MAR**, **SOD**, and **TSC**. Because of its simplicity, sodalite has drawn significant attention from computational scientists,[97–102] but as is the case with many zeolites, the properties of the **SOD** framework remain poorly understood, such as the relationships among the intra-framework and extra-framework species and their influence on the resulting vibrational properties.

X-ray crystallography is the typical first step in zeolite characterization, but complementary techniques, such as infrared and Raman spectroscopy, can be used to provide more specific information regarding bonding and local structure.[103] However, the complexity of zeolite frameworks, the presence of extraframework cations, and the possible presence of defects such as terminal hydroxyl groups have made the interpretation of experimen-

tal vibrational spectra so difficult that computational methods have become important for detailing the analysis of the structural properties and for the interpretation of vibrational spectra.

Many theoretical studies, either with or without experimental comparisons, have been performed on zeolites. For example, Konstantin et al.[98] performed a molecular dynamics (MD) study of the sodalite-cage-containing pure silica (siliceous) zeolites **SOD**, **LTA**, **FAU**, and **MFI**, to obtain their vibrational spectra. Creighton et al.[100] examined the effect of alkali metal cations as charge-compensating species in sodalite on the vibrational spectra using the Wilson GF matrix method[104] (where G^{-1} gives the kinetic energy in terms of arbitrary linear internal coordinates, while, F represents the [harmonic] potential energy in terms of these coordinates[105]). Filippone et al.[106] examined the structural, vibrational, and electronic properties of sodalite with Si/Al = 1 using MD. More recently, Mikula et al.[43] examined the differences between periodic crystals versus Si−OH or Si−H terminated cluster calculations on **SOD**. They observed that although cluster models reproduce the characteristic vibrations of **SOD**'s subunits, periodic models automatically take into account **SOD**'s long-range order and more closely predicted its infrared absorbance spectrum. The same group[107] examined ion-exchange processes in sodalite using spectroscopic techniques with the aid of periodic Hartree–Fock (HF) calculations, exchanging sodium ions in the **SOD** framework with silver, cadmium, and lead cations. The authors reported that silver cations were able to replace sodium without modifying the material's structure; the presence of cadmium led to the decomposition of the framework; and lead ion exchange caused an increase in unit cell parameter and partial decomposition of the sodalite framework. Moreover, they observed that these ions gave rise to different infrared absorbance bands in the far infrared region due to ionic sublattice vibrations.

Despite the aforementioned studies of **SOD**'s vibrational modes, to the best of our knowledge, neither theoretical nor experimental studies have been done on the influence of aluminum content on the structural and vibrational properties of **SOD**. Because catalytic

performance and aluminum content are interrelated in zeolite catalysis, indirectly probing the effects of Si/Al ratio and the aluminum sites using spectroscopic methods such as infrared (IR) and Raman, especially in combination with probe molecules adsorbed at the active sites, might be beneficial to the design of new zeolite catalysts.[108]

In this chapter, we study how varying the Si/Al ratio affects the resulting IR and Raman spectra of **SOD**, as well as its effect on structural properties, such as lattice constant, using density functional theory (DFT) with periodic boundary conditions (PBC) under the local density approximation (LDA). We also compare two of our compounds' IR spectra to measured spectra of siliceous sodalite (Si/Al $\rightarrow \infty$) and aluminosilicate sodalite (Si/Al = 1). The presence of additional peaks as well as substantial peak broadening in the asymmetric stretching region in our experiments led us to study whether the discrepancies could be explained by introducing hydroxyl groups and/or adsorbed water as defects in our model through DFT calculations. We find that peaks in the 800–1000 cm^{-1} range, which are present in the measured spectra, are consistent with terminal hydroxyl groups.

3.3 Methods

3.3.1 Computational Procedure

To make structures with Si/Al > 1, we started with natural sodalite, $Na_8Al_6Si_6O_{24}Cl_2$ (Fig. 3.1) using the asymmetric unit from Hassan et al.[109] with the space group $P\bar{4}3n$. We then substituted one aluminum atom at each step with a silicon atom, thereby increasing the Si/Al ratio. We simultaneously removed one of the (up to) four nearby sodium ions, which are present as charge-compensating extra-framework cations. We continued this procedure until we reached the siliceous form ($Si_{12}O_{24}$). In this way, we were able to generate Si/Al ratios of 1, 1.4, 2, 3, 5, 11, and ∞. Compounds with Si/Al $\in \{2, 3, 5\}$ could have different distributions of aluminum in their unit cells. However, in order to be consistent with Löwenstein's rule,[12] only certain configurations are allowed. The allowed configurations are denoted with lower case Roman numerals in Table 3.1. Furthermore, to be consis-

tent with our experimental results, we chose to have bromide as our extraframework anion in place of chloride. After replacing the first aluminum atom with silicon, there are four nearby sodium cations that could be removed, but because of the periodic boundary conditions present in our calculations and the symmetry of the framework (i.e., all sodium ions are crystallographically equivalent), all four choices gave identical results in terms of total energy and structure. Subsequently, for the other Si/Al ratios, we started from the previous structure and removed another aluminum atom and replaced it with silicon, followed by the removal of a sodium ion in a similar manner as mentioned above. This procedure meant that the two bromide anions and the two corresponding sodium cations remained virtually fixed at their crystallographic positions. The formulas of each compound are presented in Table 3.1. Note that without the other four extraframework ions (two bromide anions and two sodium cations), the sodalite unit cell collapsed; keeping them in the unit cell stabilized the structures and preserved the **SOD** framework. Only in the pure SiO_2 case were the four remaining extra-framework ions removed.

We performed all of our simulations using density functional theory (DFT)[44,110] within the local density approximation (LDA)[110–114] with plane-wave basis sets using Quantum ESPRESSO.[59] In order to have reliable results, we performed convergence tests with respect to some of the parameters in our calculations. The first test was a pseudopotential and density functional test, which was performed using six different pseudopotential/density functional combinations that were available for all the elements in sodalite from the Quantum ESPRESSO database, namely the following combinations:

NC-LDA local density approximation with norm-conserving Martins–Troullier (MT) pseudopotentials[115,116]

NC-PBE Perdew–Burke–Ernzerhoff (PBE) functional[117,118] with norm-conserving MT pseudopotentials

PAW-PBE PBE functional with nonlinear core-correction and projector augmented wave (PAW) pseudopotentials[119]

ULT-LDA Perdew–Zunger LDA[120] with nonlinear core-correction and the Rappé–Rabe–Kaxiras–Joannopoulos (RRKJ) ultrasoft pseudopotentials[121,122]

ULT-PBE PBE with nonlinear core-correction and RRKJ ultrasoft pseudopotentials

ULT-PW91 PW91[123,124] with nonlinear core-correction and Vanderbilt ultrasoft pseudopotentials[63,125,126]

The convergence test was done only on siliceous sodalite to get the infrared spectrum. Only the norm-conserving LDA pseudopotential (NC-LDA) predicted the experimental IR spectrum of siliceous **SOD**. The results of this test are provided in Figure 3.2.

This result was favorable to the aim of the study, because the current version of Quantum ESPRESSO is capable of calculating Raman spectra at the norm-conserving LDA level only. The second and third tests were convergence tests with respect to plane-wave cutoff energy and the number of k-points for sampling the first Brillouin zone. The resulting energy cutoff was 80 Ry, and a $2 \times 2 \times 2$ k-point mesh using the Monkhorst–Pack scheme[128] was found to be sufficient. After achieving the converged values from these tests, we found the equilibrium volumes for each compound using a variable-cell geometry optimization technique. The results from this step are shown in Table 3.4. In the next step, we performed phonon calculations, from which IR and Raman spectra are obtainable. The Kohn–Sham orbitals at this step were calculated only at the center of the Brillouin zone (Γ point). The theoretical spectra obtained are merely intensities at a specific wavenumber; to generate a spectrum more consistent with what might be measured, the peaks were artificially broadened using a 20 cm^{-1} full-width-at-half-maximum (FWHM) Gaussian line shape. The reason for choosing 20 cm^{-1} as the FWHM was that larger values would obscure some bands but smaller values would produce a noisy spectrum. Each of the normal modes was visualized using the tools in Refs. 129 and 130.

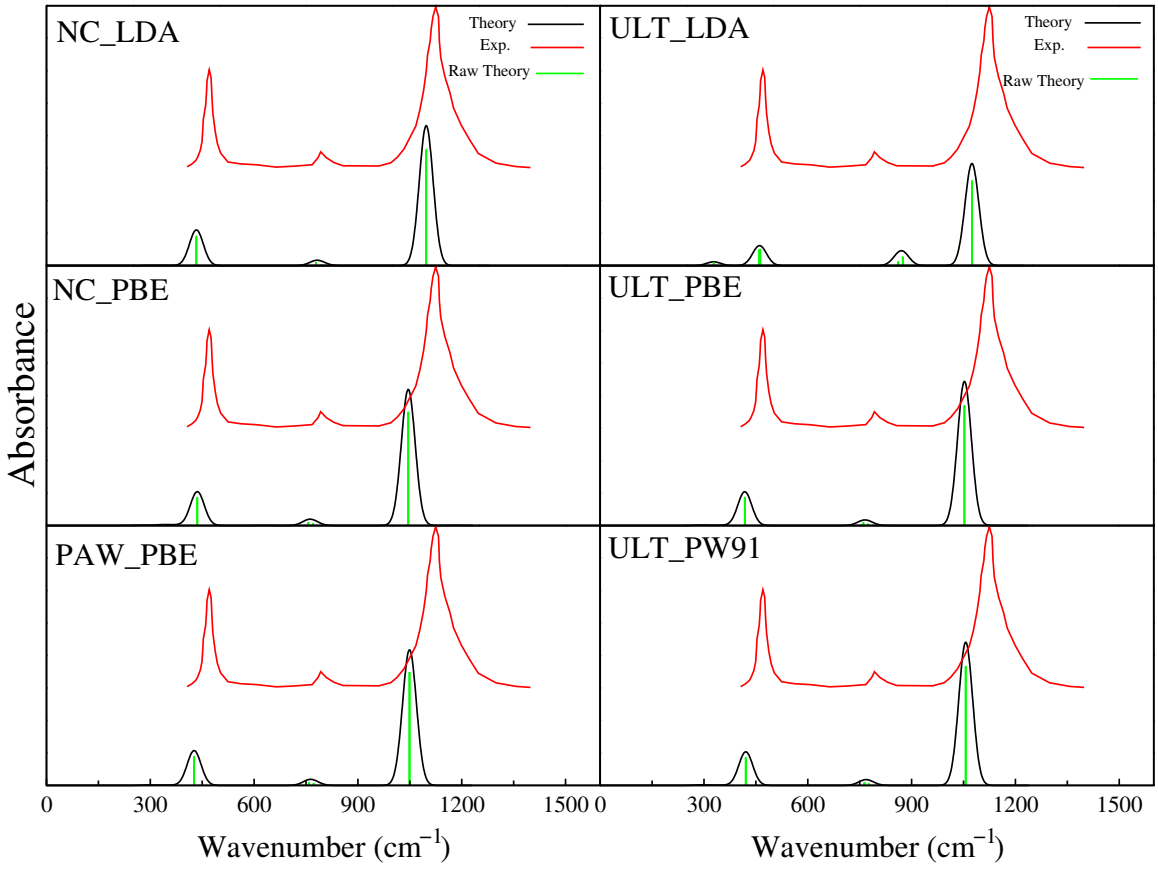

Figure 3.2. Comparison of simulated infrared spectra for siliceous sodalite using different theories. Experimental graphs are illustrated in red, simulated broadened graphs are in black, and simulated raw graphs are in green. Among these six different theories, norm-conserving LDA (NC-LDA) predicts the three characteristic bands better than others. The data for the experimental graph was adopted from Bornhauser et al.[127]

Table 3.1. Sodalite unit cells with different compositions as simulated with DFT.

Sample[a]	# Al	Formula	Si/Al ratio
T-1	6	$Na_8Br_2Si_6Al_6O_{24}$	1
T-1.4	5	$Na_7Br_2Si_7Al_5O_{24}$	1.4
T-2-i	4	$Na_6Br_2Si_8Al_4O_{24}$	2
T-2-ii	4	$Na_6Br_2Si_8Al_4O_{24}$	2
T-2-iii	4	$Na_6Br_2Si_8Al_4O_{24}$	2
T-2-iv	4	$Na_6Br_2Si_8Al_4O_{24}$	2
T-2-v	4	$Na_6Br_2Si_8Al_4O_{24}$	2
T-3-i	3	$Na_5Br_2Si_9Al_3O_{24}$	3
T-3-ii	3	$Na_5Br_2Si_9Al_3O_{24}$	3
T-3-iii	3	$Na_5Br_2Si_9Al_3O_{24}$	3
T-3-iv	3	$Na_5Br_2Si_9Al_3O_{24}$	3
T-5-i	2	$Na_4Br_2Si_{10}Al_2O_{24}$	5
T-5-ii	2	$Na_4Br_2Si_{10}Al_2O_{24}$	5
T-5-iii	2	$Na_4Br_2Si_{10}Al_2O_{24}$	5
T-11	1	$Na_3Br_2Si_{11}AlO_{24}$	11
T-S	0	$Si_{12}O_{24}$	∞

[a]In the Sample column, T stands for theoretical, the second number corresponds to the Si/Al ratio ("S" means "siliceous"), and the Roman numerals correspond to different configurations with the same Si/Al ratio, consistent with Löwenstein's Rule.

3.3.2 Design of Experiments

SOD crystals can be synthesized via hydrothermal and solvothermal synthesis routes. Numerous synthetic protocols are available in the literature for both siliceous and aluminosilicate materials. Recognizing that such protocols could yield vastly different materials, we selected two different procedures to synthesize siliceous **SOD** and another for aluminosilicate sodalite and varied the parameters in all three protocols. We synthesized siliceous **SOD** powders in a non-aqueous medium according to protocols previously reported by Shao et al.[131] and by Bibby and Dale.[132] The former is very similar to the latter except that it contains one extra reagent, pyrocatechol, which can form silicon-containing complexes. These in turn lower the number of nucleation sites, ultimately yielding larger crystals. Aluminosilicate powders were obtained via the procedures described by Stein.[133]

Besides the variations between synthetic protocols, synthesis conditions can also alter the final properties of synthetic zeolitic materials. Even for the same reaction gel composition and synthesis protocol, we hypothesize that parameters such as crystallization temperature, crystallization time, and gel aging time may influence the physical, chemical, and vibrational properties of zeolites. To ensure the synthesis of pristine **SOD**, we used a software-aided design of experiments to account for possible variability in powders synthesized from the chosen protocol as a function of several synthetic variables: aging time (τ_{aging}), crystallization temperature (T_{cryst}), and crystallization time (τ_{cryst}). Experimental parameters were obtained from the original protocol and assigned to experimental units using the statistical analysis software JMP,[134] yielding the experimental design shown in Table 3.2.

3.3.2.1 Materials

Ethylene glycol (≥ 99%), pyrocatechol (approx. 99%), sodium hydroxide (99.5%), silica sol (40% w/w suspension in H_2O), and sodium bromide (≥ 99%) were purchased from Sigma-Aldrich; sodium aluminate and sodium silicate from Fisher Scientific; and fumed silica (≥ 99.8%) from Cabot. All reagents were used as-received without further purification. Deionized water (13–15 MΩ) was obtained from an Elga Purelab Ultra water deionizer.

3.3.2.2 Syntheses

3.3.2.2.1 Siliceous Sodalite Synthesis To synthesize siliceous sodalite, we chose two well-known procedures: protocol 1 was based on the work of Bibby and Dale[132] and protocol 2 was based on the work of Shao et al.[131] These two protocols differed primarily in the composition of the reaction gel. Following **protocol 1**, 0.34 g of sodium hydroxide was dissolved in 20.67 g of ethylene glycol. Subsequently, 2.00 g of fumed silica was added to the solution, which was then stirred. According to **protocol 2**, 0.50 g of sodium hydroxide, 0.50 g of pyrocatechol, and 20.00 g of ethylene glycol were first mixed prior to the addition

Table 3.2. Synthetic parameters determined by a software-aided design of experiments. Ranges of values were suggested by the selected synthesis protocols and assigned to specified experimental conditions using JMP.[134]

Sample[a]	τ_{aging} (min)	T_{cryst} (°C)	τ_{cryst} (day)
1-5-175-9	5	175	9
1-5-175-21	5	175	21
1-5-180-9	5	180	9
1-5-180-21	5	180	21
1-1440-175-9	1440	175	9
1-1440-175-21	1440	175	21
1-1440-180-9	1440	180	9
1-1440-180-21	1440	180	21
2-5-175-9	5	175	9
2-5-175-21	5	175	21
2-5-180-9	5	180	9
2-5-180-21	5	180	21
2-1440-175-9	1440	175	9
2-1440-175-21	1440	175	21
2-1440-180-9	1440	180	9
2-1440-180-21	1440	180	9
3-1-95-2.5	1	95	2.5[b]
3-1-95-24	1	95	24[b]
3-1-150-2.5	1	150	2.5[b]
3-1-150-24	1	150	24[b]
3-5-95-2.5	5	95	2.5[b]
3-5-95-24	5	95	24[b]
3-5-150-2.5	5	150	2.5[b]
3-5-150-24	5	150	24[b]

[a]Sample coding reflects composition, protocol (1–3), aging time, crystallization temperature, and crystallization time, respectively. For example, sample 1-5-175-9 contains the following information: protocol 1, 5 min aging time, 175 °C crystallization temperature, and 9 d crystallization time.

[b]The crystallization time unit in protocol 3 is in hours.

of 2.00 g of fumed silica. Both protocols were carried out in a clean glass beaker (125 mL) using a magnetic stirrer (Fisher Scientific, Isotemp, 1200 rpm) at room temperature. After the gel was formed, it was aged for either 5 min or 24 h under the same conditions (1200 rpm, room temperature). Following aging, the gel was transferred to 23 mL Teflon-lined autoclaves and placed in an oven (Fisher Scientific, Isotemp Oven) at either 175 or 180 °C for either 9 or 21 d. After synthesis, samples were filtered (Whatman Filter Paper, Grade 4) using deionized water and acetone until the powders became white in color. They were subsequently calcined at 400 °C in a tube furnace (Thermo Scientific, Lindberg/Blue M) for 4 h with a heating and cooling rate of 0.5 °C/min. Calcined powders were ground and stored in 10 mL glass vials for further characterization.

3.3.2.2.2 Aluminosilicate Sodalite Synthesis Aluminosilicate sodalite samples were synthesized according to the protocol described by Stein[133] (protocol 3), summarized below. After synthesis, aluminosilicate samples were filtered using deionized water until the filtrate pH reached 7.0. The samples were then ground and stored in 10 mL glass vials for further characterization. Because this synthesis protocol did not use an organic structure-directing agent, calcination was unnecessary.

In **protocol 3**, a 100 mL glass beaker, 15.00 g of sodium hydroxide, and 38.33 g of sodium bromide were dissolved in 75.00 g of deionized water. After stirring until the solid reagents were fully dissolved using a magnetic stirrer at 1200 rpm and room temperature, 7.50 g of silica was added to the solution and stirred on a heated magnetic stirrer until the solution reached 95 °C. In another beaker, 10.00 g of sodium hydroxide and 3.90 g of aluminum hydroxide were dissolved in 50.00 g of deionized water (1200 rpm); the solution was heated to 95 °C. Once both solutions reached 95 °C, they were mixed in a polycarbonate bottle and stirred vigorously for either 1 or 5 min to age. Immediately after that, the final solution was transferred to 23 mL Teflon-lined autoclaves and placed in an oven (Fisher Scientific, Isotemp Oven) at either 95 or 150 °C for either 2.5 or 24 h.

Table 3.3. Chemical composition (atomic percent) of sodalite powders calculated from EDS spectra. Brown, siliceous samples have higher carbon content; the higher standard error associated with atomic percentage measurement for those samples indicates that they are chemically non homogeneous.

Aluminosilicate						
	C	O	Na	Al	Si	Br
Average	2.5	55.9	3.3	18.2	18.5	1.6
Std. Error	0.7	0.8	0.4	0.5	0.4	0.1
	Siliceous (white)			Siliceous (brown)		
	C	O	Si	C	O	Si
Average	1.3	58.4	40.3	30.2	44.9	24.9
Std. Error	0.2	2.2	2.3	8.9	7.3	4

3.3.2.3 Characterization

All samples were characterized using powder X-ray diffraction (XRD) (Rigaku Ultima IV, Cu-Kα, 0.15418 nm, 40 kV, 44 mA, 10–50° 2θ, step size 0.02°, 2°/min), and Fourier transform infrared spectroscopy (FTIR) (Nicolet 4700, 400–1600 cm^{-1}, 4 cm^{-1} resolution) in transmittance mode. For the IR spectra, samples were mixed with potassium bromide (5 mg sample + 70 mg KBr) and pressed into 10 mm pellets for FTIR characterization using a hand-held Thermo Fisher pellet press. The optimal KBr/sodalite ratio was determined by preliminary experiments (data not shown). Spectral normalization and interpolated baseline correction were performed using OriginLab. Additionally, siliceous **SOD** powders were subjected to thermogravimetric analysis (TGA) (SDT 600, 30–1000 °C with heating rate of 5 °C per minute) to confirm the removal of organic reagents via calcination and to determine their thermal stability. Chemical composition was characterized via energy-dispersive X-ray (EDX) analysis (FEI Scios DualBeam FIB SEM, 5 kV, 6.2 nA) for two siliceous and two aluminosilicate samples (Table 3.3).

3.3.2.4 EDS Discussion

Energy-dispersive X-ray spectroscopy (EDS) results indicate that synthetic sodalite powders had an atomic composition excepted from these materials. White siliceous samples had a significantly smaller carbon content when compared to the samples that remained brown after calcination, evidencing incomplete template removal for some samples. This could be due to possible differences in crystal, which is directly related to the size of diffusion path of byproducts of organic species thermal oxidation out of the crystals. Moreover, aluminosilicate samples exhibited roughly the same content of aluminum and silicon. The content of sodium and bromine were, respectively, 3.3 and 1.6 percent, substantially lower than the ratio expected from sodalite's chemical formula. This observation could be due to the existence of hydroxyl groups in the structure instead of Na^+ and Br^-.

3.4 Results and Discussion

3.4.1 Effect of Aluminum Content on Lattice Parameters and Vibrational Spectra

As shown in Table 3.4, the lattice parameter of simulated siliceous sodalite with this pseudopotential is 8.721 Å, which is 1.2 percent lower than the experimental value.[135] It should be noted, however, that the local density approximation (LDA) used here is not particularly accurate for insulating materials such as zeolites, so this agreement is likely fortuitous rather than truly representative. Real zeolite samples also have impurities such as heteroatoms and hydroxyl groups, some of which may change the measured lattice parameter. Also, DFT simulations are carried out at an energetic minimum, whereas the experimental lattice parameters were measured at room temperature.

As aluminum is introduced to the framework, the lattice parameter increases, which can be attributed to the presence of extraframework ions (sodium and bromide), and the fact that tetrahedral aluminum ($[AlO_4]^-$) is larger than tetrahedral silicon (SiO_4) due to tetrahedral aluminum's negative formal charge.

Table 3.4. Lattice parameters for the various simulated sodalites.

Compound[a]	Cell Volume (Å^3)	a (Å)	b (Å)	c (Å)	α (°)	β (°)	γ (°)
Siliceous	663.511	8.722	8.722	8.722	90.00	90.00	90.00
Siliceous (expt.[136])	687.764	8.827	8.827	8.827	90.00	90.00	90.00
Si/Al = 11	668.677	8.738	8.731	8.766	90.86	89.42	90.67
Si/Al = 5 (i)	681.266	8.792	8.792	8.815	90.18	90.18	91.29
Si/Al = 5 (ii)	662.837	8.711	8.734	8.713	90.70	90.33	89.51
Si/Al = 5 (iii)	674.250	8.698	8.806	8.805	91.24	90.12	90.12
Si/Al = 3 (i)	675.126	8.721	8.802	8.797	90.78	90.25	90.41
Si/Al = 3 (ii)	665.489	8.712	8.721	8.751	89.17	90.17	90.18
Si/Al = 3 (iii)	662.959	8.720	8.720	8.720	89.89	89.89	89.89
Si/Al = 3 (iv)	665.258	8.696	8.733	8.761	90.55	89.99	89.87
Si/Al = 2 (i)	670.505	8.692	8.794	8.766	90.40	90.29	89.70
Si/Al = 2 (ii)	667.858	8.723	8.736	8.764	90.32	89.84	89.91
Si/Al = 2 (iii)	664.645	8.740	8.740	8.701	89.83	89.83	90.02
Si/Al = 2 (iv)	667.861	8.736	8.764	8.723	89.84	89.91	90.32
Si/Al = 2 (v)	673.713	8.761	8.777	8.761	90.18	90.40	90.18
Si/Al = 1.4	672.693	8.750	8.773	8.762	89.93	90.17	90.00
Si/Al = 1	671.301	8.756	8.756	8.756	90.00	90.00	90.00
Si/Al = 1 (expt.[109])	700.700	8.882	8.882	8.882	90.00	90.00	90.00

[a]Lowercase Roman numerals denote different symmetrically distinct configurations of aluminum atoms with the same Si/Al ratio.

Differences between the simulated aluminosilicate sodalite and experiments arise because of the method of calculation, the presence of OH groups, and thermal expansion. According to Hassan et al.,[135] the sodalite lattice parameter increases smoothly and non-linearly with temperature, and based on their findings, aluminosilicate sodalite (Si/Al = 1) should have a cell parameter of 8.861 Å at absolute zero, whereas it is 8.756 Å from our simulation results. This again indicates less than -1.2 percent error.

Before discussing the details of the simulated vibrational spectra, we should mention that the absolute assignment of sodalite's vibrational bands to particular structural features is challenging because of the occurrence of different structural units with the same composition, such as single-four-membered rings (S4R) and single-six-membered rings (S6R), whose vibrational modes may overlap. Other factors that hamper absolute band assign-

ments are the presence/absence of extraframework ions, the possible presence of other non-sodalite phases, and the temperature at which the spectra were collected, among others. To interpret our simulations, we used Molden,[129] a visualization tool that allowed us to assign the calculated vibrational modes as accurately as possible. Vibrational modes for zeolites are categorized into two groups: internal and external vibrations.[137] Internal vibrations are those associated with the internal oxygen bridges Si−O−Si and Si−O−Al. These bridges undergo three types of modes: asymmetric stretching, symmetric stretching, and bending. External vibrations are those that occur within the secondary building blocks (SBU) of zeolites, such as ring vibrations; external vibrations are further classified as pseudo-lattice vibrations, which are usually in the range of 400–800 cm^{-1}, and lattice vibrations, which occur in the far-infrared (FIR) region (0–400 cm^{-1}). It is in the far-infrared region that vibrations are affected by extra-framework species and their interactions with the oxygen atoms in the framework. Generally speaking, because of the complexity of the zeolite structures and the effects of long-range order, the chances of observing overlapping vibrational modes are high. For instance, at a particular frequency, there might exist two or three different vibrational modes, but only their combination will be visible. An example is the overlap between ring vibrations and O−Si−O (or O−Al−O) bending modes. At some frequencies, these two are indistinguishable, and therefore we have specified both of these vibrational modes in our results. In the following section, we will examine each of these types of vibrations systematically as aluminum is introduced into the framework.

Figure 3.3 shows the calculated infrared spectra of sodalite with different Si/Al ratios, decreasing from the top to the bottom of the plot, from 0–1300 cm^{-1}. The most intense band in the spectrum for Si/Al $\rightarrow \infty$, which appears at 1094 cm^{-1}, originates from Si−O−Si asymmetric stretching vibrations. The next band results from the symmetric stretching of Si−O−Si bridges, which occurs at 785 cm^{-1}. Finally, the band at 437 cm^{-1} in the siliceous case is associated with Si−O−Si bending. No significant vibrational modes are observed in the far-infrared region. In the Si/Al = 11 case, the incorporation of one aluminum

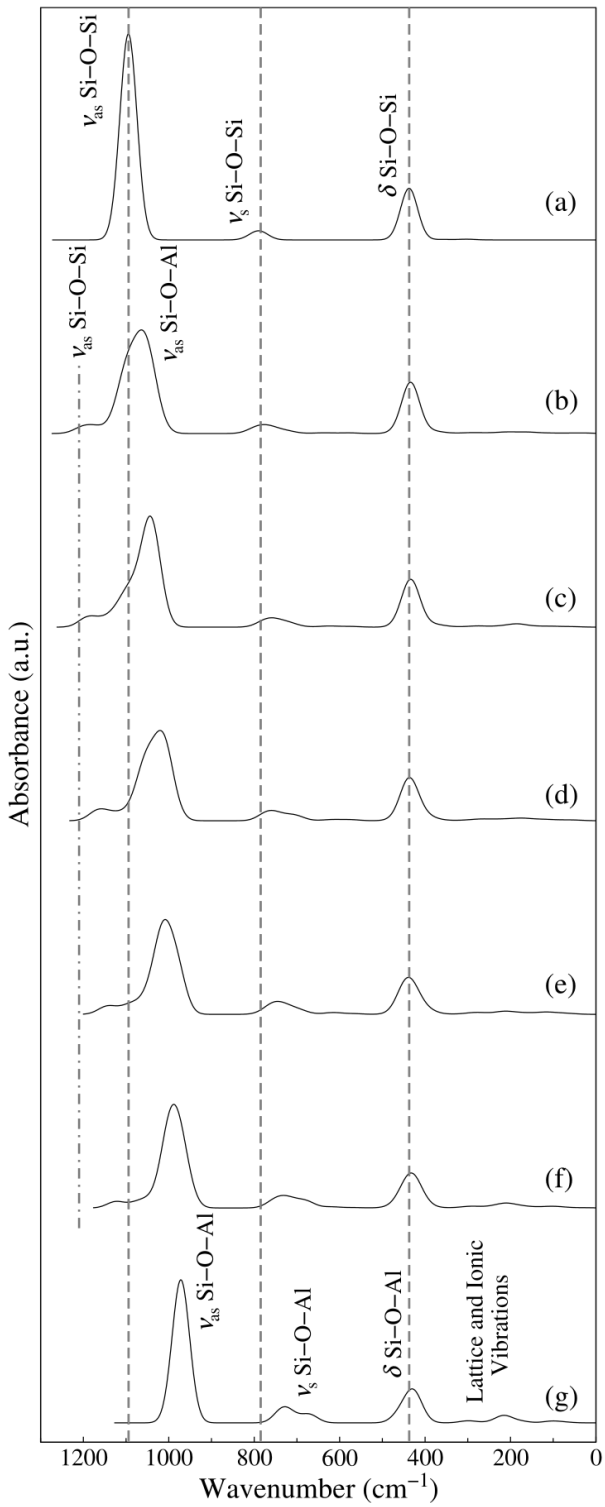

Figure 3.3. Theoretical infrared spectra of sodium bromide sodalites at different Si/Al ratios. Vertical dashed lines are drawn at the peak locations in the siliceous (Si/Al $\rightarrow \infty$) spectrum, and have wavenumbers of 1094, 785, and 437 cm^{-1}. The dash-dotted line indicates the appearance of a new peak as aluminum is introduced and how that peak shifts to lower wavenumbers gradually. The replacement of silicon by aluminum atoms likely causes variations in bond length, local dipole moment, and force constant, which leads to the observed trend. (a) siliceous, (b) Si/Al = 11, (c) Si/Al = 5, (d) Si/Al = 3, (e) Si/Al = 2, (f) Si/Al = 1.4, and (g) Si/Al = 1.

atom into the structure (yielding $Na_3Br_2AlSi_{11}O_{24}$) splits the asymmetric stretching mode into two bands. The one at higher wavenumber (1196 cm^{-1}) is the Si−O−Si asymmetric stretching vibration, whereas the one at lower wavenumber (1065 cm^{-1}) is associated with both Si−O−Al and Si−O−Si asymmetric stretching. This substitution also has the same effect on the symmetric stretching mode (Si−O−Si for the higher wavenumber and Si−O−Al for the lower wavenumber), causing a red shift from the siliceous case. However, the bending mode remains the same. Furthermore, this substitution has caused the appearance of some bands in the far-IR region, where lattice vibrations and ionic vibrations occur. Substituting another silicon atom with aluminum (Si/Al = 5) has a similar effect and causes both asymmetric and symmetric stretching modes to shift to even lower wavenumbers; the bending mode remains unchanged. Finally, in the case of Si/Al = 1, there is only one asymmetric stretching mode (968 cm^{-1}) because there is only one unique Si−O−Al bridge in the system, and two symmetric stretching bands (734 and 672 cm^{-1}). Similarly, the bending mode has not changed significantly for the aluminosilicate case, and one can see the appearance of some bands in the far-IR region. Mozgawa et al.[138] suggested that the inclusion of one aluminum atom in a particular fragment of a zeolite framework would cause the appearance of a Si−O−Al asymmetric stretching mode at a higher wavenumber than in the all-silica version of that same fragment. However, as mentioned above, that is not the case, and instead the Si−O−Al asymmetric (and symmetric) stretching modes occur at lower (or equal) wavenumbers compared with Si−O−Si ones. The reason for such behavior stems from the fact that in a zeolite, T atoms (silicon and aluminum) have to form tetrahedra with the oxygen atoms in the framework. Silicon, having four electrons in its valence shell, has no difficulty in doing so. Aluminum, having only three valence electrons, is forced to receive an additional electron from the framework. This makes the O−Al bond weaker (and longer) than the O−Si bond, causing the occurrence of the former vibrational mode at a lower wavenumber. Subsequent substitution of more silicon atoms with aluminum increases the negative charge on the framework, resulting in the red shift of both

the asymmetric and symmetric stretching modes. Finally, as previously mentioned, the inclusion of aluminum does not produce a particular trend in the far-IR region (0–400 cm^{-1}), which is associated with lattice vibrations and extra-framework sublattice vibrations. The identifications of vibrations based on their visualizations are collected in Table 3.5.

For Si/Al ratios of 2, 3, and 5, which can have different distributions of aluminum, the infrared spectra in all cases have the same shape (i.e., the same number of peaks in each region); only the intensities vary with aluminum location at the same Si/Al ratio. Their IR spectra are also presented in Figure 3.4.

Figure 3.5 shows the calculated Raman spectra of sodalite with varying aluminum content over the same range as Figure 3.3. For siliceous sodalite, the most intense Raman peak occurs at 450 cm^{-1}, which can be classified both as Si−O−Si bending and ring vibrations. The other intense band is at 172 cm^{-1}, which is from O−Si−O bending. The less intense band at 301 cm^{-1} can also be assigned to O−Si−O bending. The Si−O−Si symmetric stretching mode occurs at 800 cm^{-1}, and finally, the two peaks at 1094 and 1191 cm^{-1} are associated with asymmetric stretching. A similar pattern for the same types of vibrational modes (ν_{as}, ν_s, and δ) can be seen for the Raman spectra as well, that is, the inclusion of aluminum does not affect the ring and bending vibrations in a recognizable manner, and both asymmetric and symmetric stretching modes shift to lower wavenumbers as silicon atoms are substituted with aluminum atoms. These results are also comparable to the findings of Dutta et al.,[139] who measured the Raman spectra of zeolite A (**LTA** framework) as a function of the Si/Al ratio. The most intense band (450 cm^{-1}) has not significantly changed, whereas the bands at higher wavenumbers experience a red shift as aluminum is introduced into the structure. The identification of each band in these spectra is also given in Table 3.5. As with the infrared spectra, the shape of the Raman spectra within different configurations for Si/Al ratios of 2, 3, and 5 is the same; their graphs can be found in Figure 3.6.

Table 3.5. Results of the band identification in calculated spectra (cm^{-1}). Abbreviations: (IR), bands active for infrared; (R), bands active for Raman; (B), bands active for both infrared and Raman.

Si/Al	Lattice and Ionic Vibrations	Ring Vibrations	δ O-Si-O	δ O-Al-O	δ Si-O-Si	δ Si-O-Al	ν_s Si-O-Si	ν_s Si-O-Al	ν_{as} Si-O-Si	ν_{as} Si-O-Al
Siliceous	-	77 (R), 437(IR), 450 (R)	172 (R), 301 (R), 450 (R)	-	437 (IR)	-	679 (R), 785 (IR), 800 (R)	-	1191 (R), 1094 (IR), 1094 (R)	-
11	33 (IR), 66 (R), 169 (IR), 203 (R), 210 (IR)	203 (R), 378 (R), 434 (IR), 450 (R), 645 (R)	203 (R), 294 (IR), 378 (R), 434 (IR), 450 (R)	378 (R), 450 (R)	203 (R), 434 (IR), 450 (R)	450 (R)	573 (IR), 645 (R), 777 (IR), 789 (R)	573 (IR), 638 (IR), 645 (R)	1065 (IR), 1114 (R), 1180 (R), 1196 (IR), 1210 (IR), 1210 (R)	1065 (IR), 1114 (R), 1175 (R)
5	60 (IR), 60 (R), 106 (IR), 186 (IR), 200 (R), 278 (IR)	106 (IR), 200 (R), 352 (R), 444 (R), 625 (IR)	434 (IR), 444 (R)	434 (IR), 444 (R)	434 (IR), 622 (R)	434 (IR), 622 (R)	622 (R), 625 (IR), 773 (R), 760 (IR)	578 (IR), 625 (IR), 760 (IR)	1045 (IR), 1080 (R), 1168 (R), 1189 (IR), 1194 (R)	1045 (IR), 1080 (R), 1168 (R)
3	58 (IR), 58 (R), 177(IR), 219(R), 270 (IR)	219 (R), 270 (IR)	177 (IR), 270 (IR), 437 (IR)	270 (IR)	437 (IR), 449 (R)	437 (IR), 449 (R), 617 (IR)	622 (R), 705 (IR), 760 (IR), 770 (R)	570 (IR), 622 (R), 705 (IR)	1020 (IR), 1063 (R), 1140 (R), 1160 (IR)	1020 (IR),1063 (R), 1140 (R), 1160 (IR)
2	46 (R), 112 (IR), 212 (IR), 245 (R)	112 (IR), 245 (R), 282 (IR), 355 (R), 455 (R), 555 (R), 555 (IR)	112 (IR), 282 (IR), 455 (R)	282 (IR)	440 (IR), 453 (R), 612 (R)	440 (IR), 453 (R), 612 (R)	614 (IR), 714 (R), 746 (IR), 761 (R)	555 (R), 562 (IR), 614 (IR), 746 (IR), 761 (R)	1042 (R), 1109 (R), 1146 (IR),	1008 (IR), 1042 (R), 1146 (IR)
1.4	25 (IR), 102 (IR), 168 (IR), 179 (R), 210 (IR), 254 (R)	210 (IR), 297 (IR), 460 (R)	102 (IR), 297 (IR), 460 (R)	102 (IR), 460 (R)	432 (IR)	432 (IR), 460 (R)	612 (R), 680 (IR), 733 (IR)	612 (R), 680 (IR), 733 (IR)	1073 (R), 1124 (IR), 1124 (R)	988 (IR), 999 (R), 1073 (R)
1	73 (IR), 94 (IR), 177 (R), 215 (IR),	272 (R), 298 (IR), 468 (R), 606 (R), 734 (R)	272 (R), 298 (IR), 468 (R)	272(R), 298 (IR), 468 (R)	-	428 (IR)	-	606 (R), 672 (IR) 734 (IR), 734 (R),971 (IR)	-	968 (IR), 975 (R), 1059 (R)

So far, we have investigated the influence of aluminum and its distribution on the lattice parameter and vibrational spectra of sodalite, and the results seem to indicate a consistent trend. The next step in our study was to check our computations against experiments to show the reliability of our results. We have compared our simulated vibrational spectra for siliceous sodalite and sodalite with Si/Al = 1 with our experimental results. In the next section, we will discuss our X-ray diffraction and IR spectroscopy results from our experiments, and we will see why the comparison between simulated and experimental results led us to explore defects in sodalite computationally.

3.4.2 Crystal Structure and Thermal Stability of Synthetic Sodalite

To ensure the synthesis of pristine sodalite, we randomized three synthetic parameters (i.e., aging time, crystallization temperature, and crystallization time) based on synthesis protocols available in the literature. We first characterized the synthesized samples using X-ray diffraction (XRD). The XRD patterns of samples synthesized under all of the conditions we studied are shown in Figures 3.7 and 3.8. Only some of the conditions described in Table 3.2 yielded XRD patterns characteristic of sodalite; only materials with XRD patterns consistent with sodalite will be discussed.

For siliceous samples, the XRD patterns suggest that aging times longer than 5 min lead to the formation of non-sodalite phases: with the exception of sample 1-1440-175-21, all syntheses that actually resulted in siliceous sodalite came from gels aged for 5 min. We conclude that aging the reaction gel for too long may promote the nucleation of non-sodalite crystals and/or the polymerization of organosilica species, ultimately leading to the formation of other silica polymorphs. This observation is typical of the complexity of solvothermal syntheses of zeolitic materials. Thermogravimetric analysis showed that the siliceous sodalite powders are stable at temperatures up to 1000 °C. The average mass loss is 5 ± 2% (data not shown).

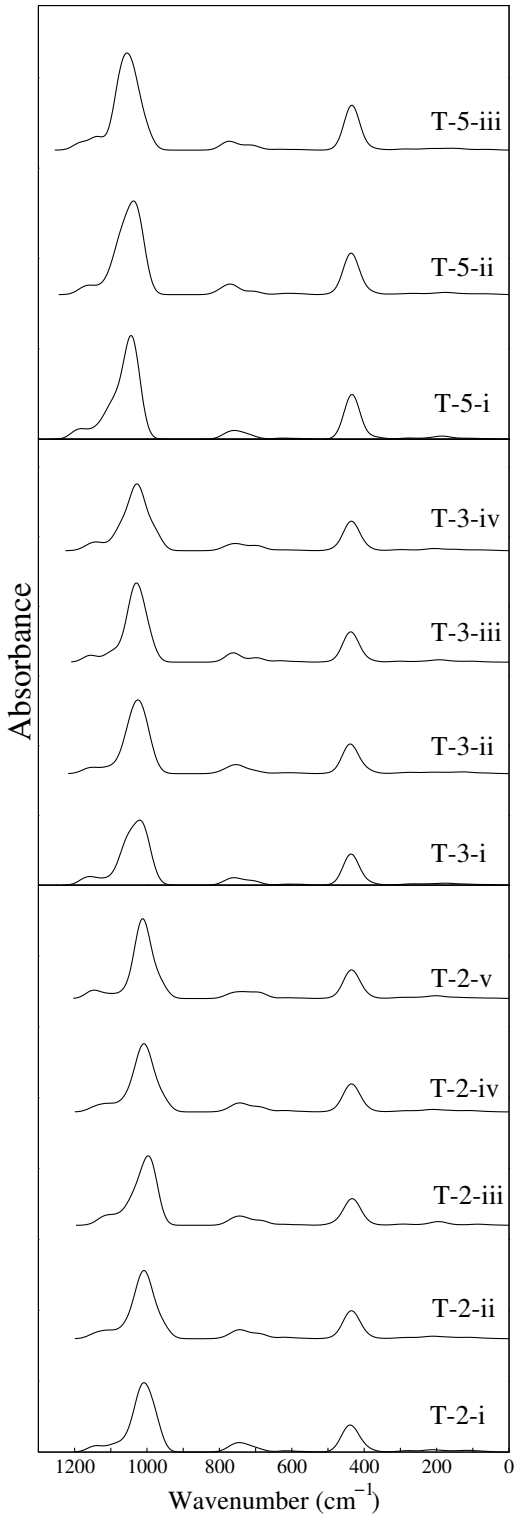

Figure 3.4. Simulated infrared spectra of Si/Al ratios 5, 3, and 2 of sodalite from the top to the bottom, respectively, as the amount of aluminum is increased. The notations are consistent with Table 1.

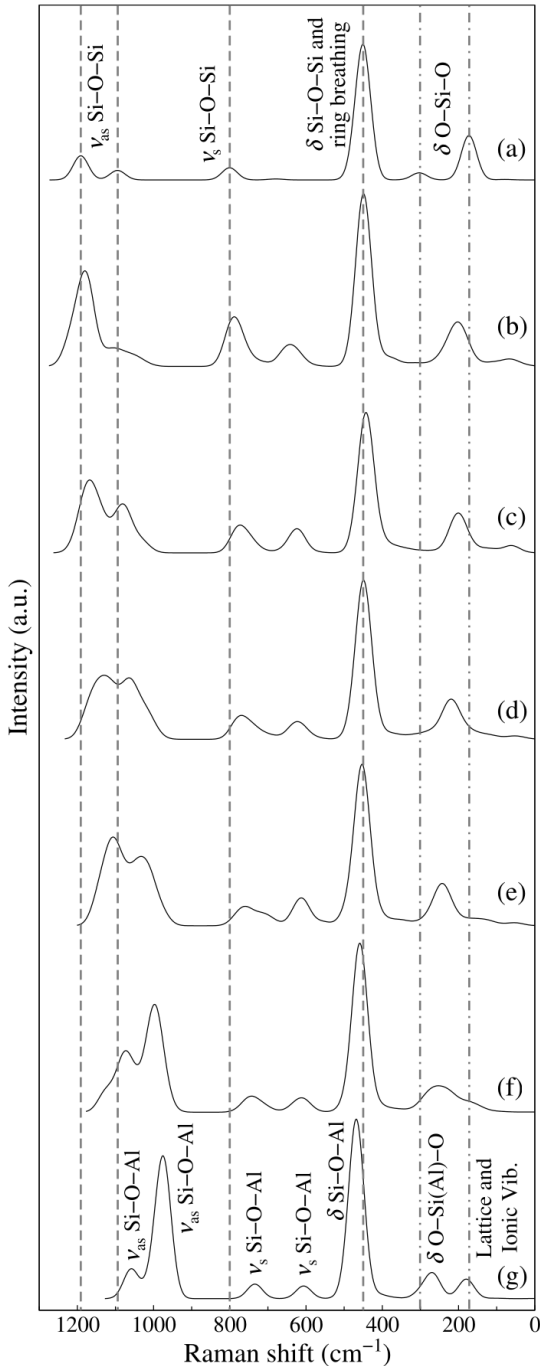

Figure 3.5. Theoretical Raman spectra of sodium bromide sodalites at various Si/Al ratios. Vertical dashed lines are drawn at the peak locations in the siliceous (Si/Al $\rightarrow \infty$) spectrum, and have wavenumbers of 1191, 1094, 800, 450, 301, and 172 cm^{-1}. Dash-dotted lines indicate the appearance of new peaks as aluminum is introduced and how that peak shifts to lower wavenumbers gradually. The replacement of silicon by aluminum atoms likely causes variations in bond length, bond strength, and polarizability, which leads to the observed trend. (a) siliceous, (b) Si/Al = 11, (c) Si/Al = 5, (d) Si/Al = 3, (e) Si/Al = 2, (f) Si/Al = 1.4, and (g) Si/Al = 1.

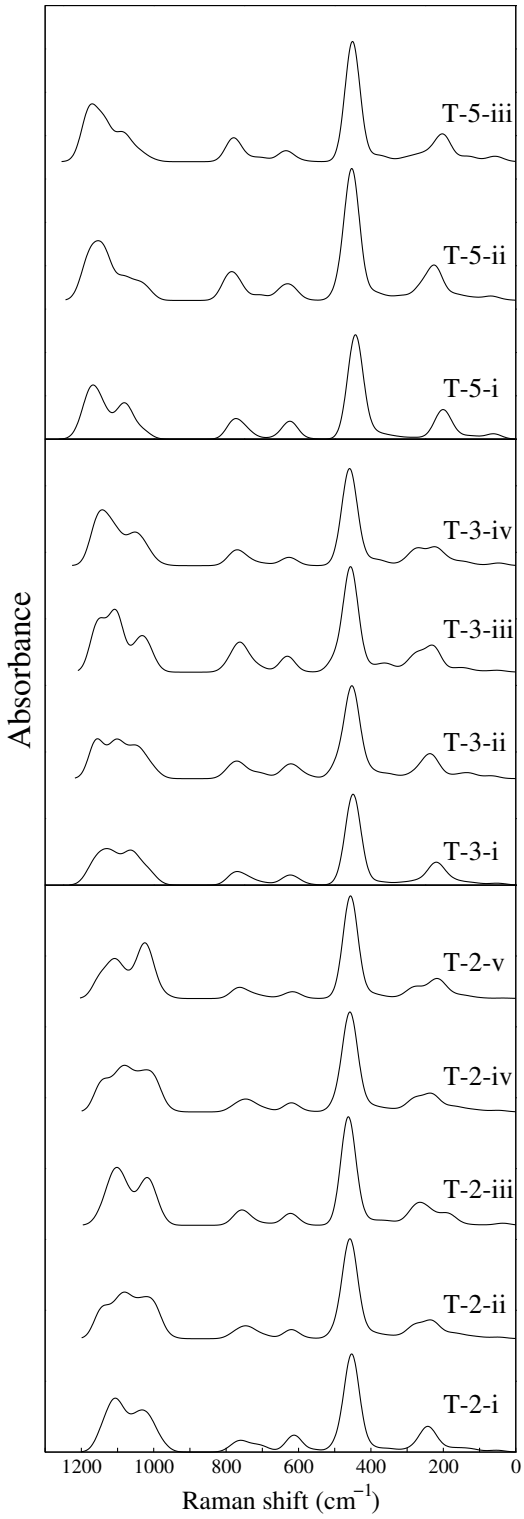

Figure 3.6. Simulated Raman spectra of Si/Al ratios 5, 3, and 2 of sodalite from the top to the bottom, respectively, as the amount of aluminum is increased. The notations are consistent with Table 1.

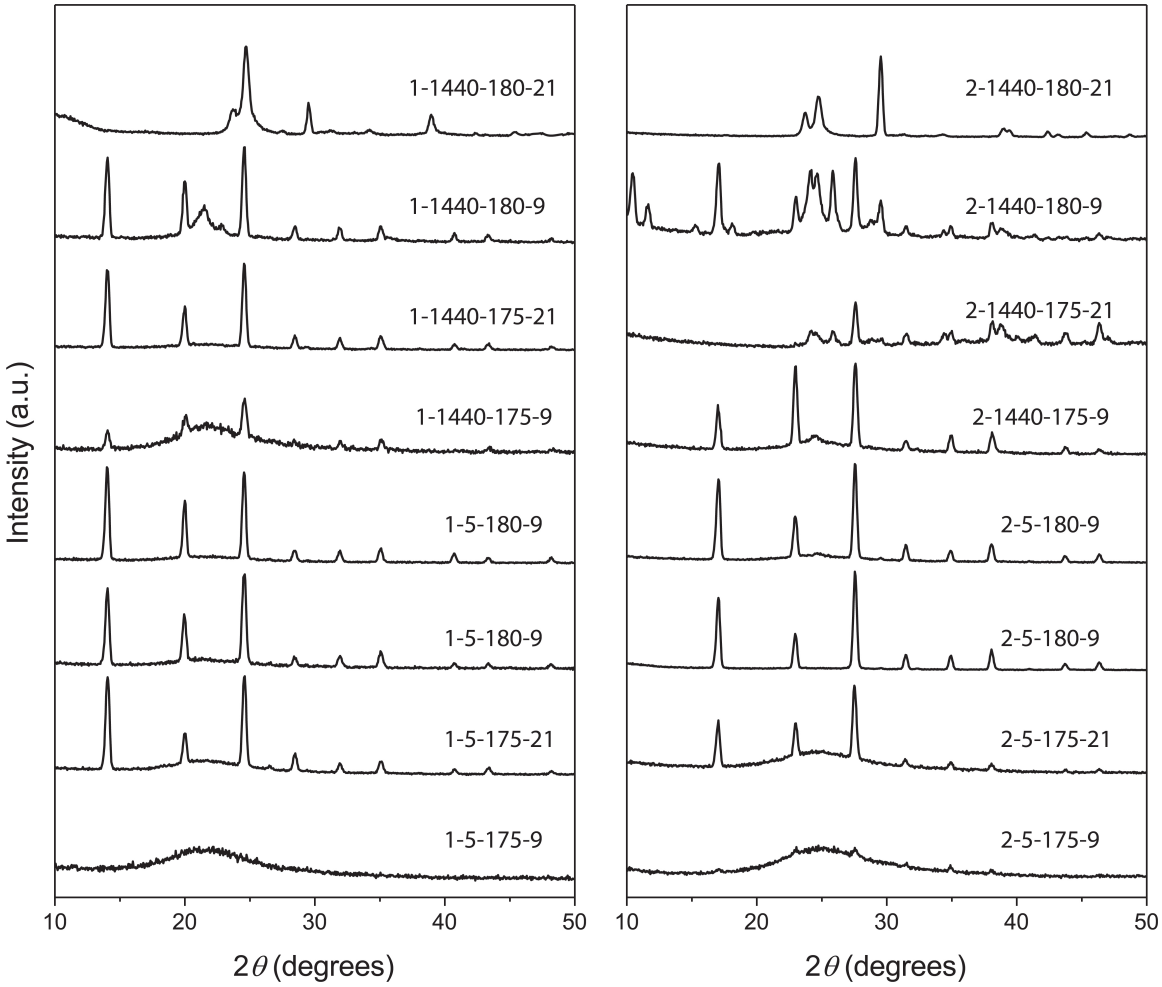

Figure 3.7. X-ray diffraction patterns of all siliceous sodalites obtained from gels aged at various times and crystallized under different conditions. The sample coding is consistent with Table 3.2. Shorter aging times seem to promote the formation of pure sodalite powders.

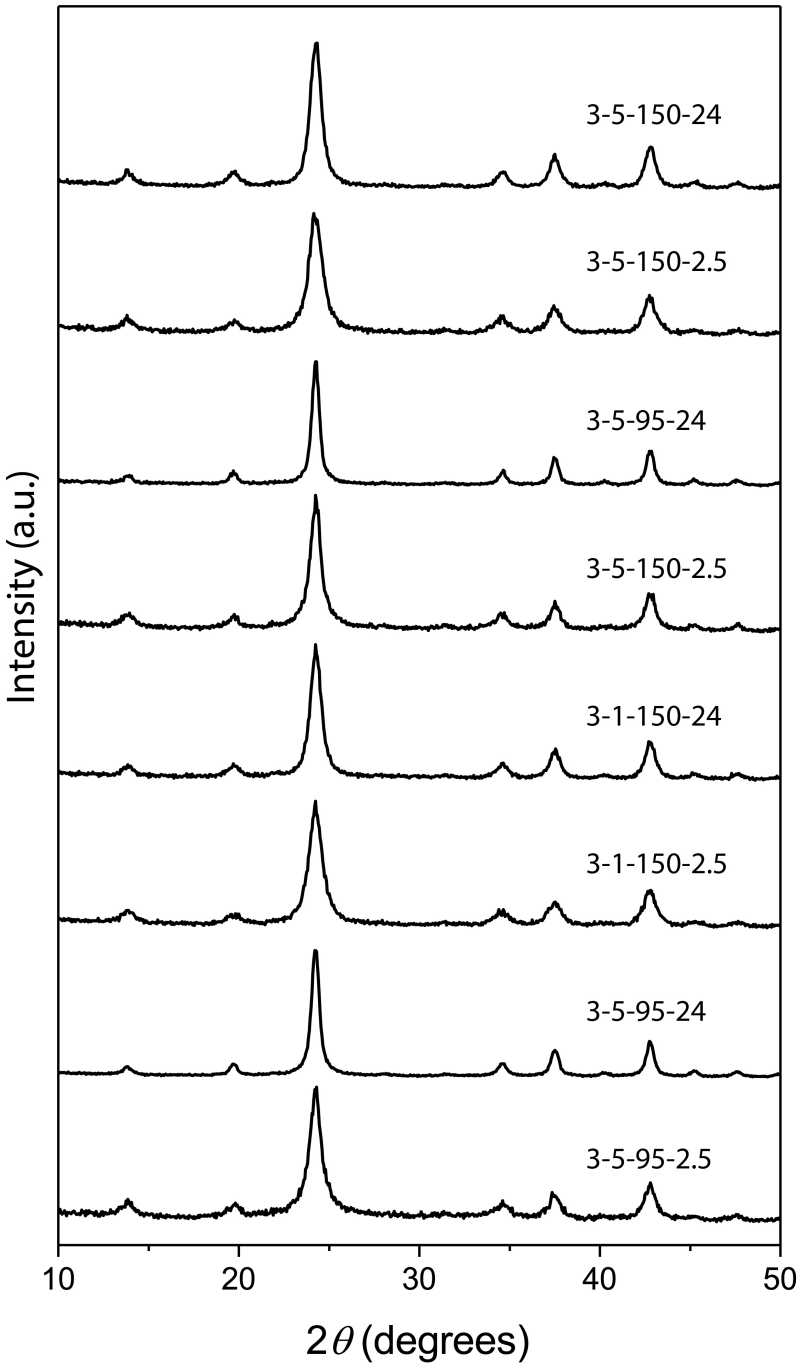

Figure 3.8. X-ray diffraction patterns of all the aluminosilicate sodalites obtained from gels aged at various times and crystallized at different conditions. The sample coding is consistent with Table 3.2.

The protocol used to make aluminosilicate sodalite, in contrast to those to make the all-silica variant, appears to be less susceptible to variations in the process variables studied here.

3.4.3 Comparison of Experimental and Simulated Infrared Spectra

We characterized synthetic sodalite using Fourier transform infrared spectroscopy (FTIR) with the intent to compare with the simulated spectra presented in Section 3.4.1. Figures 3.9 and 3.10 show the FTIR spectra of siliceous and aluminosilicate synthetic sodalite powders, respectively, compared to the calculated (DFT) spectra. As shown in these figures, DFT with this functional and pseudopotential accurately predicts sodalite's vibrational modes. The presence of smaller peaks in the experimental spectra, however, raised further questions regarding the presence of various defects in the synthesized powders. For example, the small peak around 870 cm^{-1}, present in almost all siliceous samples, can be attributed to the presence of adsorbed water and/or hydroxyl groups in these samples.[140] We explore this in depth in Sections 3.4.4 and 3.4.5.

A similar analysis is done for the spectra shown in Figure 3.10, except that only samples that matched the XRD pattern for sodalite are considered. In Figure 3.10, experimental absorbance spectra of aluminosilicate sodalite samples are shown above the DFT-predicted spectrum. These data show that simulations are able to predict the main symmetric and asymmetric stretching modes with very high accuracy. As observed in the spectra of the siliceous materials, there appears to be a substantial broadening of the peak associated with asymmetric stretching of Si−O−Al groups. In addition, as can be seen in Figure 3.10, both the symmetric stretching and bending modes of Si−O−Al bonds exhibit peak splitting in the experimental spectra. This may also be due to crystal defects and/or adsorbed water. In both Figures 3.9 and 3.10, as well as in subsequent figures, the left panel shows the higher frequency region of each spectrum. This high-wavenumber part of the spectrum, along with

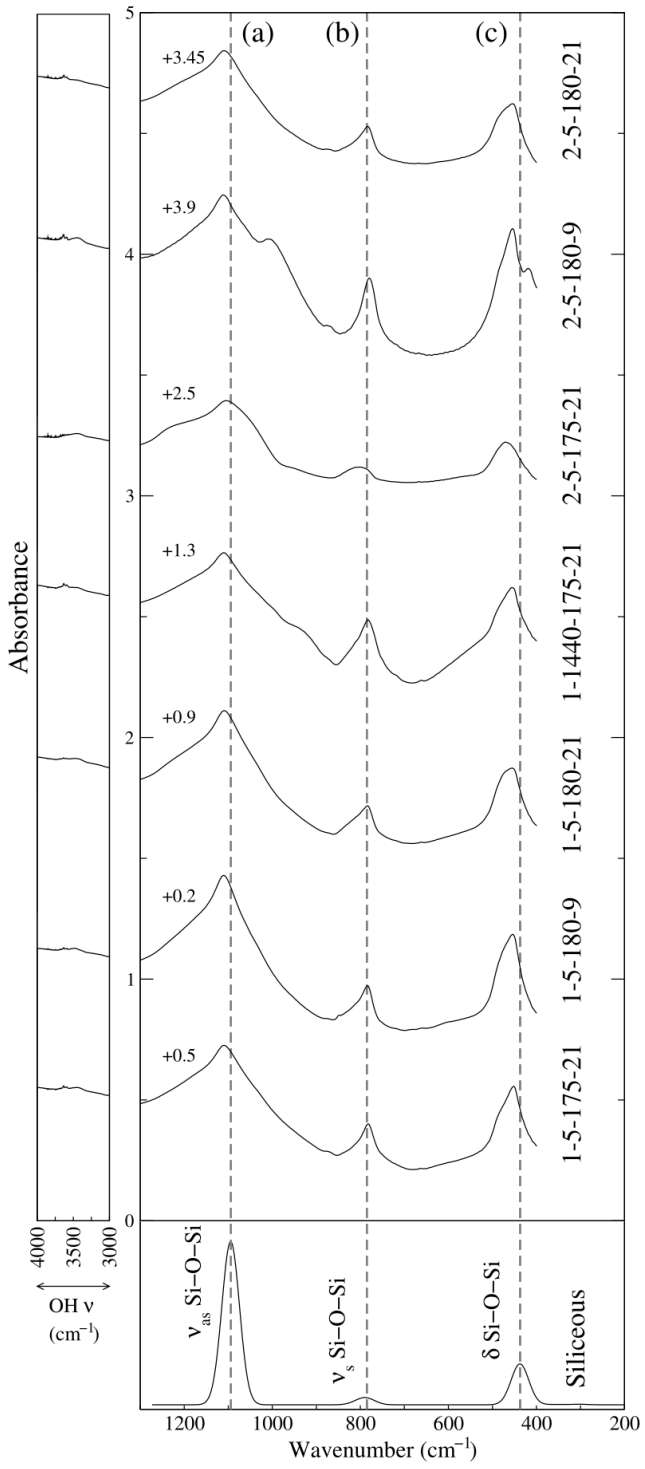

Figure 3.9. Comparison of the calculated infrared absorbance spectrum of defect-free siliceous sodalite from DFT with siliceous sodalite synthesized under several conditions (see Table 3.2). DFT calculations accurately predict the absorbance peaks, which are denoted with dashed lines: (a) ν_{as} Si−O−Si, 1094 cm^{-1}; (b) ν_{s} Si−O−Si, 785 cm^{-1}; (c) δ Si−O−Si, 437 cm^{-1}. The left panel shows the OH stretching region. Data in both the OH and framework regions have been translated vertically by the given amount to avoid overlap.

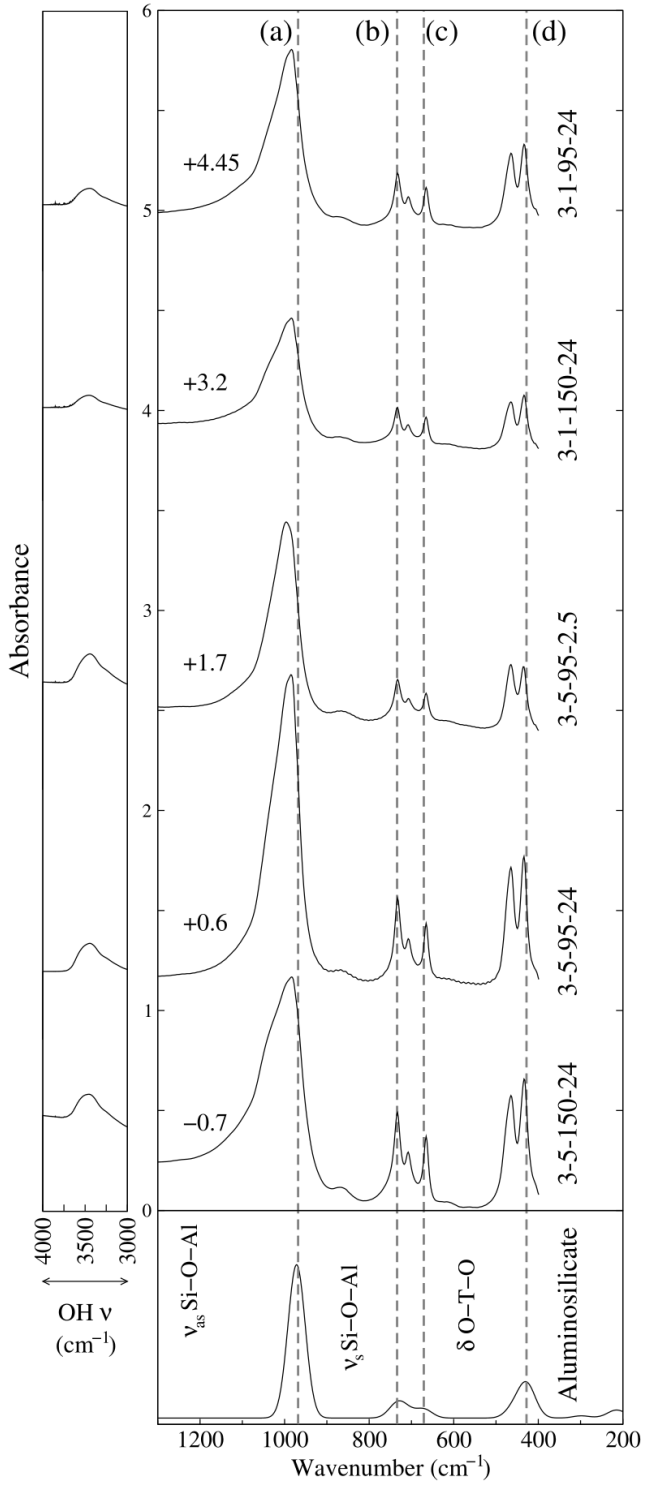

Figure 3.10. Comparison of the calculated infrared absorbance spectrum of defect-free aluminosilicate sodalite with Si/Al = 1 from DFT with aluminosilicate sodalite samples synthesized under several conditions (see Table 3.2). The dashed lines denote the DFT-calculated absorbance peaks, (a) ν_{as} (Si−O−Al), 968 cm^{-1}; (b) ν_{s} (Si−O−Al), 734 cm^{-1}; (c) ν_{s} (Si−O−Al), 672 cm^{-1}; (d) δ (Si−O−Al), 428 cm^{-1}. The left panel shows the OH stretching region. Data in both the OH and framework regions have been translated vertically by the given amount to avoid overlap.

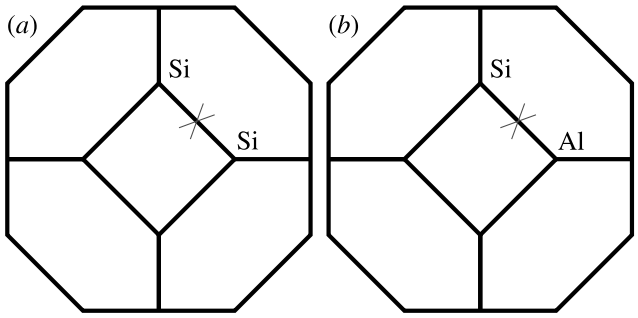

Figure 3.11. Schematic showing bonds broken by hydrolysis of one O−T bond, thereby introducing two OH groups into the framework for (a) siliceous and (b) aluminosilicate sodalite. Crosses indicate the bond that is broken, at which the defect is introduced. The OH defects are inserted on both sides of the deleted oxygen atom. The picture shows the projected view of the sodalite cage; only one bond is broken.

the framework region, is also informative in terms of identifying the the types of defects (e.g., adsorbed water, hydroxyl groups), which will be discussed in detail in Section 3.4.5.

3.4.4 Simulations of Hydroxyl Groups in Sodalite

The extra peaks in the measured infrared spectra (Figures 3.9 and 3.10) led us to introduce hydroxyl groups (OH) into the sodalite structure, such as would occur by incomplete bond formation or hydrolysis of an O−Si or O−Al bond. Two classes of defects were considered: single-water addition, which results in two OH groups and one broken O−T bond; and double-water addition, which results in four OH groups and two broken O−T bonds.

In the single-water case, we removed an oxygen atom between two tetrahedral atoms (T-atoms) and instead placed a hydroxyl group next to each T-atom, as shown in Figure 3.11. In the double-water case, we removed two oxygen atoms between two possibly-overlapping pairs of tetrahedral atoms. This results in the configurations shown in Figure 3.12. For the configuration in Figure 3.12a in materials with Si/Al = 1, there are two inequivalent configurations, which are shown in Figures 3.12e and 3.12f.

The procedure to obtain the vibrational spectra for these types of calculations was the same as that of the defect-free ones discussed earlier. When it comes to including hydroxyl

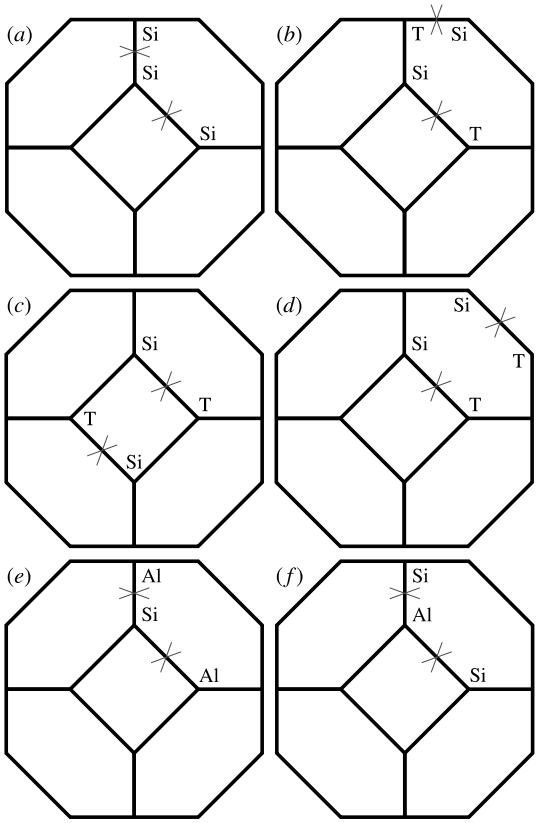

Figure 3.12. Schematic showing the unique bonds that can be hydrolyzed to form OH defects in a sodalite cage. Vertices represent tetrahedral atoms; those labeled "T" are silicon atoms in the siliceous form but are aluminum atoms in the Si/Al = 1 case. Crosses indicate the atom around which the defect is introduced. Oxygen atoms indicated by crosses are part of the same ring in each image.

groups in zeolites, one can propose different initial geometries as the starting configuration for the geometry optimization. However, in order to be confident as to the minimum-energy configuration, we compared each of our trials' total energy with the total energy of a sodalite unit cell containing adsorbed water molecules. According to available experimental data,[3] the water molecule can be adsorbed either inside or outside the sodalite cage in our one-unit-cell calculations, and there are four possible water molecule locations both inside and outside the cage. For the double-water situation, two locations for the water molecules were considered in our calculations: (i) both water molecules inside the cage, (ii) both water molecules outside the cage, and (iii) one water molecule inside and one outside the sodalite cage. This energy analysis allowed us to exclude final (geometry-optimized) configurations that were significantly different in total energy from the water–sodalite composites or those that significantly deformed and did not retain the shape of the sodalite framework. Most of the configurations, regardless of whether they included two or four hydroxyl groups, resulted in either dehydration (either inside or outside the cage) or configurations similar to those shown in Figure 3.13. For example, in the case of two OH groups in both siliceous and aluminosilicate sodalite, the defects can form a disilanol group (Figure 3.13a) and/or a water molecule inside or outside the sodalite cage. For the inclusion of four OH groups, the outcome can be both of the configurations in Figure 3.13 and/or dehydration, depending where the defect is introduced. These results are also in agreement with findings of Sokol et al.[141] Table 3.6 shows the outcome of each of the configurations in which the defects were introduced as well as their lattice parameters. The last column in Table 3.6 is a label that denotes each compound's infrared spectrum in the subsequent figures.

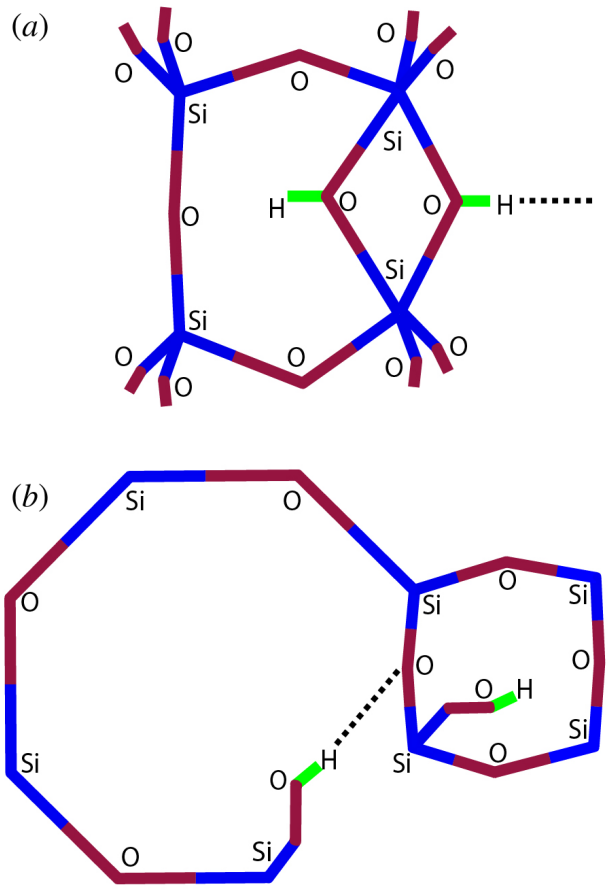

Figure 3.13. Schematic of possible final configurations of sodalite having hydroxyl defects. (a) disilanol groups and (b) nested silanol groups. Black dashed lines represent hydrogen bonds. Those hydrogen atoms that have no dashed lines are hydrogen bonded with other neighboring atoms in a three-dimensional fashion.

Table 3.6. Summary of simulation results for siliceous and aluminosilicate sodalite with and without defects.

Si/Al, #OH, bond[a]	Cell Volume (Å^3)	a (Å)	b (Å)	c (Å)	α (°)	β (°)	γ (°)	Outcome[b]	Spectrum[c]
∞	663.511	8.722	8.722	8.722	90.00	90.00	90.00	-	3.14a
∞ (expt.[136])	687.764	8.827	8.827	8.827	90.00	90.00	90.00	-	-
∞, 2OH, 3.11a	608.055	8.661	8.112	8.660	91.04	88.36	91.01	Fig. 3.13a	3.14b
∞, 2OH, 3.11a	678.848	8.797	8.774	8.796	90.22	90.55	90.21	water/outside	3.14c (black)
∞, 2OH, 3.11a	672.114	8.764	8.752	8.764	90.76	90.30	90.23	water/outside	3.14c (green)
∞, 2OH, 3.11a	662.200	8.725	8.707	8.719	89.04	90.72	89.13	water/inside	3.14d (black)
∞, 4OH, 3.12a	664.627	8.736	8.761	8.696	92.20	88.18	90.85	Fig. 3.13b + water	3.15b (black)
∞, 4OH, 3.12a	654.377	8.691	8.694	8.673	91.33	88.68	92.45	*2 water	3.15b (green)
∞, 4OH, 3.12b	633.433	8.408	8.724	8.654	89.08	91.34	86.71	Fig. 3.13a × 2	3.15c (green)
∞, 4OH, 3.12b	669.029	8.756	8.729	8.756	89.83	91.11	89.79	*2 water	3.15c (black)
∞, 4OH, 3.12c	645.589	8.800	8.614	8.555	90.65	85.76	86.74	Fig. 3.13b + water	3.15d (black)
∞, 4OH, 3.12c	599.124	8.492	8.096	8.738	92.29	88.43	87.00	*Fig. 3.13a + water	3.15d (green)
∞, 4OH, 3.12d	580.731	8.208	8.652	8.177	90.00	89.67	89.99	Fig. 3.13a × 2	3.15e (green)
∞, 4OH, 3.12d	580.198	8.094	8.840	8.118	88.35	90.35	92.15	*2 water	3.15e (black)
1	671.301	8.756	8.756	8.756	90.00	90.00	90.00	-	3.16a (black)
1 (expt.[109])	700.700	8.882	8.882	8.882	90.00	90.00	90.00	-	-
1, 2OH, 3.11b	682.581	8.696	8.854	8.868	89.21	91.33	91.12	Fig. 3.13a	3.16b (black)
1, 2OH, 3.11b	684.198	8.815	8.823	8.798	89.51	89.64	89.42	water/outside	3.16c (black)
1, 2OH, 3.11b	678.140	8.778	8.848	8.732	89.80	89.80	89.47	water/outside	3.16c (green)
1, 2OH, 3.11b	678.748	8.696	8.815	8.854	89.41	90.45	89.71	water/inside	3.16d (black)
1, 2OH, 3.11b	679.127	8.722	8.802	8.848	89.42	90.50	89.71	water/inside	3.16d (green)
1, 4OH, 3.12e	800.902	9.339	9.161	9.363	89.92	90.99	89.31	2 water	3.17b (black)
1, 4OH, 3.12f	795.986	9.324	9.218	9.261	90.27	90.50	90.19	Fig. 3.13b + water	3.17b (green)
1, 4OH, 3.12b	688.295	8.855	8.954	8.681	89.66	89.68	87.69	2 water	3.17c (black)
1, 4OH, 3.12c	694.741	8.956	8.808	8.808	90.49	90.03	89.97	2 water	3.17d (black)
1, 4OH, 3.12c	681.340	8.756	9.016	8.632	90.00	90.00	89.30	2 water	3.17e (black)

[a]The third entry in this column is the figure showing which bond(s) is/are broken. Multiple entries with the same label are slightly different initial geometries that relaxed to different entries.

[b]Final state after geometry optimization; the one with an asterisk (*) is (slightly) lower in energy than the other outcome with the same broken bonds.

[c]Corresponding infrared spectrum shown in Figures 3.14–3.17.

As can be seen in Table 3.6, the number of final geometries in the siliceous form is greater than the number of aluminosilicate geometries. In general, introducing defects that result in the formation of water tends to increase the cell volume compared to the defect-free material. In the rest of this section, we will compare the infrared spectra of defect-free sodalites (both siliceous and aluminosilicate) with those we acquired in Table 3.6 from our calculations to check the validity of our aforementioned hypothesis: whether or not the presence of adsorbed water and/or hydroxyl groups would cause the substantial peak broadening in the asymmetric stretching region and appearance of additional peaks in the infrared spectrum from experiments.

Figure 3.14 shows a comparison of infrared spectra between defect-free siliceous sodalite and siliceous sodalite containing two OH groups; the wavenumbers of each band are written above or below the associated peak. The reason why wavenumbers from 400–1300 cm^{-1} are shown is to be consistent with our experimental results, which are taken in KBr (opaque to infrared radiation below ≈ 400 cm^{-1}). As shown in Figure 3.14, the three major peaks (ν_{as} Si−O−Si, ν_{s} Si−O−Si, and δ Si−O−Si) are still obvious, even with the inclusion of the defects. Nevertheless, these defects have impacted the infrared spectra to some extent. It is only in Figure 3.14b that a disilanol group exists in the final structure (Figure 3.13a), and this is the only one of the calculations we ran that relaxed to a structure with two hydroxyl groups without the formation of water. For the rest of this section, we will only discuss the details of the peaks that are generated because of the existence of defect(s), though there are slight changes in the peaks found in the intact framework as well. Those peaks that are within the region of the dashed red lines have been discussed in Section 3.4.1.

Considering Figure 3.14b in the asymmetric stretching region (900–1300 cm^{-1}), the inclusion of the defect has caused the appearance of an additional peak at a higher wavenumber (1181 cm^{-1}), which originates from both Si−O−Si asymmetric stretching and O−H bending, and an additional peak at a lower wavenumber (994 cm^{-1}), which also results

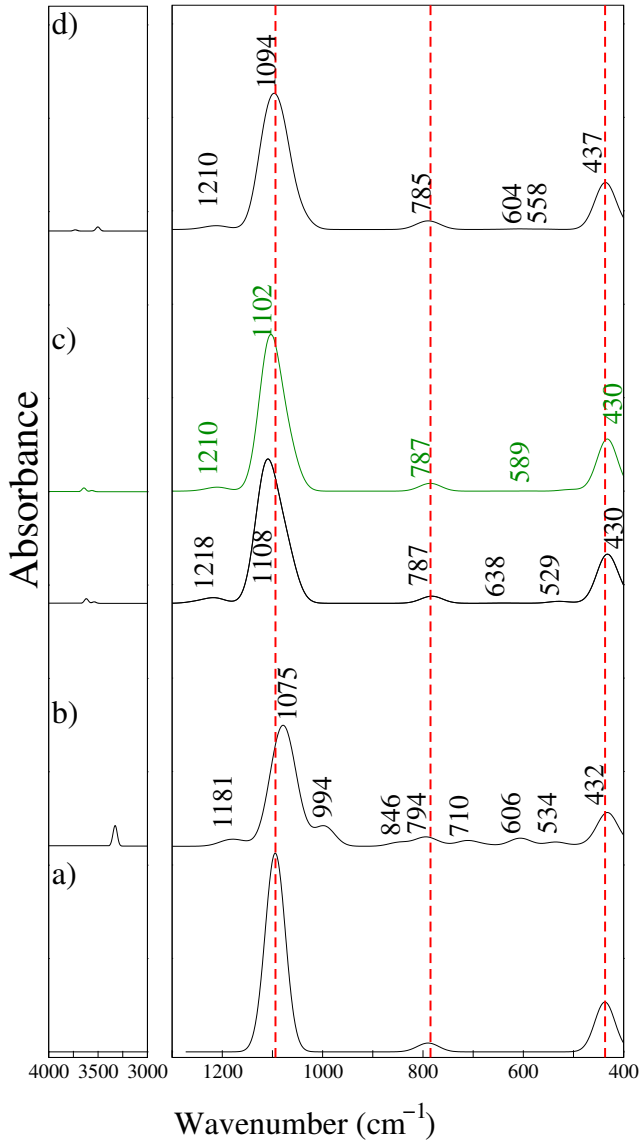

Figure 3.14. Simulated infrared spectra of siliceous sodalite with two OH defects present. The three major peaks (ν_{as} Si−O−Si at 1191 cm^{-1}, ν_s Si−O−Si at 785 cm^{-1}, and δ Si−O−Si at 437 cm^{-1}) are denoted in the defect-free siliceous case by red dashed lines, which guide the eye to see the changes from defect-free siliceous sodalite (a). Labels (b), (c), and (d) correspond to systems from Table 3.6. The left panel represnets the higher wavenumbers to show the OH stretching region from the simulations. The green spectrum refers to an alternative configuration of structure (c), as identified in Table 3.6.

from Si−O−Si asymmetric stretching. The peak at 846 cm^{-1} is from Si−OH stretching in the disilanol ring, and the rest of the peaks at 710, 606, and 534 cm^{-1} are O−H bending modes. The spectra in Figures 3.14c and 3.14d are similar to one another; the peak at the highest wavenumber is also coming from Si−O−Si asymmetric stretching, and the additional peak(s) between the bending and symmetric stretching modes (400–800 cm^{-1}) are from OH bending modes. The only vibrational mode that differs between Figures 3.14b and 3.14c is the Si−OH stretching mode, which is only present in Figure 3.14b.

Figure 3.15 shows a comparison of the IR spectrum of defect-free siliceous sodalite with the spectra of siliceous sodalite with four OH defects present. The labels for each graph are also consistent with Table 3.6, and as seen in Figure 3.15, there are two possible outcomes (black and green) for each of the four defect configurations that we introduced at the beginning of Section 3.4.4. Those spectra that have been affected the most have final geometries similar to that shown in Figure 3.13, whereas those that are least affected are the ones that resulted in dehydration of the defect, leaving adsorbed water. The same conclusion that was drawn regarding Figure 3.14 for the assignments of bands between the three major regions still applies to Figure 3.15. However, there is one additional band that occurs at a relatively higher wavenumber (1240–1295 cm^{-1}), which is associated with OH bending. The inclusion of four OH defects impacted the asymmetric stretching mode more significantly (i.e., splitting the asymmetric stretching mode and/or shifting it to lower wavenumbers) compared to the sodalites containing two OH groups. For example, in Figure 3.15e (green lines), which has a double disilanol defect, we observe more new peaks than in all other spectra.

Figures 3.16 and 3.17 show spectra for the aluminosilicate versions of the materials whose spectra are shown in Figures 3.14 and 3.15. In Figure 3.16, only case (b) resulted in the formation of a disilanol group, which caused the appearance of additional peaks at 1136, 770, and 620 cm^{-1}; these peaks are associated with Si−O−Si asymmetric stretching, Si−OH stretching, and OH bending modes, respectively. Figures 3.16c and 3.16d have

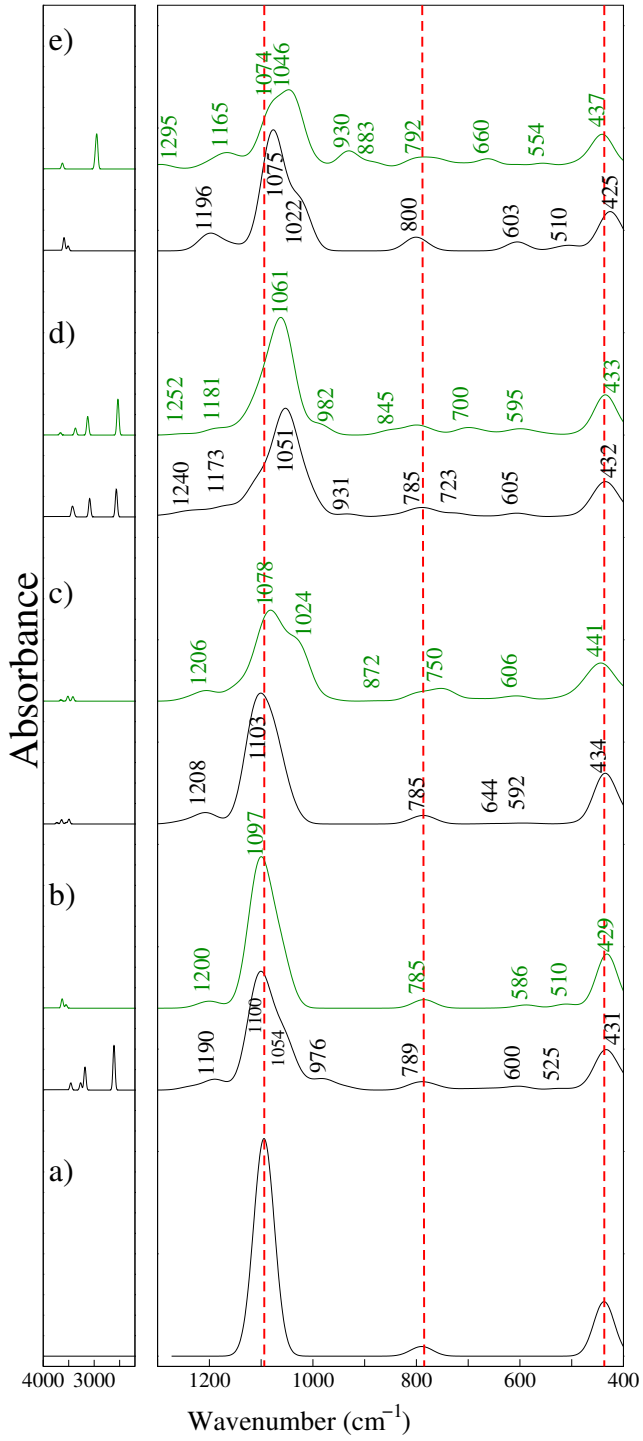

Figure 3.15. Simulated infrared spectra of siliceous sodalite with four OH defects present. The three major peaks (ν_{as} Si−O−Si at 1191 cm^{-1}, ν_s Si−O−Si at 785 cm^{-1} and δ Si−O−Si at 437 cm^{-1}) are denoted on the defect-free siliceous case and the red dotted lines are to guide the eye to see the changes from defect-free siliceous sodalite (a). Labels (b), (c), (d), and (e) correspond to systems from Table 3.6. The left panel shows the OH stretching region. The green spectra refer to alternative configurations, as denoted in Table 3.6.

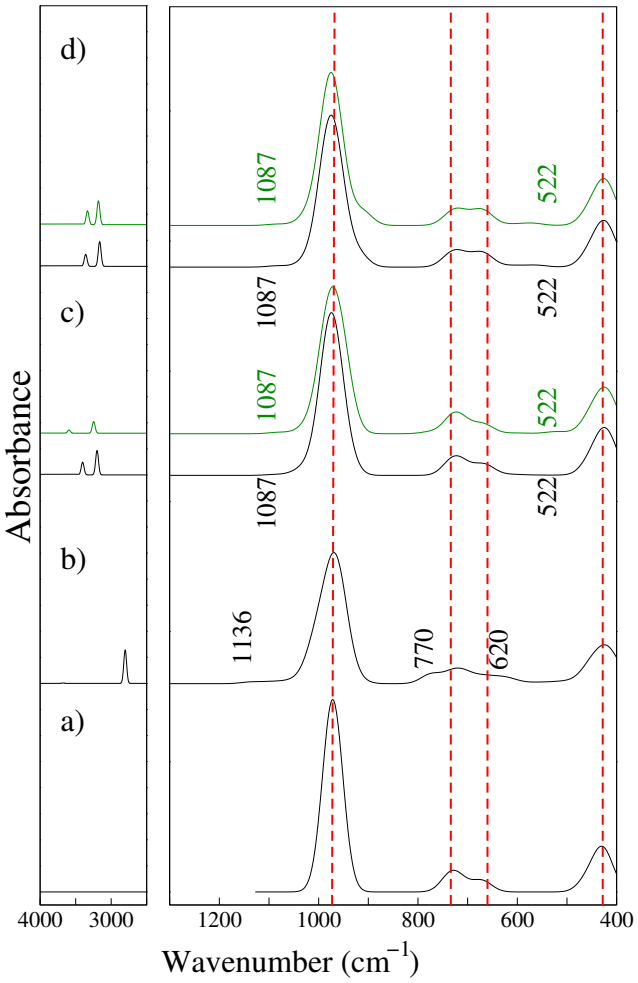

Figure 3.16. Simulated infrared spectra of aluminosilicate sodalite with two OH defects present. The three major peaks (ν_{as} Si−O−Al at 968 cm^{-1}, ν_s Si−O−Al at 734 and 672 cm^{-1}, and δ Si−O−Al at 428 cm^{-1}) are denoted in the defect-free aluminosilicate case by red dotted lines, which guide the eye to see the changes from defect-free aluminosilicate sodalite (a). Labels (b), (c), (d), and (e) correspond to systems in Table 3.6. The left panel shows the OH stretching region. The green spectra refer to alternative configurations, as denoted in Table 3.6.

the same peaks as in Figure 3.14a, and the additional peaks from Si−O−Si asymmetric stretching (1087 cm^{-1}) and O−H bending (522 cm^{-1}). The same trends are evident in Figure 3.17 for the introduction of four OH defects. In Figure 3.17b (black line), which resulted in the formation of two water molecules, this effect has caused the appearance of one band at 1085 cm^{-1}, which is associated with Si−O−Si asymmetric stretching; and one at 895 cm^{-1}, which is associated with both Si−O−Si asymmetric stretching and O−H bending. Figures 3.17c–e are quite similar; the additional peaks in the range 400–800 cm^{-1} are O−H bending modes.

Adsorbed water and/or hydroxyl groups are not the only types of defects one could model for the calculation of the vibrational spectra of these materials. The substantial peak broadening in the asymmetric stretching region and the additional peaks between the bending region and the symmetric stretching region in the experiments led us to study whether or not those observations can be explained by the inclusion of the aforementioned defect(s) in our model. Our results have shown that the asymmetric stretching modes associated with Si−O−Si bridges are very sensitive to the inclusion of non-framework species. This band can be either shifted to higher or lower wavenumbers upon the inclusion of defects, depending on both the number and configuration of defects. In addition, upon the inclusion of defect(s), additional peak(s) in the Si−O−Si asymmetric stretching region appear at higher wavenumbers. Those defects that did not result in adsorbed-water outcomes in the simulations also show additional peaks in the range 800–950 cm^{-1} associated with Si−OH stretching. Symmetric stretching and bending modes are less strongly affected, and their wavenumbers can experience both red and blue shifts. In the end, O−H bending modes appear mostly in the 400–800 cm^{-1} range for all of the configurations we studied, with some geometries producing another O−H bending mode in the Si−O−Si asymmetric stretching region. The OH stretching mode will be discussed in the following section.

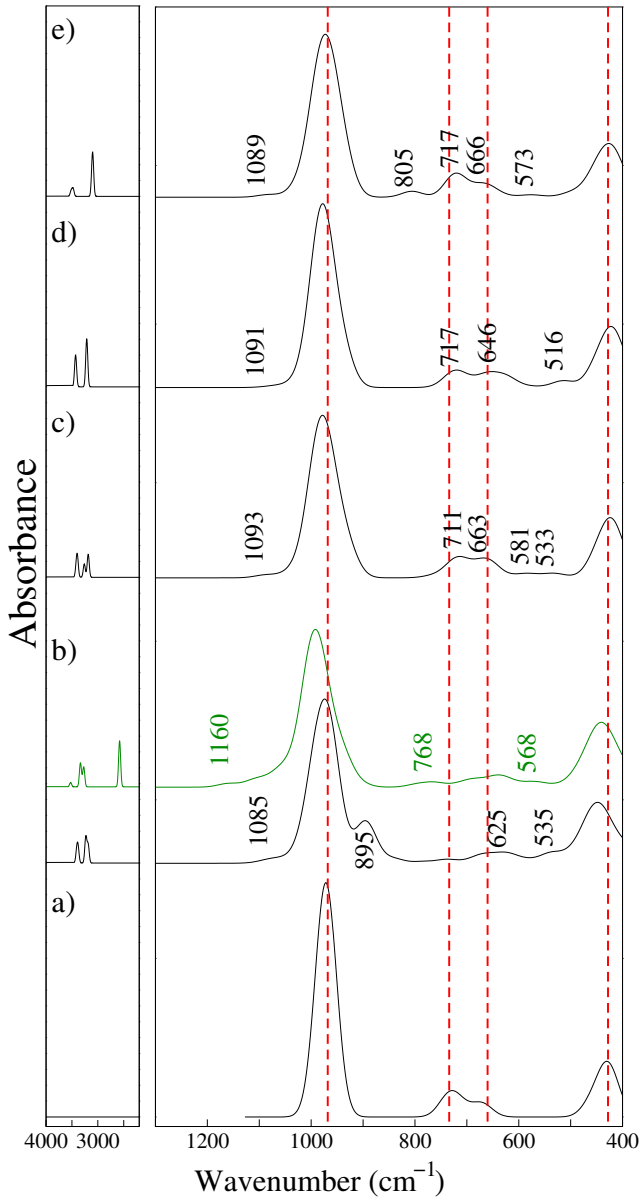

Figure 3.17. Simulated infrared spectra of aluminosilicate sodalite with four OH defects present. The three major peaks (ν_{as} Si−O−Al at 968 cm^{-1}, ν_s Si−O−Al at 734 and 672 cm^{-1}, and δ Si−O−Al at 428 cm^{-1}) are denoted on the defect-free aluminosilicate case by the red dotted lines, which guide the eye to see the changes from defect-free aluminosilicate sodalite (a). Labels (b), (c), (d) and (e) correspond to systems in Table 3.6. The left panel represents the higher wavenumbers to show the OH stretching region from the simulations. The green spectrum refers to an alternative configuration of structure (b), as denoted in Table 3.6.

3.4.5 The OH Stretching Region and Possible Defects

The defects that we introduced in our DFT supercell varied from hydroxyl groups in several configurations to adsorbed water molecules. It is worth mentioning that in order to be able to detect which types of defect are prevalent in our experiments, one needs to combine the information from the OH stretching region (usually 3000–4000 cm^{-1}) and the framework region together.[142,143] Band assignments in the OH stretching of Figures 3.14–3.17 can be found in Table 3.7. These bands, for the most part, are associated with OH stretching in adsorbed water molecules (both asymmetric and symmetric) and silanol groups. However, when it comes to interpretation of the OH stretching region in experimental infrared spectra, there are some crucial factors to be aware of. The OH stretching frequency is very sensitive to the geometrical environment in which the OH bond (present in the defect) is involved. For instance, the higher the strength of the hydrogen bond interaction (e.g., hydrogen bonding between a silanol group and an adsorbed water molecule), the lower the OH stretching frequency.[144] However, as this interaction is removed (e.g., by reducing the water content via degassing at high temperature), the band associated with OH stretching shifts to higher wavenumbers.[145] Since our experimental IR spectra were not measured in vacuo at high temperature, it is difficult to be certain as to which types of defects are present because of H-bonding (of the defects) with their surroundings (mainly with water molecules and/or framework oxygen). In other words, if the possible defect is a silanol group, the band associated with its OH stretching mode might be masked by the vibrations of OH in adsorbed water molecules.

Based on the results from DFT, the range over which the vibrations of adsorbed water molecules occur is between 3495–3730 cm^{-1} for siliceous sodalite (Figure 3.18). Most of the bands present in our samples (Figure 3.9) also fall into this region, which confirms the presence of adsorbed water. However, the presence of a well-defined shoulder at approximately 3430 cm^{-1} could indicate silanol defects or surface silanol groups in those samples. This can be explained by comparison with the band assignments from the DFT results

Table 3.7. Band assignment of the OH stretching region of Figures 9, 10, 11, and 12 in the main document. ν_s and ν_{as} stand for symmetric and asymmetric stretching modes, respectively for water molecule. The notation W is for when the vibraitonal mode is caused by the presence of adsorbed water molecule in the system, whereas Hb indicates that the vibration is due to hydrogen bond of the hydroxyl group/adsorbed water with the oxygen framework. T stands for the tetrahedral atom.

Spectrum \ Figure	Figure 9	Figure 10	Figure 11	Figure 12
Spectrum b Black	3330 disilanol OH stretching	2610 silanol OH stretching, 3179 silanol+W, 3265 silanol+W	2803 T-OH stretching, 3678 T-OH stretching	3186 Hb, 3230 Hb, 3392 Hb
Spectrum b Green	-	3550 W-ν_s, 3627 W-ν_{as}	-	2579 W+Hb, 3272 T-OH stretching, 3335 aluminol OH stretching, 3525 W+Hb
Spectrum c Black	3540 W-ν_s, 3620 W-ν_{as}	3495 W+Hb, 3553 W-ν_s, 3640 W-ν_{as}, 3730 W+Hb	3198 W-ν_s, 3401 W-ν_{as}	3182 W-ν_s, 3261 W-ν_s, 3396 W-ν_{as}
Spectrum c Green	3560 W-ν_s, 3642 W-ν_{as}	3417 double disilanol OH stretching, 3516 double disilanol OH stretching, 3649 double disilanol OH stretching	3246 W-ν_s, 3595 W-ν_{as}	-
Spectrum d Black	3502 W-ν_s, 3730 W-ν_{as}	2568 silanol+W, 3088 silanol+W, 3430 W-ν_{as}	3161 W-ν_s, 3359 W-ν_{as}	3213 W-ν_s, 3429 W-ν_{as}
Spectrum d Green	-	2533 disilanol+W, 3127 disilanol, 3370 W-ν_{as}, 3662 W-ν_{as}	3179 W-ν_s, 3333 W-ν_{as}	-
Spectrum e Black	-	3508 W-ν_s, 3591 W-ν_{as}	-	3098 W-ν_s, 3480 W-ν_{as}
Spectrum e Green	-	2945 double disilanol OH stretching, 3626 double disilanol OH stretching	-	-

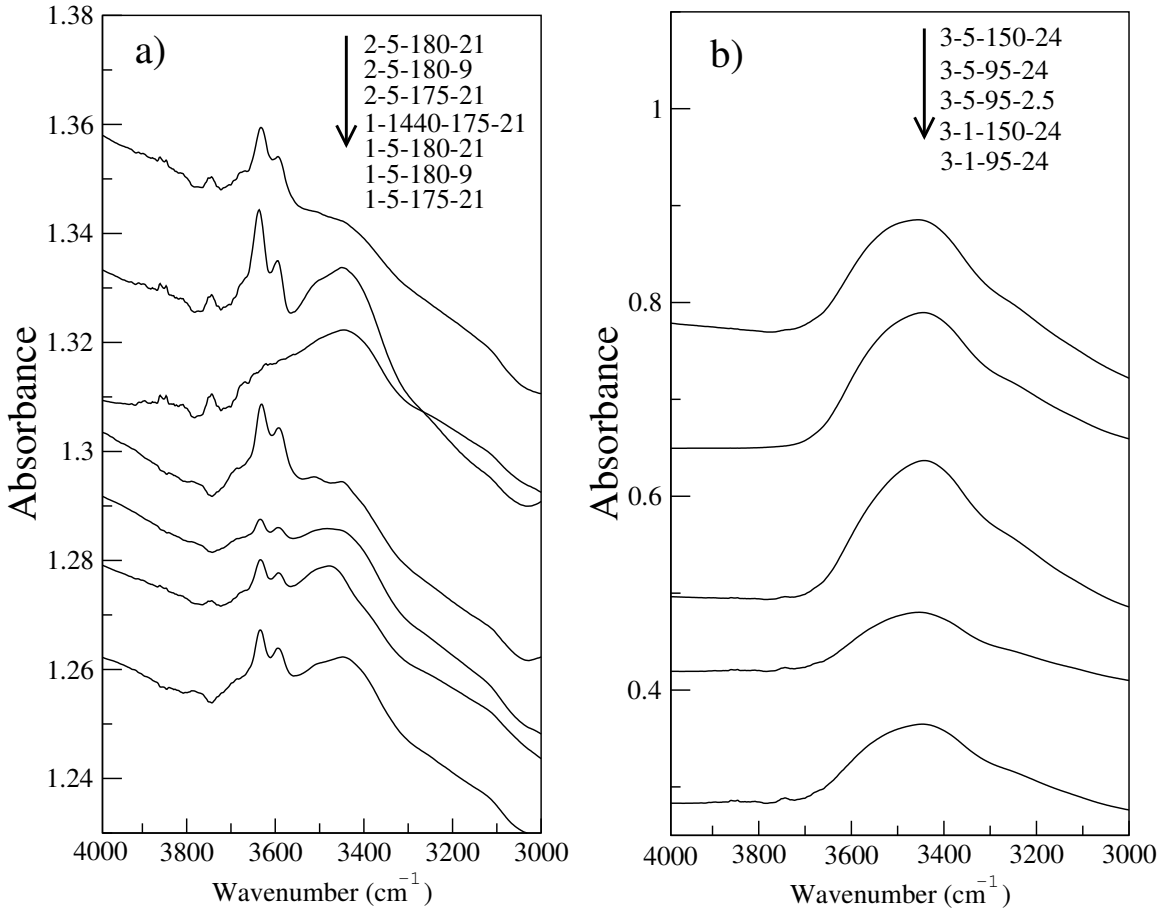

Figure 3.18. Magnified view of the experimental infrared spectra of sodalite in the OH stretching region. The left figure, (a), represents the siliceous sodalite and the right figure, (b), represents aluminosilicate sodalite.

(Table S2). The presence of such defects is also in agreement with the work of Hong et al.[146]

As seen in Figure 3.10, there is only one band in the OH stretching region for the aluminosilicate materials. This band falls in the water stretching range and confirms the presence of adsorbed water molecules in the samples. In addition, our DFT results also confirm that the most probable outcome when introducing defects in aluminosilicate sodalite is adsorbed water. This is also in agreement with the findings of Hong et al.,[146] who they found that the presence of SiO^- defects in aluminosilicate sodalites, synthesized similar to our procedure, is very minimal. Therefore, comparing the simulated vibrational spectra of these defect-induced sodalites with our experiments, we conclude that the likelihood of having silanol defects in siliceous sodalites as synthesized with these procedures is high, and that as the Si/Al ratio drops, the density of such defects is significantly reduced.

3.5 Conclusions

We have studied the effect of aluminum content and its distribution on the vibrational spectroscopy (infrared and Raman) of sodalite (**SOD** framework) using density functional theory (DFT) with periodic boundary conditions. We simulated all possible Si/Al ratios that sodalite can have in a single-unit-cell calculation, namely 1, 1.4, 2, 3, 5, 11, and ∞ (pure silica). We found a particular trend in both infrared (IR) and Raman spectra: as aluminum is introduced (Si/Al ratio decreases), the normal modes associated with asymmetric stretching vibrations shift to lower frequencies. In addition, for all intermediate Si/Al ratios (1.4 to 11), this asymmetric stretching mode splits into two peaks. The peak with the higher wavenumber, contrary to our intuition, is associated with Si−O−Si asymmetric stretching modes, whereas the one with the lower wavenumber is associated with both Si−O−Si and Si−O−Al asymmetric stretching. A similar trend was also observed for the symmetric stretching modes, which also shift to lower wavenumbers as the Si/Al ratio decreases. However, the inclusion of aluminum does not have a significant effect on

the bending modes in the IR spectra. There is more complexity to the spectra for both infrared and Raman in the lattice region vibrations (< 400 cm^{-1}) because of the presence of extra-framework cations and anions and their complex influence on lattice vibrations.

We compared our simulated infrared spectra of sodalite with Si/Al ratios of unity and infinity with experimental data. In both cases, they are in good agreement in terms of predicting the three major modes. Moreover, we have experimentally determined that aging the reaction gel for shorter times appears to favor the formation of pure siliceous sodalite powders, while longer aging times lead to the formation of other materials, which are likely blends of sodalite and other crystalline silicates. The other synthetic parameters evaluated here (crystallization time and temperature) do not seem to have a role in determining the solvothermal synthesis product. Aluminosilicate sodalite powders, in contrast to the siliceous synthesis methods, are readily obtained using the protocol of Stein,[133] with the minor variations in the synthesis conditions explored here having little effect on the final product. Variations in aging time, crystallization time, and crystallization temperature, given that the resulting material is still sodalite, do not seem to influence the infrared spectra of either aluminosilicate (Si/Al = 1) or siliceous (Si/Al $\rightarrow \infty$) forms of sodalite.

As evidenced by the comparison of calculated spectra with experimental data, density functional theory calculations are able to predict sodalite's major vibrational modes accurately. However, the presence of some additional peaks in the measured spectra brought up the question of whether they could be explained by introducing framework defects. We introduced hydroxyl groups (OH) in our computational model, as they are unavoidable defects in zeolites. The possible outcomes of the inclusion of such defects, based on our calculations, vary from healing the structure to forming adsorbed water to hydrogen-bonded disilanol groups. In order to be able to explore the effects of several defects on the vibrational spectra, we compared the results from DFT and experiments not only in the framework region but also in the OH stretching region. It has not escaped our notice that measuring the infrared spectrum in-situ at high temperatures would evaporate adsorbed wa-

ter and would make the interpretation of infrared spectra easier in the OH stretching region. However, with the help of our DFT calculations, the presence of additional peaks, as well as the broad peak in the asymmetric stretching region, can be explained by the presence of Si−OH groups and/or adsorbed water. These findings contribute to an ever-growing knowledge base of vibrational spectroscopy in the zeolite community, and provide a foundation for practical applications such as humidity sensors.

In the next chapter we explore the effect of extra-framework ions on the vibrational spectra of zeolites.

Acknowledgment

Partial financial support for this work was provided through the University of Missouri Research Board under award RB16-30. The computations for this work were performed on the high-performance computing infrastructure provided in part by Research Computing Support Services at the University of Missouri and in part by the National Science Foundation under grant number CNS-1429294.

CHAPTER 4

CALCULATED INFRARED AND RAMAN SIGNATURES OF Ag^{+}, Cd^{2+}, Pb^{2+}, Hg^{2+}, Ca^{2+}, Mg^{2+}, AND K^{+} SODALITES

This chapter was largely published as Ref. 147, an article in Microporous and Mesoporous Materials. *The authors of that article are Amir M. Mofrad, Parker Schellenberg, Caio Peixoto, Heather K. Hunt, and Karl D. Hammond from the University of Missouri.*

4.1 Summary

This chapter explores the potential of vibrational spectroscopy, an inexpensive analysis technique, for the purpose of detecting of heavy metals in water using sodalite. Computations via density functional theory of the infrared and Raman spectra of anion-free sodalites that have been exchanged with lead (II), cadmium (II), and mercury (II) ions predict a peak in the 850–880 cm^{-1} range in both the infrared and Raman spectra that is characteristic of anion-free sodalites that have been exchanged with these three heavy metal cations. This peak is distinguishable from the infrared spectra of anion-free sodalites that have been exchanged with potassium, magnesium, and calcium ions, which are naturally present in drinking water. Unfortunately, no peak in this range exists for chloro-, bromo-, or hydroxy-sodalites, and peaks in this range may be masked by the presence of magnesium hydroxysodalites, which would be expected to form in water testing applications. In addition, the signal-to-noise ratio is likely too low to provide a useful test for heavy metal contamination at the levels required for municipal water testing.

4.2 Introduction

The release of heavy metals into soil and water is a worldwide environmental concern.[148] Heavy metals tend to accumulate in the soil and in living organisms, causing health problems that affect the kidneys, the central nervous system, blood cell production (hematopoiesis), and the gastrointestinal tract.[149] The World Health Organization (WHO) recommends extremely low thresholds for acceptable levels of heavy metal cations in drinking water (2–15 ppb, depending on the metal type).[150–152] Consequently, many efforts have been made to improve existing methods for removal of such contaminants. Electrochemical treatment, adsorption, reverse osmosis, and ion exchange have all been utilized to capture heavy metal ions from water.[153–156] Chemical and electrochemical treatments, as well as reverse osmosis methods, have been shown to reduce the concentrations of heavy metals significantly, but only when ion concentrations are high (i.e., above 500 mg/L).[157,158] The major drawback of using these methods, particularly reverse osmosis, is their immense power consumption for pumping, as well as the expense involved in producing the membranes.[159] Conversely, ion exchange by zeolites has been shown to be more efficient at removing heavy metal ions from water at all concentrations, both in terms of cost and ion removal capacity.[151,159]

Zeolites are porous aluminosilicate materials used for a variety of industrial processes, such as gas separation, ion exchange, and catalysis.[7,160] In zeolites with a one-to-one ratio of silicon to aluminum (Si/Al = 1), alternating SiO_4 and AlO_4 tetrahedra (according to Löwenstein's rule[12]) are linked together in a way that creates a three-dimensional network with channels and/or pores of uniform sizes. There are, to date, 248 unique zeolite framework topologies that occur naturally and/or synthetically.[3] Sodalite (framework code **SOD**), whose structure was determined about 80 years earlier than any other zeolite,[161] is one of the simplest and most symmetrical frameworks. Because of its cage-like structure, it can host a regular array of well-defined nanoclusters, which would result in the creation of sodalite-based materials with potentially useful catalytic, magnetic, optical,

vibrational, and electronic properties.[162,163] For instance, optical applications of sodalite date from the 1970s, when photochromic and cathodochromic sodalites were used for information storage and filter optics.[14,164] Sodalite has also been modified to function as a catalyst in base-catalyzed reactions.[165] In all applications of sodalite—as with zeolites in general—synthesis and characterization techniques are important to ensure the materials have consistent and known physical and chemical properties.

Spectroscopic techniques, particularly infrared and Raman, are often used in the characterization of zeolites.[103] These techniques can identify characteristic vibrations associated with secondary building blocks (SBU), extra-framework cations, and lattice vibrations.[166–169] In particular, we anticipate there will be a measurable difference in the IR or Raman spectrum of sodalite that has been exposed to heavy metal cations compared with the natural (sodium) form. Unfortunately, due to the structural complexity of zeolites, interpretation of experimental vibrational spectra is often troublesome and relies heavily on supposition.[17] Computational tools are therefore helpful in obtaining more accurate insight into the spectroscopic properties of zeolites.

Computational vibrational spectroscopy based on density functional theory (DFT) can be helpful in interpreting zeolite vibrational spectra.[20,41,42,103] Furthermore, thanks to advancements in computing, the prediction of vibrational frequencies in zeolites has become feasible. Due to the presence of finite-size effects, employing periodic boundary condition (PBC) calculations provides better agreement between experiments and simulations than non-periodic cluster calculations.[43]

This study investigates the sensitivity of computational vibrational spectroscopy for the purpose of detecting ion exchange levels in sodalite. We hypothesize that infrared and/or Raman spectra of either partially or completely ion-exchanged anhydrous sodalite are capable of detecting the presence of contaminants such as Cd^{2+}, Pb^{2+}, and Hg^{2+} in the presence of other cations that are normally present in water, such as sodium, potassium, magnesium, and calcium.

We start by comparing the experimental and calculated infrared spectra of sodium chlorosodalite—that is, $|Na_8Cl_2|[Si_6Al_6O_{24}]$-**SOD**, which is the composition of naturally-occuring sodalite—and the equivalent bromide form, $|Na_8Br_2|[Si_6Al_6O_{24}]$-**SOD**, as well as the infrared spectra of chlorosodalites exchanged with silver, cadmium, and lead ions. We then examine the computed infrared and Raman spectra of anion-free sodalite, having formula $|Na_6|[Si_6Al_6O_{24}]$-**SOD**, and hydroxysodalite, $|Na_8(OH)_2|[Si_6Al_6O_{24}]$-**SOD**, as well as the same materials exchanged with heavy metal cations. We also consider the effects of exchange of ions normally present in water, including potassium, magnesium, and calcium ions.

The chloro- and bromo-sodalites do not show a distinct "signature" of heavy metal exchange, nor do the hydroxy-sodalites. However, the anion-free sodalites show a characteristic additional peak in the 850–880 cm^{-1}, which appears to be diagnostic of the presence of lead, cadmium, and/or mercury. Unfortunately, this peak is not expected to be particularly prominent in the experimental spectrum, and its presence may also be masked by the presence of magnesium ions: magnesium ions show a similar peak for hydroxy-sodalites, though not in anion-free sodalites. While the Raman spectrum could, in principle, be able to distinguish between these two scenarios, the practicalities of infrared and Raman spectroscopy combined with the relatively weak intensity of these peaks strongly suggest that vibrational spectroscopy will not be a viable method of detecting lead or other heavy metals in zeolites at the relevant concentrations.

4.3 Notation and Methodology

4.3.1 Simplified Notation

Natural sodalite is predominantly $|Na_8Cl_2|[Si_6Al_6O_{24}]$-**SOD**. Due to numerous possible variations that can occur when synthesizing sodalite, a variety of compositions can result

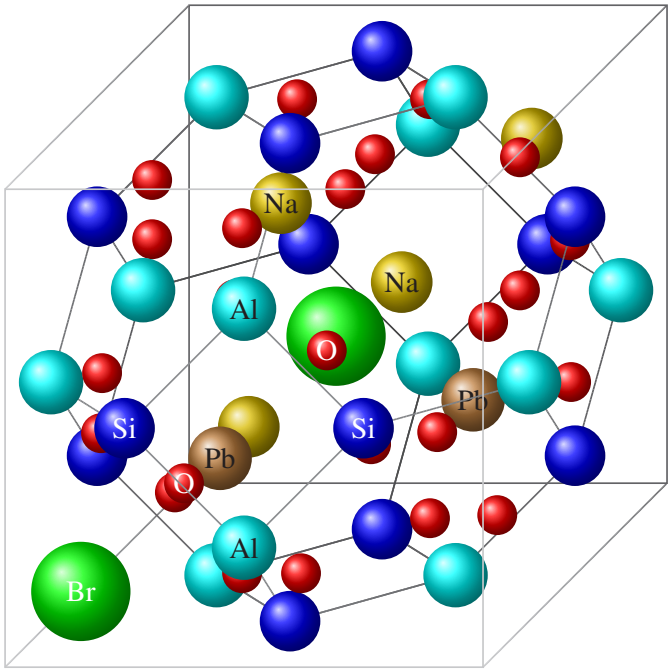

Figure 4.1. The structure of a partially-lead-exchanged sodalite (**SOD** framework). Spheres are drawn with a radius half the value of either the ionic radius (Br^-, Na^+, Pb^{2+}) or the covalent radius (Al, Si, O). Sodalite has a simpler structure, higher degree of symmetry, and smaller number of atoms per unit cell than most other zeolites.

that follow the general formula[170]

$$|M_m^{q+}X_x^{r-}|[Si_{12-n}Al_nO_{24}(H_2O)_{0-8}]\text{-}\mathbf{SOD}, \tag{4.1}$$

where $qm - rx = n$ and $n \leq 6$. Figure 4.1 shows a bromosodalite partially exchanged with lead (II) ions (it should be noted, as we will discuss later, that this structure does *not* exhibit a definitive "signature" in the vibrational spectra). In Equation 4.1, silicon and aluminum are the framework atoms; because they form tetrahedra with bridging oxygens, they are called T-atoms. The aluminum atoms that impart negative charges to the framework are compensated for by extra-framework sodium. Due to the presence of two bromide ions (or other anions), there need to be two more sodium cations per formula unit than required by the framework charge itself to neutralize the whole crystal. Therefore, in a sodalite

unit cell, there are eight sites available for monovalent cations and two sites available for monovalent anions. Additionally, as shown in Figure 4.1, the SBUs in the **SOD** framework are six single-four-membered rings (S4R) and eight single-six-membered-rings (S6R) per sodalite cage (the truncated octahedron in Figure 4.1). The cationic positions are located at the center of the S6Rs, behind or in front of the plane of the ring. The standard notation[16] for sodalites with Si/Al = 1, the only Si/Al ratio studied herein, would always contain the group $[Si_6Al_6O_{24}]$; we instead adopt the following shortened notation for convenience:

$$|C_cA_a|\text{-}\mathbf{SOD} \Longleftrightarrow |C_cA_a|[Si_6Al_6O_{24}]\text{-}\mathbf{SOD}, \tag{4.2}$$

where C refers to the cation and A refers to the anion. In the case of partial cation exchange, two cation symbols are used. For example, $|Na_8Br_2|$-**SOD** refers to $|Na_8Br_2|[Si_6Al_6O_{24}]$-**SOD**, $|Ca_3|$-**SOD** refers to anion-free $|Ca_3|[Si_6Al_6O_{24}]$-**SOD**, and $|Na_4Pb|$-**SOD** refers to partially-lead-exchanged, anion-free sodalite, $|Na_4Pb|[Si_6Al_6O_{24}]$-**SOD**. If there are no aluminum framework atoms present in the unit cell, it is referred to as siliceous sodalite, $[Si_{12}O_{24}]$-**SOD**, which is the simplest and most symmetrical of all zeolitic materials.

In the case of divalent cations (e.g., Ca^{2+}), it is necessary to iterate over all possible combinations of cation sites to find the minimum-energy configuration. From the point of view of theory, choosing anhydrous sodalite ($|Na_6|$-**SOD**) over anion-bearing sodalite ($|Na_8Cl_2|$-**SOD**) has two advantages: (i) the number of simulations to span all unique periodic unit cells is smaller in the anhydrous sodalite case than in the anion-bearing case; (ii) the cell volume of anhydrous sodalite is larger, which in principle means it might incorporate guest species more easily.

4.3.2 Electronic Structure Calculations

The crystal structure was generated with the $P\bar{4}3n$ space group (no. 218) as Felsche et al.[171] and Hassan et al.[109] suggested. The parent compound was the sodium form, $|Na_6|$-**SOD**, and we based our analyses of the ion-exchanged materials on this parent crystal.

Electronic structure calculations were performed within the DFT formalism[44,110] using norm-conserving pseudopotentials[115,116] and the local density approximation (LDA)[110–114] as implemented in Quantum ESPRESSO.[59] The reason why we chose norm-conserving LDA was primarily because the current version of Quantum ESPRESSO computes Raman frequencies only at this level of theory. Moreover, our previous work[41] showed that this set of pseudopotentials with the LDA gives reasonable IR and Raman results that agree reasonably well with experiment. We found that energies were converged with respect to basis set using a plane-wave cutoff energy of 80 Ry. The Brillouin zone was sampled using a Monkhorst–Pack[128] grid; we found that a $2 \times 2 \times 2$ grid produced a high enough k-point density for the results to be considered converged.

After the convergence test, we did a variable-volume geometry optimization in which both the ions' positions and the cell parameters were optimized simultaneously. The convergence threshold on the forces as per atom was set to 10^{-7} Ry/Bohr. The optimization used the Broyden–Fletcher–Goldfarb–Shanno (BFGS) algorithm,[172] a quasi-Newton method. The self-consistent field (SCF) calculations used a stopping criterion of 10^{-8} Ry. After geometry optimization, we performed phonon calculations based on density functional perturbation theory (DFPT)[59] at the center of the Brillouin zone (Γ point) to generate the dynamical matrix, from which vibrational frequencies were generated based on the acoustic sum rule.[76] The computed Raman activities were based on Placzek's theory of polarizability;[173] the self-consistency tolerance in the phonon calculations (`tr2_ph`) was set to 10^{-14} Ry. Both infrared and Raman spectra were line-broadened using Gaussian functions with full widths at half maxima of 20 cm^{-1} (FWHM = 20 cm^{-1}); the heights were proportional to the intensities calculated for the corresponding normal modes of vibration.

4.3.3 Experiments

In an effort to check our results, we synthesized and/or ion-exchanged many of the materials mentioned in the remainder of this study. These materials were characterized by

Table 4.1. The structural properties of sodalite unit cells with different compositions. As anions are introduced into the structure, their negative charge attracts the cations, leading to shrinkage of the unit cell. Counterintuitively, the cell size does not depend significantly on the number of ionic species.

Compound	Volume (Å^3)	a (Å)	b (Å)	c (Å)	α (°)	β (°)	γ (°)
$\|Na_6\|$-**SOD**	711.079 (713.188)*	8.926 (8.935)	8.926	8.926	89.44	90.56	89.44
$\|K_6\|$-**SOD**	765.542 (768.230)	9.148 (9.159)	9.148	9.148	90.07	90.07	90.07
$\|Cd_3\|$-**SOD**	717.958 (720.719)	8.954 (8.966)	8.955	8.955	90.68	90.68	89.32
$\|Pb_3\|$-**SOD**	693.677 (693.438)	8.852 (8.851)	8.852	8.852	90.50	90.50	89.50
$\|Na_8Cl_2\|$-**SOD**	658.030	8.698	8.698	8.698	90	90	90
$\|K_8Cl_2\|$-**SOD**	731.213	9.009	9.009	9.009	90	90	90
$\|Ag_8Cl_2\|$-**SOD**	667.487	8.739	8.739	8.739	90	90	90
$\|Cd_4Cl_2\|$-**SOD**	663.632	8.646	8.878	8.646	89.99	90.27	89.99
$\|Pb_4Cl_2\|$-**SOD**	734.823	9.026	9.023	9.026	90.17	88.47	89.83
$\|Na_8Br_2\|$-**SOD**	671.301	8.756	8.756	8.756	90	90	90
$\|K_8Br_2\|$-**SOD**	741.527	9.051	9.051	9.051	90	90	90
$\|Ag_8Br_2\|$-**SOD**	677.763	8.784	8.784	8.784	90	90	90
$\|Cd_4Br_2\|$-**SOD**	663.190	8.663	8.663	8.836	90	90	90
$\|Pb_4Br_2\|$-**SOD**	749.627	9.084	9.084	9.084	89.73	89.73	89.73

*Numbers in parentheses correspond to the same starting configuration, except that it has been forced to have cubic symmetry ($\alpha = \beta = \gamma = 90°$, and $a = b = c$). The experimental crystallographic parameters would be averages of configurations with vacancies at different sites, meaning the measured lattice parameters of any material with vacant extraframework cation sites would likely be intermediate between the two values even if the model were 100% accurate.

X-ray diffraction (XRD), energy-dispersive X-ray (EDX) analysis, and Fourier transform infrared spectroscopy (FTIR). Information of synthesis and handling procedures, instrumentation, chemicals, and characterization are discussed thoroughly in Appendix B. Many of the ion exchange procedures, in particular, were unsuccessful, so we instead compare our results primarily to previously-published experiments.

4.4 Results and Discussion

4.4.1 Structural Properties of Anhydrous and Anion-Bearing Sodalites

Table 4.1 shows the calculated structural properties of sodalite exchanged with different cations and anions. In the case of anion-containing sodalites, the cell volume is a function of both cationic radius as well as anionic radius and each atom's electronegativity. For example, according to Shannon,[174] the K^+ ionic radius is 138 pm, larger than any other

cation in Table 4.1. However, the cell volumes of $|Pb_4Cl_2|$-**SOD** and $|Pb_4Br_2|$-**SOD** are slightly larger than that of their potassium counterparts, even though there are fewer cations present in the lead cases and the Pb^{2+} ion is smaller than the K^+ ion. The reason for this is that the electronegativity of lead is significantly higher than potassium, which makes these cations less bound to the framework, resulting in a larger unit cell. Conversely, sodalites with bromide as the extra-framework anion have larger unit cells compared to chloride sodalites, as one would expect, because of the difference in ionic radius between the two anions.

For the anhydrous sodalites in Table 4.1, the cell volume of each material is larger than that of its anion-bearing counterparts, even though there are fewer cations and anions in the structure in the anion-free case. This again stems from the fact that the Coulombic forces between anions and cations draw the extra-framework cations closer to the anions and framework aluminum, causing the structure to shrink.[175]

Finally, some of the compositions in Table 4.1 yield a slight distortion from cubic symmetry. This is primarily because of the arrangement of cations when they partially occupy the structure (i.e., extraframework cation vacancies are present). This deviation from cubic symmetry at an energetic minimum is expected: Latturner et al.[176] reported a phase transition temperature of 250 °C between the non-cubic and cubic variants of anion-free sodalite, with the low-temperature structure being associated with ordered Na_3^{3+} triangles. At high temperatures, thermal vibrations are larger than the energy gained by forming these structures, and cubic symmetry is restored.

4.4.2 Comparison with Experiments

This section compares theoretical infrared spectra with both our own experimental results and findings from Mikuła et al.[107] Figures 4.2 and 4.3 shows the measured XRD patterns of the parent compound and the ion-exchanged sodalites, as well as the potassium chlorosodalite.

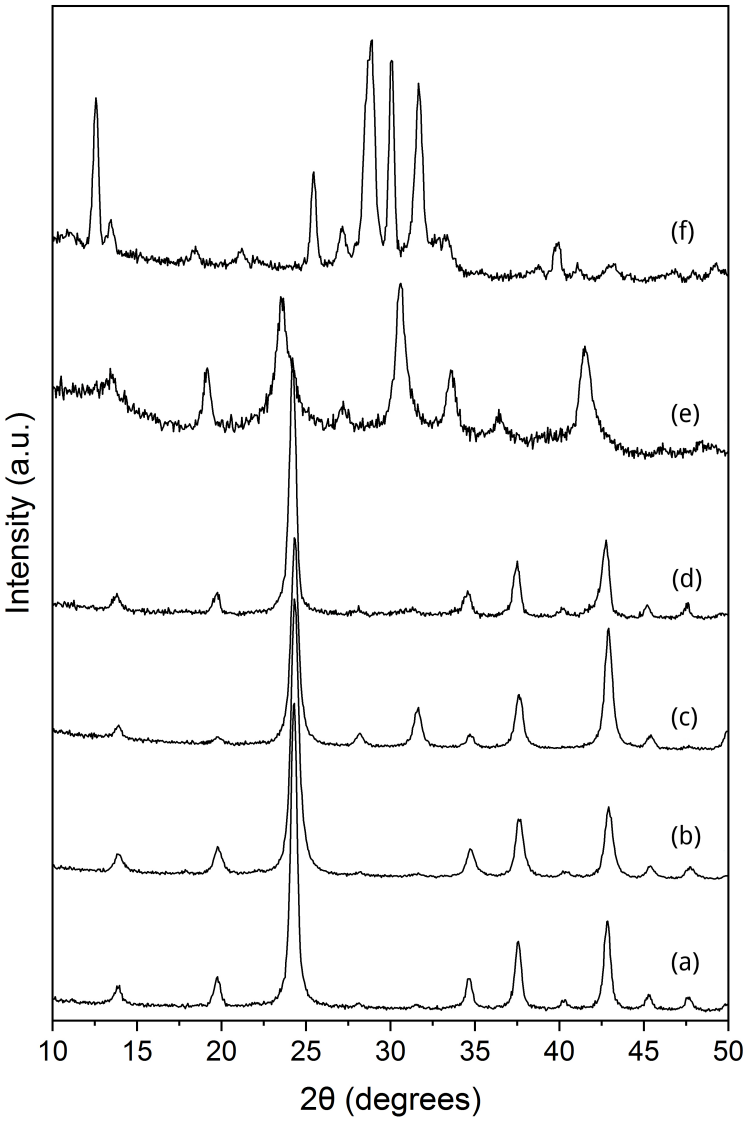

Figure 4.2. Measured XRD patterns of synthesized and attempted cation-exchanged samples. (a) parent compound (|Na_8Br_2|-**SOD**), (b) |Li_8Br_2|-**SOD**, (c) |Ag_8Br_2|-**SOD**, (d) |K_8Br_2|-**SOD**, (e) |Pb_4Br_2|-**SOD**, and (f) |K_8Cl_2|-**SOD**. Pb-exchanged sodalite shows loss of crystallinity and potassium-chloro-sodalites does not show a recognizable pattern. The rest of the samples display XRD patterns characteristic of sodalite.

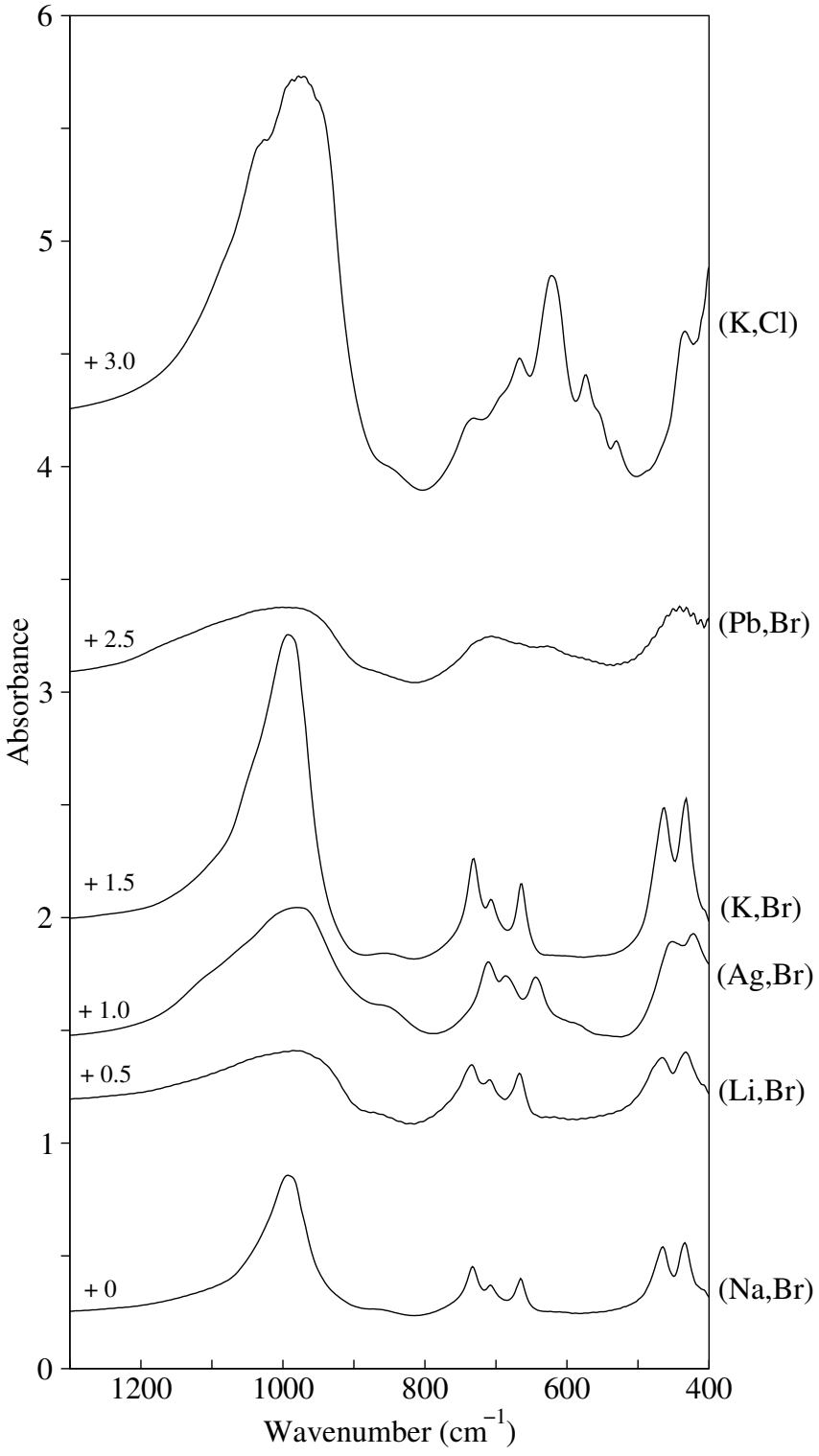

Figure 4.3. Measured Fourier transform infrared spectra of synthesized and attempted cation-exchanged samples. The values written next to the graphs on the left is the number by which they are translated from their exact absorbance values. The parent compound is at the bottom, which is sodium bromosodalite, $|Na_8Br_2|$-**SOD**, denoted (Na,Br).

Table 4.2. Chemical compositions of synthesized and ion-exchanged sodalites.

Structure	EDX chemical composition per unit cell
$\|Na_8Br_2\|$-**SOD**	$Na_{7.3}Al_{6.2}Si_6O_{32}Br_{1.4}$
$\|Pb_4Br_2\|$-**SOD**	$Pb_{4.6}Na_{0.3}Al_{6.3}Si_6O_{29}Br_{1.3}$
$\|K_8Br_2\|$-**SOD**	$K_{1.8}Na_{5.4}Al_{6.3}Si_6O_{28.8}Br_{1.5}$
$\|Ag_8Br_2\|$-**SOD**	$Ag_{10.8}Na_{0.2}Al_{6.2}Si_6O_{44.9}Br_{1.7}$
$\|Li_8Br_2\|$-**SOD**	$Li_{1.3}Na_{5.4}Al_{6.6}Si_6O_{26}Br_{1.7}$
$\|K_8Cl_2\|$-**SOD**[a]	$K_{5.5}Al_{6.1}Si_6O_{28.4}Cl_{0.7}$

[a]The XRD patterns of these materials indicate they are not sodalites.

Lead-exchange of sodium bromosodalite decomposed the crystal structure, and replacing sodium with potassium in the established protocol for sodium chlorosodalite[164] did not yield a sodalite phase; this is evident in the materials' XRD patterns. The infrared spectra of the compounds that yielded sodalite phases are not in good agreement with the IR spectra predicted by DFT (Figure 4.4) due primarily to unsuccessful ion exchange of those cations with the parent compound (Table 4.2). It should be noted that the resulting sodalites are still sodium bromosodalites ($|Na_8Br_2|$-**SOD**); consequently, any evidence of Pb^{2+}, Ag^+, Li^+ would be absent.

There are several reasons why these established ion exchange protocols were unsuccessful. The potassium chlorosodalite synthesis was a modification of the protocol for the sodium form; it appears simple replacement of sodium with potassium during synthesis is inadvisable (see Figure 4.2 f). The failed lead exchange may have been a result of pH: zeolites are synthesized in strongly basic solution (i.e., pH > 11),[177] but the lead nitrate solution in our experiments had a pH of approximately 4, which may have been low enough to damage the structure (see Figure 4.2 e). For the other ion exchanges attempted (Li^+, Ag^+, K^+), the XRD patterns indicate the resulting materials are sodalites, but EDX indicated that very little ion exchange occurred. The lithium and potassium exchange protocols were originally tested on hydroxysodalites, not bromosodalites; their failure in the bromosodalite case may indicate that the anion makes a significant difference to the mech-

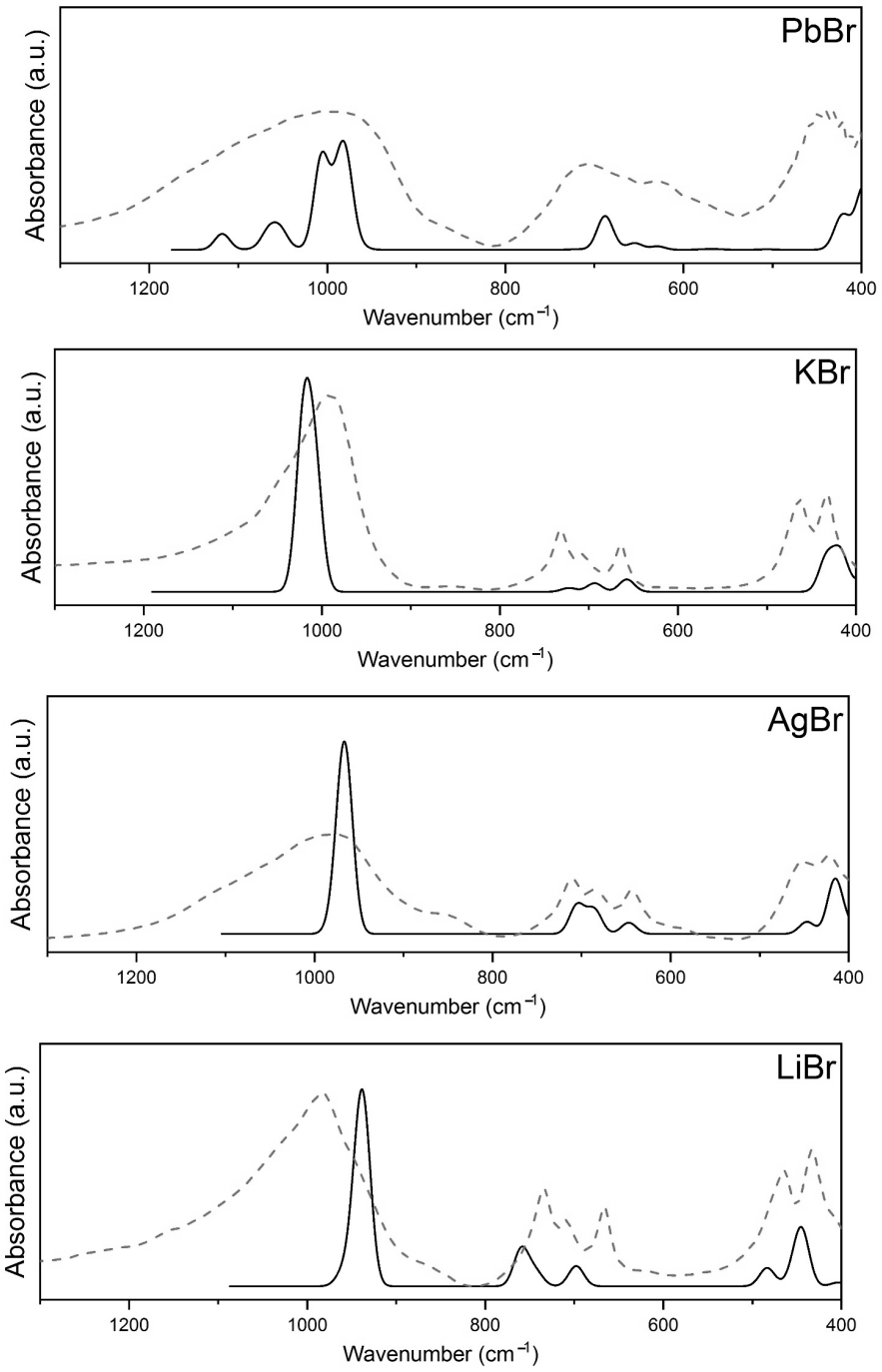

Figure 4.4. Comparison between the experimental infrared (dashed line) and simulated (solid line). $|Na_8Br_2|$–**SOD**, $Na_8Br_2Si_6Al_6O_{24}$ is the parent compound from which the attempted ion exchange occurs. The results from the simulations assume the complete exchange (i.e., $Pb_4Br_2Si_6Al_6O_{24}$). Calculated intensities have been scaled so that they are comparable in magnitude to the experiments.

anism and/or rate of ion exchange. The silver exchange protocol was also developed for hydroxysodalites, and silver halides are even less water-soluble than silver hydroxides.

In order to check the accuracy of our calculated DFT results given the unsuccessful ion exchange experiments, we compare our computational model with experimental findings of Mikuła et al.[107] for $|Pb_4Cl_2|$-**SOD**, $|Cd_4Cl_2|$-**SOD**, and $|Ag_8Cl_2|$-**SOD**. Figure 4.5 shows this comparison, along with the experimental infrared spectra and band assignments of natural sodalite as well as sodalite exchanged with Ag^+, Cd^{2+}, and Pb^{2+} cations.

It is worth mentioning that silver exchange was complete in Mikuła et al.'s work,[107] which resulted in a similar infrared spectrum compared to that of the parent $|Na_8Cl_2|$-**SOD**. Qualitatively, our results are in better agreement with experimental spectra than were the Hartree–Fock calculations in Mikuła et al.'s study. However, there is no obvious "signature" of Pb^{2+} or Cd^{2+} exchange evident in these spectra.

Changing from monovalent Ag^+ to divalent Cd^{2+}, the shape of the infrared spectrum changes significantly. The peaks in the asymmetric stretching region split into high- and low-wavenumber bands compared to natural sodalite. In addition, the symmetric stretching and bending regions show additional peaks. The reason why the shape of the IR spectrum changes and additional peaks are present for the sodalites exchanged with divalent cations is that the unit cell distorts slightly from perfect cubic symmetry, and therefore some vibrations generate changes in the dipole moment that would be IR-invisible in a perfectly cubic cell. It should be noted that such distortions would not likely be visible in a macroscopic crystal.

The agreement between experiment and simulation for cadmium is not as strong as in the silver case because (i) cadmium is not easily ion-exchanged into sodalite and the resulting IR spectrum is very sensitive to the procedure by which the ion exchange takes place,[178] and (ii) the resolution of the spectrometer might not have been high enough to be able to deconvolute the IR spectra. However, our theoretical spectrum for $|Cd_4Cl_2|$-**SOD** is in qualitative agreement with the spectrum calculated by Mikuła et al.[107]

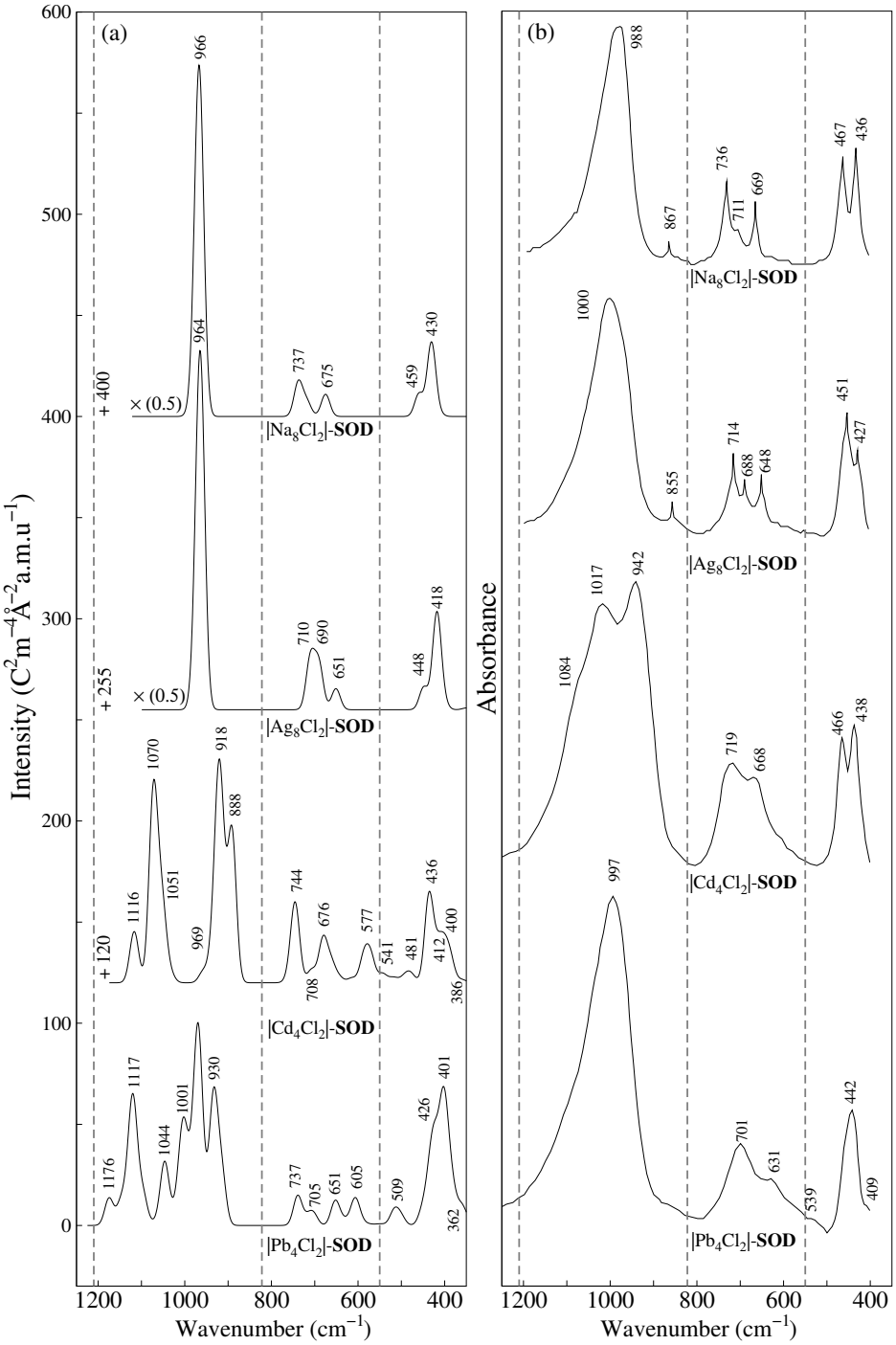

Figure 4.5. (a) Calculated and (b) measured mid-infrared spectra of chlorine-bearing sodalite exchanged with Ag^+, Cd^{2+}, and Pb^{2+}. The three regions separated by dashed lines correspond to asymmetric stretching, symmetric stretching, and bending modes from left to right. The corresponding vibrational wavenumbers are written above each peak. The intensity in the computed spectrum is proportional to absorbance. Graphs are translated and scaled by the values written next to them. Experimental data are from Mikuła et al.[107]

Finally, a similar spectrum to that in the cadmium case is seen with the infrared spectrum of $|Pb_4Cl_2|$-**SOD**. However, lead in general is more easily exchanged into sodalite compared to cadmium.[178,179]

4.4.3 Ion Exchange of Anion-Free Sodalite

This section will explore the sensitivity of theoretical vibrational spectroscopy to K^+, Cd^{2+}, and Pb^{2+} ions in anhydrous, anion-free sodalite ($|Na_6|$-**SOD**) for different possible combinations. As mentioned earlier, six out of eight cationic sites are filled in an anion-free sodalite cage by monovalent cations. Similarly, this is reduced to three sites for divalent cations, and so on.

In the first step in our approach, we assume that the three cations (Pb^{2+}, Cd^{2+}, K^+) have been partially exchanged with Na^+ ions simultaneously, such that five Na^+ ions are exchanged with K^+, Cd^{2+}, and Pb^{2+}, and only one sodium cation remains in the structure ($|NaKCdPb|$-**SOD**). We then compared the vibrational spectra of this compound with other sodalites containing only one type of cation ($|Na_6|$-, $|K_6|$-, $|Cd_3|$-, or $|Pb_3|$-**SOD**). The results from this step are shown in Figure 4.6. In the infrared spectra of compound $|NaKCdPb|$-**SOD**, there is a band at approximately 860 cm^{-1}, which also is present in the spectrum of $|Cd_3|$-**SOD** at the same wavenumber. However, because of the presence of a band at about 881 cm^{-1} in the $|Pb_3|$-**SOD**, one cannot be certain as to whether it is caused by the presence of cadmium or lead in an experiment. Nevertheless, we might (in principle) be able to conclude that the lower the wavenumber of a band around this vicinity, the more likely that it is caused by the presence of cadmium than lead.

In order to be confident in our assignment, we first consider only the effect of cadmium in the presence of sodium and potassium as background without lead being present. Figure 4.7 shows this comparison. In a neutral anhydrous sodalite, the possible configurations in a single-unit-cell calculation with these three cations present are $|Na_3KCd|$-**SOD**, $|Na_2K_2Cd|$-**SOD**, and $|NaKCd_2|$-**SOD**. These are the bottom three spectra in Figure 4.7.

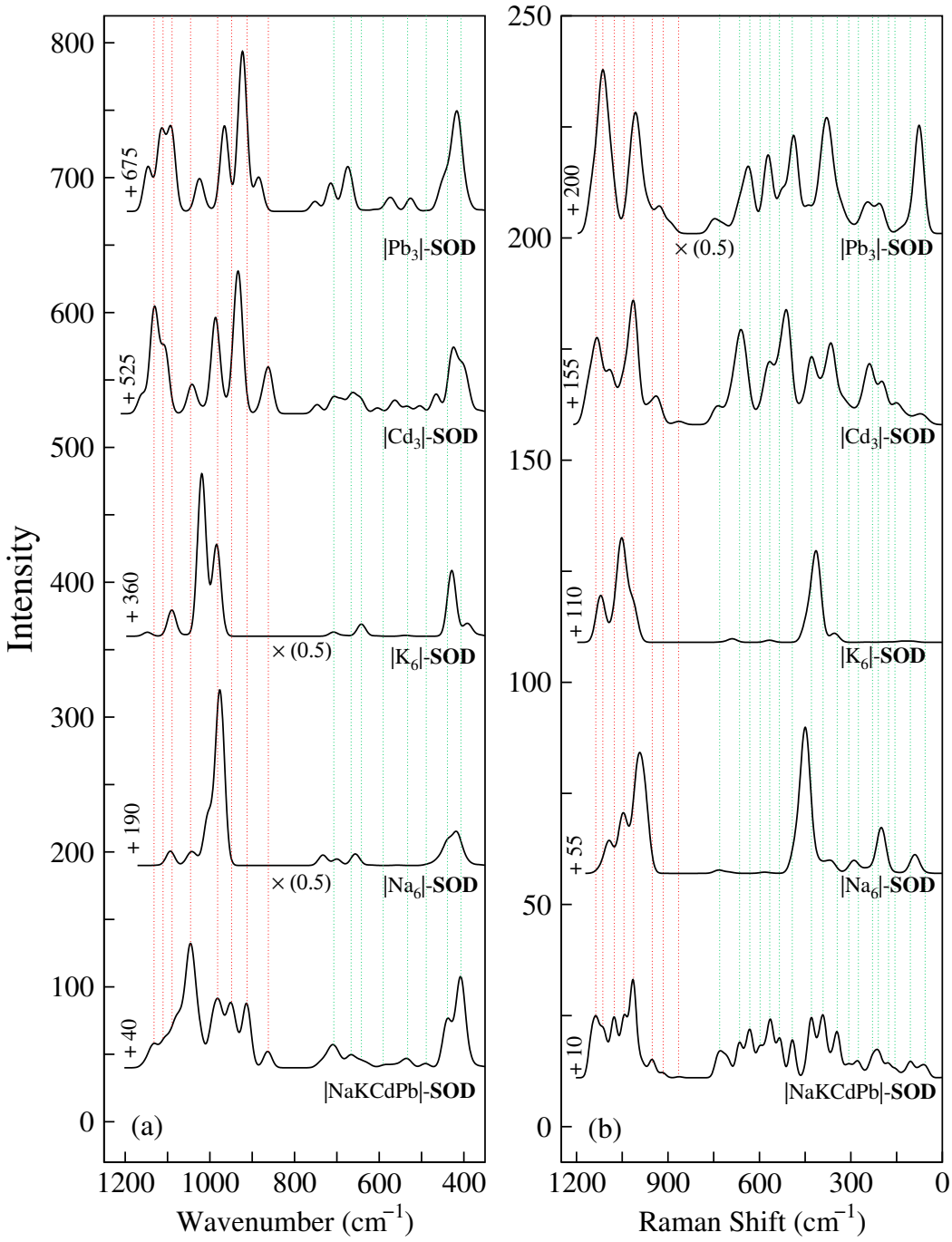

Figure 4.6. Calculated (a) mid-infrared and (b) Raman spectra of anion-free sodalite exchanged with different cations. The bottom spectrum in each graph corresponds to sodalite containing all four cations (|NaKCdPb|-**SOD**). The intensity is proportional to absorbance and has units of $C^2m^{-4}Å^{-2}$ amu^{-1} in the case of infrared; in the case of Raman, it is proportional to scattering intensity with units of $Å^4$ amu^{-1}. The values written below/above the graphs are the numbers by which they are scaled/translated. Dashed lines are to guide the eye starting from the bands in |NaKCdPb|-**SOD**. Red denotes the asymmetric stretching region and green denotes the symmetric stretching and bending modes.

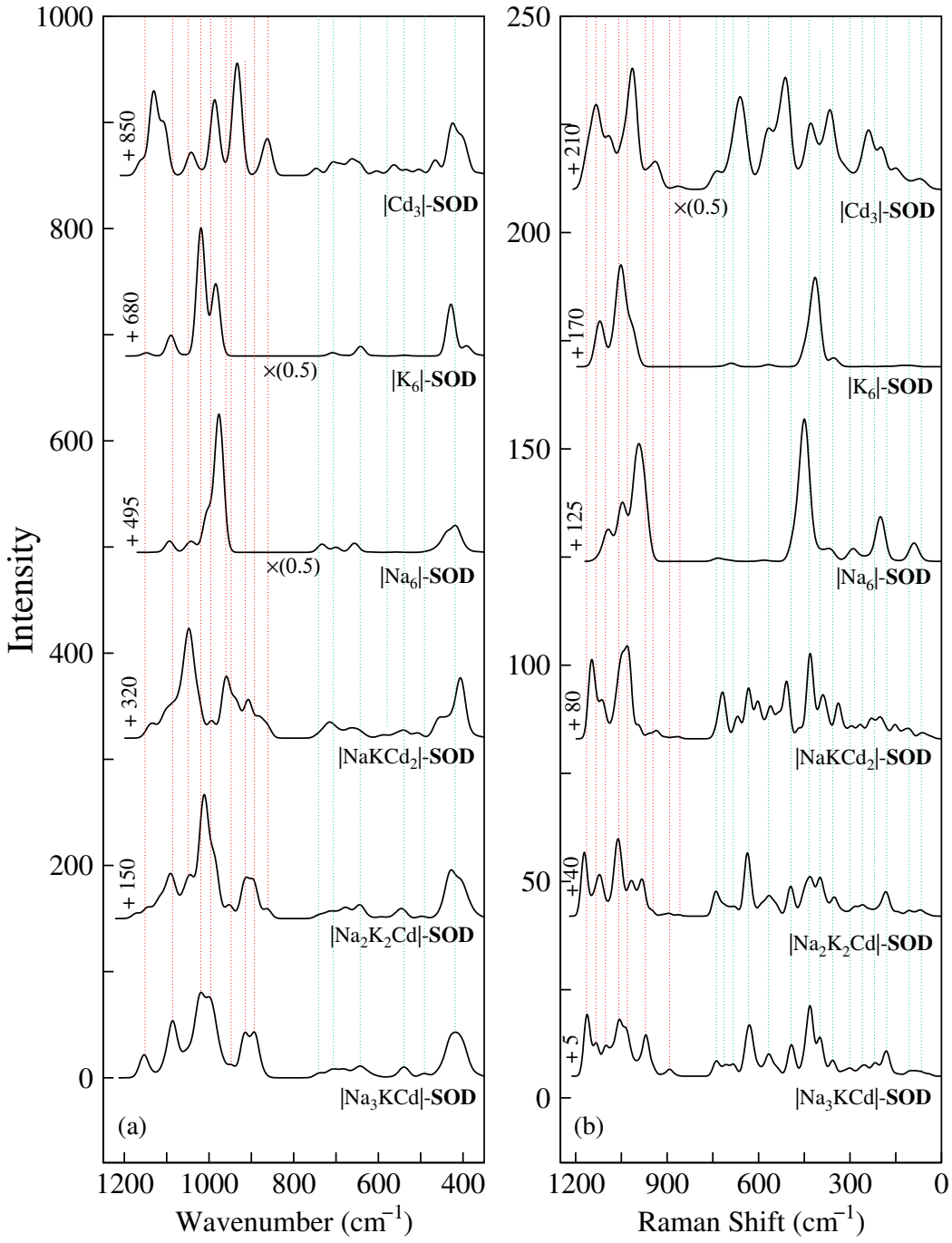

Figure 4.7. Calculated (a) mid-infrared and (b) Raman spectra of anion-free sodalites partially-exchanged with different cations. The bottom spectrum in each graph corresponds to sodalite containing Na^+, K^+, and Cd^{2+} cations. The intensity is proportional to absorbance and has units of $C^2\,m^{-4}\,Å^{-2}\,amu^{-1}$ in the case of infrared; in the case of Raman, it is proportional to scattering intensity with units of $Å^4\,amu^{-1}$. The values written below/above the graphs are the numbers by which they are scaled/translated. Dashed lines are to guide the eye starting from the bands in sodalites containing these three cations. Red denotes the asymmetric stretching region and green denotes the symmetric stretching and bending modes.

As seen in Figure 4.7, the band at approximately 860 cm^{-1} in both the infrared and Raman spectra of $|Cd_3|$-**SOD** is also observable in the materials with all three cations present (bottom three graphs in Figure 4.7). Another possible case that could occur for anhydrous anion-free sodalite in an ion exchange processes is that sodalite exchanges with potassium and lead but not cadmium. The possible configurations for this case are $|Na_3KPb|$-**SOD**, $|Na_2K_2Pb|$-**SOD**, and $|NaKPb_2|$-**SOD**.

Figure 4.8 also compares the infrared as well as Raman spectra of these three compounds with structures in which all cations are the same. The purpose of this comparison is to see whether lead is evident in the presence of background of sodium and potassium, which are ordinarily present in water resources. As shown in Figure 4.8, there is a shoulder at around 883 cm^{-1} in the infrared spectra as well as Raman spectra for all three partially-exchanged compositions that is present in $|Pb_3|$-**SOD** but not $|Na_6|$-**SOD** or $|K_6|$-**SOD**. It should be noted that there is no distinct peak in the low wavenumber range (symmetric stretching and bending modes) for any of the situations that we have discussed so far that can be traced back to $|Na_6|$-**SOD**, $|K_6|$-**SOD**, or $|Pb_3|$-**SOD**. Note that that far-infrared (FIR) does not provide any particular information about cation exchange, which is why we have discussed only the mid-infrared (MIR) range.

As an example of sodalite partially exchanged with Cd^{2+} and Pb^{2+}, we chose to study $|Na_2CdPb|$-**SOD**, which is the only possible way to create a single periodic unit cell with all three ions present. Figure 4.11 compares the vibrational spectra of the aforementioned material with sodium-only, cadmium-only, and lead-only anhydrous sodalites. Similar to our previous reasoning, the presence of a band at approximately 870 cm^{-1} in both infrared and Raman spectra is evidence of the presence of cadmium and/or lead in the structure. The key point here is that the presence of lead tends to shift this vibration to higher wavenumbers, up to 885 cm^{-1}, and cadmium red-shifts this band to 860 cm^{-1}.

Finally, in order to be convinced that this band only exists when either cadmium or lead is present in sodalite and is not caused by the presence of potassium, we compared the

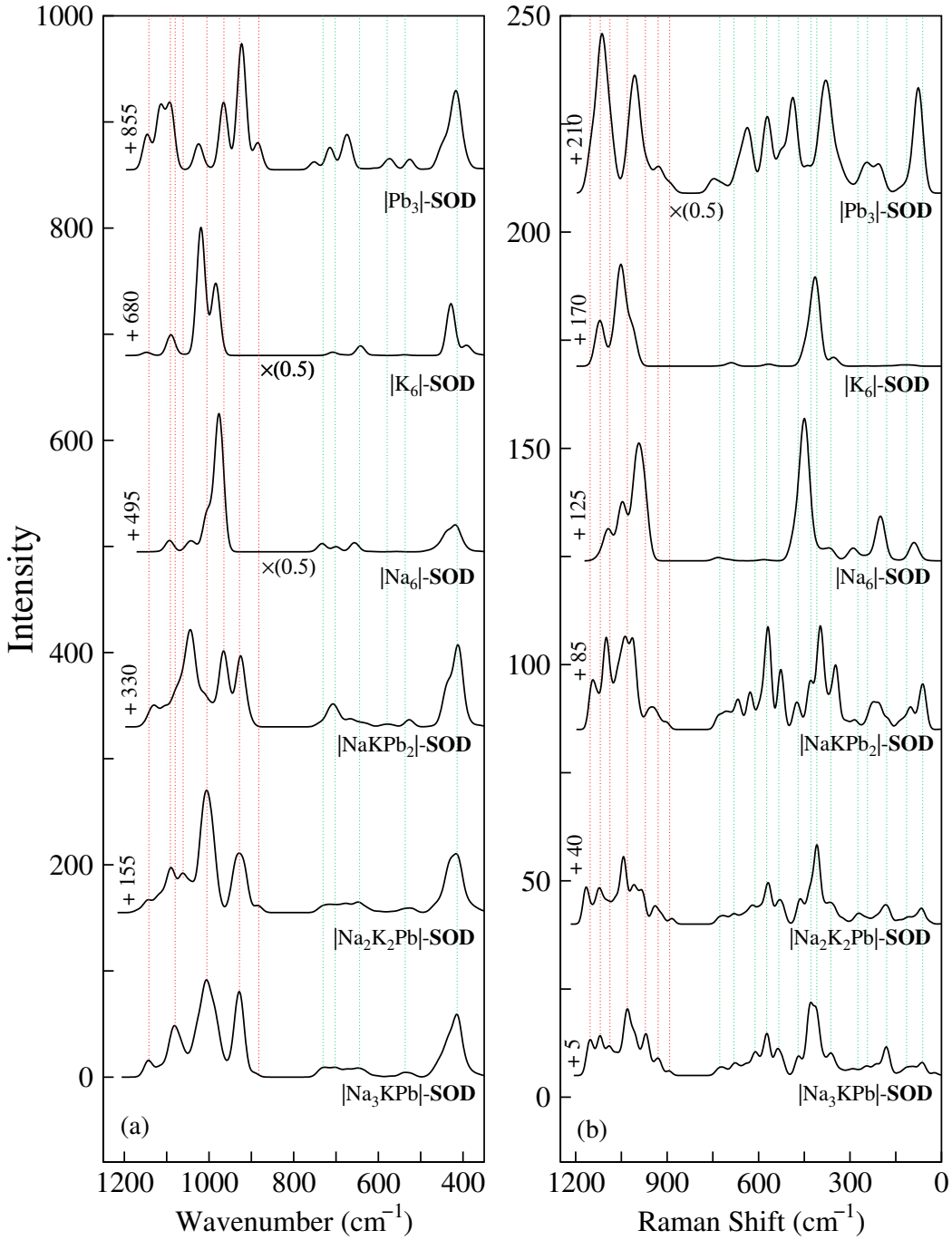

Figure 4.8. Calculated (a) mid-infrared and (b) Raman spectra of anion-free sodalite exchanged with different cations. The bottom spectrum in each graph corresponds to sodalite containing Na^+, K^+, and Pb^{2+} cations. The intensity is proportional to absorbance and has units of $C^2\,m^{-4}\,Å^{-2}\,amu^{-1}$ in the case of infrared; in the case of Raman, it is proportional to scattering intensity with units of $Å^4\,amu^{-1}$. The values written below/above the graphs are the numbers by which they are scaled/translated. Dashed lines are to guide the eye starting from the bands in sodalites containing these three cations. Red denotes the asymmetric stretching region and green denotes the symmetric stretching and bending modes.

infrared and Raman spectra of sodalite when only potassium and sodium are exchanged. The results from this comparison are provided in Figure 4.9.

Throughout the ion exchange process with potassium, no band will appear within the 860–880 cm^{-1} region, which provides more evidence that the band in the 860–880 cm^{-1} range only occurs because of cadmium and or lead. Nevertheless, one could argue that the aforementioned band might get masked by ions such as Mg^{2+}, Ca^{2+}, which are prevalent in water resources. In addition, we also have considered two other heavy metal cations, Ag^{+} and Hg^{2+}. Figure 4.12 shows that there is no band in the 860–880 cm^{-1} region for any of the compounds except for $|Hg_3|$-**SOD**, which has a shoulder at approximately 855 cm^{-1}. This observation suggests that the appearance of a band in the vicinity of 860–880 cm^{-1} in the spectra of anion-free sodalite may indicate the presence of cadmium, lead, and/or mercury. However, the relatively low intensity of this shoulder means it will be difficult to distinguish from background and/or line-broadening effects in experimental infrared spectra.

4.4.4 Infrared and Raman Signatures of Hydroxysodalite

So far, based on DFT calculations, we have observed the effects of extra-framework cations on the infrared and Raman spectra of sodalite both individually and when accompanied by other cations. Most of the peaks that are seen in a partially-exchanged hypothetical sodalite structure (i.e., sodalite that contains different extra-framework species) are similar to peaks found in the spectra of sodalites that contain only one type of extra-framework cation. In other words, if there is no overlap of bands in the spectra of sodalite containing one extra-framework species, those peaks will still appear even when other cations are present.

Following this observation, let us examine the sensitivity of the theoretical vibrational spectra of anhydrous hydroxysodalite, $|Na_8(OH)_2|$-**SOD**, after Pb^{2+}, Hg^{2+}, Cd^{2+}, K^{+}, Mg^{2+}, and Ca^{2+} exchange. The choice of hydroxysodalite over other anion-bearing sodalites, such as bromosodalites, was inspired by Golbad et al.,[179] who examined the capacity of

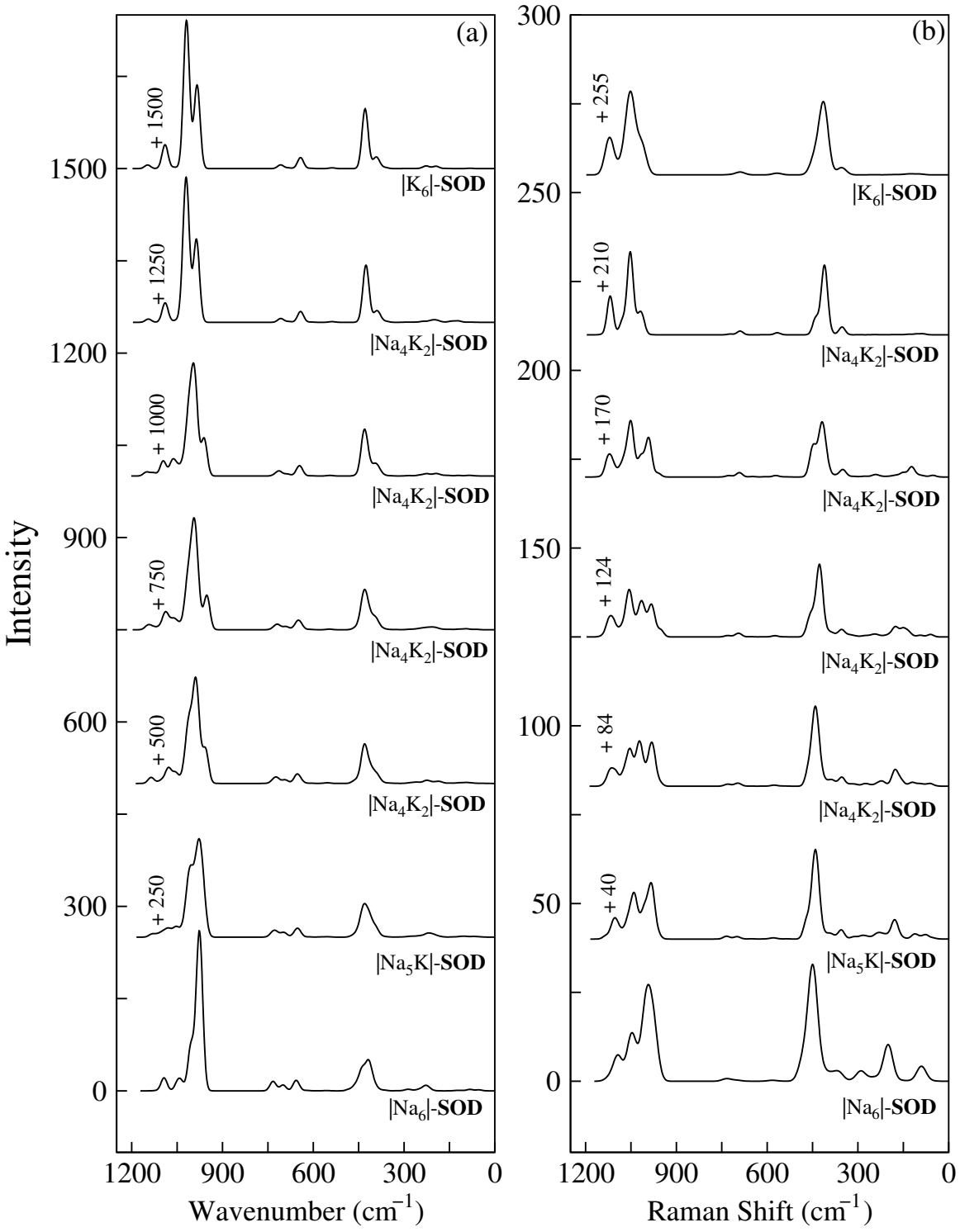

Figure 4.9. Calculated (a) infrared and (b) Raman spectra of partially-exchanged potassium with sodium in anhydrous sodalite. The intensity is proportional to absorbance and has the unit of $C^2m^{-4}Å^{-2}amu^{-1}$ in the case of infrared and $Å^4\,amu^{-1}$ for Raman. Ordinates are translated by the values written next to them.

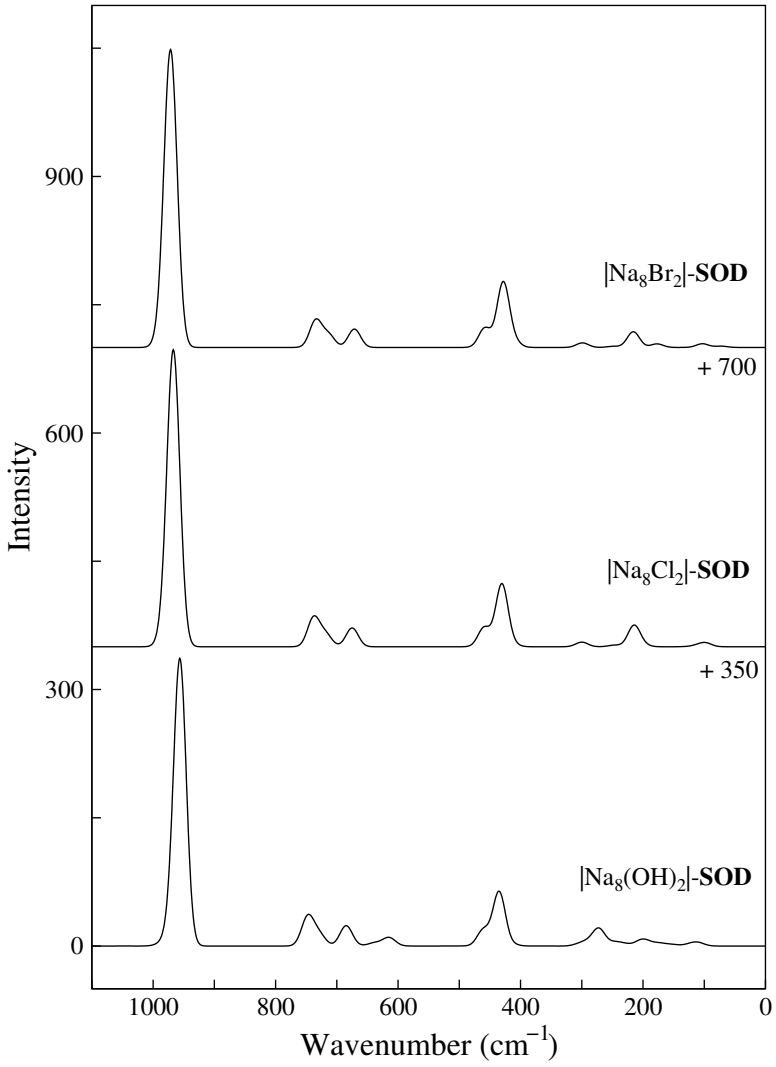

Figure 4.10. Calculated infrared spectra of hydroxy-, chloro-, and bromosodalites. The intensity is proportional to absorbance and has the unit of $C^2m^{-4}Å^{-2}amu^{-1}$. Ordinates are translated by the values written next to them.

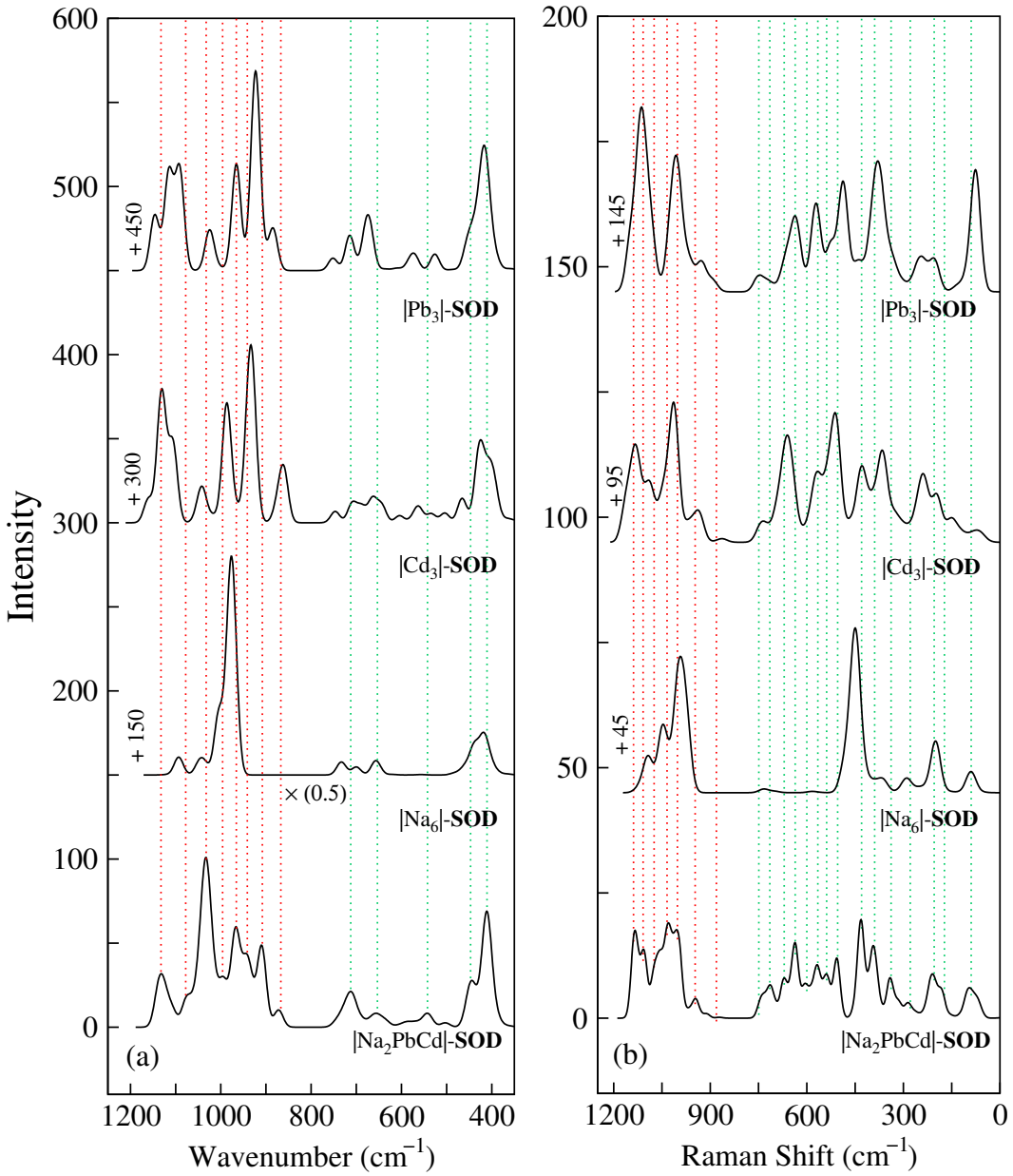

Figure 4.11. Calculated (a) mid-infrared and (b) Raman spectra of anion-free sodalite exchanged with different cations. The bottom spectrum in each graph corresponds to sodalite containing Na^+, Cd^{2+}, and Pb^{2+} cations. The intensity is proportional to absorbance and has units of $C^2\,m^{-4}Å^{-2}\,amu^{-1}$ in the case of infrared; in the case of Raman, it is proportional to scattering intensity with units of $Å^4\,amu^{-1}$. The values written below/above the graphs are the numbers by which they are scaled/translated. Dashed lines are to guide the eyes starting from the bands in sodalites containing these three cations. Red denotes the asymmetric stretching region and green denotes the symmetric stretching and bending modes.

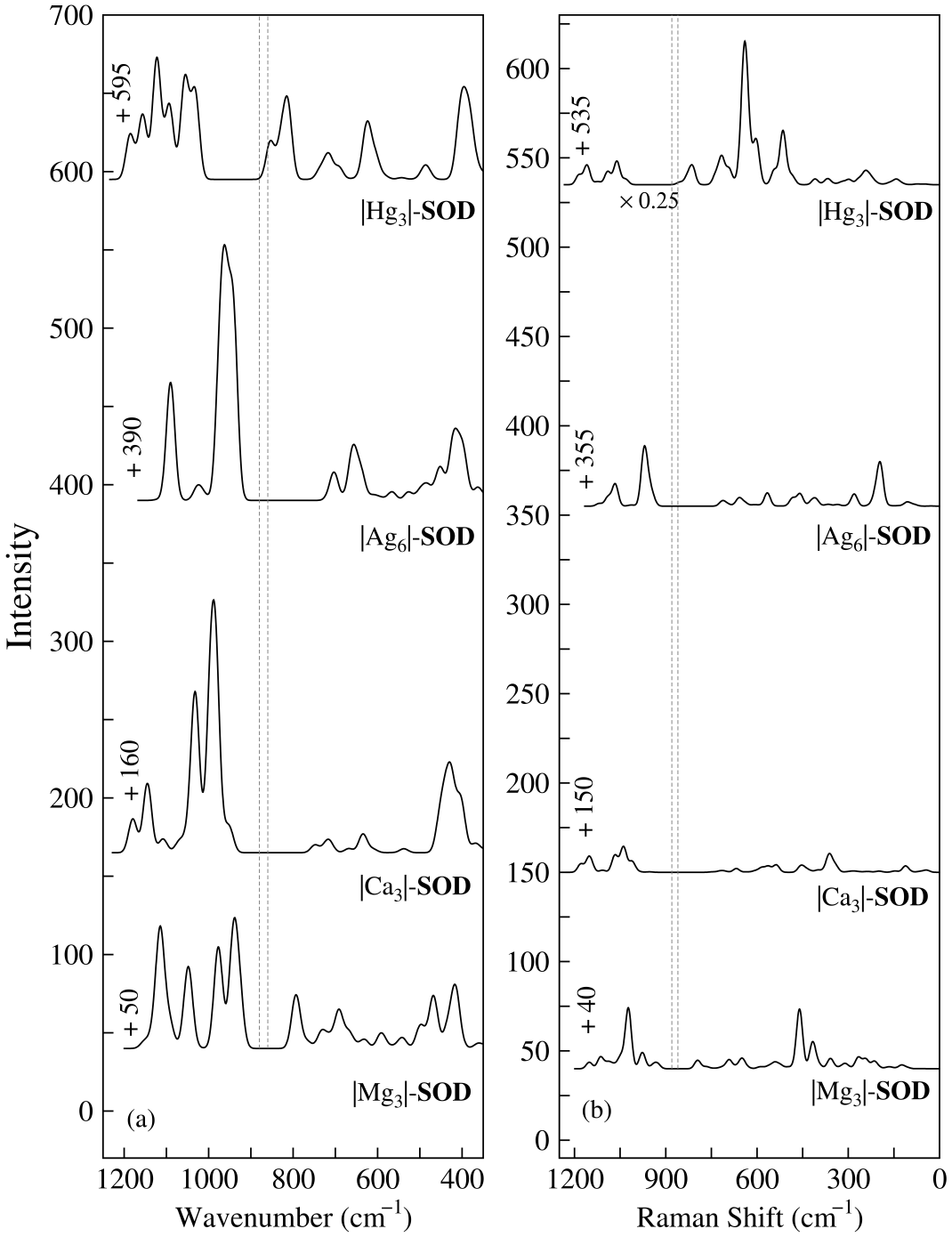

Figure 4.12. Calculated (a) mid-infrared and (b) Raman spectra of anion-free sodalite exchanged with different cations. The intensity is proportional to absorbance and has units of $C^2\ m^{-4}\ Å^{-2}\ amu^{-1}$ in the case of infrared; in the case of Raman, it is proportional to scattering intensity with units of $Å^4\ amu^{-1}$. The values written below/above the graphs are the numbers by which they are scaled/translated. Dashed lines are to guide the eye to the see the differences between compounds between 860–880 cm^{-1}.

hydroxysodalite for the removal of lead. They estimated that sodalite's cation exchange capacity is 98.1% for a solution of 100 mg/L of lead nitrate at a pH of 6 at room temperature. Equilibrium was reached after 6 h. Lack of infrared and/or Raman spectral evidence from the aforementioned investigation encouraged us to study the sensitivity of vibrational spectroscopy of hydroxysodalite with respect not only to lead but also to other extra-framework species.

Figures 4.13 and 4.14 show the mid- and high-frequency ranges, respectively, of both the infrared and Raman spectra of anhydrous hydroxysodalite for different extra-framework cations. In contrast to anion-free sodalites, $|Pb_4(OH)_2|$-**SOD**, $|Ca_4(OH)_2|$-**SOD**, $|K_8(OH)_2|$-**SOD**, and $|Na_8(OH)_2|$-**SOD** do not exhibit any bands in the 850–880 cm^{-1} range. However, for the Mg^{2+}, Cd^{2+}, and Hg^{2+} cases, there are some bands and/or shoulders either inside or in the vicinity of this range. Therefore, relying solely on the 850–880 cm^{-1} range is not an infallible indicator for the presence of heavy metals in sodalites because (i) lead-exchanged hydroxy-, chloro-, or bromo-sodalites do not have bands in this range to begin with, and (ii) magnesium-exchanged hydroxysodalite has a band which might mask the presence of heavy metals.

On the other hand, because of the presence of hydroxide anion (OH^-), the high-frequency range for the OH stretching mode should be taken into account along with the 850–880 cm^{-1} range. Figure 4.14 shows the high-frequency range of hydroxysodalite exchanged with the Na^+, Mg^{2+}, K^+, Ca^{2+}, Cd^{2+}, Hg^{2+}, and Pb^{2+} cations. The first thing to note is that OH stretching is not IR-active in some cases, such as $|Na_8(OH)_2|$-**SOD** and $|K_8(OH)_2|$-**SOD**. As seen in Figure 4.14, lead- and mercury-exchanged sodalite exhibit OH stretching bands within 30 cm^{-1} of each other. However, these vibrational modes for the $|Cd_4(OH)_2|$-**SOD** and $|Mg_4(OH)_2|$-**SOD** occur at virtually the same wavenumber ($\approx$ 3631–3633 cm^{-1}), which suggests that differentiating them would be difficult. The only possible way to distinguish magnesium-exchanged sodalites from cadmium-exchanged sodalites would be to compare their Raman spectra in the vicinity of 560 cm^{-1}, as in Figure 4.13. In these spectra, there is

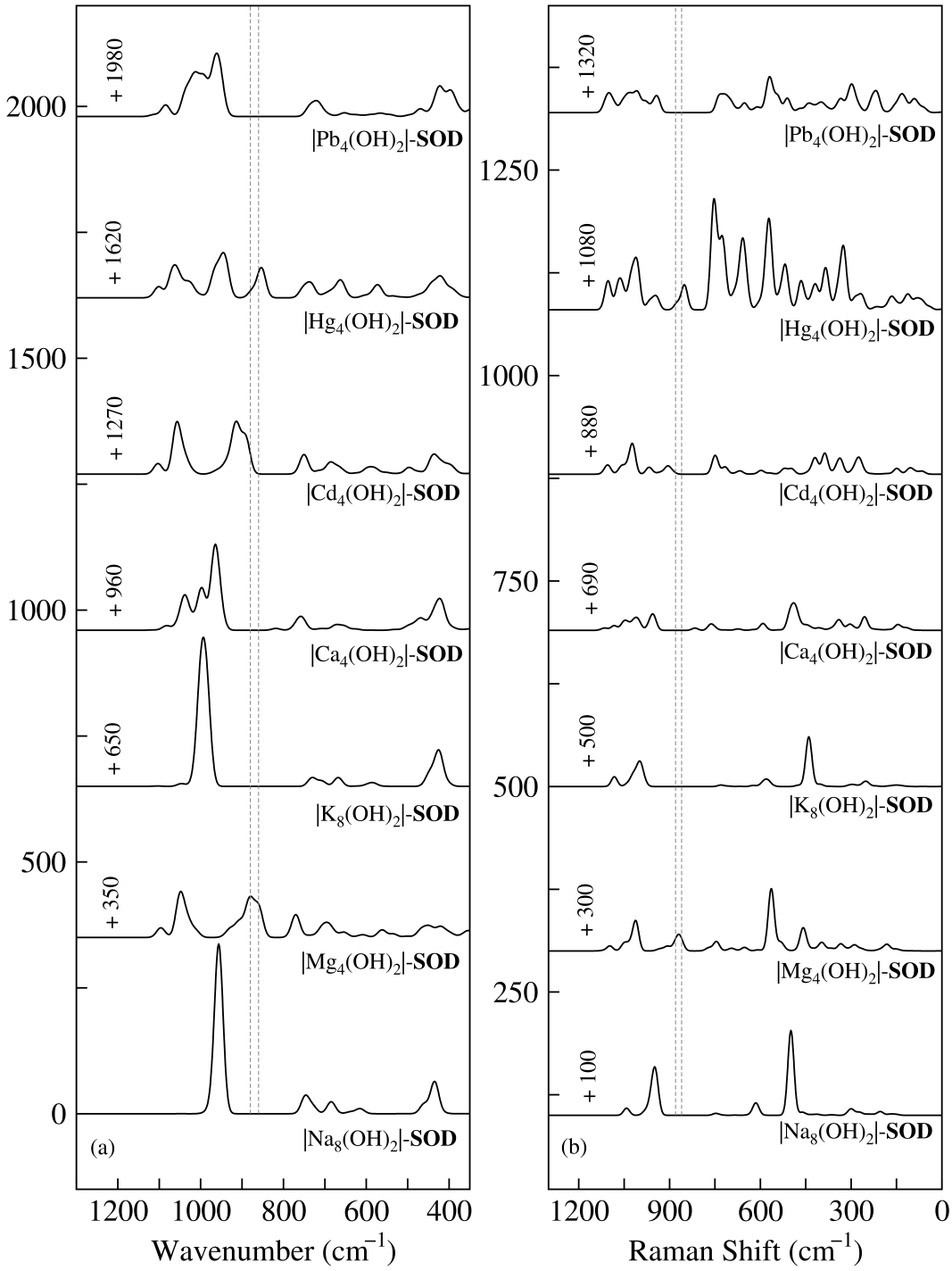

Figure 4.13. Calculated (a) mid-infrared infrared and (b) Raman spectra of anhydrous hydroxysodalite, $Na_8(OH)_2$-**SOD** as a function of different cations. The intensity is proportional to absorbance and has units of $C^2\,m^{-4}Å^{-2}\,amu^{-1}$ in the case of infrared; in the case of Raman, it is proportional to scattering intensity with units of $Å^4\,amu^{-1}$. The values written next to the graphs are the numbers by which they are translated. Dashed lines are to guide the eye to the see the differences between compounds between 860–880 cm^{-1}.

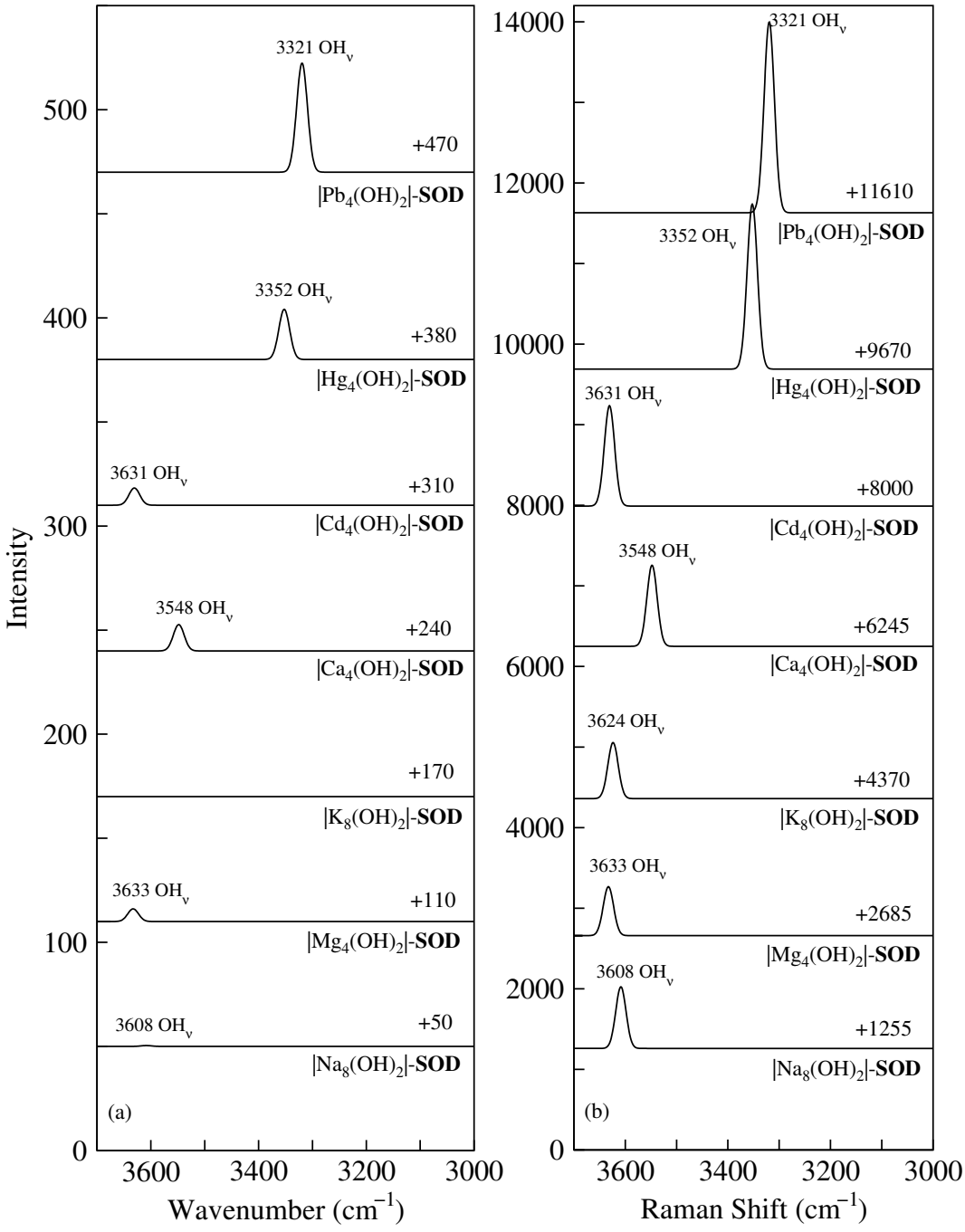

Figure 4.14. Calculated (a) infrared and (b) Raman spectra of anhydrous hydroxysodalite, $Na_8(OH)_2$-**SOD** as a function of different cations at higher frequencies. OH_ν represents the stretching mode and the intensity is proportional to absorbance and has the unit of $C^2\,m^{-4}\,Å^{-2}\,amu^{-1}$ in the case of infrared and $Å^4\,amu^{-1}$ for Raman. The values written above the graphs are the numbers by which they are translated.

a sharp peak for the magnesium-exchanged sodalite, whereas cadmium-exchanged sodalite does not exhibit this peak. Though it has been shown[180–182] that OH stretching vibrations can be detected for IR and Raman spectra in systems such as hemimorphite, water clusters, and sucrose crystals, such detection in zeolites would be challenging: the weak nature of Raman scattering combined with the strong fluorescence of zeolites often results in Raman spectra with high background levels.[20]

4.4.5 Possible Applications and Further Investigations

Our target application of this line of study was to detect lead, cadmium, or mercury in ground water. However, our investigation of anion-bearing sodalites has revealed that, though the 850–880 cm^{-1} range could conceivably provide a signature of mercury, lead, or cadmium in anion-free zeolites, such a signal would be weak and could be masked by magnesium hydroxysodalites.

To be useful as a detector, the loading of heavy metal cations on the zeolite would have to be high enough to see differences in the IR spectrum at ion concentrations at or below the relevant safety thresholds established by regulatory agencies. The lowest acceptable concentrations of lead, cadmium, and mercury in drinking water based on Environmental Protection Agency regulations[183] are 15, 5, and 2 ppb (μg/kg), respectively. According to Somerset et al.,[184,185] zeolites synthesized using coal fly ash are able to reduce lead concentrations from 1.50 to 0.25 ppb, cadmium concentrations from 0.80 to 0.45 ppb, and mercury concentrations from 0.47 ppb to 0.17 ppb. In addition, a similar study by Golbad et al.[179] showed that a loading (based on the Langmuir isotherm) of one Pb^{2+} cation per sodalite cage corresponds to a solution with a concentration as high as 2 ppm. This is significantly higher than the threshold imposed by the EPA (15 ppb). Therefore, we anticipate the intensity of the band in the 850–880 cm^{-1} range might not be high enough to detect concentrations on the order of parts per billion. However, to the best of our knowledge, there is not a study in which this question has been addressed experimentally.

In any case, a relatively sensitive spectrometer would be required to distinguish the weak shoulder that results from lead, cadmium, or mercury exchange of anion-free sodalites, even at full saturation. Fortunately, with the advancement of technology in the spectroscopy realm, there exist infrared and Raman spectrometers that have resolutions as high as 0.04 cm^{-1},[186] which is likely to be sensitive enough to resolve the bands in the 850–880 cm^{-1} range. However, more work is required to ascertain whether the infrared and Raman spectra of exchanged hydroxysodalites may enable even the qualitative detection of the heavy metals lead, cadmium, and mercury for concentrations as low as 2 ppb. At this stage, we do not anticipate IR detection of heavy metals to be sensitive enough for water resource management, primarily because the intensity of the relevant IR signals is not high enough.

4.5 Conclusions

We have examined the sensitivity of theoretical infrared and Raman spectra of sodalites to Mg^{2+}, K^{+}, Ca^{2+}, Ag^{+}, Cd^{2+}, Pb^{2+}, and Hg^{2+} ion exchange. This was done to investigate whether there exists a "signature" indicating the presence of heavy metals, even when other ions (such as potassium, magnesium, and calcium) that are normally present in ground water are present in the background. Our results suggest that the presence of bands in the 850–880 cm^{-1} range in either the IR or Raman spectra can be attributed to the presence of cadmium, lead, or mercury in anion-free sodalites. Our density functional theory (DFT) predictions are in good agreement with previously published studies.[107,178] However, the intensities of these features are likely not high enough to use them as indicators of cadmium, lead, or mercury contamination.

We anticipate that the calculated infrared and Raman spectra of ion-exchanged sodalites presented here will be useful in future experimental characterization of ion-exchanged zeolites, regardless of the final application.

Acknowledgments

Partial financial support for this work was provided by the National Science Foundation under award number DMR-1757936. Additional support was provided by the University of Missouri Research Board under award RB16-30. The computations in this work were performed on the high-performance computing infrastructure provided in part by Research Computing Support Services at the University of Missouri and in part by the National Science Foundation under grant number CNS-1429294.

CHAPTER 5

A DENSITY FUNCTIONAL THEORY STUDY OF THE VIBRATIONAL SPECTRA OF ALUMINATE SODALITE, $|M_8X_2|[Al_{12}O_{24}]$-SOD (M = Ca, Cd, Sr;X = CrO_4, MoO_4, S, SO_4, Se, SeO_3, Te, TeO_3)

This chapter was largely published as Ref. 187, an article in Microporous and Mesoporous Materials*. The authors of that article are Amir M. Mofrad and Karl D. Hammond from the University of Missouri.*

5.1 Summary

This chapter investigates the structural properties and vibrational (i.e., infrared and Raman) spectra of calcium, strontium, and cadmium aluminate sodalites with different extra-framework cations and anions using density functional theory (DFT). The anions studied in this work are CrO_4^{2-}, MoO_4^{2-}, Se^{2-}, SeO_3^{2-}, S^{2-}, SO_4^{2-}, Te^{2-}, and TeO_3^{2-}. The results are in good agreement with experiment both for structural and vibrational properties for compositions for which such properties are known from experiment. Results from DFT show that the cell parameters are a function of ionic radius as well as the number of atoms present in the structure. In addition, there is a direct correlation between the cell parameters and the frequency of Al−O−Al vibrational modes. As the cell parameter increases, the asymmetric stretching modes shift to higher wavenumbers, whereas the symmetric modes (both stretching and bending) experience a red shift.

5.2 Introduction

Sodalites (framework code **SOD**) are a well-known class of oxide materials consisting of β cages (Figure 5.1), which are formed from TO_4 tetrahedra (so-called T atoms) linked through shared four- and six-membered rings.[188] In anion-bearing sodalites, the anions are located in the centers of the cages, coordinated to four cations that sit near the centers of the six-membered rings (see Figure 5.1).[189]

The general composition of sodalite (an aluminosilicate) is, following the recommended nomenclature of the IUPAC,[16]

$$|M_m^{q+}X_x^{r-}|[Si_{12-n}Al_nO_{24}(H_2O)_{0-8}]\text{-}\mathbf{SOD}, \tag{5.1}$$

where $qm - rx = n$ and $n \leq 6$. Given these constraints, the aluminum content cannot exceed the silicon content. In other words, the Si/Al ratio in zeolites can only vary from pure silica (siliceous or Si/Al = ∞) to Si/Al = 1. This is consistent with Löwenstein's rule, which states that no Al−O−Al moieties exist in ordinary zeolites.[12] It is worth mentioning here that sodalite is considered to be a "semi-condensed" tetrahedral framework, a category that also includes cancrinite and analcime and that lies at the boundary between non-porous oxides and zeolites; amongst the semi-condensed aluminosilicates, sodalite is the most widely studied.[190]

In Equation 5.1, M and X are extra-framework cations and anions, respectively. The extra-framework cation in most natural and as-synthesized sodalites is sodium, but this cation can be exchanged to lithium, potassium, rubidium, or cesium,[163,191–193] as well as transition metals such as silver, cadmium, and lead.[107,178,179] Anions that can be occluded into aluminosilicate sodalites vary from halide (chloride, bromide, and iodide) ions[41,194] to hydroxide and other polyatomic anions such as perrhenate (ReO_4^-), nitrate (NO_3^-), and thiocyanate (SCN^-).[195–198] Due to the variety of compositions that can be created,

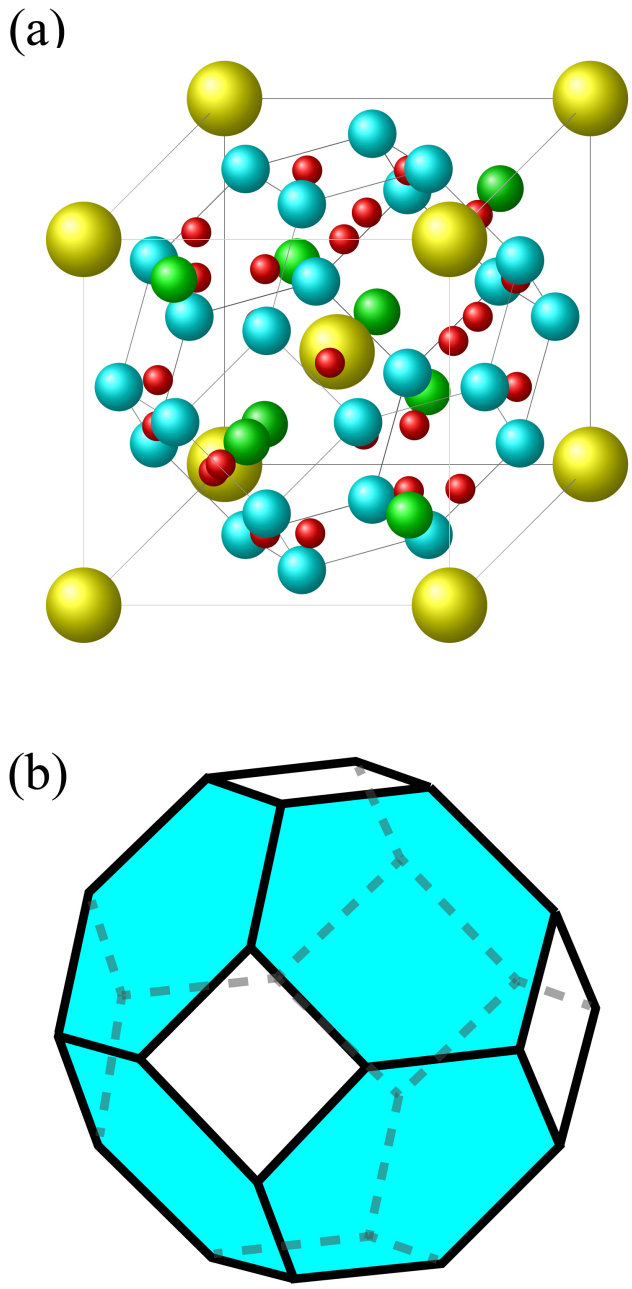

Figure 5.1. (a) Structure of calcium sulfide aluminate sodalite ($|Ca_8S_2|$-**SOD** framework; a = 8.928 Å). Colors indicate different elements: cyan, aluminum; yellow, sulfur; red, oxygen; and green, calcium. Spheres are drawn with a radius half the value of either the ionic radius (S^{2-}, Na^{+}) or the covalent radius (Al, O). (b) General 3D structure of a sodalite cage (β cage). Extra-framework cation sites are slightly inside or slightly outside the hexagonal windows (shaded).

aluminosilicate sodalites can serve in a variety of applications, including jewelry,[199] ion-exchange,[107,147,178] adsorption,[179] nuclear waste management,[193,196,197] and catalysis.[165]

It is important to note that Equation 5.1 only describes compositional variations for aluminosilicate sodalites. A more general description of the sodalite unit cell is[189]

$$|M_8X_2|[TT'O_4]_6\text{-}\mathbf{SOD}. \tag{5.2}$$

As suggested by Equation 5.2, there are up to eight sites per unit cell for extra-framework cations (Na^+) and two cites per unit cell for extra-framework anions (most commonly Cl^-). Sodalites have been reported that are ion-exchanged with Li^+, K^+, Ag^+, Tl^+, Mg^{2+}, Ca^{2+}, Sr^{2+}, Ba^{2+}, and others.[178,190] Other extra-framework anions that have been reported include Br^-, OH^-, CO_3^{2-}, $C_2O_4^{2-}$, NO_3^-, SO_4^-, ClO_4^-, CrO_4^-, MoO_4^{2-}, TeO_3^{2-}, SeO_3^{2-}, and WO_4^{2-}.[188,189,200,201] The sites T and T′ denote the corner-sharing $TT'O_4$ tetrahedra; to date, sodalites have been synthesized with T and/or T′ = Si, Al, Be, P, B, Zn, Ga, and Ge.[202–205] The reason for the presence of these extra-framework cations is to compensate for the negative formal charges on T atoms such as aluminum, gallium, and boron, which have fewer or greater than four valence electrons in the neutral atom. The presence of extra-framework cations and anions is not necessary: pure-silica variations of sodalite, with $m = n = x = 0$ in Equation (5.1), have been synthesized.[131,132]

This study aims at predicting the vibrational (i.e., infrared and Raman) as well as structural properties of aluminate sodalites, an unusual class of sodalites containing no silicon. Aluminate sodalites, in which T = T′ = Al, are unusual because they violate Löwenstein's Rule. Aluminate sodalite is the all-aluminum analog of bicchulite, an aluminum-rich (and silicon-poor) mineral with unit cell composition $|Ca_8(OH)_8|[Al_8Si_4O_{24}]$-**SOD**, which has the same framework topology as sodalite and that also violates Löwenstein's Rule.[189,201] Because of the high aluminum content in such materials, the framework is acidic, which Brenchley and Weller suggested have potential applications in catalysis and

ion exchange.[188,200] The general formula of aluminate sodalites is

$$|M_8X_2|[Al_{12}O_{24}]\text{-}\mathbf{SOD}, \tag{5.3}$$

where M $\in \{Ca^{2+}, Cd^{2+}, Sr^{2+}\}$ and X $\in \{{CrO_4}^{2-}, {MoO_4}^{2-}, {SO_4}^{2-}, {SeO_3}^{2-}, {WO_4}^{2-}, {TeO_3}^{2-}, S^{2-}, Te^{2-}, Se^{2-}\}$. Given that all materials we discuss have the same framework composition, we use the simplified notation $|M_8X_2|$-**SOD** to be equivalent to Equation (5.3) to describe aluminate sodalites from here on.

The first systematic study of aluminate sodalite was conducted in the early 1960s by Halstead et al.,[206] in which they investigated the structure of yeelimite ($|Ca_8(SO_4)_2|$-**SOD**) and its potential applications as an expanding cement. In addition, many aluminate sodalites were studied by Depmeier[207,208] during the 1980s and 1990s, which focused solely on structural properties and phase transitions of these materials. Aluminate sodalites have also received more recent attention. For instance, Maeda et al.[15] investigated the ferroelectric properties of calcium strontium tungstate aluminate sodalites, $|Ca_{8-x}Sr_x(WO_4)_2|$-**SOD**, for applications in energy-harvesting. In a study by Cuesta et al.,[209] yeelimite ($|Ca_8(SO_4)_2|$-**SOD**), another aluminate sodalite, was investigated for its applications in cements. To summarize, although aluminate sodalites are gaining some attention in pursuit of their potential applications, the literature on these materials—especially on vibrational properties (i.e., infrared and Raman spectra)—is sparse.

This study explores the effect of extra-framework cations and anions on both the structural and vibrational properties of aluminate sodalites by means of density functional theory calculations. Findings from this study will serve as a reference for characterization and will contribute to an ever-growing knowledge base of vibrational spectroscopy in the materials science community.

5.3 Theoretical Calculations

The calculations were performed using density functional theory (DFT)[44,110] with plane-wave basis sets, treating the core–valence electronic interactions via pseudopotentials as implemented in Quantum ESPRESSO.[59,60] The asymmetric unit of chromate aluminate sodalite ($|Ca_8(CrO_4)_2|$-**SOD**) from the work of Melzer et al.[210] was used to reproduce the crystal structure with the $I\bar{4}3m$ space group. This structure was used as the starting point for other compositions. The exchange–correlation functional was the local density approximation (LDA)[111–114] with the Perdew–Zunger correction for self-interaction.[120] Norm-conserving pseudopotentials were used with a plane-wave energy cutoff (`ecut`) of 80 Ry and a charge density cutoff energy (`ecutrho`) of 320 Ry. We chose LDA because the current version of Quantum ESPRESSO is only able to compute Raman frequencies at that level of theory. Our previous work[41,147] showed that this set of pseudopotentials with the LDA gives infrared and Raman results that agree reasonably well with experiment. The Brillouin zone was sampled using a Monkhorst–Pack[128] grid; we found that a $2\times2\times2$ grid produced a high-enough k-point density that the results can be considered to be converged.

Each structure underwent a variable-cell geometry optimization in which both the cell parameters and the ions' positions were changed to minimize the energy of the ground state with no symmetry constraints. The convergence threshold on force per atom was set to 10^{-7} Ry/bohr and the residual stress on the supercell was less than 0.01 kbar. We employed the Broyden–Fletcher–Goldfarb–Shanno (BFGS)[211] energy minimization algorithm, a quasi-Newton method. In addition, we set the self-consistent field (SCF) energy-convergence criterion to 10^{-8} Ry.

After geometry optimization, we performed phonon calculations using density functional perturbation theory (DFPT)[212] at the center of the Brillouin zone (Γ point). The dynamical matrix and frequencies of the harmonic phonon modes were then generated based on the acoustic sum rule.[76] The computed Raman activities were based on Placzek's theory of polarizability.[173] The criterion for self-consistency in the phonon calculations (`tr2_ph`)

was set to 10^{-14} Ry. No scaling factor was applied to the calculated wavenumbers. The simulated infrared and Raman spectra have peak heights proportional to the calculated intensities of each normal mode of vibration. Each peak was line-broadened using a Gaussian line shape with a full width at half maximum (FWHM) of 20 cm^{-1}. We used Molden to visualize the vibrational modes.[129]

5.4 Results and Discussion

5.4.1 Structural Properties of Aluminate Sodalites

Table 5.1 shows the calculated structural properties of cadmium, calcium, and strontium aluminate sodalites with different anions. For most of the compounds presented in Table 5.1, DFT predicts that the cell volume is a function of both the number of atoms (ions) present and the ionic radii of the cations and anions. For instance, in the case of cadmium sodalites, the oxidation of sulfur to sulfate increases the volume by up to ten percent. In addition, changing the anion from sulfide (with a 1.84 Å ionic radius) to telluride (with a 2.21 Å ionic radius) increases the volume by four percent. Similar trends are also evident for the calcium and strontium aluminate sodalites. The only exception is the change from MoO_4^{2-} to CrO_4^{2-}: the calcium molybdate cell is slightly (about 1%) larger than the chromium molybdate cell, but the strontium form has an essentially identical cell volume for both anions.

Lattice parameters from DFT are in reasonably good agreement with experiment for most of the structures in Table 5.1. However, in some cases, there are some discrepancies between the calculated cell parameters and the experimental values. This stems from several factors: (i) we are using an approximation (LDA) that is known to underestimate the energy of covalently-bonded systems,[215] (ii) the presence of impurities and defects in experiments can cause the unit cell to change, and (iii) the DFT calculations were carried out at an energetic minimum, whereas the experimental lattice constants were measured at room temperature or above: the sodalite lattice expands non-linearly with temperature.[135]

Table 5.1. Calculated lattice parameters of cadmium, calcium, and strontium aluminate sodalites with different anions. The cell was not restricted to orthorhombic symmetry, but all structures retained $\alpha = \beta = \gamma = 90°$. The cell volume increases as the ionic radii of the anion increases.

Compound	Volume (Å^3)	Lattice Constants (Å) (This Work)	Experimental Values (Å)
$\lvert Cd_8S_2\rvert$-**SOD**	664.477	$a = b = c = 8.726$	$a = b = c = 8.818$ [200]
$\lvert Cd_8(SO_4)_2\rvert$-**SOD**	730.280	$a = b = 8.984,\ c = 9.048$	$a = b = c = 9.099$ [200]
$\lvert Cd_8Te_2\rvert$-**SOD**	692.522	$a = b = c = 8.847$	$a = b = c = 8.940$ [189]
$\lvert Ca_8S_2\rvert$-**SOD**	711.746	$a = b = c = 8.928$	$a = b = c = 9.022$ [188]
$\lvert Ca_8(SO_4)_2\rvert$-**SOD**	738.350	$a = b = 9.069,\ c = 8.977$	$a = b = 9.219,\ c = 9.917$ [209]
$\lvert Ca_8Te_2\rvert$-**SOD**	742.061	$a = b = c = 9.053$	$a = b = c = 9.154$ [189]
$\lvert Ca_8(TeO_3)_2\rvert$-**SOD**	751.286	$a = 8.956,\ b = 9.139,\ c = 9.179$	N/A
$\lvert Ca_8Se_2\rvert$-**SOD**	723.194	$a = b = c = 8.976$	$a = b = c = 9.077$ [200]
$\lvert Ca_8(SeO_3)_2\rvert$-**SOD**	731.469	$a = 8.972,\ b = 9.050,\ c = 9.009$	$a = b = c = 9.174$ [200]
$\lvert Ca_8(CrO_4)_2\rvert$-**SOD**	758.511	$a = 9.124,\ b = 9.156,\ c = 9.078$	$a = 9.236,\ b = 9.222,\ c = 9.206$ [210]
$\lvert Ca_8(MoO_4)_2\rvert$-**SOD**	766.216	$a = b = 9.090,\ c = 9.273$	$a = b = 9.295,\ c = 9.292$ [213]
$\lvert Sr_8S_2\rvert$-**SOD**	744.747	$a = b = c = 9.064$	$a = b = c = 9.257$ [188]
$\lvert Sr_8(SO_4)_2\rvert$-**SOD**	766.376	$a = b = c = 9.151$	$a = b = c = 9.099$ [188]
$\lvert Sr_8Te_2\rvert$-**SOD**	767.221	$a = b = c = 9.155$	$a = b = c = 9.379$ [201]
$\lvert Sr_8(TeO_3)_2\rvert$-**SOD**	777.124	$a = 9.027,\ b = 9.271,\ c = 9.286$	$a = b = c = 9.425$ [201]
$\lvert Sr_8Se_2\rvert$-**SOD**	754.676	$a = b = c = 9.104$	$a = b = c = 9.303$ [200]
$\lvert Sr_8(SeO_3)_2\rvert$-**SOD**	785.956	$a = 9.210,\ b = 9.108,\ c = 9.370$	$a = b = c = 9.434$ [200]
$\lvert Sr_8(CrO_4)_2\rvert$-**SOD**	784.285	$a = 9.189,\ b = 9.170,\ c = 9.308$	$a = 9.456,\ b = 9.426,\ c = 9.405$ [214]
$\lvert Sr_8(MoO_4)_2\rvert$-**SOD**	784.094	$a = b = 9.153,\ c = 9.359$	$a = b = 9.457,\ c = 9.411$ [208]

5.4.2 Vibrational Spectra of Aluminate Sodalites

Here, we investigate the vibrational properties (i.e., infrared and Raman spectra) of aluminate sodalites with various cation and anion combinations. Figures 5.2, 5.3, and 5.4 show the calculated infrared and Raman spectra of strontium, calcium, and cadmium aluminate sodalites, respectively. The wavenumbers of each peak and shoulder are written above them in these figures. Note that structures in the sodalite family exhibit three strong absorption bands in the 400–1300 cm^{-1} range.[41,216] These bands are referred to as framework vibrational modes for T−O−T units and are composed of asymmetric stretching modes (ν_{as}), symmetric stretching modes (ν_s), and bending modes (δ).[41,147,168,200] It should be noted that, in a generic sodalite composition, T in the T−O−T unit can be Si, Al, Ge, Ga, Be, and others. In an aluminate sodalite, however, T is always aluminum. Asymmetric stretching modes generally occur at higher wavenumbers (800–1300 cm^{-1}) than symmetric stretching modes (500–800 cm^{-1}). In addition, bending modes happen at frequencies lower than symmetric stretching (300–500 cm^{-1}). Below 300 cm^{-1}, the vibrational modes are associated

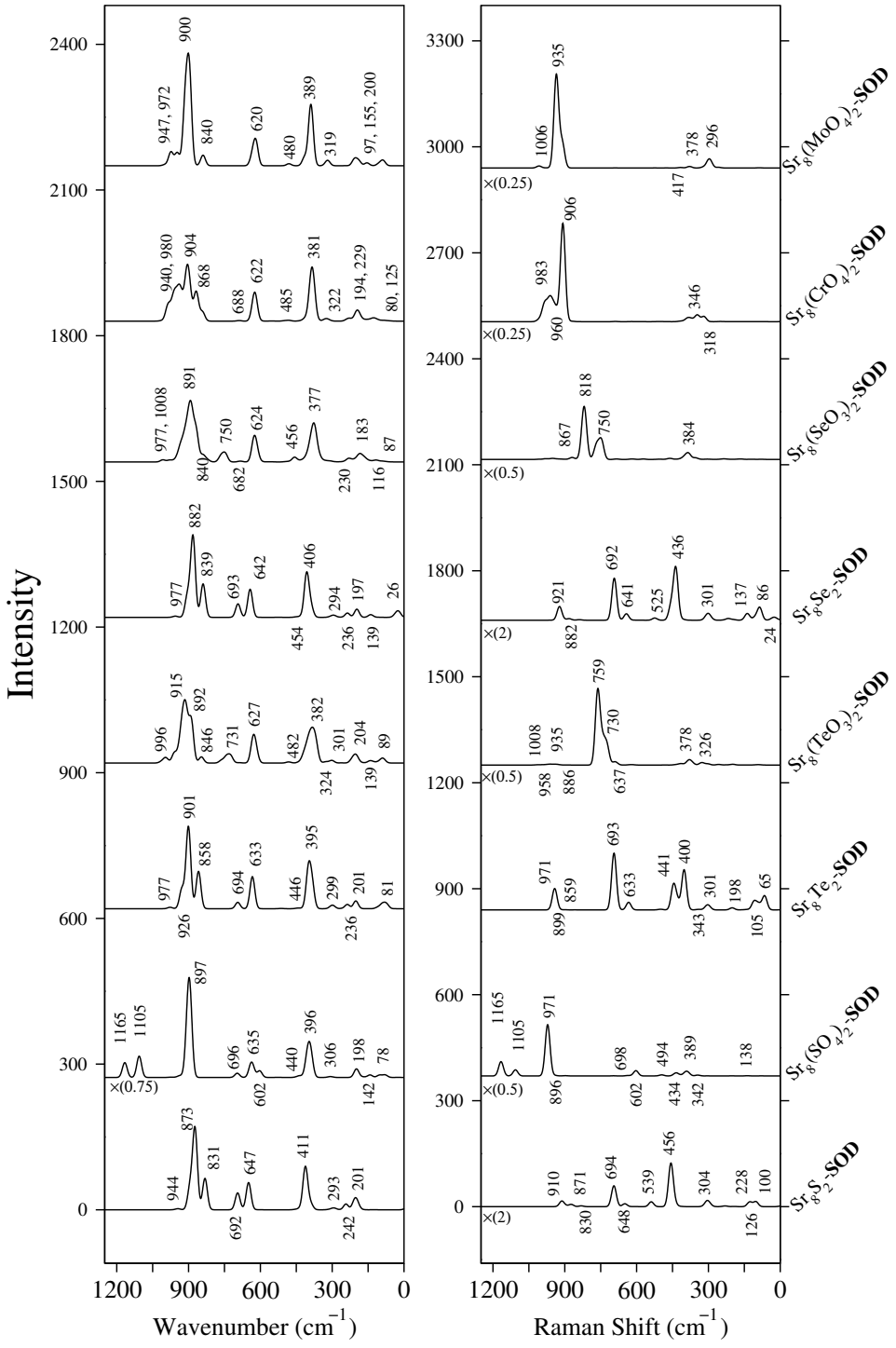

Figure 5.2. Calculated (left) infrared and (right) Raman spectra of strontium aluminate sodalites as a function of different anions. The intensity is proportional to absorbance and has units of $C^2\,m^{-4}\,Å^{-2}\,amu^{-1}$ in the case of infrared; in the case of Raman, it is proportional to scattering intensity with units of $Å^4\,amu^{-1}$. The plots are stacked so each compound is lined up. The values written below the graphs are the factors by which they are scaled. The wavenumbers are written above each peak and shoulder.

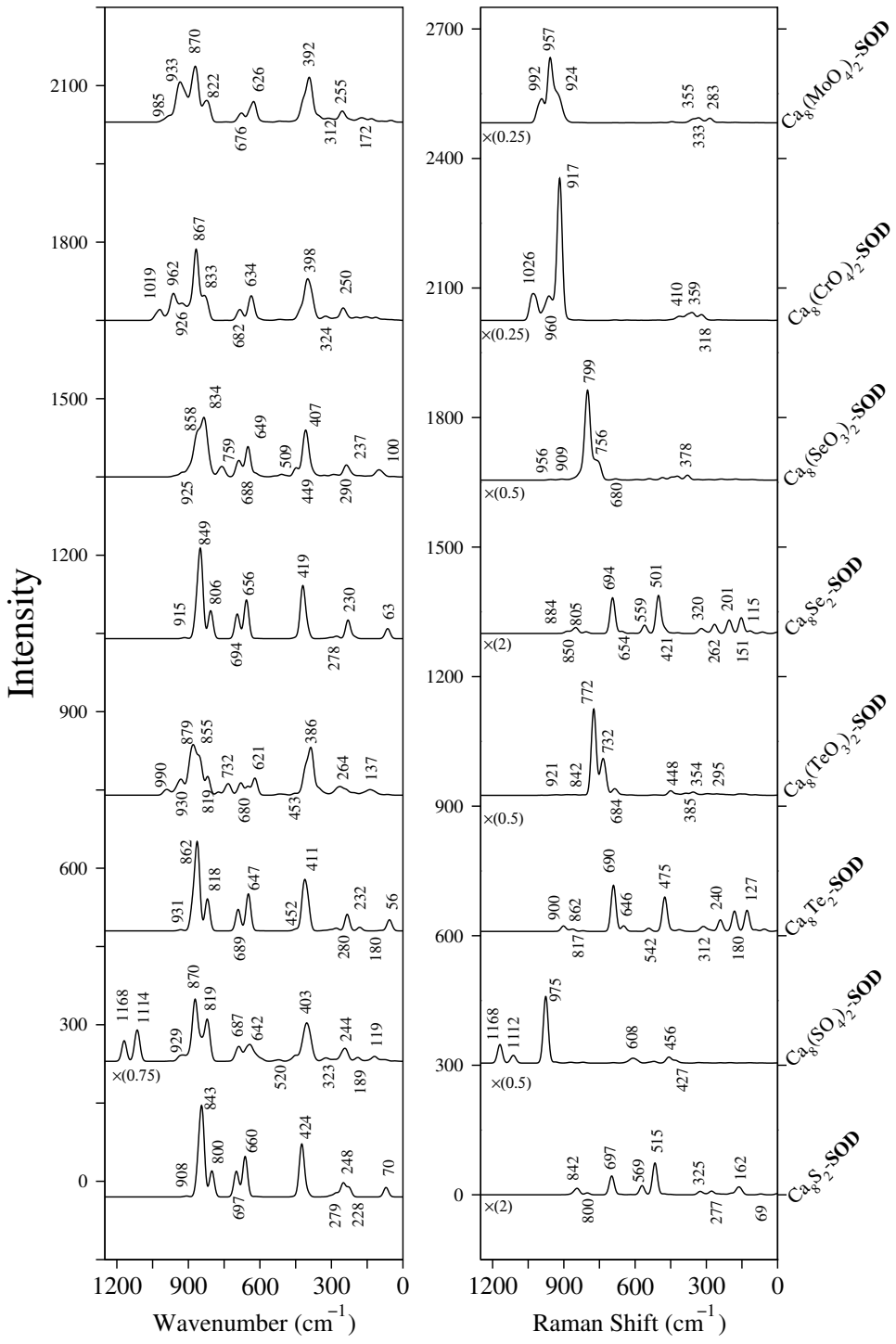

Figure 5.3. Calculated (left) infrared and (right) Raman spectra of calcium aluminate sodalites as a function of different anions. The intensity is proportional to absorbance and has units of $C^2\,m^{-4}\,Å^{-2}\,amu^{-1}$ in the case of infrared; in the case of Raman, it is proportional to scattering intensity with units of $Å^4\,amu^{-1}$. The plots are stacked so each compound is lined up. The values written below the graphs are the factors by which they are scaled. The wavenumbers are written above each peak and shoulder.

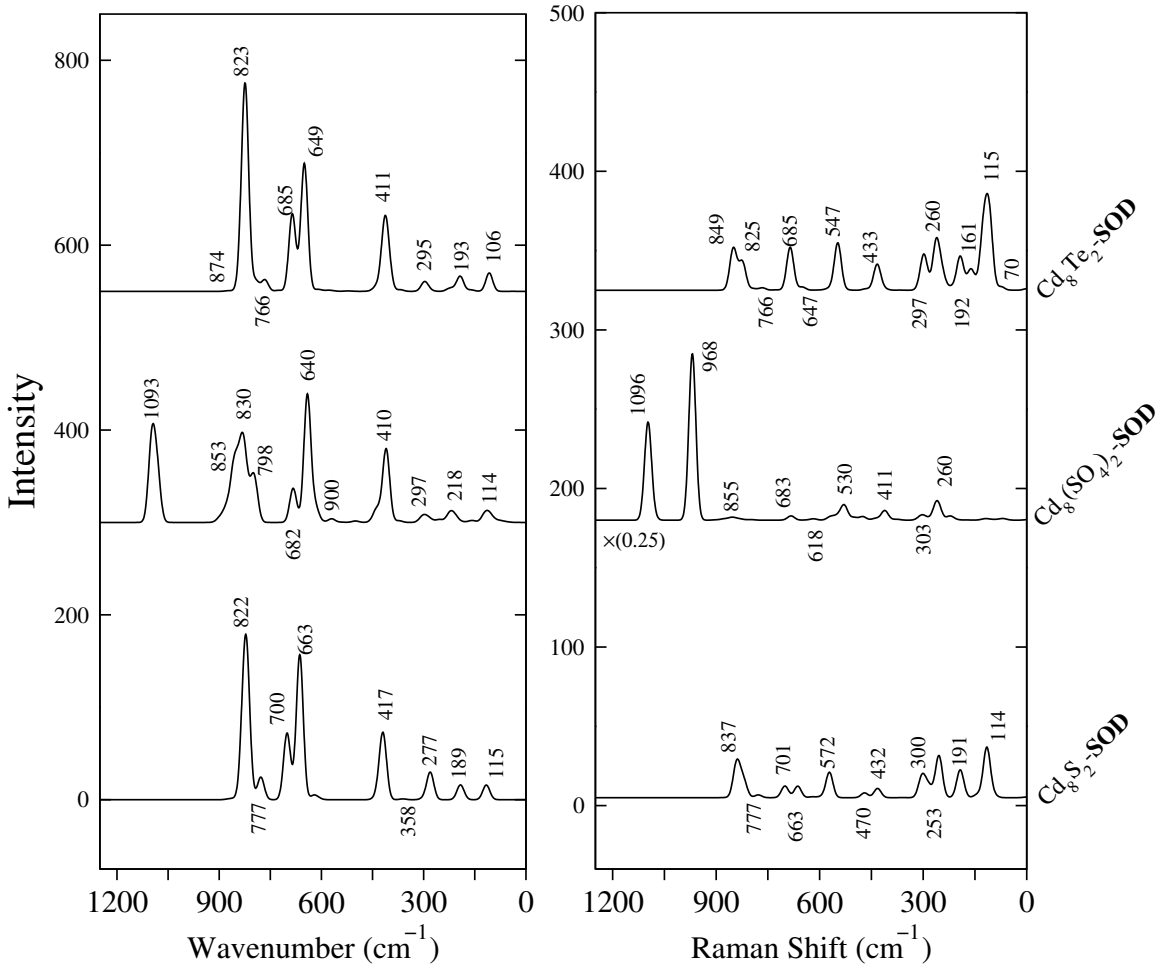

Figure 5.4. Calculated (left) infrared and (right) Raman spectra of cadmium aluminate sodalites as a function of different anions. The intensity is proportional to absorbance and has units of C^2 m^{-4} Å^{-2} amu^{-1} in the case of infrared; in the case of Raman, it is proportional to scattering intensity with units of Å^4 amu^{-1}. The plots are stacked so each compound is lined up. The values written below the graphs are the factors by which they are scaled. The wavenumbers are written above each peak and shoulder.

with lattice vibrations and extra-framework cation motion.[41,217] As shown in Figure 5.2, the asymmetric stretching mode shifts to higher wavenumbers upon oxidation for structures containing sulfur, tellurium, and selenium. In addition, as mentioned earlier, sulfur oxidation expands the unit cell, and there is consequently a direct correlation between the asymmetric stretching mode and the cell parameter: the higher the cell parameter, the higher the wavenumber of the asymmetric stretching mode.[200,216] On the other hand, symmetric modes (both stretching and bending) experience a red shift to lower wavenumbers with respect to cell size and oxidation. It should be noted that chromate and molybdate aluminate sodalites exhibit a similar spectrum in the region associated with the framework vibrations, which stems from the fact that (i) both molybdenum and chromium belong to the same group in the periodic table, and (ii) the cell volumes of these two sodalites are comparable (see Table 5.1).

There are also two additional bands (1105 and 1165 cm^{-1}) that only occur in the $|Sr_8(SO_4)_2|$-**SOD** structure: these are the S−O stretching vibrations. The E−O (E stands for any element) stretching modes are more pronounced in the Raman spectrum because many oxygen-stretching vibrations do not change the dipole moment and thus are infrared-invisible. For instance, Te−O vibrations in $|Sr_8(TeO_3)_2|$-**SOD** occur in the 730–760 cm^{-1} range and Se−O vibrations occur within the 750–820 cm^{-1} range. For chromate and molybdate strontium aluminate sodalites, the E−O stretching modes shift to higher wavenumbers (906 and 935 cm^{-1}, respectively), as seen in their Raman spectra in Figure 5.2. The relationship between the vibrational frequency and the properties of the atoms undergoing vibration is

$$\nu = \frac{1}{2\pi}\sqrt{\frac{k}{\mu}}, \tag{5.4}$$

where ν is the vibrational frequency in Hz, k is the force constant of the bond between two atoms in N/m, and μ is the reduced mass in kg, which is calculated by $\mu = m_1 m_2/(m_1 + m_2)$, where m_1 and m_2 are the rest masses of the two bonded atoms. Sulfur has the lowest atomic weight among tellurium, selenium, chromium, and molybdenum, so sulfates have

higher vibrational frequencies than other similar anions. Similar reasoning can be applied to Se−O and Te−O stretching modes. However, the Mo−O stretching mode occurs at higher frequency than the Cr−O stretching mode, even though molybdenum has a higher atomic mass. This is due to the fact that the electronegativity difference between Mo−O is higher than Cr−O, which results in a higher force constant, k, in Equation (5.4).

Figure 5.3 shows the calculated infrared and Raman spectra of calcium aluminate sodalites with the same anions as in Figure 5.2. The same conclusions can be drawn for each of the calcium aluminate sodalites as were drawn in the previous paragraph for strontium aluminate sodalites. It is noteworthy that the asymmetric stretching modes in the infrared spectra of all the structures in Figure 5.3 occur at lower wavenumbers compared to their strontium equivalents. This is in agreement with the correlation between the cell parameters and the frequency of the vibrational modes. In other words, all the cell parameters of calcium aluminate sodalites are smaller than those of strontium sodalites. Consequently, the asymmetric stretching modes in calcium aluminate sodalites shift to lower wavenumbers, whereas the symmetric stretching and bending modes shift to higher wavenumbers. In addition, the E−O stretching modes in calcium aluminate sodalites are visible in the Raman spectra in the same range as in the strontium case.

Figure 5.4 shows the calculated vibrational spectra of $|Cd_8S_2|$-**SOD**, $|Cd_8(SO_4)_2|$-**SOD**, and $|Cd_8Te_2|$-**SOD**, which are the only cadmium aluminate sodalites that have been synthesized successfully to date.[189,200] One take-away from Figure 5.4 is that the asymmetric stretching modes of cadmium aluminate sodalites shift to lower wavenumbers compared to their calcium and strontium equivalents because their unit cells are smaller. Conversely, the symmetric stretching modes shift to higher wavenumbers. The fact that these peaks shift in opposite directions means that, in cadmium sulfide aluminate sodalites (i.e., $|Cd_8S_2|$-**SOD**), distinguishing between asymmetric and symmetric stretching modes might be challenging. The only E−O stretching modes observed in the $|Cd_8(SO_4)_2|$-**SOD** structure fall within approximately 960–1100 cm^{-1}. It should be noted that the infrared and Raman spectra cal-

culated by DFT qualitatively agree well with the available literature in terms of predicting the three main vibrational modes.[188,189,200,201,216]

5.5 Conclusions

We have examined the effect of different anions on the structural and vibrational properties of calcium, strontium, and cadmium aluminate sodalites by means of electronic structure calculations. The results are in good agreement with experiments for compositions for which data are available. The predicted cell parameters change with both the size of the cation and anion as well as the number of atoms in the unit cell. Lastly, there is a correlation between the cell parameter and the Al−O−Al vibrational modes: as the cell parameter increases, the asymmetric stretching modes shift to higher wavenumbers, whereas the symmetric stretching and bending modes shift to lower wavenumbers.

These findings contribute to an ever-growing knowledge base of vibrational spectroscopy in the zeolitic materials community. We anticipate that the calculated infrared and Raman spectra of exchanged aluminate sodalites presented here will be useful in future characterization of these materials.

Acknowledgments

The computations in this chapter were performed on the high-performance computing infrastructure provided in part by Research Computing Support Services at the University of Missouri and in part by the National Science Foundation under grant number CNS-1429294.

CHAPTER 6

RELATIVE RATES OF KRYPTON AND RUBIDIUM RELEASE FROM ZEOLITE GETTERS

This chapter has been submitted but is not yet published. The authors are Amir M. Mofrad, Cannon Hackett, and Karl D. Hammond of the University of Missouri.

6.1 Summary

Zeolites such as sodalite and zeolite A are used to encapsulate radioactive ^{85}Kr for long-term storage. However, recent reports of zeolite getters removed from hot cells after over 40 years showed corrosion of the containers, suggesting that ^{85}Kr had escaped the getter and decayed to ^{85}Rb, a potent corrosive agent. This study aims to determine whether it is more likely that ^{85}Kr escaped the sodalite cages, followed by decay, or that ^{85}Rb escaped the sodalite cage after decay. We answer this question by calculating the activation energies of krypton and rubidium traversing the six-membered rings of sodalite cages using density functional theory (DFT) combined with the nudged elastic band (NEB) method and classical transition state theory. We find that it is extremely unlikely that krypton would make the jump through the window, meaning it is more likely that the non-radioactive rubidium is what escapes the getter.

6.2 Introduction

Nuclear fission has the potential to provide electrical power to the world for thousands of years based solely on proven reserves if "spent" fuel reprocessing were allowable and

safe.[218] The problem of nuclear waste management could similarly be solved by nuclear fuel reprocessing: long-lived waste products could be transmuted to short-lived isotopes or isotopes that are of essentially the same levels of radioactivity as in the ore. Commercial nuclear fuel reprocessing was curtailed in the United States during the Ford and Carter Administrations due to concerns over the proliferation of nuclear weapons, and although the ban was eventually relaxed, any reprocessing facility that would be licensed today would almost certainly have to demonstrate the capability of capturing volatile radionuclides without releasing them to the environment. The most common isotopes expected to produce gaseous products of reprocessing are tritiated water, $^{14}CO_2$, iodine (as $^{129}I_2$, $H^{129}I$, or organic iodides such as $CH_3{}^{129}I$), and noble gases.[219] The noble gas portion, which consists primarily of ^{85}Kr, is the hardest to contain, as it cannot be reacted with another compound to form a solid or liquid that would be easily stored.

The U. S. Code of Federal Regulations limits the total release of ^{85}Kr to 50,000 Ci per gigawatt-year of electrical energy produced over the entire uranium fuel cycle,[220] and the Nuclear Regulatory Commission lists maximum allowable effluent concentrations of ^{85}Kr to 7×10^{-7} μCi/ml (0.03 Bq/ml),[221] which translates to approximately 0.5 ppt ^{85}Kr by volume at standard temperature and pressure. These regulations would require any reprocessing facility to capture radiokrypton and store it until the vast majority of the ^{85}Kr has decayed.

The decay of ^{85}Kr occurs by β^- emission, forming stable ^{85}Rb through the reaction

$$^{85}_{36}\mathrm{Kr} \longrightarrow {}^{85}_{37}\mathrm{Rb} + \mathrm{e}^- + \bar{\nu}_\mathrm{e} \qquad 1.374\ \mathrm{MeV}, \tag{6.1}$$

where e^- is an electron (β^- particle) and $\bar{\nu}_e$ is the antiparticle of an electron neutrino. This reaction has a half-life of 10.756 y,[222,223] meaning that after 50 y, only 4% of the original ^{85}Kr remains. The ^{85}Rb decay product is not radioactive, but rubidium is a very reactive

alkali metal that is known to be highly corrosive.[224–226] In fact, one of the biggest concerns with storing ^{85}Kr in metal canisters is the potential for corrosion caused by rubidium.[227,228]

Several methods have been proposed over the past several decades to limit corrosion and store ^{85}Kr efficiently and economically.[227–231] The simplest is to use pressurized gas cylinders, similar to those used to store compressed gases in laboratories. Another option to store ^{85}Kr is to co-deposit it with metal vapor,[227,228,232] resulting in a metal matrix containing small amounts of ^{85}Kr ($\approx 6\%$ by mass). Unfortunately, such metal/krypton co-deposition techniques are very expensive.[233–235] An alternative that reduces costs is to use porous materials to encapsulate the gas inside the pore network. Packing canisters with strong adsorbents such as metal–organic frameworks (MOFs) and zeolites also encapsulates more ^{85}Kr than a pressurized canister.[236] Using MOFs and zeolites for nuclear waste treatment (especially ^{85}Kr encapsulation) is not new—it was first attempted in the late 1960s and early 1970s[237,238]—but there has been renewed interest in this area in recent years.[235,239] MOFs are typically far less chemically stable than zeolites and are expected to be more susceptible to damage from the β^- decay or the resulting change in framework charge than zeolites.[240]

Zeolites—crystalline aluminosilicates with three-dimensional pore networks—are relatively stable at high temperature and have numerous applications ranging from adsorption and ion exchange to catalysis.[7,160,241] Zeolites' ion-exchange capabilities also make them able to "scrub" radioactive isotopes such as ^{137}Cs and ^{90}Sr from aqueous media, exchanging them with sodium or another non-radioactive ion.[95,242,243] We focus here on using zeolites to encapsulate krypton-85.

For the purpose of ^{85}Kr encapsulation, zeolites with small windows enclosing larger pores—such as the sodalite cages found in the frameworks **SOD**, **LTA**, and **FAU**, among others—are typically used. Wire-frame depictions of the sodalite cage (β-cage) structures of sodalite (**SOD** framework) and zeolite A (**LTA** framework) and the α-cage structures of zeolite A are shown in Figure 6.1. The gas is loaded at high temperature and pressure

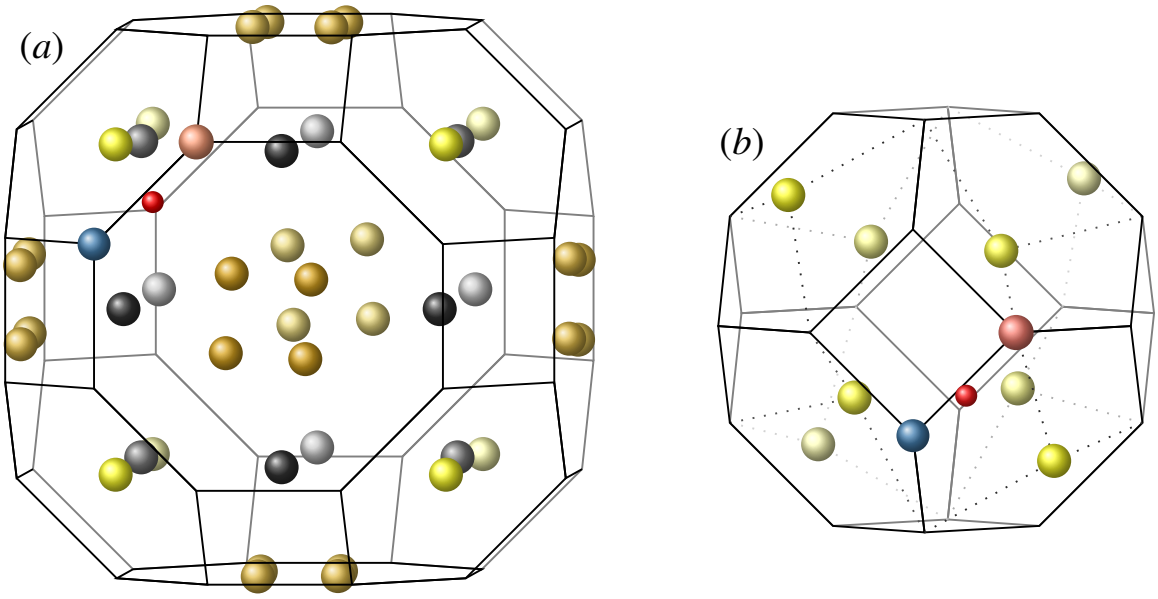

Figure 6.1. Zeolite A (**LTA** framework) consists of face-sharing α-cages (*a*), which form β-cages (*b*) at the corners. Sodalite (**SOD** framework) consists only of β-cages (*b*). Yellow balls denote sodium site I (*a*, **LTA**; *b*, **SOD**), fading to light yellow in the background; goldenrod spheres denote sodium site II, fading to light goldenrod in the background; black spheres in denote sodium site III, fading to gray in the background; red, blue, and salmon-colored balls show an oxygen, silicon, and aluminum atom, respectively, to establish a pattern. Dotted lines show whether ions are behind or in front of the six-ring.

(≈ 450–800 °C and ≈ 100 MPa).[223] The material is then cooled rapidly, with the resulting thermal contraction reducing the size of the six-membered ring of the sodalite cage just enough that krypton's rate of permation through the window is drastically reduced. Note that this requires true zeolites (i.e., aluminosilicates): so-called "siliceous" (or "pure-silica") zeolites, which are more correctly called silica polymorphs, typically have negative thermal expansion coefficients,[244–249] meaning the window size would get *smaller* when the material was heated, preventing encapsulation.

Recently, Jubin and Bruffey[233,250,251] investigated five canisters that were used in the 1970s at Idaho National Laboratory for ^{85}Kr storage in zeolite 5A. These canisters, which had been recently removed from a hot cell, were heavily corroded, and two had ruptured in storage. The heavy corrosion suggested that the getter had failed, leaking ^{85}Kr into the

container and resulting in rubidium-induced corrosion of the metal. The results of a compositional analysis confirmed the presence of the elements normally present in zeolite 5A, as well as krypton and rubidium.

The authors of the aforementioned studies presumed that krypton had escaped the sodalite cages (β-cages), decayed to rubidium, and corroded the container (in that order). However, we hypothesize that there are three possible mechanisms:

1. Krypton escapes the sodalite cage and then decays to rubidium, which then makes its way to the container walls, causing corrosion.

2. Krypton remains trapped inside the sodalite cage, where it decays to a rubidium atom. The rubidium atom eventually diffuses out of the sodalite cage and makes its way out of the zeolite phase onto the container wall.

3. Krypton remains trapped inside the sodalite cage, where it decays to a rubidium atom. This atom rapidly donates an electron to the framework, forming Rb^+, which takes on the role of an extra-framework cation. The Rb^+ ion permeates the sodalite cage and diffuses by ion exchange to the container wall, causing corrosion.

Based on the relative sizes of the three species (the ionic/atomic radii increase in the order $Rb^+ < Kr < Rb$), we expect the Rb^+ mechanism to be the most relevant.

In this study, we use density functional theory (DFT) to calculate the relative migration rates of krypton and rubidium in sodalite and zeolite A. These rates are estimated from transition state theory based on jumps that cross the six-membered ring of the sodalite cages, with each system intended to test a different aspect of the three mechanisms mentioned above. This includes the effects of different extra-framework cations (i.e., Na^+, K^+, and Ca^{2+} in zeolite A). Our results indicate that the difference between the two rubidium mechanisms is not readily discernable or important, and that the most likely explanation for observed corrosion of the metal canisters containing ^{85}Kr-loaded zeolite getters is that krypton remains trapped in the getter until it decays. This indicates that using sodalite or

zeolite A as a ^{85}Kr-encapsulation material is more viable than recent experimental observations indicate, provided a corrosion-proof container is used or a method of neutralizing the rubidium decay products can be found.

6.3 Description of Computations

6.3.1 Crystal Structures and Compositions

We considered several structures: anion-free sodalite ($|Na_6|[Si_6Al_6O_{24}]$-**SOD**, following the recommended notation[16]), chloro- and bromo-sodalites ($|Na_8Cl_2|[Si_6Al_6O_{24}]$-**SOD** and $|Na_8Br_2|[Si_6Al_6O_{24}]$-**SOD**, respectively), siliceous sodalite ($[Si_{12}O_{24}]$-**SOD**), zeolite 3A (KA, $|K_{12}|[Si_{12}Al_{12}O_{48}]$-**LTA**), zeolite 4A (NaA, $|Na_{12}|[Si_{12}Al_{12}O_{48}]$-**LTA**), zeolite 5A (CaA, $|Ca_6|[Si_{12}Al_{12}O_{48}]$-**LTA**), and siliceous A ($[Si_{24}O_{48}]$-**LTA**). The crystal structures were reproduced from the work of Hassan et al.[109] (for chloro- and bromo-sodalites) and from the Database of Zeolite Structures[3] (for anion-free sodalites). The asymmetric unit of sodalite was based on the $P\bar{4}3n$ space group (#218). The crystal structure of zeolite A was drawn from International Zeolite Association (IZA) website,[3] based on the $Pm\bar{3}m$ space group (#221), which is the unit cell for siliceous case.

There is one symmetrically-distinct cation site in the sodalite, and three in zeolite A. The three cation sites in zeolite A are located just inside the six-membered ring (site I), in the plane of the eight-membered ring (site II), and just inside the four-membered ring (site III).[252] All of these sites are inside the α-cage, and not all sites are occupied in any given unit cell repeat. In particular, the aluminum distribution determines which of the images equivalent to site II will be occupied.

Zeolites generally obey Löwenstein's Rule,[12] which states that no Al−O−Al moieties can exist in aluminosilicates. One consequence of this is that the smallest unit cell for zeolite A with Si/Al = 1 (i.e., ordinary zeolite A) is the size of a $2\times2\times2$ block of siliceous A. This extra repeat is necessary to create a crystal that obeys Löwenstein's Rule. Unfortunately, such a unit cell would contain 672 atoms, which is too large for tractable plane-wave

DFT calculations. Instead, we modified the unit cell of siliceous A to include aluminum atoms and extra-framework cations consistent with Si/Al = 1 *only* in the vicinity of the diffusing krypton or rubidium species, with T-atoms elsewhere being exclusively silicon. This allows calculations on zeolite A to be done with less than 1/4 as many electrons, making the computations tractable. The local environment seen by the diffusing species should still be reflective of the local environment in the real material during the jump.

6.3.2 Electronic Structure Calculations

6.3.2.1 Periodic (Plane-Wave) Models

Electronic structure calculations were performed with density functional theory using a periodic supercell with plane-wave basis sets, as implemented in Quantum ESPRESSO.[59,60] Unless otherwise specified, our calculations used norm-conserving pseudopotentials[115,116] combined with the local density approximation (LDA),[110–114] which we denote NC-LDA. This choice of exchange–correlation functional and pseudopotential has been shown to predict reasonable results for zeolite vibrational modes in our previous studies.[41,147,187]

As a test of the robustness of the calculated values, we performed some calculations using the LDA and the Perdew–Zunger self-interaction correction[120] and nonlinear core-correction with Rappé–Rabe–Kaxiras–Joannopoulos (RRKJ) ultra-soft pseudopotentials (ULT-LDA).[121,122] We performed another set using the Perdew–Burke–Ernzerhoff (PBE) functional[117,118] with the norm-conserving Martins–Troullier (MT) pseudopotentials (NC-PBE),[115] and the PBE functional with non-linear core correction and the projector augmented wave (PAW) method[119] (PAW-PBE). In all cases, the Brillouin zone was sampled using a Monkhorst–Pack[128] grid in which a $2 \times 2 \times 2$ grid produced a high enough k-point density for the results to be considered converged. The Kohn–Sham electronic states were expanded in plane waves up to different kinetic energy cutoffs and charge densities for different PPs. Table 6.1 shows the converged values of different PPs.

Table 6.1. Cutoff parameters for plane-wave energies and densities, denoted `ecut` and `ecutrho`, respectively, in Quantum ESPRESSO.

Method[a]	`ecut` (Ry)	`ecutrho` (Ry)
NC-LDA	80	320
ULT-LDA	70	700
NC-PBE	80	320
PAW-PBE	85	510

[a]pseudopotential and density functional

We performed a variable-volume (`vc-relax`) geometry optimization in which both the ions' positions and the cell parameters were optimized simultaneously for all initial structures in this study. We used the Broyden–Fletcher–Goldfarb–Shanno (BFGS) algorithm,[172] a quasi-Newton method, using a force-per-atom stopping criterion of 10^{-7} Ry/bohr.

After geometry optimization of the sodalite structures, we introduced the encapsulate (Kr, Rb, or Rb^+) into the system at two positions: slightly inside the six-membered ring and inside a sodalite cage (the initial state), and slightly outside the same six-membered ring, inside an adjacent sodalite cage (the final state). In the case of zeolite A, the adsorbates were introduced into the system same way as sodalite structures, except the final state was inside the α cage.

To find the migration energy (activation energy of diffusion), we used the climbing-image nudged elastic band (CI-NEB) method[253–255] to find the minimum energy pathway (MEP) between the initial and final states. In some cases, a non-climbing-image NEB calculation was performed to estimate the MEP, followed by another calculation involving a climbing image. We used CI-NEB as implemented in Quantum ESPRESSO with five images using the same optimization algorithm (BFGS) as for the geometry optimization. Figure 6.2 shows a schematic of the initial guess (i.e., the initial pathway assigned to the images before the NEB procedure is carried out) for both sodalite and zeolite A. The green

hexagon is the six-membered ring involved in the jump; the transition state occurs when the diffusing species lies on that plane.

6.3.2.2 Cluster Models

Zeolites are electronic insulators, so the migration energy and other similar properties typically depend only on the local electronic environment. Given the finite-size effects that can plague periodic calculations, we calculated the migration energies of krypton, rubidium atom, and rubidium ion with finite-size cluster models for the siliceous cases, to determine how reliable the periodic (plane-wave) DFT results are. Cluster models obviously carry their own finite-size effects, but such effects manifest differently than in periodic calculations, providing a complementary result. This approach has been used to great effect in the past to study diffusion, adsorption, and chemical reactions in zeolites.[19,256,257]

We used the embedded cluster approach via the two-layer ONIOM[258,259] method as implemented in Gaussian 16 [Ref. 260] to calculate the optimized structures and energies of the transition, initial, and final states. We used an overall ("whole," denoted "W") cluster containing 378 tetrahedral (Si, Al) atoms, which will hereafter be called a 378 T cluster. The cluster was truncated after oxygen atoms, and the outermost oxygen atoms were fixed at their crystallographic coordinates. The high-level ("quantum," denoted "Q") layer was a 42 T cluster consisting of two adjacent sodalite cages sharing a six-membered ring. Note that a smaller quantum layer would suffer from inaccurate results due to the incomplete cage structure—for example, we initially used an 18 T quantum cluster, which produced a significantly higher migration energy (data not shown) because the krypton atom was able to escape the (open) cage and interact only with the low-level layer and/or the terminal OH groups (thus lowering the energy of the initial state). The interaction between the total and quantum cluster is purely structural—that is, there is mechanical embedding but not electronic embedding. The quantum layer was terminated by oxygen atoms, with implicit hydrogens added to make an OH-terminated quantum cluster. The energy of an ONIOM

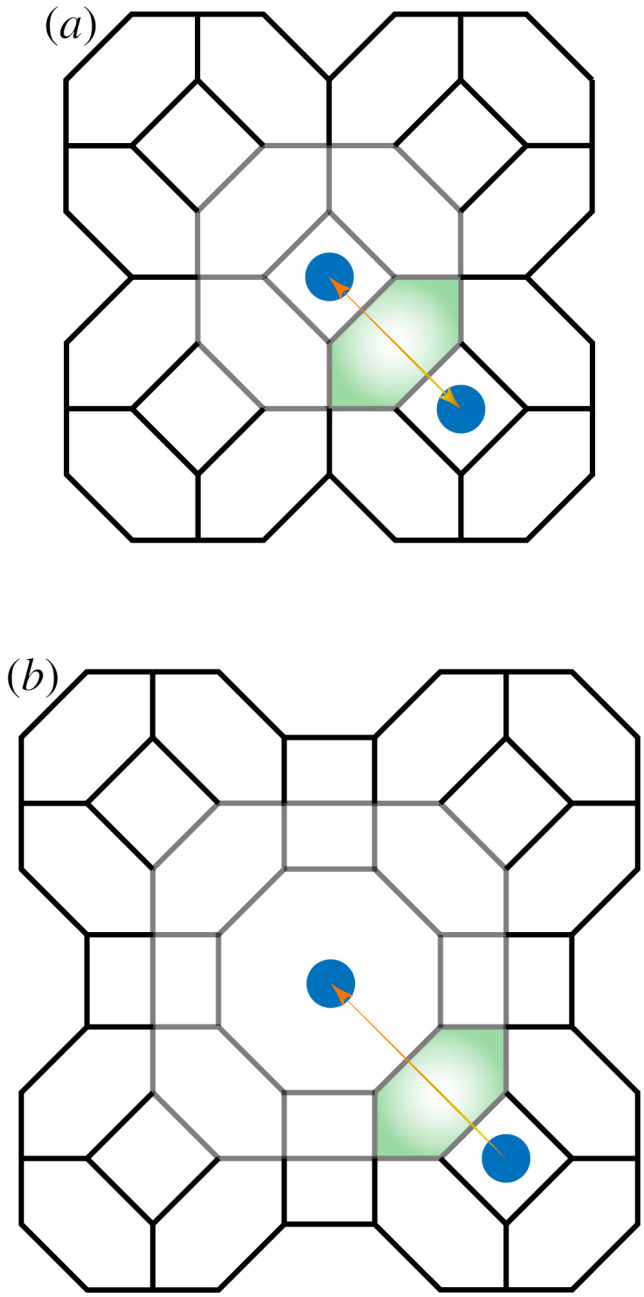

Figure 6.2. Schematic of krypton diffusion in (*a*) sodalite (**SOD**) and (*b*) zeolite A (**LTA**). The "escape" of krypton from the sodalite cage is modeled as a jump through the six-membered ring (green). The transition state for the minimum energy pathway occurs when krypton is at the center of the ring.

calculation is

$$E_{\mathrm{ONIOM}} = E_{\mathrm{high}}(\mathrm{Q}) + E_{\mathrm{low}}(\mathrm{W}) - E_{\mathrm{low}}(\mathrm{Q}). \tag{6.2}$$

We used the Universal Force Field (UFF)[261] for the low level of theory, with silicon, oxygen, aluminum, rubidium, and krypton being represented by the UFF atom types `Si3`, `O_3_z` (an oxygen type designed specifically for zeolites), `Al3`, `Rb`, and `Kr4+4`, respectively.

The high level of theory was DFT with either the local spin density approximation (LSDA, equivalent to the LDA for spin-paired systems) or the hybrid exchange–correlation functional B3LYP.[56,262,263] We used the 6-311G(d,p) triple-ζ basis set[264,265] for all elements except rubidium; we used the SDD basis set[57,266,267] for rubidium, and also ran a comparison using the SDD basis set for krypton as well. This method of using mixed basis sets was used previously by Sung et al.[268] for barium and Agarwal et al.[22] for rubidium and cesium in zeolites, and is necessary for "heavy" elements beyond the third row of the periodic table for which more common basis sets are unavailable. The choice of B3LYP/6-311G(d,p):UFF with the ONIOM method has been shown to yield reasonably accurate zeolitic geometries and vibrational frequencies, as well as proton jump rates.[19,256,269,270] Geometry optimizations were performed with no symmetry constraint for both transition and initial/final states using the "quadratic coupling" method of Vreven et al.[271,272] The Berny algorithm[273] was used to optimize to transition states, starting from an initial guess with the krypton or rubidium atom in the center of the six-membered ring and other atoms near their crystallographic positions. A frequency calculation was also performed for each transition state to verify that the quantum layer was optimized to a transition state (i.e., had only one imaginary frequency).

Figure 6.3 shows a snapshot of the siliceous sodalite cluster with a krypton atom, optimized to a transition state. We used the same cluster for rubidium. In the case of rubidium ion, one of the silicon atoms in the six-membered ring was substituted with aluminum, and the rubidium ion acted as an extra-framework cation.

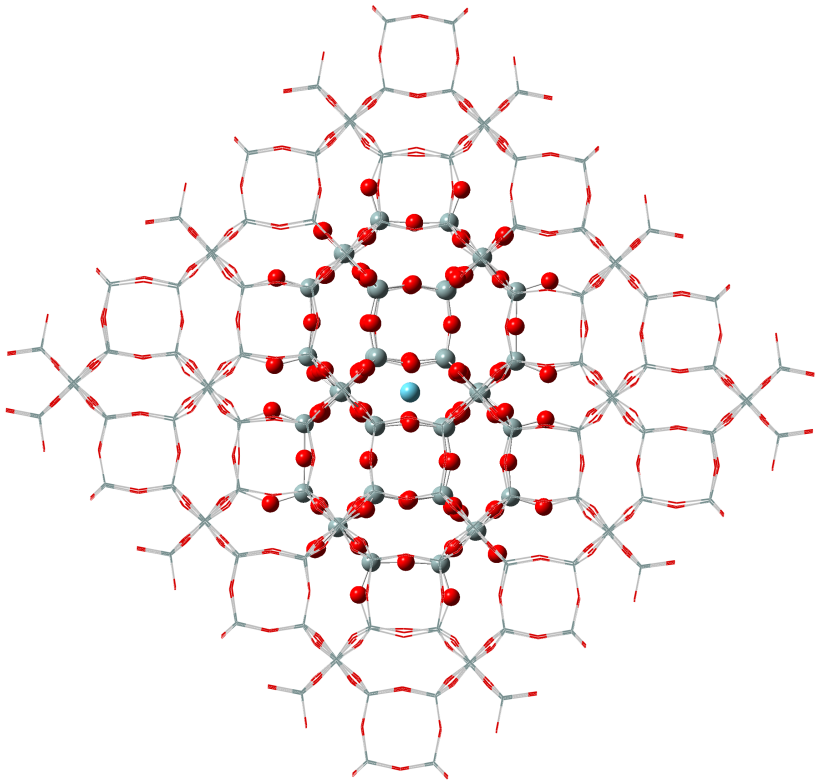

Figure 6.3. Snapshot of krypton (cyan) at its transition state in an ONIOM (layered) calculation as implemented in GAUSSIAN. The total system contains 378 T atoms. The high-level cluster containing 42 T atoms (two β-cages) is modeled with quantum-mechanical methods and is shown with balls and sticks. The low-level layer is modeled using UFF and is represented by wireframes. Silicon and oxygen atoms are gray and red, respectively.

6.3.3 Rate Estimation

Assuming that a jump through the six-membered ring of a sodalite cage is the rate-limiting step of krypton or rubidium migration in sodalite-like zeolites, a reasonably accurate estimate of the rate of diffusion can be approximated from classical transition state theory, originally developed for chemical reactions by Eyring, Polanyi, and Wigner[274–277] and extended to materials as described by Vineyard.[278] The diffusion coefficient of krypton or rubidium in zeolites can be described by $D = L^2\Gamma$, where L is a characteristic length and Γ is the rate of a jump.[279] Classical harmonic transition state theory gives the rate expression

$$\Gamma_{\mathrm{hTST}} = \frac{k_B T}{h} \frac{Q^{\ddagger}}{Q} \exp\left(\frac{-\Delta E_A}{k_B T}\right), \tag{6.3}$$

where Γ_{hTST} is the jump rate from harmonic transition state theory (hTST), k_B is the Boltzmann constant, T the absolute temperature at which diffusion occurs, and h is the Planck constant. The quantity ΔE_A is the difference between the ground state electronic energies of the transition state and the initial state; $Q^{\ddagger}$ and Q are the total vibrational partition functions of the transition state and initial state, respectively, with the normal mode in $Q^{\ddagger}$ associated with vibration of the transition state along the minimum-energy pathway removed. Expanding the partition functions in Equation 6.3 gives

$$\begin{aligned}
\Gamma_{\mathrm{hTST}} &= \frac{k_B T}{h} \left[\frac{\prod_{j=1}^{3N-4} \left(\frac{e^{-h\nu_j/2k_BT}}{1 - e^{-h\nu_j/k_BT}} \right)^{\ddagger}}{\prod_{i=1}^{3N-3} \left(\frac{e^{-h\nu_i/2k_BT}}{1 - e^{-h\nu_i/k_BT}} \right)} \right] \exp\left(\frac{-\Delta E_A}{k_B T}\right) \\
&= \frac{k_B T}{h} \left[\frac{\prod_{i=1}^{3N-3} \left(1 - e^{-h\nu_i/k_BT}\right)}{\prod_{j=1}^{3N-4} \left(1 - e^{-h\nu_j/k_BT}\right)^{\ddagger}} \right] \exp\left(\frac{-(\Delta E_A + \Delta E_{\mathrm{ZPE}})}{k_B T}\right),
\end{aligned} \tag{6.4}$$

where N is the number of atoms present in the system. The three translational modes are not included in the rate expression (and, given that the crystal is at rest, the frequencies of these

modes will be zero based on the acoustic sum rule[76]). The fourth mode excluded from the transition state (‡) terms corresponds to the "upside-down" well, which has an imaginary frequency and is associated with vibration of the transition state along the minimum-energy pathway to form the product state. The term ΔE_{ZPE} is the zero-point energy, and is the sum of all $\frac{1}{2}h\nu$ terms for each real-valued vibrational frequency in the transition state, minus similar terms from the initial state.

We computed the pre-exponential factor for the diffusion of krypton and rubidium in siliceous sodalite so as to confirm whether the NEB calculation had converged to a first-order saddle point (transition state) and to estimate the error associated with ignoring the terms in brackets in Equation 6.4. This requires a phonon calculation using density functional perturbation theory (DFPT)[212] at the center of the Brillouin zone (Γ point). The dynamical matrix and frequencies of the harmonic phonon modes were then generated based on the acoustic sum rule.[76] The criterion for self-consistency in the phonon calculations (`tr2_ph`) was set to 10^{-14} Ry.

6.4 Results and Discussion

With the goal of determining whether an encapsulated ^{85}Kr atom leaves the sodalite cage before or after it undergoes decay, we will explore several parameters, including calculation method, extra-framework cations and anions, and structure (i.e., sodalite vs. zeolite A), starting from the base case of siliceous sodalite, $[Si_{12}O_{24}]$-**SOD**. We expected, prior to this study, that the migration energies will be in the order $E_{A,\mathrm{Rb}} > E_{A,\mathrm{Kr}} > E_{A,\mathrm{Rb}^+}$ due to the relevant covalent or ionic radii, as shown in Figure 6.4. It should be noted that the ionic radii are scaled by a factor of $(\sqrt{5}-1)/2 \approx 0.6$ in the images, which makes it possible to see through the windows.

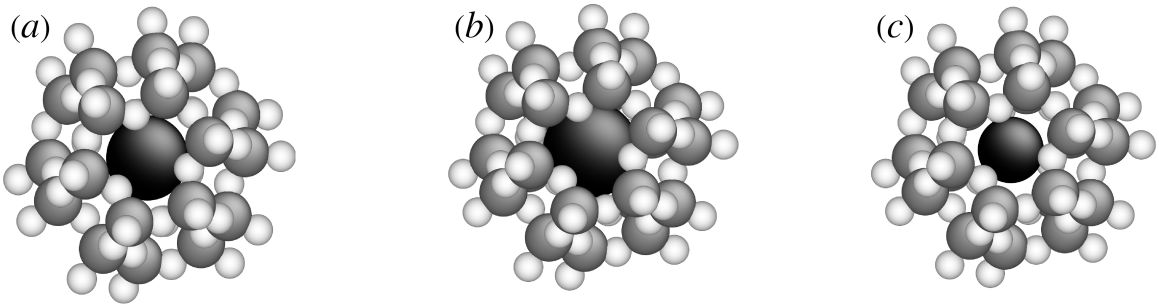

Figure 6.4. Space-filling representation of an entrapped species inside a siliceous sodalite cage. (*a*) entrapped krypton, (*b*) entrapped rubidium atom, and (*c*) entrapped rubidium ion. Images created with AtomEye.[280] The atoms' radii are scaled by 0.6 for clarity.

6.4.1 High-Silica and Siliceous Sodalite

Table 6.2 shows the calculated migration energies of krypton and rubidium in siliceous sodalite, as well as Rb^+ in high-silica sodalite. To model the diffusion of Rb^+, we substituted one silicon atom (belonging to the six-membered ring through which the jump occurs) with an aluminum atom. This way, rubidium behaves like an extra-framework cation, but is not impeded by the presence of other ions. As seen in Table 6.2, the migration energy of krypton is significantly higher than that of either rubidium atom or rubidium ion. This is somewhat counter-intuitive, because the van der Waals radius of rubidium atom is higher than that of krypton (3.21 Å for Rb and 2.25 Å for Kr). The reason for this result is the presence of the loosely-bound valence electron in rubidium, which is easily removed and shared between the oxygen atoms nearby. The loss of an electron causes the rubidium atom to behave more like Rb^+ (1.66 Å) while traversing the six-membered ring.

Based on the vibrational analysis, we calculated the product of the partition functions (the first bracketed term in Equation 6.4) for ^{85}Kr, ^{85}Rb, and $^{85}Rb^+$ in only siliceous (high-silica) sodalite. Following the same order as Table 6.2, these values are 1.030×10^{-4} for Kr, 0.159 for Rb, and 0.044 and 0.269 for Rb^+, respectively. Multiplying these values by the Boltzmann factor calculated in Table 6.2 (third column) will result in an even smaller

Table 6.2. Migration energies and approximate jump rates of Kr, Rb, and Rb^+ in high-silica sodalite calculated with norm-conserving pseudopotentials and the LDA.

Species[a]	E_A (eV)	E_A (kJ/mol)	$\frac{k_B T}{h} \exp(-E_A/k_B T)$ (s^{-1})[b]
Kr	1.923	185.541	1.94×10^{-20}
Rb	0.441	42.550	2.18×10^{5}
Rb^+	0.336, 0.160[c]	32.419, 15.438	1.30×10^{7}, 1.22×10^{10}

[a]The Rb^+ structure is all-silica except for one aluminum atom on the ring through which the ion jumps.

[b]The Boltzmann factor (last column) is calculated at $T = 298$ K.

[c]Multiple values indicate asymmetric migration pathways

rate for krypton compared to rubidium. In other words, it is even less likely for Kr to escape a sodalite cage than it would appear to be if we assumed $Q^{\ddagger}/Q \approx 1$.

6.4.2 Effect of Pseudopotential and Density Functional

Norm-conserving pseudopotentials with the LDA (NC-LDA) yield infrared spectra for sodalites that are in reasonable agreement with experiment.[41] However, the energetics associated with the LDA are known to be inaccurate, particularly for covalently-bonded compounds, so we examined other levels of theory to ensure the trend we saw for krypton vs. rubidium jumps in sodalite with NC-LDA held for more accurate functionals and different pseudopotentials.

Table 6.3 shows activation energies for krypton and rubidium jumping through a six-membered ring in sodalite calculated with norm-conserving pseuopotentials with the LDA (NC-LDA), norm-conserving pseudopotentials with the PBE functional (NC-PBE), LDA with ultra-soft pseudopotentials (ULT-LDA), and PBE with the projector augmented wave method (PAW-PBE).

Table 6.3 shows that all four psuedopotential/density functional combinations predict a significantly higher activation energy for krypton diffusion in siliceous sodalite than for rubidium diffusion. It is worth mentioning that the difference between krypton and rubidium

Table 6.3. Activation energies (in eV) of krypton and rubidium jumps through a six-membered in siliceous sodalite using different density functionals and pseudopotentials.

	Activation Energy (eV)			
Species	NC-LDA	NC-PBE	ULT-LDA	PAW-PBE
Kr	1.923	2.482	1.857	2.417
Rb	0.441	0.853	1.196	1.534

migration energies for norm-conserving pseudopotentials is similar (≈ 1.5 eV), whereas this difference is half of that for ultra-soft pseudopotentials and the PAW method.

We also did a calculation with the van der Waals effect[281,282] (`vdw_corr` parameter in Quantum ESPRESSO) turned on for the NC-LDA case. The only difference this effect had was to increase the values of the migration energies for all the species, resulting in having the same energy difference between Kr and Rb or Rb^+ (data not shown). However, the trend still remains the same.

6.4.3 Aluminosilicate Sodalite

Table 6.4 shows the activation energies of krypton and rubidium diffusion in aluminosilicate sodalite (sodalites with Si/Al = 1) with different combinations of extra-framework ions. In the anion-free cases, specifically those with sodium and potassium being the extra-framework cations ($|Na_6|[Si_6Al_6O_{12}]$-**SOD** and $|K_6|[Si_6Al_6O_{12}]$-**SOD**, respectively), not all cation sites are occupied, meaning that there are two cases to consider: (i) the encapsulated atom jumps through a six-membered ring that is partially blocked by an extra-framework cation, and (ii) the encapsulated atom jumps through an unblocked six-membered ring. We denote these two jumps $\mathbf{SOD}_{\mathrm{i}}$ and $\mathbf{SOD}_{\mathrm{ii}}$, respectively. To save space, only the cations are given in this section (e.g., $|Na_6|$-$\mathbf{SOD}_{\mathrm{i}}$ denotes a jump through a blocked six-membered ring in anion-free sodalite). The minimum energy pathway for rubidium in anion-free sodalites is different than the rest of the compounds in Table 6.4: due to the presence of two empty cation sites in anion-free sodalites, the diffusion of rubidium involves a jump from one site

in one cage to another site in the adjacent cage. Therefore, a $2 \times 1 \times 1$ supercell was used for rubidium in anion-free sodalites to avoid self-interaction issues. Because all the cation sites in chloro- and bromo-sodalites are occupied, the pathway is shorter and diffusion can be modeled with a single unit cell.

As seen in Table 6.4, the migration energy of krypton in $|Na_6|[Si_6Al_6O_{24}]$-**SOD**$_{ii}$ (empty ring) is slightly smaller than in siliceous sodalite ($[Si_{12}O_{24}]$-**SOD**). This is due to the fact that the inclusion of extra-framework cations expands the cell, thereby lowering the migration energy. Unsurprisingly, the migration energy in the $|Na_6|$-**SOD**$_{i}$ case is higher than in the $|Na_6|$-**SOD**$_{ii}$ case. This is expected, because krypton has to push a sodium cation out of the way in the former case. On the other hand, the migration energy of rubidium in both cases of $|Na_6|$-**SOD** is higher than in the siliceous case. This is due to the fact that in anion-free sodalite, rubidium travels from one cation site in one cage, through a six-membered ring, and finally sits on a cation site inside another cage; in contrast, in siliceous sodalite, the migration pathway is significantly shorter and involves only one six-membered ring. The barrier in case (i), a blocked window, is universally higher than that in case (ii), an open window. It is worth mentioning that the inclusion of cations with higher ionic radii (such as K^+) expands the cell, which reduces the activation energy for the diffusion of krypton. However, due to the Coulombic repulsion between rubidium and potassium ions, the activation energy of rubidium diffusion is higher for potassium-exchanged sodalite than for ordinary (sodium) sodalite. In chloro- and bromo-sodalites, all windows are blocked and there is less empty space within the cage, and therefore the migration energy for krypton (an inert gas) increases even more. However, due to the attractive forces between chloride or bromide ions and rubidium ions, the activation energy of rubidium diffusion decreases significantly, which is in agreement with a similar study done by Edgar et al.[283] in which the activation energy of sodium cations decreases in the presence of extra-framework chlorides in the sodalite cage.

Table 6.4. Migration energies (in eV) of krypton and rubidium in aluminosilicate sodalites with different extra-framework ions.

System[a]	Kr	Rb
$\|Na_6\|$-**SOD**$_i$	2.627, 2.647[b]	1.574
$\|Na_6\|$-**SOD**$_{ii}$	1.444, 1.464	0.767, 0.714
$\|K_6\|$-**SOD**$_i$	1.549	4.945
$\|K_6\|$-**SOD**$_{ii}$	1.129	0.938, 0.936
$\|Na_8Cl_2\|$-**SOD**	1.918	0.596
$\|Na_8Br_2\|$-**SOD**	2.089, 1.739	0.495

[a]In the anion-free cases (six cations per cell), diffusion can occur when (i) the six-ring is blocked and (ii) when the six-ring is empty; these are denoted $|X_6|$-**SOD**$_i$ and $|X_6|$-**SOD**$_{ii}$, respectively.

[b]Two values indicate an asymmetric migration pathway.

6.4.4 Siliceous Sodalite vs. Siliceous A

So far, we have been able to conclude that the migration energy of krypton is much higher than rubidium in both siliceous and aluminosilicate sodalites. However, zeolite getters used for krypton encapsulation are typically zeolite A (**LTA** framework), which shares the sodalite cage (β-cage) structure with the **SOD** framework but also contains larger α-cages. As a first step, we calculated the migration energies in siliceous A ($[Si_{24}O_{48}]$-**LTA**). Table 6.5 shows the migration energies for Kr, Rb, and Rb^+ in siliceous (or, for Rb^+, high-silica) sodalite and siliceous/high-silica zeolite A based on a single unit cell. It should be noted that in sodalite, diffusion occurs between two adjacent β-cages, whereas in zeolite A, it is between a β-cage and an adjacent α-cage. The migration energies of krypton in sodalite and zeolite A are similar, but those of Rb and Rb^+ are more sensitive to the framework topology. In addition, zeolite A always results in an asymmetric migration pathway because of the difference in geometry. The most important conclusion from Table 6.5 is that the migration energy for krypton is significantly higher than that of Rb and Rb^+ in siliceous A, a similar trend to that found for siliceous sodalite.

Table 6.5. Comparison between the migration energies (in eV) of Kr, Rb, and Rb^+ in siliceous sodalite (**SOD**) and siliceous zeolite A (**LTA**).

Species	**SOD**	**LTA**
Kr	1.923	1.852, 1.787 [a]
Rb	0.441	0.390, 0.222
Rb^+	0.336, 0.160	0.380, 0.116

[a]Two values indicate an asymmetric migration pathway. The larger number in the **LTA** case is the activation energy to escape the β-cage.

6.4.5 Zeolite A, Si/Al = 1 (Locally)

As discussed in the Introduction, siliceous zeolitic materials are poor choices for encapsulation because of their negative thermal expansion coefficients, and it is also much more common for natural and synthetic sodalite and zeolite A to have Si/Al = 1. The alternation between silicon and aluminum in zeolites complicates the description of the unit cell in zeolite A, because the structure would need to be two full unit cells in each Cartesian direction to produce a structure with Si/Al = 1 that did not violate Löwenstein's Rule. A DFT simulation of a full $2\times2\times2$ supercell is not tractable, so we instead created a $2\times1\times1$ supercell that is all-silica except for the six-membered ring connecting the β-cage containing the encapsulated species to the adjacent α-cage. In other words, only three (or, in the case of divalent cations, four) T-sites are replaced by aluminum, with the rest being silicon. Figure 6.5 shows a $2\times1\times1$ supercell of zeolite A (blue lines) with this substitution, along with one of its periodic images to complete the β-cage. We examined zeolites 3A (KA), 4A (NaA), and 5A (CaA); in the CaA case, only sites I and II are occupied, and there are four aluminum atoms instead of 3 because it is otherwise impossible to neutralize the entire supercell.

Table 6.6 shows krypton and rubidium migration energies for our modified zeolite A. There are different possible configurations as to where the extra-framework cations sit in NaA and KA, whereas there is only one possible configuration for CaA. Similar to the

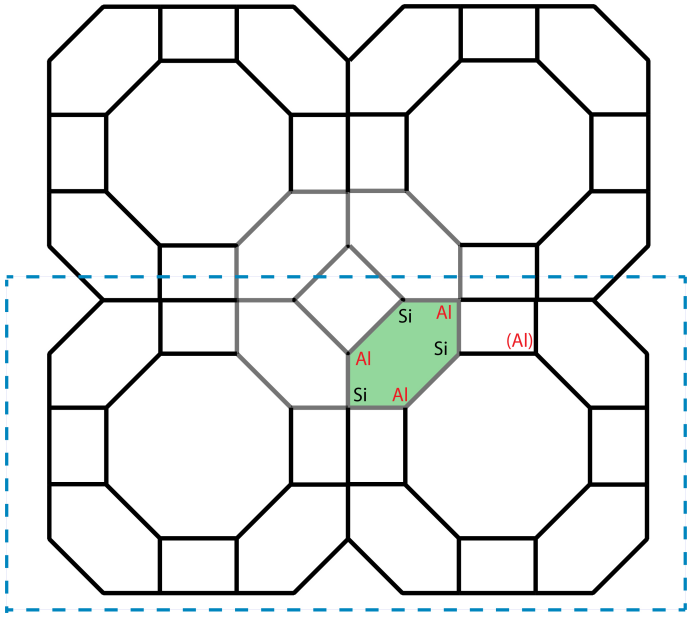

Figure 6.5. Schematic representation of modified zeolite A structure. A $2 \times 1 \times 1$ supercell (blue lines) is used in the simulation; the jump occurs across the green window in which the six-membered ring has an Si/Al = 1 when sodium and/or potassium are used as extra-framework cations. When calcium is the extra-framework cation, one extra silicon atom is substituted with an aluminum atom, denoted as (Al).

siliceous materials and to sodalite with Si/Al = 1, krypton has a higher migration energy in zeolite A compared to rubidium for all three cations.

It should be noted that the activation energies of krypton and rubidium diffusion in CaA (zeolite 5A) are both extremely high. The pre-exponential factors corresponding to the activation energies for escaping the β-cage, ignoring the partition function ratios (bracketed terms in Equation 6.4), are 1.26×10^{-51} s^{-1} for krypton and 2.61×10^{-32} s^{-1} for rubidium. While the rate of this jump would clearly be faster for rubidium than for krypton, the result of this calculation is that *neither* species should be able to traverse the six-membered ring "windows" in zeolite 5A. This raises the question of whether there is another mechanism present that we are missing (such as distortion of the β-cage structure due to the energy released by β^- decay), and even whether the rubidium that caused the corrosion observed experimentally came from ^{85}Kr that was encapsulated inside the β-cages in the first place.

Table 6.6. Migration energies (in eV) of krypton and rubidium in zeolite A with a local Si/Al ratio of 1.

		Cation Locations[a]			
Guest	Host	II, III, III	I, II, III	II, II, III	I, II
Kr	NaA	1.200, 1.198[b]	1.513, 1.511	1.087, 1.085	
Rb	NaA	0.306, 0.052	1.041, 0.832	0.265, 0.010	
Kr	KA	1.363, 1.361	1.747, 1.740	1.223, 1.211	
Rb	KA	0.351, 0.017	0.663, 0.432	0.359, 0.101	
Kr	CaA				3.766, 3.745
Rb	CaA				2.624, 2.218

[a]Cation sites are denoted by Roman numerals and are shown in Figure 6.1.
[b]Two numbers indicate an asymmetric migration pathway.

Certainly, the overwhelming evidence from these calculations is that if krypton is encapsulated inside the β-cages of zeolite 5A, it should not escape on human-observable time scales.

6.4.6 Comparison of Periodic and Cluster Models

This section investigates the difference between migration energies from plane-wave basis sets (periodic calculations) in Quantum ESPRESSO and calculations using cluster models in GAUSSIAN. The details of the calculations are discussed in Section 6.3.2.2. We calculated the migration energies of Kr, Rb in siliceous sodalite and Rb^+ in high-silica sodalite using both the local spin density approximation (LSDA) and the hybrid functional B3LYP. The results from this investigation are shown in Table 6.7. It is important to note that these are the results in which the quantum cluster size contains 42 T atoms (two adjacent β-cages). The migration energy of Kr is significantly higher compared to the migration energies of Rb and Rb^+, which is qualitatively consistent with the periodic calculations in previous sections. Although the results for the B3LYP functional seem to overestimate the migration energy in Table 6.7, it should be noted that in general, reaction barrier heights calculated with B3LYP are underestimated compared to the true values.[284] The trend from

Table 6.7. Activation energies (in eV) of Kr, Rb, and Rb^+ diffusion from cluster models of siliceous or high-silica sodalite.

		Density Functional	
Guest	Basis Set	LSDA	B3LYP
Kr	6-311G(d,p)	1.218	2.071
Kr	SDD	1.204	1.356
Rb	SDD	0.159, 0.160[a]	0.894
Rb^+	SDD	0.505, 0.495	0.827, 0.817

[a]Two values indicate an asymmetric migration pathway.

the cluster models is the same as in periodic models; that is, the activation energy of Kr diffusing through sodalite is higher than that for Rb and Rb^+.

6.5 Conclusions

We computed the activation energies associated with the diffusion of krypton and rubidium through sodalite and zeolite A using density functional theory and the nudged elastic band method. The motivation behind this study was to assess possible mechanisms of rubidium release from zeolite getters used to encapsulate ^{85}Kr for long-term storage. We found that the migration energy of krypton is significantly higher than that of rubidium, whether the framework is charged or not. Inclusion of extra-framework cations in anion-free sodalites decreases the migration energies for krypton, primarily due to the expansion of the unit cell. On the other hand, the migration energy of rubidium is higher in anion-free sodalites than their siliceous counterparts, and the presence of extra-framework anions increases the migration energy of krypton and decreases it for rubidium due to Coulombic interactions between rubidium and the extra-framework anions. Similar trends were observed for zeolite A, regardless of which extra-framework cations (Na^+, K^+, or Ca^{2+}) were present.

The trend $E_{A,\mathrm{Kr}} > E_{A,\mathrm{Rb}} > E_{A,\mathrm{Rb}^+}$ was unexpected because the relative sizes follow the order $r_{\mathrm{Rb}} > r_{\mathrm{Kr}} > r_{\mathrm{Rb}^+}$, but this trend is easily explained by the spreading out of the electron density associated with the loosely-bound valence electron of rubidium atom across the oxygen atoms nearby. Different density functionals and pseudopotentials or basis sets give qualitatively, though not quantitatively, similar results: the rate of rubidium permeation vastly exceeds that of krypton permeation.

The overall conclusion is that it is far more likely that ^{85}Kr decays *before* escaping from the β-cages of zeolite A, and rubidium subsequently leaves the zeolite structure and causes the corrosion observed in experiments. Using zeolites for encapsulating ^{85}Kr should therefore be considered with this mechanism in mind. Future work should investigate variables such as level of hydration, which may affect the migration energies of krypton and rubidium. It should be noted that the predicted rate of rubidium permeation in zeolite 5A (CaA), while still orders of magnitude faster than that of krypton, is extremely low, indicating that neither species should escape the β-cages of CaA. The fact that such release has been observed experimentally suggests that there may be another mechanism at play that we have not taken into account.

Acknowledgments

The computations for this chapter were performed on the high-performance computing infrastructure provided in part by Research Computing Support Services at the University of Missouri and in part by the National Science Foundation under grant number CNS-1429294.

CHAPTER 7

SUMMARY, CONCLUSIONS, AND FUTURE WORK

7.1 Zusammenfassung

The literal translation of the above word reads "summary". However, the word-by-word translation is zusammen (tying) and fassung (together).[(1)] Accordingly, the purpose of this chapter is to tie together the conclusions drawn from each chapter of this dissertation. To recap, the main goal of this dissertation was to study different properties of zeolites, specifically sodalite-like materials, by means of density functional theory (DFT) calculations with the following objectives: (1) construct a database of vibrational properties (i.e., infrared and Raman spectra), which can be used as a reference for other scientists/experimentalists, and (2) provide additional interpretations that are difficult if not impossible to acquire experimentally in zeolite science. We explored the first objective by predicting the vibrational spectra of sodalite structures in three distinct scenarios: (i) effect of Si/Al ratio, (ii) effect of extra-framework ions, and (iii) effect of framework substitution. For our second objective, we specifically looked into an experimental observation—corrosion of metal canisters used to encapsulate ^{85}Kr—with the help of DFT and the nudged elastic band (NEB) method. Below we summarize our findings for both objectives in turn.

7.1.1 Predicted Vibrational Spectra

In Chapter 3, we predicted the vibrational properties of siliceous and bromosodalites, from which we concluded that the results obtained by norm-conserving LDA were in good

[(1)] The choice of this German word was inspired by Ref. 285.

agreement with experimental infrared spectra of siliceous and bromosodalites. The presence of broad peaks in the infrared spectra led us to the second part of the study, in which we attempted to answer the question of whether defects in zeolites caused this broadening. We introduced defects by inserting silanol terminations in both siliceous sodalite and bromosodalite. Although these types of defects are not the only possible defects present in sodalite (or other zeolitic materials), the results in Chapter 3 showed that such defects can be responsible for the presence of broad peaks as well as additional bands in the measured spectra.

We then extended our inquiry to a wide range of sodalites with different extra-framework cations in Chapter 4. The initial purpose of this exploration was to develop a database of infrared and Raman spectra of virtually any possible theoretical sodalite. We capitalized on the unique structure of sodalite, which can incorporate cations only or cations and anions, as long as the framework is electrically neutral. In the process of constructing this database, we hypothesized that theoretical vibrational spectra were sensitive enough to detect certain heavy metals in water. The motivation behind this exploration lies in the ion exchange property of zeolites.[(2)] We hypothesized that if sodalite—in an ideal world—is ion exchanged with a water sample that is contaminated with cadmium, mercury, and lead, would there be a "signature" band associated with the presence of these contaminants. It turned out that for anion-free sodalites, there is a band in the 850–880 cm^{-1} range that is indicative of the presence of cadmium, mercury, and/or lead. It should be stressed that although DFT predicted this signature band, due to practical limitations of infrared spectroscopy, this signal will likely be obscured in an experiment. Therefore, we concluded that with the present instrumentation and spectroscopy techniques, this signature band might not be a reliable indicator of the presence of heavy metals captured by sodalite. Nevertheless, our infrared and

[(2)] Among different zeolites, sodalite is not the best candidate for ion exchange processes, as the windows are small and ion exchange is consequently slow. However, from the computational point of view, it was the best structure to carry out all the "heavy" calculations with.

Raman database remains valuable and can always serve as a reference for experimentalists to compare their results.

In Chapter 5, we developed a database of aluminate sodalites, which have the same framework as aluminosilicate sodalite but only contain $[AlO_4]^-$ tetrahedra. One of the interesting properties of these materials is that they disobey Löwenstein's aluminum avoidance rule. In addition, their ability to incorporate different types of anions opens up applications in the areas of electronic materials and optics. Despite having potential applications, the (spectroscopic) literature for these materials is sparse. We calculated the structural properties as well as the vibrational spectra (i.e., infrared and Raman spectra) for aluminate sodalites that have been previously synthesized. The results from DFT were in good agreement with the available literature. In addition, we observed the sensitivity of asymmetric stretching modes with respect to cell size; that is, the higher the cell volume, the more the asymmetric stretching vibrational mode experiences a blue shift. Furthermore, the E–O vibrational mode's frequency, where E is an anion, was also systematically described by the type of bond and the masses involved.

7.1.2 Gas Encapsulation

The motivation behind this work was to test three possible mechanisms that resulted in the corrosion of canisters used in the 1970s to entrap ^{85}Kr at Idaho National Laboratory. We first compared the activation energies of krypton, rubidium, and rubidium ion diffusion in siliceous and aluminosilicate sodalites. The results for siliceous sodalite showed that the activation energy associated with the diffusion of krypton was significantly higher than that of both rubidium and rubidium ion. Inclusion of extra-framework cations into the anion-free sodalite structure decreases the activation energy of Kr diffusion, primarily due to the expansion of the cell. On the other hand, the activation energy of Rb is higher in anion-free sodalites than in their siliceous counterparts (though still lower than Kr) because the minimum energy pathway for rubidium in anion-free sodalites involves a complex,

high-activation-energy pathway. The presence of extra-framework anions increases the activation energy for krypton, whereas for rubidium, this energy barrier decreases due the Coulombic interactions between rubidium and the extra-framework anions. In order to find the correct mechanism, we then investigated this comparison in siliceous A and a modified zeolite A (4A, 3A, and 5A). Similar trends were observed for the **LTA** framework: the activation energy associated with diffusion of krypton through the windows of sodalite cage is higher than the activation energy of rubidium diffusion.

The reason why krypton has a higher activation energy than rubidium can be attributed in part to the difference between the radii of these species. Due to the electronegative nature of oxygen atoms in the zeolite framework as well as the presence of one loose electron in the valence shell of rubidium, upon diffusion, a rubidium atom loses and/or shares the unpaired electron. This causes the radius of rubidium to be as small as 1.66 Å, whereas the van der Waals radius of krypton is 2.25 Å. Embedded cluster calculations, as implemented in GAUSSIAN, predicted the same trends as periodic plane-wave calculations with Quantum ESPRESSO. The activation energies of both krypton and rubidium for the modified zeolite 5A are high, meaning that neither krypton nor rubidium should escape the structure on a human-observable time scale.

Based on the results of this study, we conclude that the following mechanism might be responsible for the observed corrosion of canisters used at INL for ^{85}Kr entrapment: krypton remains captured inside the zeolite; it decays to rubidium with a half-life of 10.8 years, and rubidium (or rubidium ion) leaves the zeolite structure and causes the corrosion. Therefore, using zeolites for storing ^{85}Kr should have further consideration of the decay product, corrosive rubidium.

7.2 Suggested Future Directions

By the end of this dissertation, we envision different routes one can follow. I outline suggestions for future work below, specifically based on the conclusions of this dissertation.

7.2.1 Extending a Database

With the help of computational power as well as improvements in first-principles theories/algorithms, one suggestion is to extend a database of infrared and Raman spectra of industrially important zeolites as well as with different possible combinations of extra-framework and adsorbate species occluded inside them. Scientists in the community, either from experimental or theoretical groups, can benefit from such databases as benchmarks for their results. In addition, these databases can serve in the areas of materials design, in which large data sets can be used in neural networks (NN) for the purpose of materials (in our case, zeolite) discovery.

7.2.2 Wastewater Treatment

Although the results from our theoretical investigations in Chapter 4 provided useful information about the presence of heavy metals in sodalite, detecting heavy metals with sodalites combined with infrared spectroscopy might not be feasible in practice, as the infrared signal is not easy to differentiate from other signals likely to be present. Looking back at the study, however, some suggestions using zeolites can be made, specifically in the area of wastewater treatment/heavy metals removal. One suggestion, for example, would be to use zeolites with larger pores such as clinoptilolite, chabazite, or mordenite. Another suggestion is to conduct similar studies in which there are some water molecules present within the structure to consider a more realistic model than anhydrous zeolite.

7.2.3 Krypton-85 Immobilization

As mentioned in Section 7.1.2, DFT predicted that although zeolite A and sodalite should entrap krypton, these getters might not hold the decay product, rubidium. This conclusion was drawn using a modified zeolite A structure with $\mathrm{Si/Al} = 1$ locally. One suggestion would be to conduct a similar study using the actual unit cell of zeolite A with $\mathrm{Si/Al} = 1$, which is the same size as a $2 \times 2 \times 2$ unit cell of siliceous A. One might also explore the effects of compositional variation/substitution on zeolite A used as a krypton

getter. For instance, instead of using common extra-framework cations (Na, K, etc.), one can explore the effect of other cations. Another suggestion to tackle this challenge would be to use aluminate sodalites. These sodalites can have divalent cations in the framework, resulting in a crowded structure which might hinder the escape of rubidium.

7.3 Schluss

In a nutshell, zeolites are interesting materials because of their unique structural properties, which allow them to selectively incorporate certain species. The scientific research on these materials are nearing almost a century since the work of the father of synthetic zeolites, Richard Barrer, and new breakthroughs are being made at a significant pace. Most advancements are either targeted at the discovery of new zeolitic materials that possess certain properties (optical, magnetic, vibrational, etc.), or towards optimizing existing zeolites for new applications. Relying solely on experimental research might lack accuracy and may come at a price, hindering progress. Employing computational techniques along with experimental research paves the road to more efficient research, ultimately resulting in further development.

APPENDIX A

COMMON SYNTHESIS AND CHARACTERIZATION TECHNIQUES

Although this dissertation is mainly focused on the computational aspects of zeolites, it is worth explaining to some extent the common experimental synthesis and characterization techniques in zeolites.

A.1 Synthesis

A.1.1 Zeolites

From the economic and environmental aspects, it is beneficiary to use natural waste/ substances to synthesize zeolites. These materials vary from clay minerals, volcanic glasses to fly ash, rice husk, etc. Zeolites synthesized from materials, of course, cannot be used for certain commercial applications since they are not pure enough. Therefore, there will always be a demand for synthetic zeolites. As of 2020, different methods are used to synthesize zeolites. The most common ones are hydrothermal syntheses, the molten salt method, the fusion method, alkali metal activation, microwave-assisted syntheses, and syntheses via dialysis.[286] The hydrothermal method is the most common one used in zeolite synthesis. In Chapters 3 and Appendix B, we discussed the details of these methods. For the detailed information of other methods, the interested reader is referred to Refs 287–291.

A.1.2 Aluminate Sodalites

The synthesis of aluminate sodalites is pretty straightforward, as long as a stoichiometric mixture of the analytical components is used. Here we discuss the sample preparation

of calcium sulfate aluminate sodalite, $|Ca_8(SO_4)_2|[Al_{12}O_{24}]$-**SOD**. The initial components are calcite ($CaCO_3$), aluminum oxide (Al_2O_3), and gypsum ($CaSO_4 \cdot 2\,H_2O$), which usually are ground for 1 h in an agate mortar with ethanol to become powder. Next, the resulting powder is pelletized (on the order of 20 mm in diameters) and is heated ($\approx$ 1300°C) for 4 h. Finally, it has to be slowly cooled.[209,292]

A.2 X-Ray Diffraction

In this characterization technique, the sample is placed at the center of the instrument and is irradiated by beams of X-rays. The setup consists of an X-ray tube and a detector tube, both moving in a synchronized fashion. The beam scattered off the sample is recorded in a graph by peaks which are related to the atomic structure of the sample. When a sample is shined by X-rays, a special interference effect occurs that can be used to measure the distance between the atoms.[(1)] The equation that holds the relation between the scattered wavelengths and the distance between the crystal planes in a structure can be written as

$$n\lambda = 2d \sin\theta, \tag{A.1}$$

where d is the space between the planes, λ is the wavelength of the incident light, and θ is the angle between the beam source and the sample. Equation A.1 is also known as Bragg's Law. Figure A.1 illustrates the whole concept of XRD and its theory. In zeolite science, XRD helps to identify whether the sample contains any crystalline phases or not, it also provides information on lattice constant, atomic positions, symmetry, and other useful information. For a comprehensive description of XRD technique in zeolites, please check the book Zeolite Characterization and Catalysis-A Tutorial by Chester and Derouane.[293]

[(1)] Interference occurs when scattered X-rays interact with each other in two ways. If the scattered waves are in alignment, the scattered signal is amplified, which is called constructive interference. If the scattered waves are not in alignment, the signal is destroyed, which is called destructive interference.

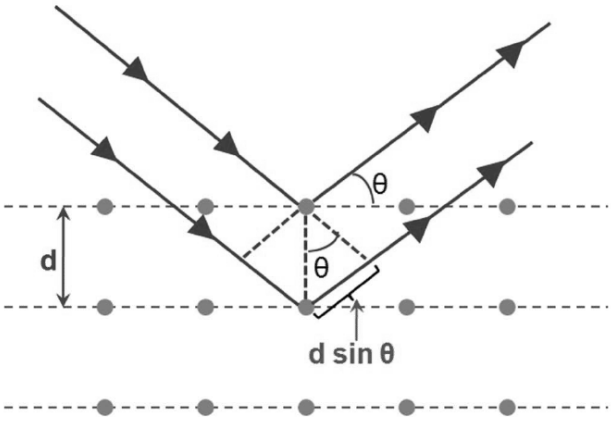

Figure A.1. Schematic of Bragg's law, reprinted with permission from Ref. 294.

A.3 Solid-State Nuclear Magnetic Resonance

Although XRD can provide insights about the periodic structure of a crystalline lattice, nuclear magnetic resonance (NMR) spectroscopy can be used as an analytical tool with a high sensitivity for chemical bonds in the local structure of the resonating nuclei—framework atoms, extra-framework species, adsorbate complexes, and surface sites—in zeolites. The phenomenon of NMR, which was discovered by Bloch and Purcell,[295,296] relies on the fact some of the atoms in zeolites possess isotopes with nuclear spin, making these nuclei "NMR-active." ^{1}H, ^{11}B, ^{17}O, ^{27}Al, ^{29}Si, ^{31}P, ^{51}V, ^{67}Zn, and ^{71}Ga are some of the common isotopes in zeolite science used for NMR spectroscopy.[293] To characterize surface OH groups as well as extra-framework cations, ^{1}H, ^{7}Li, ^{23}Na, and ^{133}Cs NMR are used. In addition, ^{29}Si and ^{27}Al are used for Si/Al ratio estimation and extra-framework aluminum characterization, respectively. More information on NMR in zeolites can be found in Ref. 297.

A.4 Infrared and Raman Spectroscopy

Infrared: The theory behind infrared (IR) spectroscopy is that a vibration belonging to a molecule or solid should undergo an excitation upon interacting with infrared light.

In order for the excitation to be detectable, the vibration itself should change the dipole moment. In other words, if the dipole moment of a specific vibration (called a vibrational mode) changes during the vibration, that vibrational mode will be visible in the IR spectrum and is called IR-active. A hetero nuclear diatomic molecule such as CO has only one vibrational mode and is IR-active, whereas, for the homo diatomic molecule N_2, the vibrational mode is IR inactive.

There are three main vibrational modes associated with a three-body entity: asymmetric stretching, symmetric stretching, and bending modes. [(2)] There are $3N - 5$ and $3N - 6$ vibrational modes for a linear and nonlinear triatomic molecule, respectively, N being the total numbers of atoms.

Each vibration has a frequency (ν) associated with it and is usually described using a harmonic oscillator:

$$\nu = \frac{1}{2\pi}\sqrt{\frac{k}{\mu}}, \tag{A.2}$$

where k is the force constant and μ is the reduced mass, defined by $\mu = \frac{m_1 m_2}{m_1 + m_2}$ between two atoms with masses m_1 and m_2.

Raman: Raman spectroscopy is another characterization technique in which the theory lies in the vibrational energy level of a system. However, the principle in Raman spectroscopy is that the polarizability of a molecule should change upon interacting with light. Most of the modes that are IR-inactive can be observed in the Raman spectra. Although it is a useful technique in terms of providing insights into the structure of a sample, acquiring Raman spectra for zeolites is xa hard task, primarily due to the strong fluorescence background.

[(2)] Wagging, scissoring, twisting, and rocking are other types of bending modes.

A.5 EDX

Energy dispersive X-ray (EDX) analysis, also known as EDS,[3] is an X-ray technique to identify elemental composition of materials.[4] EDX systems are part of electron microscopy instruments[5] in which beams of electrons excite the atoms belonging to the surface of the specimen. The excited atoms then emit specific wavelengths of X-rays that are characteristic of the atomic structure of the elements. The spectra generated by EDX consists of certain peaks associated with certain elements with their composition.

A.6 Thermal Gravimetric Analysis (TGA)

Zeolites must be activated (heated) before their use. The activation process takes place by heating zeolites under vacuum.[6] Thermal gravimetric analysis (TGA) is a useful technique to find the required temperature to desorb species from zeolites. In other words, TGA allows to measure the mass of a sample as a function of temperature or time.[7] Some zeolites exhibit continuous mass loss with increasing temperature, such as analcime and natrolite. However, laumonite and heulandite show distinct steps in this process.[298] A typical setup starts with placing a zeolite sample into a ceramic crucible on a sensitive microbalance. The crucible is controlled by a computer oven in which a flowing gas stream controls the background atmosphere. To overcome the problem of oxidation, nitrogen is usually used.

[3] EDS refers to energy dispersive spectroscopy, EDX refers to energy dispersive X-ray analysis.

[4] The amount of sample needed for the experiment is as small as few cubic micrometers.

[5] Scanning electron microscope (SEM), transmission electron microscope (TEM), scanning and transmission electron microscopy (STEM), etc.

[6] The activation process is similar to that of regenerating zeolites.

[7] TGA is not necessarily associated with heating of materials. Sometimes the sample is also cooled down.

APPENDIX B

SUPPORTING INFORMATION OF CHAPTER 4

B.1 Experimental Design and Characterization

B.1.1 Synthesis

B.1.1.1 Materials and Equipment

All reagents listed in the experimental procedures were used as-received, without further purification. All deionized water was sourced from an Elga Purelab Ultra® water deionizer at 13–15 MΩ. All Teflon® equipment was cleaned prior to use by first soaking in an HF bath for at least 24 h before being washed with deionized water followed by acetone. A Fisher Scientific Isotemp magnetic stirring hot plate was used for all stirring and or heating steps that specify use of a hot plate. A Thermo Scientific Heratherm OGH180 Advanced Protocol Oven was used for all steps that specify the use of an oven.

B.1.1.2 Sodium Bromosodalite

We hydrothermally synthesized sodium bromosodalite according to the procedures presented by Stein et al.[164] First, 10.060 g of Fisher Chemical certified ACS NaOH pellets (> 97%) and 3.912 g of Sigma-Aldrich reagent grade $Al(OH)_3$ powder (50.0–57.5% Al_2O_3) were combined with 50 mL deionized water in a 500 mL polyethylene bottle. The mixture was heated to 95°C and stirred at 350 RPM on a hot plate until dissolved. In a separate 500 mL polyethylene bottle, 15.042 g of Fisher Chemical certified ACS NaOH pellets (> 97%), 38.583 g of Sigma-Aldrich ReagentPlus® NaBr powder (>99%), and 75 mL of

deionized water were combined and stirred at 350 RPM on a hot plate until dissolved. Next, 7.516 g of Ludox® HS-40 colloidal silica (40 wt.% silica suspension in H_2O) was added to the bromide mixture before heating the mixture to 95°C while stirring at 350 RPM on a hot plate. The two solutions were combined, sealed, and shaken vigorously by hand for 5 min before being transferred to Teflon®-lined Parr Autoclaves. The autoclaves were then paced in the oven at 90°C for 24 h to promote the formation of sodalite crystals. The autoclaves were removed from the oven and cooled to ambient temperature before recovering the sodalite crystals by vacuum filtration using Whatman® 125 mm Grade 1 qualitative filter paper (11 μm particle retention). After recovery, the sodalite crystals were left in the Büchner funnel and washed with 750 mL deionized water to remove excess NaOH and NaBr. Washing was done 150 mL at a time and repeated until the filtrate pH fell below 8 using MilliporeSigma colorpHast® pH-indicator strips. The washed sample was left to dry on the filter paper under ambient conditions for 24 h before being transferred to a Teflon® petri dish and dried in an oven at 110°C for 24 h to remove excess moisture. The finished product weight was 5.725 g, achieving 67.35% of the maximum theoretical yield. Each sodium bromosodalite sample was ground with a mortar and pestle and analyzed before being used to produce the subsequent ion-exchanged samples.

B.1.1.3 Potassium chlorosodalite

Synthesis of potassium chlorosodalite by a similar procedure to the sodium bromosodalite synthesis described above was also attempted. Nearly the same procedure was followed, but with the sodium-containing reagents replaced with potassium-containing reagents to determine if sodium is pertinent to the formation of the sodalite phase by hydrothermal methods. Therefore, we used KOH, $Al(OH)_3$, KCl, colloidal silica (40% SiO_2), and deionized water as reagents. First, 14.058 g of Fisher Chemical certified ACS KOH pellets (>85.0%) and 3.925 g of Sigma-Aldrich reagent grade $Al(OH)_3$ powder (50.0–57.5% Al_2O_3) were combined with 50 mL deionized water in a clean 500 mL polyethylene bottle.

The mixture was heated to 95°C and stirred at 350 RPM on a hot plate until dissolved. In a separate clean 500 mL polyethylene bottle, 21.036 g of Fisher Chemical certified ACS KOH pellets (> 85.0%), 27.948 g of J.T. Baker 'Baker Analyzed' ® Reagent KCl crystal (99.8%), and 75 mL of deionized water were combined and stirred at 350 RPM on a hot plate until dissolved. Next, 7.473 g of Ludox® HS-40 colloidal silica (40 wt.% silica suspension in H_2O) was added to the chloride mixture before heating the mixture to 95°C while stirring at 350 RPM on a hot plate. The two solutions were then sealed and shaken vigorously by hand for 5 min before being transferred to Teflon® lined Parr Autoclaves. The autoclaves were placed in an oven at 95°C for 47 h in order to promote the formation of sodalite crystals. The autoclaves were then removed from the oven and cooled to ambient temperature before washing the sodalite crystals with deionized water to remove excess KOH and KCl. The washing procedure was done using a centrifuge in an effort to reduce the time required to wash the crystals. This was done by first mixing the contents of the autoclaves with 300 mL of deionized water in a 500 mL polyethylene bottle and stirring at 700 RPM for 10 minutes. This mixture was transferred to 50 mL centrifuge tubes and centrifuged in a Jouan BR4i centrifuge at 6000 RPM for 10 minutes. The liquid from each centrifuge tube was decanted off, and fresh 300 mL of deionized water was added. The tubes were shaken vigorously by hand before being centrifuged again at 6000 RPM for 10 minutes. This process was repeated until the pH of the liquid fell below 8 using MilliporeSigma colorpHast® pH-indicator strips, which happened after seven cycles. The washed sample was then recovered by vacuum filtration using Whatman® 125 mm Grade 1 qualitative filter paper (11 μm particle retention). The sample was then left to dry on the filter paper under ambient conditions for 24 h before being transferred to a Teflon® petri dish and dried in an oven at 100°C for 24 h to remove excess moisture. The finished product weight was 6.490 g, achieving 73.57 percent of the maximum theoretical yield. The X-ray pattern (Figure 4.2(f)) indicates that the resulting material was not sodalite, so samples from this synthesis were not used for ion exchange.

B.1.2 Ion Exchange

B.1.2.1 Sodium Bromosodalite

The sodium bromosodalite samples were subjected to various ion exchange procedures to exchange their extra-framework Na^+ ions with Pb^{2+}, K^+, Ag^+, or Li^+. The exchange procedure for lead bromosodalite was done in accordance with the procedure described by Eiden-Assmann.[178] For lead exchange, a 0.1 M $Pb(NO_3)_2$ solution was first prepared by weighing 3.317 g of Sigma-Aldrich L6285 lead(II) nitrate powder (> 98.0%) into a 100 mL volumetric flask and filling to the 100 mL mark with deionized water. Next, 0.468 g of the synthesized sodium bromosodalite sample was placed in a 23 mL Teflon®-lined Parr Autoclave and 18 mL of the 0.1 M $Pb(NO_3)_2$ solution were added. This process was repeated for a total of four autoclaves. Note that the solution was made so as to contain the exact stoichiometric amount of lead required for full exchange with the extra-framework Na^+ ions, in an attempt to prevent damage to the sodalite framework that may be caused by excess lead.[178] The sealed autoclaves were placed in an oven at 110°C for 24 h before being removed and cooled to ambient temperature. The sodalite crystals were recovered by vacuum filtration using Whatman® 125 mm Grade 1 qualitative filter paper (11 μm particle retention). After recovery, the sodalite crystals were left in the vacuum filtration setup and washed with 500 mL deionized water to remove sodium ions and excess $Pb(NO_3)_2$. The washed sample was left to dry on the filter paper in ambient conditions for 24 h before being transferred to a Teflon® petri dish and dried in an oven at 60°C for 24 h. The final weight of the lead-exchanged sodalite sample was 2.052 g, representing a 9.8% increase in weight.

B.1.2.2 Potassium Bromosodalite

The exchange procedure for potassium bromosodalite was done in accordance with the procedure described by Aprea et al.[163] For potassium exchange, a 1 M KNO_3 solution was first prepared by weighing 10.117 g of Sigma-Aldrich puriss. KNO_3 powder (>99.0%) into

a 100 mL volumetric flask and filling to the 100 mL mark with deionized water. Next, 2.006 g of the synthesized sodium bromosodalite sample were placed in a sealable 500 mL polyethylene bottle along with 100 mL of the 1M KNO_3 solution. Note that the exchange solution was prepared to contain excess potassium, as this was expected to produce a desirable extent of exchange without adverse effects on the sodalite structure.[163] The container was sealed and stirred continuously at 700 RPM and ambient temperature for 24 h on a Fisher Scientific Isotemp magnetic stirring hot plate. The sodalite was then recovered by vacuum filtration using Whatman® 125 mm Grade 1 qualitative filter paper (11 μm particle retention). The sample was placed in a clean sealable 500 mL polyethylene bottle along with 100 mL of freshly-made 1M KNO_3 solution in an attempt to drive equilibrium towards higher potassium ion concentrations within the sodalite framework. The process was repeated for a total of three 24 h agitated ion exchange cycles at room temperature. After the third filtration, the sample was washed with 350 mL deionized water to remove sodium and excess KNO_3. The washed sample was left to dry on the filter paper under ambient conditions for 24 h before being transferred to a Teflon® petri dish and dried in an oven at 80°C for 24 h. The finished product weight was 1.679 g, representing a 16.3% decrease in weight.

B.1.2.3 Silver Bromosodalite

The exchange of silver bromosodalite followed the procedure described by Borhade et al.[299] For silver exchange, sodium bromosodalite was combined with 1 M $AgNO_3$ solution in an autoclave at elevated temperature. Note that the mixture was prepared so as to contain the exact stoichiometric amount of silver required for full exchange with the extra-framework sodium ions. This was done in an attempt to prevent the precipitation of silver. All steps of the silver exchange were performed in the dark to avoid the reduction of silver ion to silver metal. First, 2.635 g of Sigma-Aldrich 99.9999% trace metal basis $AgNO_3$ and 2.000 g of the synthesized sodium bromosodalite were combined with 15.5 mL

of deionized water in a 23 mL Teflon®-lined Parr Autoclave. The autoclave was sealed and shaken vigorously by hand before being placed in the oven at 100°C for 48 h. The autoclaves were removed from the oven and cooled to ambient temperature before recovering the sodalite crystals by vacuum filtration using Whatman® 125 mm Grade 1 qualitative filter paper (11 μm particle retention). Note at this point that the sample was completely black, indicating reaction of some of the silver ions to form silver oxide. After recovery, the sample was left in the vacuum filtration setup (Buchner funnel) and washed with 450 mL deionized water to remove excess Na and $AgNO_3$. The washed sample was left to dry on the filter paper in ambient conditions for 24 h before being ground with a mortar and pestle and transferred to a Teflon® petri dish to dry in the oven at 100°C for 24 h. The finished product was stored in an opaque black sample vial.

B.1.2.4 Lithium Bromosodalite

The exchange procedure for lithium bromosodalite was done in accordance with the procedure described by Aprea et al.[163] For lithium exchange, a 1 M $LiNO_3$ solution was first prepared by weighing 6.898 g of J. T. Baker 'Baker Analyzed'® Reagent $LiNO_3$ crystal (98.2%) into a 100 mL volumetric flask and filling to the 100 mL mark with deionized water. Next, 2.001 g of the synthesized sodium bromosodalite sample was placed in a sealable 500 mL polyethylene bottle along with 100 mL of the 1M $LiNO_3$ solution. Note the exchange solution was prepared to contain excess lithium, as this was expected to produce a desirable extent of exchange without adverse effects on the sodalite structure. The container was sealed and stirred continuously at 700 RPM and ambient temperature for 24 h on a Fisher Scientific Isotemp magnetic stirring hot plate. The sodalite was then recovered by centrifuging in a Jouan BR4i centrifuge at 6000 RPM for 10 min and decanting off the ion exchange solution. The sample was placed in a clean sealable 500 mL polyethylene bottle along with 100 mL of freshly made 1 M $LiNO_3$ solution. The process was repeated for a total of three 24 h agitated ion exchange cycles at room temperature. After the third ex-

change, the sample was recovered by vacuum filtration using Whatman® 125 mm Grade 1 qualitative filter paper (11 μm particle retention) The sample was left in the vacuum filtration setup and washed with 200 mL deionized water to remove sodium and excess $LiNO_3$. The washed sample was left on the filter paper and dried in the oven at 80°C for 1.5 h before being ground in a mortar and pestle and again washed in the vacuum filtration setup with an additional 250 mL of deionized water. The washed sample was then left to dry on the filter paper in ambient conditions for 24 h before being transferred to a Teflon® petri dish and dried in an oven at 60°C for 24 h to remove excess moisture.

B.1.3 Characterization

X-ray diffraction (XRD) patterns were collected under ambient conditions, with each sample on a zero-background glass slide. Data were collected using a diffractometer (Rigaku UltimaIV, 40 kV, 44 mA) with a Cu-K_α source (average wavelength 0.154 nm) over the range of $10° < 2\theta < 50°$ with a step size of 0.05° and scan rate of 2°/min. The XRD data are shown in Figure 4.2.

Compositional analysis of the parent material, $|Na_8Br_2|$-**SOD**, cation-exchanged samples (Li, K, Ag, Pb), and $|K_8Cl_2|$-**SOD** material were conducted using an energy-dispersive X-ray (EDX) spectrometer (Bruker Quantax 200 Silicon Drift Detector with Xflash6) operated at 20 kV and 1.6 nA. The results are shown in Table 4.2.

Fourier transform infrared (FTIR) spectra of all samples were recorded using a Nicolet 4700 FT-IR spectrometer with a scan range of 400–4000 cm^{-1} by pelleting the powdered sodalite sample with KBr (5 mg sodalite mixed with 70 mg KBr) into 10 mm pellets using a hand-held Thermo Fisher pellet press. The results are shown in Figure 4.3.

BIBLIOGRAPHY

1. Hammond, K. D. Quantifying Defects in Zeolites and Zeolite Membranes. Ph.D. Dissertation, University of Massachusetts Amherst, 2010.

2. Barthelmy, D. Mineralogy Database. 2014; `http://webmineral.com/`.

3. Baerlocher Ch. and McCusker L. B., Database of Zeolite Structures. `http://iza-structure.org/databases/`.

4. Inglezakis, V. J.; Zorpas, A. A. *Handbook of Natural Zeolites*; Bentham Science Publishers, 2012.

5. Barr, T. L. The Nature of the Relative Bonding Chemistry in Zeolites: An XPS Study. *Zeolites* **1990**, *10*, 760–765.

6. Sánchez, A. G. Computational Study of Adsorption and Diffusion in Zeolites with Cations. Doctoral Dissertation, Universidad Pablo de Olavide, 2011.

7. Auerbach, S. M.; Carrado, K. A.; Dutta, P. K. *Handbook of Zeolite Science and Technology*; CRC Press: New York, 2003.

8. Masoudian, S. K.; Sadighi, S.; Abbasi, A. Synthesis and Characterization of High Aluminum Zeolite X from Technical Grade Materials. *Bull. Chem. React. Eng. Catal.* **2013**, *8*, 54.

9. Hunt, H. K. I. Development of Facile Route to Fluoride-Mediated, Pure-Silica Zeolite Thin Films II. Removal of Structure-Directing Agents from Molecular Sieves via the Use of Photolabile Structure-directing Agents. Ph.D. Dissertation, California Institute of Technology, 2010.

10. Barrer, R. Chemical Nomenclature and Formulation of Compositions of Synthetic and Natural Zeolites. *Pure Appl. Chem.* **1979**, *51*, 1091–1100.

11. Baerlocher, C.; Meier, W.; D.H, O. *Atlas Of Zeolite Framework Types*, 6th ed.; Elsevier, 2007.

12. Loewenstein, W. The Distribution of Aluminum in the Tetrahedra of Silicates and Aluminates. *Am. Mineral.* **1954**, *39*, 92–96.

13. Kaiheriman, M.; Maimaitinaisier, A.; Rehiman, A.; Sidike, A. Photoluminescence Properties of Green and Red Luminescence from Natural and Heat-Treated Sodalite. *Phys. Chem. Mineral.* **2014**, *41*, 227–235.

14. Hassib, A.; Beckman, O.; Annersten, H. Photochromic Properties of Natural Sodalite. *J. Phys. D Appl. Phys.* **1977**, *10*, 771–777.

15. Maeda, Y.; Wakamatsu, T.; Konishi, A.; Moriwake, H.; Moriyoshi, C.; Kuroiwa, Y.; Tanabe, K.; Terasaki, I.; Taniguchi, H. Improper Ferroelectricity in Stuffed Aluminate Sodalites for Pyroelectric Energy Harvesting. *Phys. Rev. Appl.* **2017**, *7*, 034012–034020.

16. McCusker, L.; Liebau, F.; Engelhardt, G. Nomenclature of Structural and Compositional Characteristics of Ordered Microporous and Mesoporous Materials with Inorganic Hosts: (IUPAC Recommendations 2001). *Micropor. Mesopor. Mater.* **2003**, *58*, 3–13.

17. Van Speybroeck, V.; Hemelsoet, K.; Joos, L.; Waroquier, M.; Bell, R. G.; Catlow, C. R. A. Advances in Theory and Their Application Within the Field of Zeolite Chemistry. *Chem. Soc. Rev.* **2015**, *44*, 7044–7111.

18. Schwanke, A. J.; Balzer, R.; Pergher, S. In *Handbook of Ecomaterials*; Martínez, L. M. T., Kharissova, O. V., Kharisov, B. I., Eds.; Springer International Publishing: Cham, 2017; Chapter 1, pp 1–22.

19. Agarwal, V.; Huber, G. W.; Conner, W. C.; Auerbach, S. M. DFT Study of Nitrided Zeolites: Mechanism of Nitrogen Substitution in HY and Silicalite. *J. Catal.* **2010**, *269*, 53–63.

20. Hammond, K. D.; Gharibeh, M.; Tompsett, G. A.; Dogan, F.; Brown, A. V.; Grey, C. P.; Auerbach, S. M.; Conner, W. C. Optimizing the Synthesis of Nitrogen-Substituted Zeolites. *Chem. Mater.* **2010**, *22*, 130–142.

21. Hammond, K. D.; Conner, W. C., Jr. In *Adv. Catal.*; Gates, B. C., Jentoft, F. C., Eds.; Academic Press: Burlington, 2013; Vol. 56; Chapter 1, pp 1–101.

22. Agarwal, V.; Conner, W. C.; Auerbach, S. M. DFT Study of Nitrogen-Substituted FAU: Effects of Ion Exchange and Aluminum Content on Base Strength. *J. Phys. Chem.* **2011**, *115*, 188–194.

23. Hammond, K. D.; Auerbach, S. M. In *Silica and Silicates in Modern Catalysis*; Halasz, I., Ed.; Research Signpost: Kerala, India, 2010; Chapter 2, pp 29–47.

24. Tilocca, A. Molecular Dynamics Simulations of Reactive and Diffusive Processes in Different Zeolite Structures. Ph.D. Dissertation, Universitá degli Studi di Sassari Dipartimento di Chimica, 2000.

25. Lucy, C. A. Evolution of Ion-Exchange: From Moses to the Manhattan Project to Modern Times. *J. Chromatogr.* **2003**, *1000*, 711–724.

26. Dyer, A. In *Introduction to Zeolite Science and Practice*; Čejka, J., van Bekkum, H., Corma, A., Schüth, F., Eds.; Stud. Surf. Sci. Catal.; Elsevier, 2007; Vol. 168; Chapter 16, pp 525–553.

27. Canfield, G. M.; Bizimis, M.; Latturner, S. E. Sodalite Ion Exchange in Polyethylene Oxide Oligomer Solvents. *J. Mater. Chem.* **2007**, *17*, 4530–4534.

28. Henson, N. J. Computer Simulation of Zeolites. Ph.D. Dissertation, University of Oxford, 1996.

29. Guan, Q.; Deng, L.; Zhang, D.; Ning, P.; Kong, Z.; He, L. Preparation of Tetraethylenepentamine-Functionalized 4A Zeolite for Effective Removal of Phosphate in Water. *Appl. Organomet. Chem.* **2020**, *34*, e5861–e5872.

30. Dickson, J. O.; Harsh, J. B.; Flury, M.; Pierce, E. M. Immobilization and Exchange of Perrhenate in Sodalite and Cancrinite. *Micropor. Mesopor. Mater.* **2015**, *214*, 115–120.

31. Dickson, J. O.; Harsh, J. B.; Lukens, W. W.; Pierce, E. M. Perrhenate Incorporation Into Binary Mixed Sodalites: The Role of Anion Size and Implications for Technetium-99 Sequestration. *Chem. Geol.* **2015**, *395*, 138–143.

32. Neeway, J. J.; Qafoku, N. P.; Williams, B. D.; Snyder, M. M.; Brown, C. F.; Pierce, E. M. Evidence of Technetium and Iodine Release from a Sodalite-Bearing Ceramic Waste Form. *Appl. Geo. Chem.* **2016**, *66*, 210–218.

33. Maddrell, E.; Gandy, A.; Stennett, M. The Durability of Iodide Sodalite. *J. Nucl. Mater.* **2014**, *449*, 168–172.

34. Wachinski, A. M. *Environmental Ion Exchange: Principles and Design*; CRC Press, 2016.

35. Cundy, C. S.; Cox, P. A. The Hydrothermal Synthesis of Zeolites: History and Development from the Earliest Days to the Present Time. *Chem. Rev.* **2003**, *103*, 663–702.

36. van Hooff, J.; Roelofsen, J. In *Introduction to Zeolite Science and Practice*; van Bekkum, H., Flanigen, E., Jansen, J., Eds.; Stud. Surf. Sci. Catal.; Elsevier, 1991; Vol. 58; Chapter 7, pp 241–283.

37. Jentys, A.; Lercher, J. In *Introduction to Zeolite Science and Practice*; van Bekkum, H., Flanigen, E., Jacobs, P., Jansen, J., Eds.; Stud. Surf. Sci. Catal.; Elsevier, 2001; Vol. 137; Chapter 8, pp 345–386.

38. Van Der Graaff, W.; Pidko, E.; Hensen, E. In *Zeolites in Sustainable Chemistry Synthesis, Characterization and Catalytic Applications*; Xiao, E. F., Meng, X., Eds.; Springer: Berlin, Heidelberg, 2016; Vol. 347; Chapter 10, pp 347–372.

39. Zecchina, A.; Areán, C. O. Diatomic Molecular Probes for Mid-IR Studies of Zeolites. *Chem. Soc. Rev.* **1996**, *25*, 187–197.

40. Knözinger, H.; Huber, S. IR Spectroscopy of Small and Weakly Interacting Molecular Probes for Acidic and Basic Zeolites. *J. Chem. Soc., Faraday Trans.* **1998**, *94*, 2047–2059.

41. Mofrad, A. M.; Peixoto, C.; Blumeyer, J.; Liu, J.; Hunt, H. K.; Hammond, K. D. Vibrational Spectroscopy of Sodalite: Theory and Experiments. *J. Phys. Chem.* **2018**, *122*, 24765–24779.

42. Król, M.; Mozgawa, W.; Jastrzębski, W. Theoretical and Experimental Study of Ion-exchange Process on Zeolites from 5-1 Structural Group. *J. Porous Mater.* **2016**, *23*, 1–9.

43. Mikuła, A.; Król, M.; Koleżyński, A. The Influence of the Long-Range Order on the Vibrational Spectra of Structures Based on Sodalite Cage. *Spectrochim. Acta A Mol. Biomol. Spectros.* **2015**, *144*, 273–280.

44. Hohenberg, P.; Kohn, W. Inhomogeneous Electron Gas. *Phys. Rev.* **1964**, *136*, B864–B871.

45. Kohn, W.; Sham, L. J. Self-Consistent Equations Including Exchange and Correlation Effects. *Phys. Rev.* **1965**, *140*, A1133–A1138.

46. Kittel, C. *Introduction to Solid State Physics. Fifth Edition*; Wiley: New York, 1976.

47. Labanowski, J. K.; Andzelm, J. W. *Density Functional Methods in Chemistry*; Springer Science & Business Media: New York, 2012.

48. Dobson, J. F.; Vignale, G.; Das, M. P. *Electronic Density Functional Theory: Recent Progress and New Directions*; Springer Science & Business Media: Queensland, Australia, 2013.

49. Born, M.; Oppenheimer, R. Zur Quantentheorie der Molekeln. *Annalen der Physik* **1927**, *389*, 457–484.

50. Slater, J. C. A Simplification of the Hartree–Fock Method. *Phys. Rev.* **1951**, *81*, 385–390.

51. Szabo, A.; Ostlund, N. S. *Modern Quantum Chemistry: Introduction to Advanced Electronic Structure Theory*; Dover: Mineola, New York, 2012.

52. Magnasco, V. *Methods of Molecular Quantum Mechanics*; John Wiley & Sons, Ltd: West Sussex, UK, 2009; Chapter 8, pp 133–139.

53. Perdew, J. P.; Tao, J.; Staroverov, V. N.; Scuseria, G. E. Meta-Generalized Gradient Approximation: Explanation of a Realistic Nonempirical Density Functional. *J. Chem. Phys.* **2004**, *120*, 6898–6911.

54. Tao, J.; Perdew, J. P.; Staroverov, V. N.; Scuseria, G. E. Climbing the Density Functional Ladder: Nonempirical Meta–Generalized Gradient Approximation Designed for Molecules and Solids. *Phys. Rev. Lett.* **2003**, *91*, 146401.

55. Kulik, H. J. First-Principles Transition-Metal Catalysis: Efficient and Accurate Approaches for Studying Enzymatic Systems. Ph.D. Dissertation, Massachusetts Institute of Technology, 2004.

56. Becke, A. D. Density-Functional Thermochemistry. III. The Role of Exact Exchange. *J. Chem. Phys.* **1993**, *98*, 5648–5652.

57. Pritchard, B. P.; Altarawy, D.; Didier, B.; Gibson, T. D.; Windus, T. L. New Basis Set Exchange: An Open, Up-to-Date Resource for the Molecular Sciences Community. *J. Chem. Info. Mod* **2019**, *59*, 4814–4820.

58. Pickett, W. E. Pseudopotential Methods in Condensed Matter Applications. *Comput. Phys. Rep.* **1989**, *9*, 115–197.

59. Giannozzi, P.; Baroni, S.; Bonini, N.; Calandra, M.; Car, R.; Cavazzoni, C.; Ceresoli, D.; Chiarotti, G. L.; Cococcioni, M.; Dabo, I.; Dal Corso, A.; de Gironcoli, S.; Fabris, S.; Fratesi, G.; Gebauer, R.; Gerstmann, U.; Gougoussis, C.; Kokalj, A.; Lazzeri, M.; Martin-Samos, L.; Marzari, N.; Mauri, F.; Mazzarello, R.; Paolini, S.; Pasquarello, A.; Paulatto, L.; Sbraccia, C.; Scandolo, S.; Sclauzero, G.; Seitsonen, A. P.; Smogunov, A.; Umari, P.; Wentzcovitch, R. M. QUANTUM ESPRESSO: A Modular and Open-Source Software Project for Quantum Simulations of Materials. *J. Phys. Condens. Matter* **2009**, *21*, 395502.

60. Giannozzi, P.; Andreussi, O.; Brumme, T.; Bunau, O.; Buongiorno Nardelli, B.; Calandra, M.; Car, R.; Cavazzoni, C.; Ceresoli, D.; Cococcioni, M.; Colonna, N.; Carnimeo, I.; Dal Corso, A.; de Gironcoli, S.; Delugas, P.; DiStasio, R. A.; Ferretti, A.; Floris, A.; Fratesi, G.; Fugallo, G.; Gebauer, R.; Gerstmann, U.; Giustino, F.; Gorni, T.; Jia, J.; Kawamura, M.; Ko, H.-Y.; Kokalj, A.; Küçükbenli, E.; Lazzeri, M.; Marsili, M.; Marzari, N.; Mauri, F.; Nguyen, N. L.; Nguyen, H.-V.; de-la Roza, A. O.; Paulatto, L.; Poncé, S.; Rocca, D.; Sabatini, R.; Santra, B.; Schlipf, M.; Seitsonen, A. P.; Smogunov, A.; Timrov, I.; Thonhauser, T.; Umari, P.; Vast, N.; Wu, X.; Baroni, S. Advanced Capabilities for Materials Modelling with Quantum ESPRESSO. *J. Phys. Condens. Matter* **2017**, *29*, 465901.

61. Hamann, D. R.; Schlüter, M.; Chiang, C. Norm-Conserving Pseudopotentials. *Phys. Rev. Lett.* **1979**, *43*, 1494–1497.

62. Christian, M. Modeling Dispersion Interactions on Metal Surfaces Using the Exchange-Hole Dipole Moment. Ph.D. Dissertation, Dalhousie University, 2018.

63. Vanderbilt, D. Soft Self-Consistent Pseudopotentials in a Generalized Eigenvalue Formalism. *Phys. Rev. B* **1990**, *41*, 7892–7895.

64. Laasonen, K.; Car, R.; Lee, C.; Vanderbilt, D. Implementation of Ultrasoft Pseudopotentials in *ab initio* Molecular Dynamics. *Phys. Rev. B* **1991**, *43*, 6796–6799.

65. Blöchl, P. E. Projector Augmented-Wave Method. *Phys. Rev. B* **1994**, *50*, 17953–17979.

66. Andersen, O. K. Linear Methods in Band Theory. *Phys. Rev. B* **1975**, *12*, 3060–3083.

67. Dove, M. T.; Dove, M. T. *Introduction to Lattice Dynamics*; Cambridge University Press: New York, NY, 1993; Vol. 4.

68. Noffsinger, J. D. The Electron-Phonon Interaction from First Principles. Ph.D. Dissertation, University of California, Berkeley, 2011.

69. Baroni, S.; Giannozzi, P.; Testa, A. Green's-Function Approach to Linear Response in Solids. *Phys. Rev. Lett.* **1987**, *58*, 1861–1864.

70. Feynman, R. P. Forces in Molecules. *Phys. Rev.* **1939**, *56*, 340–343.

71. Giannozzi, P.; Baroni, S. In *Handbook of Materials Modeling: Methods*; Yip, S., Ed.; Springer Netherlands: Dordrecht, 2005; pp 195–214.

72. Nakamura, K.; Higuchi, S.; Ohnuma, T. In *Perturbation Methods with Applications in Science and Engineering*; Bakırtaş, İ., Ed.; IntechOpen: Rijeka, 2018; Chapter 1, pp 1–17.

73. Vast, N.; Sjakste, J.; Kané, G.; Trinité, V. *Electronic Transport: Electrons, Phonons and Their Coupling within the Density Functional Theory*; 2016; pp 31–96.

74. Henkelman, G. Methods for Calculating Rates of Transitions with Application to Catalysis and Crystal Growth. Ph.D. Dissertation, University of Washington, 2001.

75. Laidler, K. J. *Chemical Kinetics 3rd Edition*; Pearson Education: New Delhi, India, 2008.

76. Pick, R.; Cohen, M.; Martin, R. Microscopic Theory of Force Constants in the Adiabatic Approximation. *Phys. Rev. B* **1970**, *1*, 910–920.

77. Sheppard, D.; Terrell, R.; Henkelman, G. Optimization Methods for Finding Minimum Energy Paths. *J. Chem. Phys.* **2008**, *128*, 134106.

78. Henkelman, G.; Jóhannesson, G.; Jónsson, H. In *Theoretical Methods in Condensed Phase Chemistry*; Schwartz, S. D., Ed.; Springer Netherlands: Dordrecht, 2002; Chapter 10, pp 269–302.

79. Jónsson, H.; Mills, G.; Jacobsen, K. W. *Classical and Quantum Dynamics in Condensed Phase Simulations*; Citeseer: Lerici, Italy, 1998; Chapter 16, pp 385–404.

80. Everett, D. H. Manual of Symbols and Terminology for Physicochemical Quantities and Units, Appendix II: Definitions, Terminology and Symbols in Colloid and Surface Chemistry. *Pure Appl. Chem.* **1972**, *31*, 577–638.

81. Li, J.-R.; Kuppler, R. J.; Zhou, H.-C. Selective Gas Adsorption and Separation in Metal–Organic Frameworks. *Chem. Soc. Rev.* **2009**, *38*, 1477–1504.

82. Murray, L. J.; Dinca, M.; Long, J. R. Hydrogen Storage in Metal–Organic Frameworks. *Chem. Soc. Rev.* **2009**, *38*, 1294–1314.

83. Inagaki, M.; Konno, H.; Tanaike, O. Carbon Materials for Electrochemical Capacitors. *J. Power Sources* **2010**, *195*, 7880–7903.

84. Tosheva, L.; Valtchev, V. P. Nanozeolites: Synthesis, Crystallization Mechanism, and Applications. *Chem. Mater.* **2005**, *17*, 2494–2513.

85. Ma, Y.; Tong, W.; Zhou, H.; Suib, S. L. A Review of Zeolite-Like Porous Materials. *Micropor. Mesopor. Mater.* **2000**, *37*, 243–252.

86. Lu, X.; Peng, Y.; Wang, Z.; Yan, Y. Rapid Fabrication of Highly *b*-Oriented Zeolite **MFI** Thin Films Using Ammonium Salts as Crystallization-Mediating Agents. *Chem. Commun.* **2015**, *51*, 11076–11079.

87. Barrer, R. *Hydrothermal Chemistry of Zeolites*; Academic Press: London, 1982.

88. Hammond, K. D.; Tompsett, G. A.; Auerbach, S. M.; Conner, W. C. Apparatus for Measuring Physical Adsorption on Intact Supported Porous Membranes. *J. Porous Mater.* **2007**, *14*, 409–416.

89. Hong, M.; Falconer, J. L.; Noble, R. D. Modification of Zeolite Membranes for H_2 Separation by Catalytic Cracking of Methyldiethoxysilane. *Ind. Eng. Chem. Res.* **2005**, *44*, 4035–4041.

90. Vallee, S. J.; Conner, W. C. Effects of Microwaves and Microwave Frequency on the Selectivity of Sorption for Binary Mixtures on Oxides. *J. Phys. Chem. C* **2008**, *112*, 15483–15489.

91. Iwai, Y.; Oka, N.; Yamanishi, T. Influence of Framework Silica-to-Alumina Ratio on the Water Adsorption and Desorption Characteristics of **MFI**-CaX/CaY Zeolite. *J. Phys. Chem. Solid* **2009**, *70*, 881–888.

92. Wang, C.; Cao, L.; Huang, J. Influences of Acid and Heat Treatments on the Structure and Water Vapor Adsorption Property of Natural Zeolite. *Surf. Interface Anal.* **2017**, *49*, 1249–1255.

93. Bonilla, G.; Tsapatsis, M.; Vlachos, D. G.; Xomeritakis, G. Fluorescence Confocal Optical Microscopy Imaging of the Grain Boundary Structure of Zeolite **MFI** Membranes Made by Secondary (Seeded) Growth. *J. Membr. Sci.* **2001**, *182*, 103–109.

94. Maesen, T.; Marcus, B. In *Introduction to Zeolite Science and Practice*, 2nd ed.; van Bekkum, H., Flanigen, E. M., Jacobs, P. A., Jansen, J. C., Eds.; Stud. Surf. Sci. Catal.; 2001; Vol. 137; Chapter 1, pp 1–9.

95. Borai, E. H.; Harjula, R.; Malinen, L.; Paajanen, A. Efficient Removal of Cesium from Low-Level Radioactive Liquid Waste Using Natural and Impregnated Zeolite Minerals. *J. Hazard. Mater.* **2009**, *172*, 416–422.

96. Somerset, V.; Petrik, L.; Iwuoha, E. *Application of Hydrothermal Synthesised Zeolites in the Removal of Cadmium, Lead and Arsenic Ions from Mine Wastewater: Handbook of Zeolites: Structure, Properties and Applications*; Nova Science Pub.: New York, New York, 2009; Chapter 13, pp 375–393.

97. Nicholas, J. B.; Hopfinger, A. J.; Trouw, F. R.; Iton, E. Molecular Modeling of Zeolite Structure. 2. Structure and Dynamics of Silica Sodalite and Silicate Force Field. *J. Am. Chem. Soc.* **1991**, *113*, 4792–4800.

98. Smirnov, K. S.; Bougeard, D. Molecular Dynamics Study of the Vibrational Spectra of Siliceous Zeolites Built from Sodalite. *J. Phys. Chem.* **1993**, *97*, 9434–9440.

99. Iyer, K. A.; Singer, S. J. Local-Mode Analysis of Complex Zeolite Vibrations: Sodalite. *J. Phys. Chem.* **1994**, *98*, 12670–12678.

100. Creighton, J. A.; Deckman, H. W.; Newsam, J. M. Computer Simulation and Interpretation of the Infrared and Raman Spectra of Sodalite Frameworks. *J. Phys. Chem.* **1994**, *98*, 448–459.

101. Sankey, O. F.; Demkov, A. A.; Lenosky, T. Electronic Structure of Black Sodalite. *Phys. Rev. B* **1998**, *57*, 15129–15139.

102. Astala, R.; Auerbach, S. M.; Monson, P. A. Density Functional Theory Study of Silica Zeolite Structures: Stabilities and Mechanical Properties of **SOD**, **LTA**, **CHA**, **MOR**, and **MFI**. *J. Phys. Chem. B* **2004**, *108*, 9208–9215.

103. Bordiga, S.; Lamberti, C.; Bonino, F.; Travert, A.; Thibault-Starzyk, F. Probing Zeolites by Vibrational Spectroscopies. *Chem. Soc. Rev.* **2015**, *44*, 7262–7341.

104. Wilson, E. B., Jr.; Decius, J. C.; Cross, P. C. *Molecular Vibrations: The Theory of Infrared and Raman Vibrational Spectra*; McGraw-Hill: New York, 1955.

105. Wilson, E. B. Some Mathematical Methods for the Study of Molecular Vibrations. *J. Chem. Phys.* **1941**, *9*, 76–84.

106. Filippone, F.; Buda, F.; Iarlori, S.; Moretti, G.; Porta, P. Structural and Electronic Properties of Sodalite: An *ab Initio* Molecular Dynamics Study. *J. Phys. Chem.* **1995**, *99*, 12883–12891.

107. Mikuła, A.; Król, M.; Koleżyński, A. Experimental and Theoretical Spectroscopic Studies of Ag-, Cd- and Pb-Sodalite. *J. Mol. Struct.* **2016**, *1126*, 110–116.

108. Liu, C.; Li, G.; Hensen, E. J.; Pidko, E. A. Relationship Between Acidity and Catalytic Reactivity of Faujasite Zeolite: A Periodic DFT Study. *J. Catal.* **2016**, *344*, 570–577.

109. Hassan, I.; Grundy, H. D. The Crystal Structures of Sodalite-Group Minerals. *Acta Crystallogr. B* **1984**, *40*, 6–13.

110. Kohn, W.; Sham, L. J. Self-Consistent Equations Including Exchange and Correlation Effects. *Phys. Rev.* **1965**, *140*, A1133–A1138.

111. Thomas, L. H. The Calculation of Atomic Fields. *Proc. Camb. Phil. Soc.* **1927**, *23*, 542–548.

112. Fermi, E. Eine statistische Methode zur Bestimmung einiger Eigenschaften des Atoms und ihre Anwendung auf die Theorie des periodischen Systems der Elemente. *Z. Phys.* **1928**, *48*, 73–79.

113. Dirac, P. A. M. Note on Exchange Phenomena in the Thomas Atom. *Proc. Camb. Phil. Soc.* **1930**, *26*, 376–385.

114. Vosko, S. H.; Wilk, L.; Nusair, M. Accurate Spin-Dependent Electron Liquid Correlation Energies for Local Spin-Density Calculations: A Critical Analysis. *Can. J. Phys.* **1980**, *58*, 1200–1211.

115. Troullier, N.; Martins, J. L. Efficient Pseudopotentials for Plane-Wave Calculations. *Phys. Rev. B* **1991**, *43*, 1993–2006.

116. Perdew, J. P.; Wang, Y. Accurate and Simple Analytic Representation of the Electron-Gas Correlation Energy. *Phys. Rev. B* **1992**, *45*, 13244–13249.

117. Perdew, J. P.; Burke, K.; Ernzerhof, M. Generalized Gradient Approximation Made Simple. *Phys. Rev. Lett.* **1996**, *77*, 3865–3868.

118. Perdew, J. P.; Burke, K.; Ernzerhof, M. Generalized Gradient Approximation Made Simple (Errata). *Phys. Rev. Lett.* **1997**, *78*, 1396.

119. Kresse, G.; Joubert, D. From Ultrasoft Pseudopotentials to the Projector Augmented-Wave Method. *Phys. Rev. B* **1999**, *59*, 1758–1775.

120. Perdew, J. P.; Zunger, A. Self-Interaction Correction to Density-Functional Approximations for Many-Electron Systems. *Phys. Rev. B* **1981**, *23*, 5048–5079.

121. Rappe, A. M.; Rabe, K. M.; Kaxiras, E.; Joannopoulos, J. D. Optimized Pseudopotentials. *Phys. Rev. B* **1990**, *41*, 1227–1230.

122. Rappe, A. M.; Rabe, K. M.; Kaxiras, E.; Joannopoulos, J. D. Erratum: Optimized Pseudopotentials [Phys. Rev. B 41, 1227 (1990)]. *Phys. Rev. B* **1991**, *44*, 13175.

123. Perdew, J. P.; Chevary, J. A.; Vosko, S. H.; Jackson, K. A.; Pederson, M. R.; Singh, D. J.; Fiolhais, C. Atoms, Molecules, Solids, and Surfaces: Applications of the Generalized Gradient Approximation for Exchange and Correlation. *Phys. Rev. B* **1992**, *46*, 6671–6687.

124. Perdew, J. P.; Chevary, J. A.; Vosko, S. H.; Jackson, K. A.; Pederson, M. R.; Singh, D. J.; Fiolhais, C. Erratum: Atoms, Molecules, Solids, and Surfaces: Applications of the Generalized Gradient Approximation for Exchange and Correlation. *Phys. Rev. B* **1993**, *48*, 4978.

125. Laasonen, K.; Car, R.; Lee, C.; Vanderbilt, D. Implementation of Ultrasoft Pseudopotentials in *ab initio* Molecular Dynamics. *Phys. Rev. B* **1991**, *43*, 6796–6799.

126. Laasonen, K.; Pasquarello, A.; Car, R.; Lee, C.; Vanderbilt, D. Car–Parrinello Molecular Dynamics with Vanderbilt Ultrasoft Pseudopotentials. *Phys. Rev. B* **1993**, *47*, 10142–10153.

127. Bornhauser, P.; Bougeard, D. Intensities of the Vibrational Spectra of Siliceous Zeolites by Molecular Dynamics Calculations. I. Infrared Spectra. *J. Phys. Chem.* **2001**, *105*, 36–41.

128. Monkhorst, H. J.; Pack, J. D. Special Points for Brillouin-Zone Integrations. *Phys. Rev. B* **1976**, *13*, 5188–5192.

129. Schaftenaar, G.; H., N. J. Molden: A Pre- and Post-Processing Program for Molecular and Electronic Structures. *J. Comput. Aided Mol. Des.* **2000**, *14*, 123–134.

130. Weber, R.; Wirtz, L.; Togo, A.; Pedro, S. J.; Miranda, H. Phonon Website: Visualize Phonon Vibrational Modes. 2018; `http://henriquemiranda.github.io/phononwebsite/`.

131. Shao, C.; Li, X.; Qiu, S.; Xiao, F.-S. The Role of Pyrocatechol as a Complex Agent for Silicon in the Synthesis of Large Single Crystals of Silica-Sodalite Zeolite. *Micropor. Mesopor. Mater.* **1999**, *33*, 215–222.

132. Bibby, D. M.; Dale, M. P. Synthesis of Silica-Sodalite from Non-Aqueous Systems. *Nature* **1985**, *317*, 157–158.

133. Stein, A. In *Verified Syntheses of Zeolitic Materials*, 2nd ed.; Robson, H., Lillerud, K. P., Eds.; Elsevier: Amsterdam, 2001; Chapter 83, pp 251–253.

134. SAS Institute, I. JMP Version 13.2. 2016; `http://www.jmp.com`.

135. Hassan, I.; Antao, S. M.; Parise, J. B. Sodalite: High-Temperature Structures Obtained from Synchrotron Radiation and Rietveld Refinements. *Am. Mineral.* **2004**, *89*, 359–364.

136. Richardson, J. W.; Pluth, J. J.; Smith, J. V.; Dytrych, W. J.; Bibby, D. M. Conformation of Ethylene Glycol and Phase Change in Silica Sodalite. *J. Phys. Chem.* **1988**, *92*, 243–247.

137. Flanigen, E. M.; Khatami, H.; Szymanski, H. A. In *Molecular Sieve Zeolites—1*; Gould, R. F., Ed.; Advances in Chemistry; American Chemical Society: Washington, 1971; Vol. 101; Chapter 16, pp 201–227.

138. Mozgawa, W.; Jastrzębski, W.; Handke, M. Vibrational Spectra of D4R and D6R Structural Units. *J. Mol. Struct.* **2005**, *744–747*, 663–670.

139. Dutta, P. K.; Del Barco, B. Raman Spectroscopy of Zeolite A: Influence of Silicon/Aluminum Ratio. *J. Phys. Chem.* **1988**, *92*, 354–357.

140. McMillan, P. F.; Remmele, R. L. Hydroxyl Sites in SiO_2 Glass: A Note on Infrared and Raman Spectra. *Am. Mineral.* **1986**, *71*, 772–778.

141. Sokol, A.; Catlow, C. R. A.; Garces, J. M.; Kuperman, A. Defect Centers in Microporous Aluminum Silicate Materials. *J. Phys. Chem. B* **1998**, *102*, 10647–10649.

142. Bordiga, S. and Ugliengo, P. and Damin, A. and Lamberti, C. and Spoto, G. and Zecchina, A. and Spanò, G. and Buzzoni, R. and Dalloro, L. and Rivetti, F., Hydroxyls Nests in Defective Silicalites and Strained Structures Derived upon Dehydroxylation: Vibrational Properties and Theoretical Modelling. *Top. Catal.* **2001**, *15*, 43–52.

143. Bordiga, S.; Roggero, I.; Ugliengo, P.; Zecchina, A.; Bolis, V.; Artioli, G.; Buzzoni, R.; Marra, G.; Rivetti, F.; Spanò, G.; Lamberti, C. Characterisation of Defective Silicalites. *J. Chem. Soc. Dalton Trans.* **2000**, *21*, 3921–3929.

144. Pascale, F.; Ugliengo, P.; Civalleri, B.; Orlando, R.; D'Arco, P.; Dovesi, R. Hydrogarnet Defect in Chabazite and Sodalite Zeolites: A Periodic Hartree–Fock and B3-LYP Study. *J. Chem. Phys.* **2002**, *117*, 5337–5346.

145. Kawai, T.; Tsutsumi, K. A Study on the Surface Silanol Groups Developed by Hydrothermal and Acid Treatment of Faujasite Type Zeolites. *J. Colloid Interface Sci.* **1999**, *212*, 310–316.

146. Hong, S. B.; Camblor, M. A. SiO- Defects in As-Synthesized Pure-Silica and Aluminosilicate Sodalites. *Chem. Mater.* **1997**, *9*, 1999–2003.

147. Mofrad, A. M.; Schellenberg, P. S.; Peixoto, C.; Hunt, H. K.; Hammond, K. D. Calculated Infrared and Raman Signatures of Ag^{+}, Cd^{2+}, Pb^{2+}, Hg^{2+}, Ca^{2+}, Mg^{2+}, and K^{+} Sodalites. *Micropor. Mesopor. Mater.* **2020**, *296*, 109983.

148. Joseph, L.; Jun, B.-M.; Flora, J. R.; Park, C. M.; Yoon, Y. Removal of Heavy Metals from Water Sources in the Developing World Using Low-Cost Materials: A Review. *Chemosphere* **2019**, *229*, 142–159.

149. Saran, L. M.; Pissarra, T. C. T.; Silveira, G. A.; Constancio, M. T. L.; de Melo, W. J.; Alves, L. M. C. Land Use Impact on Potentially Toxic Metals Concentration on Surface Water and Resistant Microorganisms in Watersheds. *Ecotoxicol. Environ. Saf.* **2018**, *166*, 366–374.

150. Ghosh, R.; Sahu, A.; Pushpavanam, S. Removal of Trace Hexavalent Chromium from Aqueous Solutions by Ion Foam Fractionation. *J. Hazard. Mater.* **2019**, *367*, 589–598.

151. Li, Y.; Bai, P.; Yan, Y.; Yan, W.; Shi, W.; Xu, R. Removal of Zn^{2+}, Pb^{2+}, Cd^{2+}, and Cu^{2+} from Aqueous Solution by Synthetic Clinoptilolite. *Micropor. Mesopor. Mater.* **2019**, *273*, 203–211.

152. Liu, F.; Xiong, W.; Feng, X.; Shi, L.; Chen, D.; Zhang, Y. A Novel Monolith ZnS-ZIF-8 Adsorption Material for Ultraeffective Hg (II) Capture from Wastewater. *J. Hazard. Mater.* **2019**, *367*, 381–389.

153. Chen, G. Electrochemical Technologies in Wastewater Treatment. *Separ. Purif. Meth.* **2004**, *38*, 11–41.

154. Charerntanyarak, L. Heavy Metals Removal by Chemical Coagulation and Precipitation. *Water Sci. Technol.* **1999**, *39*, 135–138.

155. Dabrowski, A.; Hubicki, Z.; Podkoscielny, P.; Robens, E. Selective Removal of the Heavy Metal Ions from Waters and Industrial Wastewaters by Ion-Exchange Method. *Chemosphere* **2004**, *56*, 9323–9331.

156. González Vázquez, O. F.; Moreno Virgen, M. d. R.; Hernández Montoya, V.; Tovar Gómez, R.; Alcántara Flores, J. L.; Pérez Cruz, M. A.; Montes Morán, M. A. Adsorption of Heavy Metals in the Presence of a Magnetic Field on Adsorbents with Different Magnetic Properties. *Ind. Eng. Chem. Res.* **2016**, *55*, 9323–9331.

157. Dirisu, G.; Okonkwo, U.; Okokpujie, I.; Fayomi, O. Comparative Analysis of the Effectiveness of Reverse Osmosis and Ultraviolet Radiation of Water Treatment. *J. Ecol. Eng.* **2019**, *20*, 61–75.

158. Fu, F.; Wang, Q. Removal of Heavy Metal Ions from Wastewaters: A Review. *J. Environ. Manag.* **2011**, *92*, 407–418.

159. Zhao, M.; Xu, Y.; Zhang, C.; Rong, H.; Zeng, G. New Trends in Removing Heavy Metals from Wastewater. *Appl. Microbiol. Biotechnol.* **2016**, *100*, 6509–6518.

160. Čejka, J.; van Bekkum, H.; Corma, A.; Schüth, F. *Introduction to Zeolite Science and Practice*, 3rd ed.; Stud. Surf. Sci. Catal.; Elsevier, 2007; Vol. 168.

161. Baur, W. H.; Fischer, R. X. A Historical Note on the Sodalite Framework: The Contribution of Frans Maurits Jaeger. *Micropor. Mesopor. Mater.* **2008**, *116*, 1–3.

162. Ozin, G. A.; Kuperman, A.; Stein, A. Advanced Zeolite, Materials Science. *Angew. Chem. Int. Ed.* **1989**, *28*, 359–376.

163. Aprea, P.; Caputo, D.; Gargiulo, N.; de Gennaro, B.; Iucolano, F.; Liguori, B.; Colella, C. Ion Exchange Kinetics and Thermodynamics of Hydrosodalite, a Narrow Pore Zeolite. *J. Porous Mater.* **2014**, *21*, 643–651.

164. Stein, A.; Ozin, G. A.; MacDonald, P. M.; Stucky, G. D.; Jelinek, R. Silver, Sodium Halosodalites: Class A Sodalites. *J. Am. Chem. Soc.* **1992**, *114*, 5171–5186.

165. Shanbhag, G. V.; Choi, M.; Kim, J.; Ryoo, R. Mesoporous Sodalite: A Novel, Stable Solid Catalyst for Base-Catalyzed Organic Transformations. *J. Catal.* **2009**, *264*, 88–92.

166. Ma, Y.; Liu, Z.; Geng, A.; Vogt, T.; Lee, Y. Structural and Spectroscopic Studies of Alkali-Metal Exchanged Stilbites. *Micropor. Mesopor. Mater.* **2016**, *224*, 339–348.

167. Łodziński, M.; Wrzalik, R.; Sitarz, M. Micro-Raman Spectroscopy Studies of Some Accessory Minerals from Pegmatites of the Sowie Mts and Strzegom-Sobótka Massif, Lower Silesia, Poland. *J. Mol. Struct.* **2005**, *744–747*, 1017–1026.

168. Flanigen, E. M.; Khatami, H.; Szymanski, H. A. In *Molecular Sieve Zeolites-I*; Flanigen, E. M., Sand, L. B., Eds.; Adv. Chem.; American Chemical Society: Washington, DC, August 1, 1974; Chapter 16, pp 201–229.

169. Makreski, P.; Jovanovski, G.; Kaitner, B. Minerals from Macedonia. XXIV. Spectra-Structure Characterization of Tectosilicates. *J. Mol. Struct.* **2009**, *924-926*, 413–419.

170. Moloy, E. C.; Cygan, R. T.; Bonhomme, F.; Teter, D. M.; Navrotsky, A. Molecular Simulations of Anhydrous $Na_6[Al_6Si_6O_{24}]$ Sodalite. *Chem. Mater.* **2004**, *16*, 2121–2133.

171. Felsche, J.; Luger, S.; Baerlocher, C. Crystal Structures of the Hydro-Sodalite $Na_6[AlSiO_4]_6(8\,H_2O)$ and of the Anhydrous Sodalite $Na_6[AlSiO_4]_6$. *Zeolites* **1986**, *6*, 367–372.

172. Hennig, P.; Kiefel, M. Quasi-Newton Methods: A New Direction. *J. Mach. Learn. Res.* **2013**, *14*, 843–865.

173. Placzek, G. In *Handbuch der Radiologie*; Marx, E., Ed.; Akademische Verlagsgesellschaft: Leipzig, 1934; Vol. 1; pp 205–374.

174. Shannon, R. D. Revised Effective Ionic Radii and Systematic Studies of Interatomic Distances in Halides and Chalcogenides. *Acta Crystallogr. B* **1976**, *32*, 751–767.

175. Brik, M.; Kityk, I. Modeling of Lattice Constant and Their Relations with Ionic Radii and Electronegativity of Constituting Ions of AXY Cubic Crystals (A=K, Cs, Rb, Tl; X=Tetravalent Cation, Y=F, Cl, Br, I). *J. Phys. Chem. Solid* **2011**, *72*, 1256–1270.

176. Latturner, S. E.; Sachleben, J.; Iversen, B. B.; Hanson, J.; Stucky, G. D. Covalent Guest-Framework Interactions in Heavy Metal Sodalites: Structure and Properties of Thallium and Silver Sodalite. *J. Phys. Chem.* **1999**, *103*, 7135–7144.

177. Lechert, H. In *Verified Syntheses of Zeolitic Materials*; Robson, H., Lillerud, K. P., Eds.; Elsevier Science: Amsterdam, 2001; Chapter 5, pp 33–38.

178. Eiden-Assmann, S. New Heavy Metal-Hydro-Sodalites Containing Cd^{2+}, Ag^{+} or Pb^{2+}: Synthesis by Ion-Exchange and Characterisation. *Mater. Res. Bull.* **2002**, *37*, 875–889.

179. Golbad, S.; Khoshnoud, P.; Abu-Zahra, N. Hydrothermal Synthesis of Hydroxy Sodalite from Fly Ash for the Removal of Lead Ions from Water. *Int. J. Environ. Sci. Technol.* **2017**, *14*, 135–142.

180. Kolesov, B. Raman Investigation of H2O Molecule and Hydroxyl Groups in the Channels of Hemimorphite. *Am. Mineral.* **2006**, *91*, 1355–1362.

181. Sun, Q. The Raman OH Stretching Bands of Liquid Water. *Vib. Spectros.* **2009**, *51*, 213–217.

182. Giermańska, J.; Szostak, M. M. Polarized Raman and Infrared Spectra of OH Stretching Vibrations in the Sucrose Crystal. *J. Raman Spectros.* **1991**, *22*, 107–109.

183. *National Primary Drinking Water Regulations, Tech. Rep. 816-F-09-004*; U. S. Environmental Protection Agency, (May) 2009; `https://www.epa.gov/sites/production/files/2016-06/documents/npwdr_complete_table.pdf`.

184. Somerset, V.; Petrik, L.; Iwuoha, E. Alkaline Hydrothermal Conversion of Fly Ash Filtrates Into Zeolites 2: Utilization in Wastewater Treatment. *J. Environ. Sci. Health B* **2005**, *40*, 1627–1636.

185. Somerset, V.; Petrik, L.; Iwuoha, E. Alkaline Hydrothermal Conversion of Fly Ash Precipitates Into Zeolites 3: The Removal of Mercury and lead Ions from Wastewater. *J. Environ. Manag.* **2008**, *87*, 125–131.

186. Baraldi, A.; Bertoli, P.; Capelletti, R.; Ruffini, A.; Scacco, A. High-Resolution Vibrational Spectroscopy of Pb-OH Defects in $KMgF_3$ Fluoroperovskite Single Crystals. *Phys. Rev. B* **2001**, *63*, 134302.

187. Mofrad, A. M.; Hammond, K. D. A Density Functional Theory Study of the Vibrational Spectra of Aluminate Sodalite, $|M_8X_2|[Al_{12}O_{24}]$-**SOD** (M = Ca, Cd, Sr; X = CrO_4, MoO_4, S, SO_4, Se, SeO_3, Te, TeO_3). *Micropor. Mesopor. Mater.* **2020**, *309*, 110466.

188. Brenchley, M. E.; Weller, M. T. Synthesis and Structure of Sulfide Aluminate Sodalites. *J. Mater. Chem.* **1992**, *2*, 1003–1005.

189. Dann, S. E.; Weller, M. T. The Preparation, Characterization and Structure of $Ca_8[AlO_2]_{12}Te_2$ and $Cd_8[AlO_2]_{12}Te_2$; Two New Members of the Sodalite Family. *J. Mater. Chem.* **1998**, *8*, 1029–1031.

190. Weller, M. T. Where Zeolites and Oxides Merge: Semi-Condensed Tetrahedral Frameworks. *J. Chem. Soc. Dalton Trans.* **2000**, 4227–4240.

191. Jiang, M. R. M.; Weller, M. T. The Ionic Conductivity of (Ag, Na)-Nitrite Sodalites. *Solid State Ionics* **1991**, *46*, 341–345.

192. Weller, M.; Wong, G. Characterization of Novel Sodalites by Neutron Diffraction and Solid-State NMR. *Solid State Ionics* **1989**, *32–33*, 430–435.

193. Ofer-Rozovsky, E.; Haddad, M. A.; Bar-Nes, G.; Borojovich, E.; Binyamini, A.; Nikolski, A.; Katz, A. Cesium Immobilization in Nitrate-Bearing Metakaolin-Based Geopolymers. *J. Nucl. Mater.* **2019**, *514*, 247–254.

194. Chong, S.; Peterson, J. A.; Riley, B. J.; Tabada, D.; Wall, D.; Corkhill, C. L.; McCloy, J. S. Glass-Bonded Iodosodalite Waste Form for Immobilization of ^{129}I. *J. Nucl. Mater.* **2018**, *504*, 109–121.

195. Dickson, J. O.; Harsh, J. B.; Flury, M.; Lukens, W. W.; Pierce, E. M. Competitive Incorporation of Perrhenate and Nitrate into Sodalite. *Environ. Sci. Technol.* **2014**, *48*, 12851–12857.

196. Dickson, J. O.; Harsh, J. B.; Flury, M.; Pierce, E. M. Immobilization and Exchange of Perrhenate in Sodalite and Cancrinite. *Micropor. Mesopor. Mater.* **2015**, *214*, 115–120.

197. Pierce, E. M.; Lilova, K.; Missimer, D. M.; Lukens, W. W.; Wu, L.; Fitts, J.; Rawn, C.; Huq, A.; Leonard, D. N.; Eskelsen, J. R.; F. Woodfield, B.; Jantzen, C. M.; Navrotsky, A. Structure and Thermochemistry of Perrhenate Sodalite and Mixed Guest Perrhenate/Pertechnetate Sodalite. *Environ. Sci. Technol.* **2017**, *51*, 997–1006.

198. Borhade, A. V.; Kshirsagar, T. A.; Dholi, A. G. Novel Synthesis of Ultramarine Blue from Waste Coal Fly Ash Via Thiocyanate Aluminosilicate Sodalite. *J. Sulfur. Chem.* **2016**, *37*, 632–645.

199. Kondo, D.; Beaton, D. Hackmanite/Sodalite from Myanmar and Afghanistan. *Gems. Gemol.* **2009**, *45*, 38–43.

200. Brenchley, M. E.; Weller, M. T. Structures of Strontium Selenite and Strontium Selenide Aluminate Sodalites and the Relationship of Framework Structure to Vibrational Spectra in Aluminate Sodalites. *Chem. Mater.* **1993**, *5*, 970–973.

201. Dann, S. E.; Weller, M. T. The Structures of Strontium Tellurite and Strontium Telluride Aluminate Sodalites Studied by Powder Neutron Diffraction, EXAFS, IR, and MAS NMR Spectroscopies. *J. Mater. Chem.* **1996**, *6*, 1717–1721.

202. Armstrong, J. A.; Weller, M. T. New Sodalite Frameworks; Synthetic Tugtupite and a Beryllosilicate Framework with a 3:1 Si:Be Ratio. *Dalton Trans.* **2006**, 2998–3005.

203. Johnson, G. M.; Weller, M. T. In *Progress in Zeolite and Microporous Materials*; Chon, H., Ihm, S.-K., Uh, Y. S., Eds.; Stud. Surf. Sci. Catal.; Elsevier, 1997; Vol. 105; pp 269–275.

204. Johnson, G. M.; Mead, P. J.; Weller, M. T. Structural Trends in the Sodalite Family. *Phys. Chem. Chem. Phys.* **1999**, *1*, 3709–3714.

205. Johnson, G. M.; Mead, P. J.; Weller, M. T. Synthesis of a Range of Anion-Containing Gallium and Germanium Sodalites. *Micropor. Mesopor. Mater.* **2000**, *38*, 445–460.

206. Halstead, P. E.; Moore, A. E. The Composition and Crystallography of an Anhydrous Calcium Aluminosulphate Occurring in Expanding Cement. *J. Appl. Chem.* **1962**, *12*, 413–417.

207. Depmeier, W. Structure of Cubic Aluminate Sodalite $Ca_8[Al_{12}O_{24}](WO_4)_2$ in Comparison with Its Orthorhombic Phase and with Cubic $Sr_8[Al_{12}O_{24}](CrO_4)_2$. *Acta Crystallogr. B* **1988**, *44*, 201–207.

208. Depmeier, W. Aluminate Sodalites–A Family with Strained Structures and Ferroic Phase Transitions. *Phys. Chem. Miner.* **1988**, *15*, 419–426.

209. Cuesta, A.; De la Torre, A. G.; Losilla, E. R.; Peterson, V. K.; Rejmak, P.; Ayuela, A.; Frontera, C.; Aranda, M. A. G. Structure, Atomistic Simulations, and Phase Transition of Stoichiometric Yeelimite. *Chem. Mater.* **2013**, *25*, 1680–1687.

210. Melzer, R.; Depmeier, W. A Structural Study of Aluminate Sodalite $Ca_8[Al_{12}O_{24}](CrO_4)_2$(CACr). *Cryst. Res. Technol.* **1996**, *31*, 459–467.

211. Billeter, S. R.; Curioni, A.; Andreoni, W. Efficient Linear Scaling Geometry Optimization and Transition-State Search for Direct Wavefunction Optimization Schemes in Density Functional Theory Using a Plane-Wave Basis. *Comput. Mater. Sci.* **2003**, *27*, 437–445.

212. Baroni, S.; de Gironcoli, S.; Dal Corso, A.; Giannozzi, P. Phonons and Related Crystal Properties from Density-Functional Perturbation Theory. *Rev. Mod. Phys.* **2001**, *73*, 515–562.

213. van Smaalen, S.; Dinnebier, R.; Katzke, H.; Depmeier, W. Structural Characterization of the High-Temperature Phase Transitions in $Ca_8[Al_{12}O_{24}](MoO_4)_2$ Aluminate Sodalite Using X-ray Powder Diffraction. *J. Solid State Chem.* **1997**, *129*, 130–143.

214. Többens, D. M.; Depmeier, W. Superstructure of Strontium Chromate Aluminate Sodalite at Low Temperatures. *Z. Kristallogr.* **2001**, *216*, 586–590.

215. Kohanoff, J. *Electronic Structure Calculations for Solids and Molecules: Theory and Computational Methods*; Cambridge University Press, 2006.

216. Henderson, C.; Taylor, D. Infrared Spectra of Aluminogermanate- and Aluminate-Sodalites and a Re-Examination of the Relationship Between T−O Bond Length, T−O−T Angle and the Position of the Main I.R. Absorption Band for Compounds with Framework Structures. *Spectrochim. Acta A Mol. Biomol. Spectros.* **1979**, *35*, 929–935.

217. Godber, J.; Ozin, G. A. Fourier Transform Far-Infrared Spectroscopic Study of Cation and Anion Dynamics in M,X-Sodalites. *J. Phys. Chem.* **1988**, *92*, 4980–4987.

218. Benedict, M. Electric Power from Nuclear Fission. *Bull. Atom. Scient.* **1971**, *27*, 8–16.

219. Soelberg, N. R.; Garn, T. G.; Greenhalgh, M. R.; Law, J. D.; Jubin, R.; Strachan, D. M.; Thallapally, P. K. Radioactive Iodine and Krypton Control for Nuclear Fuel Reprocessing Facilities. *Sci. Technol. Nucl. Install.* **2013**, *2013*, 702496.

220. Environmental Radiation Protection Standards for Nuclear Power Operations. Code of Federal Regulations, Section 190.10, Title 40, 2010.

221. Standards for Protection Against Radiation. Code of Federal Regulations, Title 10, Volume 1, Chapter 1, 2017; www.nrc.gov/reading-rm/doc-collections/cfr/part020/appb/Krypton-85.html.

222. Christensen, A. B.; Del Debbio, J. A.; Knecht, D. A.; Tanner, J. E.; Cossel, S. C. Immobilization of Krypton-85 in Zeolite 5A. Proceedings of the 17th DOE Nuclear Air Cleaning Conference. Springfield, Virginia, 1983.

223. Christensen, A. B.; Del Debbio, J. A.; Knecht, D. A.; Tanner, J. E. *Loading and Leakage of Krypton Immobilized in Zeolites and Glass*; 1980.

224. Pinchback, T.; Winkel, J.; Matlock, D.; Olson, D. Corrosion of Structural Alloys in Liquid Rubidium. *Nucl. Technol.* **1981**, *54*, 201–207.

225. Nicholas, M.; Trevena, P. *Screening of Materials for Embrittlement by Rubidium*; Harwood Academic for the Commission of the European Communities: Oxford, 1983.

226. Amateau, M. F. *The Effect of Molten Alkali Metals on Containment Metals and Alloys at High Temperatures*; Defense Metals Information Center, Battelle Memorial Institute: Columbus, Ohio, USA, 1962; Vol. 169.

227. Whitmell, D. Immobilization of Krypton in a Metallic Matrix. *J. Brit. Nucl. Soc.* **1982**, *21*, 181–187.

228. Whitmell, D. S. Choice of Materials for the Immobilization of 85-Krypton in a Metallic Matrix by Combined Ion Implantation and Sputtering. Proceedings of the 18th DOE Nuclear Airborne Waste Management and Air Cleaning Conference. Springfield, Virginia, 1985; pp 667–682.

229. Penzhorn, R. D. *Alternative Processes for the Long-Term Storage of Kr-85*; Kernforschungszentrum Karlsruhe GmbH: Germany, 1977.

230. Knecht, D. A. Evaluation of Methods for Immobilizing Krypton-85. *Trans. Am. Nucl. Soc.* **1977**, *27*, 444–445.

231. Miyake, M.; Konishi, T.; Suzuki, T.; Osada, S.; Kojima, H. Fixation of Krypton in Type-A Zeolites and Its Leakage Characteristics. *Zeolites* **1984**, *4*, 291–294.

232. Gombert, D. *Appendixes for Global Nuclear Energy Partnership Integrated Waste Management Strategy Waste Treatment Baseline Study*; Idaho National Laboratory, 2007.

233. Jubin, R. T.; Bruffey, S. H. Analysis of Legacy ^{85}Kr Waste Form Samples-16319. Annual Waste Management Conference (WM2016), Phoenix, Arizona. 2016.

234. Jubin, R. T. *Milestone Report-M4FT-15OR03120210-Multi-lab Analytical Plan for Analysis of Legacy ^{85}Kr Samples*; 2015.

235. Jubin, R. T.; Strachan, D. *Assessments and Options for Removal and Immobilization of Volatile Radionuclides from the Processing of Used Nuclear Fuel*; 2015.

236. Mueller, U.; Schubert, M.; Teich, F.; Puetter, H.; Schierle-Arndt, K.; Pastre, J. Metal–Organic Frameworks—Prospective Industrial Applications. *J. Mater. Chem.* **2006**, *16*, 626–636.

237. Barrer, R. M.; Vaughan, D. E. W. Trapping of Inert Gases in Sodalite and Cancrinite Crystals. *J. Phys. Chem. Solid* **1971**, *32*, 731–743.

238. Barrer, R. M.; Vaughan, D. E. W. Trapping and Diffusion of Rare Gases in Phillipsite, Zeolite K–M and Other Silicates. *Trans. Faraday Soc.* **1971**, *67*, 2129–2136.

239. Ho, T. M.; Howes, T.; Bhandari, B. Encapsulation of Gases in Powder Solid Matrices and Their Applications: A Review. *Powder Technol.* **2014**, *259*, 87–108.

240. Marks, N.; Carter, D.; Sassi, M.; Rohl, A.; Sickafus, K.; Uberuaga, B.; Stanek, C. Chemical Evolution via Beta Decay: A Case Study in Strontium-90. *J. Phys. Condens. Matter* **2013**, *25*, 065504.

241. Weckhuysen, B. M.; Yu, J. Recent Advances in Zeolite Chemistry and Catalysis. *Chem. Soc. Rev.* **2015**, *44*, 7022–7024.

242. Lee, H. Y.; Kim, H. S.; Jeong, H.-K.; Park, M.; Chung, D.-Y.; Lee, K.-Y.; Lee, E.-H.; Lim, W. T. Selective Removal of Radioactive Cesium from Nuclear Waste by Zeolites: On the Origin of Cesium Selectivity Revealed by Systematic Crystallographic Studies. *J. Phys. Chem.* **2017**, *121*, 10594–10608.

243. Liang, J.; Li, J.; Li, X.; Liu, K.; Wu, L.; Shan, G. The Sorption Behavior of **CHA**-Type Zeolite for Removing Radioactive Strontium from Aqueous Solutions. *Separ. Purif. Technol.* **2020**, *230*, 115874.

244. Carey, T.; Corma, A.; Rey, F.; Tang, C. C.; Hriljac, J. A.; Anderson, P. A. The Effect of Extra Framework Species on the Intrinsic Negative Thermal Expansion Property of Zeolites with the **LTA** Topology. *Chem. Commun.* **2012**, *48*, 5829–5831.

245. Leardini, L.; Martucci, A.; Cruciani, G. The Unusual Thermal Expansion of Pure Silica Sodalite Probed by *in situ* Time-Resolved Synchrotron Powder Diffraction. *Micropor. Mesopor. Mater.* **2012**, *151*, 163–171.

246. Attfield, M. P.; Sleight, A. W. Strong Negative Thermal Expansion in Siliceous Faujasite. *Chem. Commun.* **1998**, 601–602.

247. Woodcock, D. A.; Lightfood, P. Negative Thermal Expansion in the Siliceous Zeolites Chabazite and ITQ-4: A Neutron Powder Diffraction Study. *Chem. Mater.* **1999**, *11*, 2508–2514.

248. Bhange, D. S.; Ramaswamy, V. Negative Thermal Expansion in Silicalite-1 and Zirconium Silicalite-1 Having **MFI** Structure. *Materials Research Bulletin* **2006**, *41*, 1392–1402.

249. Bhange, D. S.; Ramaswamy, V. Thermal Expansion Studies of Silicalite-2 Molecular Sieves of **MEL** (ZSM-11) Topology. *J. Porous Mater.* **2012**, *19*, 301–305.

250. Bruffey, S. H.; Jubin, R. T. Analysis of Krypton-85 Legacy Waste Forms: Part I. *Nucl. Technol.* **2017**, *200*, 159–169.

251. Jubin, R. T.; Bruffey, S. H. Analysis of Krypton-85 Legacy Waste Forms: Part II. *Nucl. Technol.* **2018**, *205*, 830–846.

252. Pluth, J. J.; Smith, J. V. Accurate Redetermination of Crystal Structure of Dehydrated Zeolite A. Absence of Near Zero Coordination of Sodium. Refinement of Si,Al-Ordered Superstructure. *J. Am. Chem. Soc.* **1980**, *102*, 4704–4708.

253. Mills, G.; Jónsson, H.; Schenter, G. K. Reversible Work Transition State Theory: Application to Dissociative Adsorption of Hydrogen. *Surf. Sci.* **1995**, *324*, 305–337.

254. Mills, G.; Jónsson, H. Quantum and Thermal Effects in H_2 Dissociative Adsorption: Evaluation of Free Energy Barriers in Multidimensional Quantum Systems. *Phys. Rev. Lett.* **1994**, *72*, 1124–1127.

255. Henkelman, G.; Uberuaga, B. P.; Jónsson, H. A Climbing Image Nudged Elastic Band Method for Finding Saddle Points and Minimum Energy Paths. *J. Chem. Phys.* **2000**, *113*, 9901–9904.

256. Viswanathan, U.; Fermann, J. T.; Toy, L. K.; Auerbach, S. M.; Vreven, T.; Frisch, M. J. Modeling Proton Jumps in HY Zeolite: Effects of Acid Site Heterogeneity. *J. Phys. Chem. C* **2007**, *111*, 18341–18347.

257. Jones, A. J.; Carr, R. T.; Zones, S. I.; Iglesia, E. Acid Strength and Solvation in Catalysis by **MFI** Zeolites and Effects of the Identity, Concentration and Location of Framework Heteroatoms. *J. Catal.* **2014**, *312*, 58–68.

258. Vreven, T.; Morokuma, K.; Farkas, Ö.; Schlegel, H. B.; Frisch, M. J. Geometry Optimization with QM/MM, ONIOM, and Other Combined Methods. I. Microiterations and Constraints. *J. Comput. Chem.* **2003**, *24*, 760–769.

259. Dapprich, S.; Komáromi, I.; Byun, K.; Morokuma, K.; Frisch, M. J. A New ONIOM Implementation in Gaussian98. Part I. The Calculation of Energies, Gradients, Vibrational Frequencies and Electric Field Derivatives. *J. Mol. Struct.* **1999**, *461–462*, 1–21.

260. Frisch, M. J.; Trucks, G. W.; Schlegel, H. B.; Scuseria, G. E.; Robb, M. A.; Cheeseman, J. R.; Scalmani, G.; Barone, V.; Petersson, G. A.; Nakatsuji, H.; Li, X.; Caricato, M.; Marenich, A. V.; Bloino, J.; Janesko, B. G.; Gomperts, R.; Mennucci, B.; Hratchian, H. P.; Ortiz, J. V.; Izmaylov, A. F.; Sonnenberg, J. L.; Williams-Young, D.; Ding, F.; Lipparini, F.; Egidi, F.; Goings, J.; Peng, B.; Petrone, A.; Henderson, T.; Ranasinghe, D.; Zakrzewski, V. G.; Gao, J.; Rega, N.; Zheng, G.; Liang, W.; Hada, M.; Ehara, M.; Toyota, K.; Fukuda, R.; Hasegawa, J.; Ishida, M.; Nakajima, T.; Honda, Y.;

Kitao, O.; Nakai, H.; Vreven, T.; Throssell, K.; Montgomery, J. A., Jr.; Peralta, J. E.; Ogliaro, F.; Bearpark, M. J.; Heyd, J. J.; Brothers, E. N.; Kudin, K. N.; Staroverov, V. N.; Keith, T. A.; Kobayashi, R.; Normand, J.; Raghavachari, K.; Rendell, A. P.; Burant, J. C.; Iyengar, S. S.; Tomasi, J.; Cossi, M.; Millam, J. M.; Klene, M.; Adamo, C.; Cammi, R.; Ochterski, J. W.; Martin, R. L.; Morokuma, K.; Farkas, O.; Foresman, J. B.; Fox, D. J. Gaussian~16 Revision B.01. 2016; Gaussian Inc. Wallingford CT.

261. Rappé, A. K.; Casewit, C. J.; Colwell, K.; Goddard III, W. A.; Skiff, W. M. UFF, a Full Periodic Table Force Field for Molecular Mechanics and Molecular Dynamics Simulations. *J. Am. Chem. Soc.* **1992**, *114*, 10024–10035.

262. Lee, C.; Yang, W.; Parr, R. G. Development of the Colle-Salvetti Correlation-Energy Formula into a Functional of the Electron Density. *Phys. Rev. B* **1988**, *37*, 785–789.

263. Krishnan, R.; Binkley, J. S.; Seeger, R.; Pople, J. A. Self-Consistent Molecular Orbital Methods. XX. A Basis Set for Correlated Wave Functions. *J. Chem. Phys.* **1980**, *72*, 650–654.

264. Hehre, W. J.; Ditchfield, R.; Pople, J. A. Self-Consistent Molecular Orbital Methods. XII. Further Extensions of Gaussian-Type Basis Sets for Use in Molecular Orbital Studies of Organic Molecules. *J. Chem. Phys.* **1972**, *56*, 2257–2261.

265. Hariharan, P. C.; Pople, J. A. The Influence of Polarization Functions on Molecular Orbital Hydrogenation Energies. *Theor. Chim. Acta* **1973**, *28*, 213–222.

266. Schuchardt, K. L.; Didier, B. T.; Elsethagen, T.; Sun, L.; Gurumoorthi, V.; Chase, J.; Li, J.; Windus, T. L. Basis Set Exchange: A Community Database for Computational Sciences. *J. Chem. Info. Mod* **2007**, *47*, 1045–1052.

267. Fuentealba, P.; Preuss, H.; Stoll, H.; Szentpály, L. V. A Proper Account of Core-polarization with Pseudopotentials: Single Valence-Electron Alkali Compounds. *Chem. Phys. Lett.* **1982**, *89*, 418–422.

268. Sung, C.-Y.; Broadbelt, L. J.; Snurr, R. Q. A DFT Study of Adsorption of Intermediates in the NO_x Reduction Pathway Over BaNaY Zeolites. *Catal. Today* **2008**, *136*, 64–75.

269. Andersson, M. P.; Uvdal, P. New Scale Factors for Harmonic Vibrational Frequencies Using the B3LYP Density Functional Method with the Triple-ζ Basis Set 6-311+G(d,p). *J. Phys. Chem.* **2005**, *109*, 2937–2941.

270. Fermann, J. T.; Blanco, C.; Auerbach, S. Modeling Proton Mobility in Acidic Zeolite Clusters. I. Convergence of Transition State Parameters from Quantum Chemistry. *J. Chem. Phys.* **2000**, *112*, 6779–6786.

271. Vreven, T.; Frisch, M. J.; Kudin, K. N.; Schlegel, H. B.; Morokuma, K. Geometry Optimization with QM/MM Methods II: Explicit Quadratic Coupling. *Mol. Phys.* **2006**, *104*, 701–714.

272. Vreven, T.; Byun, K. S.; Komáromi, I.; Dapprich, S.; Montgomery, J. A.; Morokuma, K.; Frisch, M. J. Combining Quantum Mechanics Methods with Molecular Mechanics Methods in ONIOM. *J. Chem. Theor. Comput.* **2006**, *2*, 815–826.

273. Schlegel, H. B. Optimization of Equilibrium Geometries and Transition Structures. *J. Comput. Chem.* **1982**, *3*, 214–218.

274. Eyring, H. The Activated Complex in Chemical Reactions. *J. Chem. Phys.* **1935**, *3*, 107–115.

275. Eyring, H. The Theory of Absolute Reaction Rates. *Trans. Faraday Soc.* **1938**, *34*, 41–48.

276. Evans, M. G.; Polanyi, M. Some Applications of the Transition State Method to the Calculation of Reaction Velocities, Especially in Solution. *Trans. Faraday Soc.* **1935**, *31*, 875–894.

277. Wigner, E. The Transition State Method. *Trans. Faraday Soc.* **1938**, *34*, 29–41.

278. Vineyard, G. H. Frequency Factors and Isotope Effects in Solid State Rate Processes. *J. Phys. Chem. Solid* **1957**, *3*, 121–127.

279. Heinola, K.; Ahlgren, T. Diffusion of Hydrogen in BCC Tungsten Studied with First Principle Calculations. *J. Appl. Phys.* **2010**, *107*, 113531.

280. Li, J. AtomEye: An Efficient Atomistic Configuration Viewer. *Model. Simulat. Mater. Sci. Eng.* **2003**, *11*, 173–177, `http://li.mit.edu/Archive/Graphics/A/`.

281. Barone, V.; Casarin, M.; Forrer, D.; Pavone, M.; Sambi, M.; Vittadini, A. Role and Effective Treatment of Dispersive Forces in Materials: Polyethylene and Graphite Crystals as Test Cases. *J. Comput. Chem.* **2009**, *30*, 934–939.

282. Grimme, S. Semiempirical GGA-Type Density Functional Constructed with a Long-Range Dispersion Correction. *J. Comput. Chem.* **2006**, *27*, 1787–1799.

283. Jordan, E.; Bell, R. G.; Wilmer, D.; Koller, H. Anion-Promoted Cation Motion and Conduction in Zeolites. *J. Am. Chem. Soc.* **2006**, *128*, 558–567.

284. Zhang, I. Y.; Wu, J.; Xu, X. Extending the Reliability and Applicability of B3LYP. *Chem. Commun.* **2010**, *46*, 3057–3070.

285. Latturner, S. E. Modification of the Electronic Properties of Inorganic Cage Compounds: Tuning Guest-Framework Interactions in Sodalites and Clathrates. Ph.D. Dissertation, University of California, Santa Barbara, 2000.

286. Król, M. Natural vs. Synthetic Zeolites. *Crystals* **2020**, *10*, 622–629.

287. Park, M.; Choi, C. L.; Lim, W. T.; Kim, M. C.; Choi, J.; Heo, N. H. Molten-Salt Method for the Synthesis of Zeolitic Materials: I. Zeolite Formation in Alkaline Molten-Salt System. *Micropor. Mesopor. Mater.* **2000**, *37*, 81–89.

288. Zhang, M.; Zhang, H.; Xu, D.; Han, L.; Niu, D.; Tian, B.; Zhang, J.; Zhang, L.; Wu, W. Removal of Ammonium from Aqueous Solutions Using Zeolite Synthesized from Fly Ash by a Fusion Method. *Desalination* **2011**, *271*, 111–121.

289. Takeda, H.; Hashimoto, S.; Yokoyama, H.; Honda, S.; Iwamoto, Y. Characterization of Zeolite in Zeolite-Geopolymer Hybrid Bulk Materials Derived from Kaolinitic Clays. *Materials* **2013**, *6*, 1767–1778.

290. Querol, X.; Alastuey, A.; López-Soler, A.; Plana, F.; Andrés, J. M.; Juan, R.; Ferrer, P.; Ruiz, C. R. A Fast Method for Recycling Fly Ash: Microwave-Assisted Zeolite Synthesis. *Environ. Sci. Technol.* **1997**, *31*, 2527–2533.

291. Tanaka, H.; Eguchi, H.; Fujimoto, S.; Hino, R. Two-Step Process for Synthesis of a Single Phase Na-A Zeolite from Coal Fly Ash by Dialysis. *Fuel* **2006**, *85*, 1329–1334.

292. Winnefeld, F.; Barlag, S. Calorimetric and Thermogravimetric Study on the Influence of Calcium Sulfate on the Hydration of Ye'elimite. *J. Therm. Anal. Calorim.* **2010**, *101*, 949–957.

293. Chester, A. W.; Derouane, E. G. *Zeolite Characterization and Catalysis*; Springer: New York, 2009; Vol. 360.

294. Sulochanadev, B. Structure and Regulation of Yeast Glycogen Synthase. Ph.D. Dissertation, Indiana University, 2010.

295. Bloch, F. Nuclear Induction. *Phys. Rev.* **1946**, *70*, 460–474.

296. Purcell, E. M.; Torrey, H. C.; Pound, R. V. Resonance Absorption by Nuclear Magnetic Moments in a Solid. *Phys. Rev.* **1946**, *69*, 37–38.

297. Stepanov, A. In *Zeolites and Zeolite-Like Materials*; Sels, B. F., Kustov, L. M., Eds.; Elsevier: Amsterdam, 2016; pp 137–188.

298. Wang, J. Thermodynamics of Dehydration and Hydration in Natrolite and Analcime. M.S. Thesis, University of Florida, 2006.

299. Borhade, A.; G. Wakchaure, S.; G. Dholi, A. Synthesis, Infrared and X-Ray Diffraction Studies of Mixed Halogen Sodalites and Sodalites Containing Silver Derivatives. *Indian. J. Chem.* **2007**, *46A*, 942–946.

VITA

Amir Mehdi Mofrad was born in Arak, Iran (pronounced e:ra:n). He moved with his family to Tehran at the age of four so his father could finish his doctoral studies in pathology. Amir obtained his B.S. in chemical engineering from Sharif University of Technology in 2014. He then moved to United States for his doctoral studies in chemical engineering in January 2015 at the University of Missouri in Columbia. During his studies as a Ph.D. student, he presented his work at three national conferences in the U.S. In 2018, he was elected by the Asian Affairs Center to be the lecturer of Aspen Plus for Korean exchange students. He was the recipient of the top poster presentation award at the Research and Creative Activities Forum (RCAF) held by Graduate Professional Council (GPC) in 2019. In addition, he was awarded the "People's Choice" award at the three-minute thesis (3MT) competition the same year. During the Spring 2020 semester at Mizzou, he received the "Outstanding Chemical Engineering Ph.D. Student" award. One of Amir's hobbies is to play pool. Throughout his time in graduate school, he participated in several tournaments held both at Mizzou and in Columbia, and won a couple of trophies. He will join Ted Besmann's group at University of South Carolina in Columbia (he really loves Columbia), where he will be working on predicting the thermodynamic properties of molten salts using electronic structure methods.